Studies of Ambient Organic and Inorganic Aerosol in Southern California

Thesis by

Joseph James Ensberg

In Partial Fulfillment of the Requirements

for the Degree of

Doctor of Philosophy

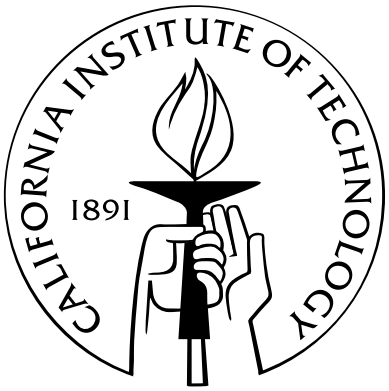

California Institute of Technology

Pasadena, California

2014

(Defended 14 March 2014)

To my beautiful wife, my wonderful family, and my amazing friends.

Acknowledgements

Extending my gratitude to the people I've encountered during my academic career is one of the greatest honors of my life.

I thank my graduate advisor, John Seinfeld, for being an outstanding mentor. I am grateful for the intellectual freedom John has given me to work on challenging projects with some of the smartest people I've ever met. In addition, John's open-door policy, fast email responses, and scientific expertise have been some of my greatest resources during my time at Caltech. Every accomplishment I have for the rest of my life will be in some way attributable to the skills I learned while I was in John's research group.

I thank my undergraduate advisor, Donald Dabdub, for also being an outstanding mentor, and for convincing me to pursue my PhD in Chemical Engineering at Caltech. It was during Donald's engineering programming courses at UCI that I realized I wanted my career to focus on numerical analysis. Donald has had a profound impact on my life, and I always try to emulate the passion with which he embraces research, as well as activities such as art, wine, chess, classical guitar, and world traveling. I hope I can have an equally positive impact on someone else's life.

I thank Marc Carreras-Sospedra for the incredible amount of help he gave me during my time in the CESLab at UCI, and for being a great guy. I am positive that one of the main reasons this thesis exists is because of Marc's day-to-day guidance with answering my engineering questions and helping me develop good coding practices.

I thank Rick Flagan and Paul Wennberg for serving on my PhD committee, and for always being available for scientific discussions. I hope that Paul frames the 20 dollar bill he took from me when I lost our bet on whether it would be possible to measure SOA mass yields on the order

of 100% from single-ring aromatic oxidation. I thank Jose Jimenez, Patrick Hayes, and all of the other scientists and engineers I have collaborated with for the constructive input they've given me regarding the studies within this thesis. From the Chemical Engineering staff, I'd also like to thank Suresh Guptha, Yvette Grant, and Kathy Bubash for all of their help.

I thank the modelers that were here when I first arrived: Havala Pye, Zach Lebo, and Jean Chen. Specifically, I am indebted to Havala for training me when I first arrived at Caltech, and for always being available when I needed advice. I thank Renee McVay, Bill Napier, and Jennifer Walker, the next generation of modelers, for learning everything I could teach so quickly and easily. I thank Jill Craven for having one of the best personalities I have ever encountered, and for all of the priceless conversations we have had over the years. I also thank Jill Craven and Andrew Metcalf for helping me get through the gauntlet that was my first CalNex project. I thank Andi Zuend and Manabu Shiraiwa for all of the modeling discussions we've had, and for showing me that some of the most productive people I've ever met take regular coffee breaks every day. I thank Lindsay Yee, Christine Loza, Kate Schilling, Matt Coggon, and Xuan Zhang for giving me tremendous insight into the experimental side of the group. I also thank the rest of the Seinfeld/Flagan research group, both present and past: Puneet Chhabra, Jason Suratt, ManNin Chan, Andy Downard, Jason Gamba, Mandy Grantz, Xerxes Lopez-Yglesias, Johannes Leppa, Wilton Mui, Becky Schwantes, Natasha Hodas, Scott Hersey, Tran Nguyen, Kelvin Bates, and Arthur Chan, all of whom have done their part to ensure Caltech's scientific reputation is second to none.

Special thanks to the ChEESE(G)PSer group, consisting of Chemical Engineering, Environmental Science and Engineering, Geology, and Planetary Science graduate students for all of the fun lunches and all of the hilarious softball games.

I thank my entire Chemical Engineering class: Kai Yuet, Amy Fu, Devin Wiley, Brett Babin, Jeff Bosco, Denise Ko, Clint Regan (honorary ChE), and Tristan Day. I extend a special thanks to my drinking buddy Tristan for all of our unforgettable conversations, and for being one of my groomsmen.

I thank the Aspire community for being a wonderful group of people and for providing a quiet

place to gather my thoughts every week. The Caltech Counseling Center also has my sincere gratitude for helping me during an especially trying time, and for helping so many other Caltech students deal with a variety of emotional challenges.

It is impossible to convey adequately how much I owe to my wonderful family. The love and support my family provides are two of the things I value most in my life. From a young age, my parents, Stephen and Theresa Ensberg, instilled in me my love of learning. Specifically, my mother taught me the value of free time and of thinking creatively, and I attribute a great portion of my success to this, as well as to her unflagging availability during my childhood. My father taught me the value of consistency, stability, and of having a solid work ethic. Following my father's example, I have always tried to interact with, and learn from, as many scientific and non-scientific people as possible. I attribute an enormous fraction of my success to the lessons I learned from both my parents. I thank my brother, Luke, for his advice throughout the years and for sharing my love of engineering, and my sister, Vessela, for her support and for giving me her insight into graduate school and finding a career. I thank my extended family for all of their love and support. I thank my grandparents, Stuart and Gloria Ensberg, for all of the encouragement they've given me throughout the years and for their generous contributions to my education. I also thank Zemin, Yiming, and David Jiang for welcoming me into their family and for their support throughout my graduate school experience.

Lastly, I thank my loving wife, Jenny. You have always been my greatest source of joy and support. I love you and I can't wait to begin the next chapter of our life together. We made it!

Abstract

The negative impacts of ambient aerosol particles, or particulate matter (PM), on human health and climate are well recognized. However, owing to the complexity of aerosol particle formation and chemical evolution, emissions control strategies remain difficult to develop in a cost effective manner. In this work, three studies are presented to address several key issues currently stymieing California's efforts to continue improving its air quality.

Gas-phase organic mass (GPOM) and CO emission factors are used in conjunction with measured enhancements in oxygenated organic aerosol (OOA) relative to CO to quantify the significant lack of closure between expected and observed organic aerosol concentrations attributable to fossil-fuel emissions. Two possible conclusions emerge from the analysis to yield consistency with the ambient organic data: (1) vehicular emissions are not a dominant source of anthropogenic fossil SOA in the Los Angeles Basin, or (2) the ambient SOA mass yields used to determine th SOA formation potential of vehicular emissions are substantially higher than those derived from laboratory chamber studies. Additional laboratory chamber studies confirm that, owing to vapor-phase wall loss, the SOA mass yields currently used in virtually all 3D chemical transport models are biased low by as much as a factor of 4. Furthermore, predictions from the Statistical Oxidation Model suggest that this bias could be as high as a factor of $\sim$8 if the influence of the chamber walls could be removed entirely.

Once vapor-phase wall loss has been accounted for in a new suite of laboratory chamber experiments, the SOA parameterizations within atmospheric chemical transport models should also be updated. To address the numerical challenges of implementing the next generation of SOA models in atmospheric chemical transport models, a novel mathematical framework, termed the Moment

Method, is designed and presented. Assessment of the Moment Method strengths and weaknesses provide valuable insight that can guide future development of SOA modules for atmospheric CTMs.

Finally, regional inorganic aerosol formation and evolution is investigated via detailed comparison of predictions from the Community Multiscale Air Quality (CMAQ version 4.7.1) model against a suite of airborne and ground-based meteorological measurements, gas- and aerosol-phase inorganic measurements, and black carbon (BC) measurements over Southern California during the CalNex field campaign in May/June 2010. Results suggests that continuing to target sulfur emissions with the hopes of reducing ambient PM concentrations may not the most effective strategy for Southern California. Instead, targeting dairy emissions is likely to be an effective strategy for substantially reducing ammonium nitrate concentrations in the eastern part of the Los Angeles Basin.

Contents

List of Tables

List of Figures

Chapter 1

Introduction

Atmospheric aerosols, liquid and/or solid particulate matter (PM) suspended in ambient air, play a central role in climate change and human health. Specifically, the total mass concentration, size distribution, and chemical composition of aerosol particles determine their ability to influence cloud formation and the extent to which they reduce visibility by scattering and/or absorbing light. With respect to human health, inhalation of any aerosol population has hazardous health effects. However, fine particles (particles less than 2.5 μm in vacuum-aerodynamic diameter) are able to travel deeply into the human respiratory system and have been linked to irritation, reduced lung function, irregular heartbeat, heart attacks, and premature death (USEPA, 2004).

The physical (e.g., size, number concentration) and chemical (e.g., composition, oxidation state) characteristics of ambient aerosol particles are governed by the relative strength of various emission sources, both anthropogenic (e.g., vehicular emissions) and biogenic (e.g., volcanic, lightning, terrestrial-biogenic, and sea-spray emissions), and the local meteorology, such as boundary layer height, incident sunlight, cloud coverage, wind speed, temperature, and relative humidity. The relative importance of each emission source is obscured by complex, non-linear, and often unknown chemistry and microphysics that convert gaseous species into secondary inorganic and organic aerosols. An additional complicating factor is that, owing to the relatively long atmospheric lifetime of aerosols (days to weeks), the air quality of certain regions may be as sensitive to local emissions as it is to emissions occurring 100-1000s of kilometers upwind. All of these factors make improving air quality challenging.

A conceptually trivial solution to reducing the controllable fraction of ambient aerosol concentrations would be to cease all anthropogenic emissions. However, when formulating emission regulations and pollution control strategies, consideration should be given to financial factors such as the cost and availability of current emission reduction technologies (e.g., perfect catalytic converters, battery-powered transportation, effective carbon sequestration), the cost of fuel processing (e.g., petroleum, coal, hydrogen), and the limited funding available for atmospheric research and the development of new emission technologies. Because of these issues, removing all anthropogenic emissions is currently not technologically/economically feasible, especially in developing countries such as China and In-

dia. Therefore, the challenge is to improve air quality as efficiently, and therefore inexpensively, as possible.

To this end, Chapter 2 addresses the current debate in California regarding the relative importance of emissions from gasoline- and diesel-fueled vehicles. Based on the highly resolved speciation profiles of gasoline and diesel fuel, *Gentner et al.* (2012) estimated that diesel exhaust is responsible for 2 to 7 times more SOA than gasoline exhaust in California. On the other hand, from measurements of the weekday-weekend cycle of organic aerosol, black carbon, single-ring aromatic hydrocarbons, CO, and oxides of nitrogen ($NO_x = NO + NO_2$) in the Los Angeles Basin, *Bahreini et al.* (2012) and *Hayes et al.* (2013) conclude that emissions from gasoline-fueled vehicles dominate the SOA budget. In Chapter 2, measurements from both studies are placed in a unified context from which two possible conclusions emerge: (1) ambient SOA mass yields are significantly higher (e.g., factor of $\sim$5) than those derived from typical laboratory chamber experiments, or (2) vehicular emissions are not a dominant source of oxygenated organic aerosol attributable to fossil activity. Although neither possibility can be categorically ruled out at this point, additional laboratory chamber studies, presented in Appendix A, confirm that, owing to vapor-phase wall loss, the toluene SOA mass yields derived using historical experimental protocols are biased low by as much as a factor of 4. Furthermore, predictions from the Statistical Oxidation Model of *Cappa and Wilson* (2012) suggest that this bias could be as high as a factor of $\sim$8 if the influence of the chamber walls could be removed entirely. This finding likely explains persistent and significant underprediction of SOA levels by existing atmospheric models in urban areas (*de Gouw et al.*, 2005; *Volkamer et al.*, 2006; *Johnson et al.*, 2006; *de Gouw et al.*, 2008; *Kleinman et al.*, 2008; *Matsui et al.*, 2009).

Chapter 3 provides insight into the numerical challenges of implementing the next-generation SOA models into atmospheric chemical transport models. Significant progress has been made in the development of 2-Dimensional models to represent the formation and evolution of SOA (*Pankow and Barsanti*, 2009; *Donahue et al.*, 2011; *Cappa and Wilson*, 2012; *Zhang and Seinfeld*, 2012). However, the gap between the new class of 2D SOA models and the computational requirements of 3D CTMs has not been bridged. Specifically, each SOA model, except the FGOM of *Zhang and Seinfeld* (2012),

represents the evolution of the SOA-forming chemistry via a matrix of properties. In a 3D CTM, the advection-diffusion equation requires each matrix to be defined over the entire 3D grid so that matrices can be transported between grid cells. Since a typical 3D grid may contain thousands of grid cells, this poses a severe computational burden. Consequently, the Odum 2-product model (*Odum et al.*, 1996), although now out of date, remains the most commonly used SOA parameterization in state-of-the-art 3D CTMs (*Barsanti et al.*, 2013). Therefore, computational simplifications need to be devised to implement any of the 2D SOA models in a 3D model. In Chapter 3, we describe a new computational approach, termed the Oxidation State/Volatility Moment Method (hereafter referred to as the Moment Method). We focus on the 2D-VBS as exemplary of the new class of SOA models for demonstrating the strengths and limitations of the new approach.

In Chapter 4, predictions from the Community Multiscale Air Quality (CMAQ version 4.7.1) model are evaluated against a suite of airborne and ground-based measurements comprising meteorological variables, inorganic gas- and aerosol-phase compositions, and black carbon (BC) concentrations over Southern California during the CalNex field campaign in May/June 2010. Ground-based measurements are from the CalNex Pasadena ground site, and airborne measurements took place onboard the Center for Interdisciplinary Remotely-Piloted Aircraft Studies (CIRPAS) Navy Twin Otter and the NOAA WP-3D aircraft. With the current sulfur emission inventory based on emission factors from 2008, long-range transport of sulfate accounts for a substantial fraction (22-82%) of the sulfate in Los Angeles Basin. This suggests that targeting sulfur emissions with the hopes of reducing ambient PM concentrations is not the most effective strategy for Southern California. Severely underpredicted NH_3 emissions from dairy facilities, and not the exclusion of crustal species, are the dominant source of measurement/model disagreement in the eastern Los Angeles Basin. Therefore, targeting dairy emissions is likely to be an effective strategy for substantially reducing ammonium nitrate concentrations in the eastern part of the Los Angeles Basin. Adding gas-phase NH_3 measurements and size-resolved measurements, up to 10 μm, of nitrate and various cations (e.g., Na^+, Ca^{2+}, K^+, Mg^{2+}) to routine monitoring stations in the Los Angeles Basin would facilitate interpreting day-to-day fluctuations in fine and coarse inorganic aerosol greatly. Future work should focus

on improving and assessing the treatment of anthropogenic and fugitive dust emissions, as well as continuing to characterize the fraction of ambient particulate matter attributable to local emissions versus long-range transport.

Bibliography

Bahreini, R., Middlebrook, A. M., de Gouw, J. A., Warneke, C., Trainer, M., Brock, C. A., Stark, H., Brown, S. S., Dube, W. P., Gilman, J. B., Hall, K., Holloway, J. S., Kuster, W. C., Perring, A. E., Prevot, A. S. H., Schwarz, J. P., Spackman, J. R., Szidat, S., Wagner, N. L., Weber, R. J., Zotter, P., and Parrish D. D.: Gasoline emissions dominate over diesel in formation of secondary organic aerosol mass, *Geophys. Res. Lett.*, *39*, L06805, 2012.

Barsanti, K. C., Carlton, A. G., and Chung, S. H. (2013), Analyzing experimental data and model parameters: implications for predictions of SOA using chemical transport models, *Atmos. Chem. Phys.*, *13*, 12073-12088.

Cappa, C. and Wilson, K. R. (2012), Multi-generation gas-phase oxidation, equilibrium partitioning, and the formation and evolution of secondary organic aerosol, *Atmos. Chem. Phys.*, *12*, 9505-9528.

de Gouw, J. A., Middlebrook, A. M., Warneke, C., Goldan, P. D., Kuster, W. C., Roberts, J. M., Fehsenfeld, F. C., Worsnop, D. R., Canagaratna, M. R., Pszenny, A. A. P., Keene, W. C., Marchewka, M., Bertman, S. B., and Bates T. S.: Budget of organic carbon in a polluted atmosphere: Results from the New England Air Quality Study in 2002, *J. Geophys. Res.-Atmos.*, *110*, D16305, 2005.

de Gouw, J. A., Brock, C. A., Atlas, E. L., Bates, T. S., Fehsenfeld, F. C., Goldan, P. D., Holloway, J. S., Kuster,Lerner, B. M., Matthew, B. M., Middlebrook, A. M., Onasch, T. B., Peltier, R. E., Quinn, P. K., Senff, C. J., Stohl, A., Sullivan, A. P., Trainer, M., Warneke, C., Weber, R. J., and Williams, E. J. : Sources of particulate matter in the northeastern United States: 1. Direct emissions and secondary formation of organic matter in urban plumes, *J. Geophys. Res.-Atmos.*, *113*, D08301, 2008.

Donahue, N. M., Epstein, S. A., Pandis, S. N., and Robinson, A. L. (2011), A two-dimensional volatility basis set: 1. organic-aerosol mixing thermodynamics, *Atmos. Chem. Phys.*, *11*, 3303-3318.

Gentner, D. R., Isaacman, G., Worton, D. R., Chan, A. W. H., Dallmann, T. R., Davis, L., Liu, S., Day, D. A., Russell, L. M., Wilson,Weber, R., uha, A., Harley, R. A., and Goldstein A. H.: Elucidating secondary organic aerosol from diesel and gasoline vehicles through detailed characterization of organic carbon emissions, *PNAS*, *109*, 18318–18323, 2012.

Hayes, P. L., Ortega, A. M., Cubison, M. J., Froyd, K. D., Zhao, Y., Cliff, S. S, Hu, W. W., Toohey, D. W, Flynn, J. H., Lefer, B. L., Grossberg, N., Alvarez, S., Rappengluck, B., Taylor, J. W., Allan, J. D., Holloway, J. S., Gilman, J. B., Kuster, W. C., de Gouw, J. A., Massoli, P., Zhang, X., Liu, J., Weber, R. J., Corrigan, A. L., Russell, L. M., Isaacman, G., Worton, D. R., Kreisberg, N. M., Goldstein, A. H., Thalman, R., Waxman, E. M., Volkamer, R., Lin, Y. H., Surratt, J. D., Kleindienst, T. E., Offenberg, J. H., Dusanter, S., Griffith, S., Stevens, P. S., Brioude, J., Angevine, W. M., Jimenez, J. L. : Organic Aerosol Composition and Sources in Pasadena, California during the 2010 CalNex Campaign , *J. Geophys. Res.-Atmos.*, *118*, 2013.

Johnson, D., Utembe, S. R., Jenkin, M. E., Derwent, R. G., Hayman, G. D., Alfarra, M. R., Coe, H., and McFiggans, G. : Simulating regional scale secondary organic aerosol formation during the TORCH 2003 campaign in the southern UK, *Atmos. Chem. Phys.*, *6*, 403-418, 2006.

Kleinman, L. I., Springston, S. R., Daum, P. H., Lee, Y. N., Nunnermacker, L. J., Senum, G. I., Wang, J., Weinstein-Lloyd, J., Alexander, M. L., Hubbe, J., Ortega, J., Canagaratna, M. R., and Jayne, J. : The time evolution of aerosol composition over the Mexico City plateau, *Atmos. Chem. Phys.*, *8*, 1559–1575, 2008.

Matsui, H., Koike, M., Takegawa, N., Kondo, Y., Griffin, R. J., Miyazaki, Y., Yokouchi, Y., and Ohara, T.: Secondary organic aerosol formation in urban air: Temporal variations and possible contributions from unidentified hydrocarbons, *J. Geophys. Res.-Atmos.*, *114*, D04201, 2009.

Odum, J. R., Hoffmann, T.,Bowman, F., Collins, D., Flagan, R. C., Seinfeld, J. H. (1996), Gas/Particle Partitioning and Secondary Organic Aerosol Yields, *Environ. Sci. Technol.*, *30*, 2580–2585.

Pankow, J. F., and Barsanti, K. C. (2009), The carbon number-polarity grid: A means to manage the complexity of the mix of organic compounds when modeling atmospheric organic particulate matter, *Atmos. Environ.*, *43*, 2829-2835.

United States Environmental Protection Agency (USEPA): Air Quality Criteria for Particulate Matter (Final Report, Oct 2004), Environmental Protection Agency, Washington, DC, EPA 600/P-99/002aF-bF, 2004.

Volkamer, R., Jimenez, J. L., San Martini, F., Dzepina, K., Zhang, Q., Salcedo, D., Molina, L. T., Worsnop, D. R., and Molina, M. J. : Secondary organic aerosol formation from anthropogenic air pollution: Rapid and higher than expected, *Geophys. Res. Lett.*, *33*, L17811, 2006.

Zhang, X., and Seinfeld, J. H. (2012), A Functional Group Oxidation Model (FGOM) for SOA formation and aging, *Atmos. Chem. Phys. Discuss.*, *12*, 32565-32611.

Chapter 2

Emission Factor Ratios, SOA Mass Yields, and the Impact of Vehicular Emissions on SOA Formation *

*Reproduced with permission from "Emission Factor Ratios, SOA Mass Yields, and the Impact of Vehicular Emissions on SOA Formation" by Ensberg, J. J., Hayes, P. L., Jimenez, J. L., Gilman, J. B., Kuster, W. C., de Gouw, J. A., Holloway, J. S., Gordon, T. D., Jathar, S., Robinson, A. L., and Seinfeld, J. H., *Atmospheric Chemistry and Physics*, 14, 2383-2397, doi:10.5194/acp-14-2383-2014.

2.1 Abstract

The underprediction of ambient secondary organic aerosol (SOA) levels by current atmospheric models in urban areas is well established, yet the cause of this underprediction remains elusive. Likewise, the relative contribution of emissions from gasoline- and diesel-fueled vehicles to the formation of SOA is generally unresolved. We investigate the source of these two discrepancies using data from the 2010 CalNex experiment carried out in the Los Angeles Basin (*Ryerson et al.*, 2013). Specifically, we use gas-phase organic mass (GPOM) and CO emission factors in conjunction with measured enhancements in oxygenated organic aerosol (OOA) relative to CO to quantify the significant lack of closure between expected and observed organic aerosol concentrations attributable to fossil-fuel emissions. Two possible conclusions emerge from the analysis to yield consistency with the ambient data: (1) vehicular emissions are not a dominant source of anthropogenic fossil SOA in the Los Angeles Basin, or (2) the ambient SOA mass yields used to determine SOA formation potential of vehicular emissions are substantially higher than those derived from laboratory chamber studies.

2.2 Introduction

Emissions in California have significantly decreased over time (*Warneke et al.*, 2012). However, two important issues concerning the sources of organic aerosol in urban areas remain generally unresolved: (1) What is the relative impact of emissions from gasoline- and diesel-fueled vehicles on the formation of secondary organic aerosol (SOA) (*Bahreini et al.*, 2012; *Gentner et al.*, 2012; *Hayes et al.*, 2013); (2) What is the cause of the significant underprediction of SOA levels by existing atmospheric models in urban areas (*de Gouw et al.*, 2005; *Volkamer et al.*, 2006; *Johnson et al.*, 2006; *de Gouw et al.*, 2008; *Kleinman et al.*, 2008; *Matsui et al.*, 2009)? We investigate the source of these two issues based on a detailed analysis of data in the Los Angeles atmosphere; the procedures we use to analyze these issues are likely to be applicable to major urban areas worldwide. Based on the highly resolved speciation profiles of gasoline and diesel fuel, *Gentner et al.* (2012) estimated that diesel exhaust is responsible for 2 to 7 times more SOA than gasoline exhaust in California. On the other hand, from

measurements of the weekday-weekend cycle of organic aerosol, black carbon, single-ring aromatic hydrocarbons, CO, and oxides of nitrogen (NO_x = NO + NO_2) in the Los Angeles Basin, *Bahreini et al.* (2012) and *Hayes et al.* (2013) conclude that emissions from gasoline-fueled vehicles dominate the SOA budget. Notably, the conclusions of *Bahreini et al.* (2012) and *Hayes et al.* (2013) are based on the observation that diesel activity has a clear weekday-weekend cycle, whereas measured CO mixing ratios and the enhancement of SOA with respect to CO exhibit virtually no weekday-weekend cycle when segregated by photochemical age. Nevertheless, as acknowledged by *Hayes et al.* (2013), the conclusions of *Bahreini et al.* (2012) and *Hayes et al.* (2013) presume that vehicular emissions are the dominant source of anthropogenic fossil SOA in the L.A. Basin.

2.3 Ambient Measurements

Ambient data (CO, NO_x, NO_y, O_3, OH, VOCs, submicron non-refractory (nrPM1) organic aerosol) at the Pasadena ground site were collected during the 2010 CalNex experiment (*Ryerson et al.*, 2013). The CalNex Pasadena ground site was located 18 km northeast of downtown Los Angeles on the California Institute of Technology (Caltech) campus in Pasadena, California (34.1406 N, 118.1225 W, 236 m above mean sea level). The measurement period was May 15 2010 00:00–June 16 2010 00:00 (local time). The prevailing wind direction during daytime in Pasadena was from the southwest due to the sea-breeze, which brought air masses from the Pacific Ocean across central Los Angeles to Pasadena.

CO concentrations were measured by two vacuum-UV resonance fluorescence instruments (AL5001 & AL5002, Aerolaser) (*Gerbig et al.*, 1999). CO emissions in Los Angeles are attributable almost exclusively to vehicular emissions (*Griffin et al.* (2007), `http://www.arb.ca.gov/app/emsinv/emssumcat.php`), with minor contributions from cooking and oxidation of biogenic emissions (*Hayes et al.*, 2013; *Allan et al.*, 2010). A Fluorescence Assay by Gas Expansion (FAGE) instrument was utilized to determine the OH concentration (*Dusanter et al.*, 2009). The concentration of O_3 was measured by UV differential absorption (49c Ozone Analyzer, Thermo Scientific). An in-situ Gas Chromatography Mass Spectrometry (GC-MS) instrument provided the mixing ratios for a variety of

VOCs (*Gilman et al.*, 2009). NO_x and NO_y concentrations were measured using chemiluminescence (42i- TL with Mo converter, Thermo Scientific), and NO_2 was measured with Cavity Enhanced Differential Optical Absorption Spectroscopy (CE-DOAS) (*Thalman and Volkamer*, 2010). Concentrations of submicron non-refractory (nrPM1) organic aerosol particles were measured using an Aerodyne High Resolution Time-of-Flight Aerosol Mass Spectrometer (hereinafter referred to as "AMS") (*DeCarlo et al.*, 2006). The OA mass spectral matrix was deconvolved into components using PMF, a receptor-based factorization model (*Paatero et al.*, 1994). The OA components from the PMF analysis were identified by their mass spectra, diurnal cycles, and elemental composition, as well as by the concentration ratios and correlations of their time series with tracers. These components are: (1) Hydrocarbon-like Organic Aerosol (HOA), (2) Cooking- Influenced Organic Aerosol (CIOA), (3) Local Organic Aerosol (LOA), (4) Semi-Volatile Oxygenated Organic Aerosol (SV-OOA), and (5) Low-Volatility Oxygenated Organic Aerosol (LV-OOA). The HOA component has been previously described as a surrogate for primary combustion OA, and the SV-OOA and LV-OOA components as surrogates for "fresher" and "aged" SOA, respectively. (*Zhang et al.*, 2007; *Aiken et al.*, 2008; *Jimenez et al.*, 2009; *Ulbrich et al.*, 2009). As discussed in *Hayes et al.* (2013), the LOA component exhibits high frequency fluctuations most likely resulting from local sources in close proximity to the Pasadena ground site. However, since LOA represents only ∼5% of the total OA budget, this factor is not considered further.

Figure 2.1 shows measured PMF factor concentrations normalized by CO enhancement (ΔCO is the difference between the ambient CO and the estimated background CO (105 ppb)) as functions of photochemical age (see *Hayes et al.* (2013) for a detailed description of how this figure was constructed). The photochemical age of the air mass over the Pasadena site was calculated by two methods: (1) from the ratio of 1,2,4-trimethylbenzene to benzene concentrations, as described in *Parrish et al.* (2007); and (2) by defining the photochemical age as $-\log_{10}(NO_x/NO_y)$ similar to *Kleinman et al.* (2008). Both methods give very similar results, and all photochemical ages were calculated for reference using an average OH radical concentration of 1.5×10^6 molecules cm^{-3}. For reference, the daily (day and night) OH radical concentration averaged over the entire campaign

at the Pasadena site was 1.3×10^6 molecules cm^{-3}. Note that the OH-exposure, which is fully constrained by the measured evolution of the benzene/trimethyl-benzene ratio, is the only quantity needed for calculating the fraction of VOC that has reacted (e.g. frac = (1 - exp(k OH-exposure)). Therefore, choosing a different OH radical concentration will not influence our results because the OH exposures remain the same. Owing to the formation of SOA, the OOA factors are enhanced (increased) with respect to ΔCO as the photochemical age of the air mass increases. As shown in Figure 2.1B, the enhancement of OOA (SV-OOA + LV-OOA) relative to ΔCO after 0.45 days of photochemical processing is 48 μg OOA sm^{-3} (ppmv CO)$^{-1}$ (48 is the difference between 58, which occurs at 0.45 days, and 10, which occurs at 0 days), whereas the ratio of POA (HOA + CIOA) to ΔCO is relatively constant (i.e. no enhancement) at 9.6 μg (HOA+CIOA) sm^{-3} (ppmv CO)$^{-1}$. Note that the average OOA enhancement corresponds to an average OH-exposure of 58.3×10^9 molec cm^{-3} s ($\sim$0.45 days), and that the average POA/ΔCO value is very similar to the value of 9.4 μg POA sm^{-3} (ppmv CO)$^{-1}$ assumed by both *Bahreini et al.* (2012) and *Gentner et al.* (2012).

In this study, we are primarily interested in the fraction of OOA attributable to anthropogenic fossil activity. Based on the ^{14}C analysis presented in *Zotter et al.* (2013), 70% of the SV-OOA enhancement corresponds to the fraction of OOA that is attributable to anthropogenic fossil-fuel activity. Some anthropogenic SOA, such as from cooking emissions, will be non-fossil. Therefore, we note that at 0.45 days of photochemical processing, 70% of the SV-OOA enhancement is equal to $\sim$25$\pm$9 μg SV-OOA sm^{-3} (ppmv CO)$^{-1}$ (Figure 2.1C), where $\pm$9 μg SV-OOA sm^{-3} (ppmv CO)$^{-1}$ is the propagated uncertainty associated with the OOA and CO measurements.

2.4 Results and Discussion

2.4.1 Emission Ratios and Required SOA Yields

Fuel-sales data reported by the California Department of Transportation (`http://www.dot.ca.gov/hq/tsip/otfa/tab/documents/mvstaff/mvstaff08.pdf`) indicate that diesel and gasoline fuel sales in all California counties upwind of Pasadena during 2010 represented approximately 13% and

87% of total fuel sales (county-wide) by volume, respectively. Therefore, on average, for every liter of fuel combusted on-road and upwind of Pasadena in 2010, the following can be assumed:

$$[\text{L gas}] = 0.87 \times [\text{L fuel}] \tag{2.1}$$

$$[\text{L dies}] = 0.13 \times [\text{L fuel}] \tag{2.2}$$

Figure 2.2A shows the chemical speciation profile and the compound-specific SOA mass yields ($Y = \Delta SOA/\Delta Hydrocarbon$) for a composite fuel comprising 13% diesel fuel and 87% gasoline fuel (by volume), based on detailed chemical-speciation profiles (see Tables S5, S6, and S8 of *Gentner et al.* (2012)). As shown in Figure 2.2A, the 2010 composite fuel composition is dominated by species with fewer than 12 carbon atoms, with the largest contributions coming from branched alkanes and single-ring aromatics. Note that the percentages listed in the legend of Figure 2A sum to ~90%, which corresponds to the unprecedented level of mass closure *Gentner et al.* (2012) obtained in characterizing gasoline and diesel fuel. *Gentner et al.* (2012) estimated the SOA mass yields for pure gasoline and pure diesel fuel using a combination of measured SOA mass yields derived from laboratory-chamber experiments and approximate SOA mass yields based on box-modeling. Based on the level of oxidation effectively constrained by experimental measurements, the SOA mass yields reported by *Gentner et al.* (2012) are expected to be representative of the first several generations of photochemical oxidation. The compound-specific SOA mass yields reported by *Gentner et al.* (2012) are given in Figure 2.2B, and Figure 2.2C shows the product of the estimated yields and the weight percent (by carbon) of the individual species in liquid fuel. In contrast to the cumulative distribution shown in Figure 2.2A, roughly 50% of the expected SOA mass is attributable to species with fewer than 12 carbons and 50% is attributable to species with more than 12 carbons. Note that single-ring aromatics are predicted to make the most significant contribution to the SOA budget (Figure 2.2C). The analysis in the present study implicitly assumes that the SOA yields from *Gentner et al.* (2012), which were mostly determined based on chamber experiments with individual compounds, apply to the complex Los Angeles atmosphere, consistent with the limited evidence available for complex

precursor mixtures (*Odum et al.*, 1997, 1996).

Vehicular exhaust emissions include water, CO, CO_2, NO_x, and partially combusted hydrocarbons, as well as a large contribution from unburned fuel that escapes combustion. *Gentner et al.* (2012) argue that unburned fuel in exhaust emissions is the dominant source of newly formed SOA attributable to vehicular activity. Emission factors reported by *Gentner et al.* (2012), which are based on CalNex 2010 measurements at the Caldecott Tunnel in Oakland, CA, for CO and for noncombusted gas-phase organic mass (GPOM) emitted in the exhaust of gasoline and diesel engines are:

$$\mathrm{EF_{CO,gas}} = 14.7 \pm 5.88 \text{ g CO (L gas)}^{-1} \tag{2.3}$$

$$\mathrm{EF_{CO,dies}} = 4.5 \pm 1.80 \text{ g CO (L dies)}^{-1} \tag{2.4}$$

$$\mathrm{EF_{GPOM,gas}} = 0.45 \pm 0.18 \text{ g GPOM (L gas)}^{-1} \tag{2.5}$$

$$\mathrm{EF_{GPOM,dies}} = 1.01 \pm 0.40 \text{ g GPOM (L dies)}^{-1} \tag{2.6}$$

where the uncertainties are assumed to be ±40% based on average values reported in Tables S5 and S6 of *McDonald et al.* (2013). Therefore, the total amount of non-combusted GPOM and CO emitted per liter of combusted fuel is:

$$\mathrm{GPOM} = \mathrm{EF_{GPOM,gas}} \times [\text{L gas}] + \mathrm{EF_{GPOM,dies}} \times [\text{L dies}] \tag{2.7}$$

$$\mathrm{CO} = \mathrm{EF_{CO,gas}} \times [\text{L gas}] + \mathrm{EF_{CO,dies}} \times [\text{L dies}] \tag{2.8}$$

Substituting equations (1-2) into equations (7-8) and dividing gives the amount of GPOM that is emitted per unit of CO mass emitted (defined here as $\mathrm{EF_{GPOM,CO}}$):

$$\mathrm{EF_{GPOM,CO}} = \frac{[\mathrm{GPOM}]}{[\mathrm{CO}]} = \frac{\mathrm{EF_{GPOM,gas}} \times 0.87 + \mathrm{EF_{GPOM,diesel}} \times 0.13}{\mathrm{EF_{CO,gas}} \times 0.87 + \mathrm{EF_{CO,diesel}} \times 0.13} \tag{2.9}$$

$$\mathrm{EF_{GPOM,CO}} = 0.039 \pm 0.019 \text{ g GPOM (g CO)}^{-1} \tag{2.10}$$

Converting g to μg and normalizing the numerator and denominator by air volume at standard

conditions (273 K and 1 atm), equation (10) can be written as:

$$\mathrm{EF_{GPOM,CO}} = 0.039 \pm 0.019 \ \mu\mathrm{g\ GPOM\ sm^{-3}} (\mu\mathrm{g\ CO\ sm^{-3}})^{-1} \tag{2.11}$$

The CO emission units μg CO sm^{-3} in equation (11) can be converted to ppmv CO by using the following conversion factor, which is applicable at 273 K and 1 atm:

$$\mathrm{EF_{GPOM,CO}} = 0.039 \pm 0.019 \ \mu\mathrm{g\ GPOM\ sm^{-3}} (\mu\mathrm{g\ CO\ sm^{-3}})^{-1} \times 1250 \ \mu\mathrm{g\ CO\ sm^{-3}} (\mathrm{ppmv\ CO})^{-1} \tag{2.12}$$

$$\mathrm{EF_{GPOM,CO}} = 48.9 \pm 24.3 \ \mu\mathrm{g\ GPOM\ sm^{-3}} (\mathrm{ppmv\ CO})^{-1} \tag{2.13}$$

We assume that $\mathrm{EF_{GPOM,CO}}$ given by equation (13) is representative of the average vehicle-fleet, and that the 70% of the SV-OOA concentrations that are comprised of fossil carbon at the Pasadena ground site are attributable to vehicular emissions (*Bahreini et al.*, 2012; *Hayes et al.*, 2013). Using $\mathrm{EF_{GPOM,CO}}$ and 70% of the SV-OOA enhancement (25±9 μg OOA sm^{-3} (ppmv CO)$^{-1}$) given in Figure 2.1B, the average aggregate SOA mass yield required to obtain mass closure at the Pasadena ground site, $\mathrm{Y_{req}}$, can be determined as follows:

$$\mathrm{Y_{req}} = \frac{\Delta \mathrm{SOA}}{\Delta \mathrm{GPOM}} = \frac{25 \pm 9 \ \mu\mathrm{g\ SOA\ sm^{-3}} (\mathrm{ppmv\ CO})^{-1}}{48.9 \pm 24.3 \ \mu\mathrm{g\ GPOM\ sm^{-3}} (\mathrm{ppmv\ CO})^{-1}} = 51.1 \pm 31.4\% \tag{2.14}$$

This required overall SOA mass yield is to be compared with the estimated yields reported in *Gentner et al.* (2012) (Figure 2) for pure gasoline fuel and pure diesel fuel, which are 2.3±0.7% and 15±5%, respectively. Based on the estimated yields for pure liquid gasoline and diesel fuel, the predicted SOA mass yield for a fuel comprising 87% gasoline and 13% diesel is 5.5% (Figure 2.3A). Note that the required SOA mass yield is a lower bound because it is based on the assumption that 100% of the GPOM reacts within 0.45 days (OH-exposure = $\sim$58.3×10^9 molec cm^{-3} s) of being emitted. As shown in Table 2.1, the fraction of hydrocarbon reacted for an OH-exposure of 58.3×10^9 molec cm^{-3} s is between 0.07 and 0.74 for several hydrocarbons abundant in gasoline and diesel fuel.

To account for partial reaction of the emitted hydrocarbons, we reduce each chemical constituent of the emitted GPOM (Figure 2.2A) by the fraction that would react after 0.45 days of photochemical aging. The partially reacted $EF_{GPOM,CO}$ (equation (13)) is then determined by summing over all partially-reacted GPOM components. The total fraction of GPOM reacted after 0.45 days of photochemical aging ranges from 0.66 at 100% diesel to 0.43 at 100% gasoline, and is 0.47 for fuel usage of 13% diesel and 87% gasoline (by volume). Reducing the $EF_{GPOM,CO}$ by a factor of 0.47 increases the required yield by a factor of 2.13 (Y_{req} = 2.13×51.1±31.4% = 108.7±66.9%).

The analysis thus far is based on the county-specific fuel usage of 13% diesel and 87% gasoline (by volume). However, the dependence of the required overall SOA mass yield on any fractional fuel usage ($f_{gas} + f_{dies} = 1$) is calculated as:

$$EF_{GPOM,CO}(f_{gas}, f_{dies}) = \frac{EF_{GPOM,gas} \times f_{gas} + EF_{GPOM,dies} \times f_{dies}}{EF_{CO,gas} \times f_{gas} + EF_{CO,dies} \times f_{dies}} \times FR(f_{gas}, f_{dies}) \quad (2.15)$$

$$Y_{req} = \frac{25 \pm 9\ \mu g\ OOA\ sm^{-3}(ppmv\ CO)^{-1}}{EF_{GPOM,CO}(f_{gas}, f_{dies})} \quad (2.16)$$

where $FR(f_{gas},f_{dies})$ is the fraction of GPOM reacted (FR = Fraction Reacted) after 0.45 days of photochemical aging for a given fractional fuel usage. The predictions of equation (16) are shown in Figure 2.3A. Note that, as a result of gasoline having a higher EF_{CO} and a lower EF_{GPOM} than its diesel counterpart, the required overall SOA mass yield increases as the fraction of gasoline increases. In other words, the emission ratio EF_{GPOM}/EF_{CO} decreases as the fraction of gasoline use increases, thereby requiring a greater fraction of the emitted GPOM to be converted to SOA to match observations at the Pasadena ground site. Also shown in Figure 2.3A are the SOA mass yields predicted, Y_{pred}, based on the values reported by *Gentner et al.* (2012) as a function of fractional fuel usage, which are calculated as:

$$Y_{pred} = \frac{Y_{gas} \times EF_{GPOM,gas} \times f_{gas} + Y_{dies} \times EF_{GPOM,dies} \times f_{dies}}{EF_{GPOM,gas} \times f_{gas} + EF_{GPOM,dies} \times f_{dies}} \quad (2.17)$$

where Y_{gas} = 0.023±0.007 and Y_{dies} = 0.15±0.05. As shown in Figure 2.3A, the required and

predicted SOA yields match if the fuel usage is 3% gasoline and 97% diesel, and the propagated error-bars intersect when the fuel usage is 40% gasoline and 60% diesel, both of which are far from the reported fuel usage of 87% gasoline and 13% diesel. For reference, the closest any county in California comes to the required fuel usage is Glenn County (Northern California), which had fuel sales that were 58% gasoline and 42% diesel.

2.4.2 Potential Explanations

2.4.2.1 Emission Factor Uncertainty

Given the discrepancy between predictions and observations of aggregate SOA mass yields shown in Figure 2.3A, one deduces that for SOA predictions and observations to match (i.e. for the black and green lines in Figure 2.3A to cross at $f_{gas} = 0.87$), (1) the predicted aggregate SOA mass yield (green line) must be higher, or (2) the required SOA mass yield (black line) must be lower, or both (1) and (2) are true. One way by which the required composite SOA mass yield decreases is via an overall increase in the ratio of EF_{GPOM}/EF_{CO}, either by reducing EF_{CO} and/or increasing EF_{GPOM}. To assess the accuracy of the emission factors reported in *Gentner et al.* (2012), we consider those reported in *Fujita et al.* (2012), given in Table 2.2. During August 2010, *Fujita et al.* (2012) measured emission factors for CO and total (products of incomplete combustion + non-combusted hydrocarbons + evaporative emissions) non-methane hydrocarbons (NMHC) obtained from tunnel measurements in Van Nuys, California, which is ∼32 km west of the Pasadena ground site. Based on the results presented in *Fujita et al.* (2012) (Table 2.2), emission ratios measured in the Van Nuys tunnel range from 52.5 to 164 μg NMHC sm^{-3} $(ppmvCO)^{-1}$, with an average value of 97.5 μg NMHC sm^{-3} $(ppmvCO)^{-1}$. Similarly to *Gentner et al.* (2012), *Fujita et al.* (2012) derived these fleet-average emission factors from vehicles traveling through a tunnel at near-constant speeds of approximately 40 mph, and excluded cold-start emissions, idle emissions, and diurnal and hot-soak evaporative hydrocarbon emissions. The *Gentner et al.* (2012) value is consistent with the lower end of the values reported in *Fujita et al.* (2012). The spread of values reported by *Fujita et al.* (2012) is most likely attributable to the fact that the emission factors derived include products

of incomplete combustion and evaporative emissions during stabilized running conditions.

We examine the sensitivity of the required composite SOA mass yield by increasing the $EF_{GPOM,gas}$ reported by *Gentner et al.* (2012) by a factor of 2.35, which increases the total $EF_{GPOM,CO}$ given by equation (13) by a factor of 2 (increasing $EF_{GPOM,CO}$ from 48.9 to 98.3 μg GPOM sm^3 (ppmv CO)$^{-1}$ at 87% gasoline and 13% diesel) to match the mean value reported by *Fujita et al.* (2012) (Figure 2.3B). As shown in Figure 2.3B, increasing $EF_{GPOM,gas}$ by a factor of 2.35 reduces the required SOA mass yields. However, this also reduces the predicted yields, since the SOA yield from pure gasoline is lower and since the gasoline terms in equation (17) have a larger impact than the diesel terms. The net result is that the required and predicted yields still match if the fuel usage is 3% gasoline and 97% diesel, and the propagated error-bars still intersect when the fuel usage is 40% gasoline and 60% diesel. Note that if the $EF_{GPOM,gas}$ were increased even further, the predicted yield (equation (17)) would asymptotically approach Y_{gas} and the required yield would approach zero (equation (16)). In this analysis, we have assumed the evaporative emissions and products of incomplete combustion have the same SOA mass yield as the tail-pipe exhaust emissions. However, evaporative emissions will be enriched in small alkanes under ambient conditions. According to Figure 2 of *Gentner et al.* (2012), the SOA mass yield of evaporative emissions is expected to be lower than tail-pipe emissions by a factor of $\sim$10. Therefore, this analysis represents a conservative upper limit since evaporative emissions are not expected to contribute substantially to the SOA budget. The SOA formation potential of products of incomplete combustion and incomplete catalytic converter oxidation are examined more thoroughly in Section 3.2.4.

McDonald et al. (2013) recently assessed long-term trends (1990-2010) in $EF_{GPOM,CO}$ emission ratios for several U.S. urban areas. As shown in Figure 3B of *McDonald et al.* (2013), owing to differences in driving conditions and engine loads, the $EF_{GPOM,CO}$ emission ratios derived from tunnel measurements such as those of *Gentner et al.* (2012) and *Fujita et al.* (2012) may be lower than those derived from on-road studies in Los Angeles by a factor of 2.7. Therefore, to determine the upper limit of $EF_{GPOM,CO}$ that should be used in this analysis, we increase the overall (gas + diesel) $EF_{GPOM,CO}$ (equation (13)) by a factor of 2.7. Doing so reduces the required yield (equation

(14)) by a factor of 0.37 ($Y_{req} = 0.37 \times 108.7\% = 40.2\%$). As shown in Figure 2.3C, when the overall $EF_{GPOM,CO}$ is increased by a factor of 2.7, the predicted and required yields match if the fuel usage is 35% gasoline and 65% diesel, and the propagated uncertainties intersect if the fuel usage is 65% gasoline and 35% diesel.

Given the lack of agreement between predicted and required SOA mass yields (Figure 2.3) when using the emission ratios from *Fujita et al.* (2012), *Gentner et al.* (2012), and *McDonald et al.* (2013), if the SV-OOA/ΔCO enhancements shown in Figure 2.1C are primarily attributable to vehicular emissions, at least one of the following must be true: (1) vehicular emission rates of gas-phase organic mass (relative to CO) are substantially larger than those recently measured; or (2) the SOA mass yields of pure gasoline and pure diesel exhaust are substantially (i.e. a factor of ~ 3–16) higher than what has been measured previously. In the next section, we explore possibility (1) in the context of drive-cycle phases (e.g. cold-start emissions, idle emissions, hot-soak evaporative emissions, diurnal evaporative emissions, etc.) that were not the focus of the analysis by Gentner et al., but are assessed more closely in this study.

2.4.2.2 Emission Ratios from other Drive-cycle Phases

By sampling emissions within urban tunnels for sufficient periods of time, *Fujita et al.* (2012) and *Gentner et al.* (2012) estimated average emission factors. However, neither study included emissions from drive-cycle phases other than stabilized running in the emission factors used in this study. To estimate the impact of drive-cycle phase on emission-factor ratio, we use the California EMission FACtor model (EMFAC2011, `http://www.arb.ca.gov/emfac/`) combined with summer 2010 data for the South Coast Air Basin of California. Emission factors are weighted and aggregated by vehicle-year populations and speed distributions, and include all drive-cycle components (i.e. running, idle, start, diurnal evaporative, hot-soak evaporative, running evaporative, and resting evaporative). Emission factor ratios, based on daily-average emission rates, for all EMFAC2011 gasoline and diesel vehicle types are given in Tables 2.3 and 2.4, respectively. As shown in Table 2.3, EMFAC2011 predicts gasoline emission-factor ratios that are generally consistent with the values

reported by *Fujita et al.* (2012) and are ∼2-3.5 times higher than the value reported by *Gentner et al.* (2012). Based on the results shown in Figure 2.3B, increasing the gasoline emission-factor ratio by ∼2.5 reduces both the predicted and required SOA mass yields, which does not improve agreement. As shown in Table 2.4, the diesel emission-factor ratios predicted by EMFAC2011 are very similar to the value reported by *Gentner et al.* (2012). These results show that the required and predicted yields do not match even if all drive-cycle phases are accounted for. Therefore, one concludes that either the SOA mass yields for gasoline and diesel exhaust are significantly higher than what has been previously reported, or non-vehicular source categories contribute significantly to the anthropogenic fossil OOA budget measured at the Pasadena ground site. Both of these possibilities are explored in the next section.

2.4.2.3 Ambient NMHC/ΔCO ratios

The analysis up to this point has been based on measured and predicted NMHC/CO vehicular emission ratios and measured ambient OOA/ΔCO ratios at the Pasadena ground site. This analysis is now extended to include all upwind NMHC source categories (vehicular and non-vehicular) by comparing measured ambient NMHC/ΔCO ratios to measured ambient OOA/ΔCO at the Pasadena ground site. The four main source categories of NMHC in Southern California, not including trans-Pacific transport, which is thought to be unimportant for SOA formation in the L.A. Basin due to long transport times and intense dilution, are stationary, areawide, mobile, and natural (non-fossil). Based on the 2009 Almanac Emission Projection Data reported by the CARB (`http://www.arb.ca.gov/app/emsinv/emssumcat.php`), the 2010 annual emissions of reactive organic gas (ROG) and CO from each source are given in Table 2.5. Note that CARB reports ROG emission rates, which are similar to NMHC, but do not include several low-reactive organic compounds such as ethane, acetone, CFCs, and HCFCs. As shown in Table 2.5, on-road motor vehicles are reported to contribute ∼27-29% of all ROG emissions in the South Coast Air Basin and Los Angeles County. Mobile sources other than on-road vehicles (e.g. aircraft, trains, ocean-going vessels, and off-road equipment such as fork-lifts) are reported to contribute ∼21% of the ROG emissions.

Figure 2.4 shows two lumped NMHC concentrations (e.g. single-ring aromatics and small alkanes), normalized by ΔCO, as functions of photochemical age. See Table 2.6 for a list of all compounds included in Figure 2.4. As shown in Figure 2.4, similarly to the roughly linear increases in OOA/ΔCO with increasing photochemical age, gas-phase alkane (C_6,C_9-C_{11}) and single-ring aromatic concentrations both exhibit roughly linear decreases with increasing photochemical age. Note that adding the normalized alkanes and single-ring aromatic concentrations at zero photochemical age suggests an emission ratio of $\sim$55 μg GPOM sm^{-3} (ppmv CO)$^{-1}$, which is similar to the estimated emission ratio given by equation (13). Although this is not proof, the linear decrease in normalized NMHC concentrations with photochemical age, and the similarity between estimated emission ratios are both consistent with vehicular exhaust being the dominant source of these compounds. Furthermore, in contrast to the numbers given in Table 2.5, *Borbon et al.* (2013) found that emissions from gasoline-powered vehicles dominated the urban anthropogenic NMHC budget during CalNex.

One particularly interesting feature of Figure 2.4 is that even if all upwind sources of linear alkanes (C_6,C_9-C_{11}) and single-ring aromatics are accounted for, the required aggregate SOA mass yield is still $\sim$92% (92 = OOA/ΔCO slope divided by negative NMHC/ΔCO slope = 57/62). This required yield may be overestimated because only light straight-chain (C_6,C_9-C_{11}) alkane and single-ring aromatic ($<C_{12}$) concentration measurements are available, whereas the majority of alkanes in the ambient are expected to be branched (Figure 2.2C). That being said, the required yield of 92% is still inexplicably large considering that the single-ring aromatic component of vehicular exhaust is expected to produce $\sim$2.5 times more SOA than the alkane component (Figure 2.2C). A similar correspondence between the magnitude of aromatic hydrocarbon decreases and SOA increases was observed by *de Gouw et al.* (2005) in the 2002 New England Air Quality Study. It is possible that alkanes and aromatics with 12 or more carbon atoms are contributing to the SOA budget. However, alkanes and aromatics ($\geq C_{12}$) attributable to vehicular activity are abundant only in diesel exhaust, and not in gasoline exhaust. If alkanes ($\geq C_{12}$) were contributing substantially to the L.A. SOA budget, one would expect to see a significant decrease in OOA concentrations on the weekends when diesel activity is reduced by $\sim$50%. However, this possibility is not supported by the conclusions of

Hayes et al. (2013) and *Bahreini et al.* (2012), or the emission ratio analysis presented in this study.

2.4.2.4 Incomplete Combustion/Catalytic Converter Oxidation Products

The analysis presented thus far is based on the assumption that unburned fuel in exhaust emissions is the dominant source of newly formed SOA attributable to vehicular activity (*Gentner et al.*, 2012). However, recent work suggests that products of incomplete combustion and products of incomplete catalytic converter oxidation may be efficient SOA precursors. Specifically, *Gordon et al.* (2013) used a laboratory chamber to investigate SOA formation from photooxidation of tail-pipe emissions from 15 light-duty gasoline vehicles (LDGVs) spanning a wide range of types, model years and emission standards. The 15 LDGVs are grouped according to model year into three vehicle classes termed preLEV (LDGVs manufactured prior to 1995), LEV1 (LDGVs manufactured between 1995 and 2003), and LEV2 (LDGVs manufactured 2004 or later). For each vehicle class, *Gordon et al.* (2013) report median emission factors for CO, median emission factors for all non-methane organic gases (NMOG), median emission factors for speciated and non-speciated organic gases that are expected to be SOA precursors, and aggregate SOA mass yields required to obtain mass closure for each chamber experiment ($Y^{SOA}_{veh.class}$). These quantities include products of incomplete combustion and catalytic conversion, and are given in Table 2.7 for reference.

We first calculate a fleet-average LDGV NMOG emission factor based on the values reported by *Gordon et al.* (2013) (see Table 2.7):

$$\begin{aligned} EF^{fleet}_{NMOG} &= (\text{Fleet Fraction}, \text{preLEV}) \times EF^{preLEV}_{NMOG} \\ &+ (\text{Fleet Fraction}, \text{LEV1}) \times EF^{LEV1}_{NMOG} \\ &+ (\text{Fleet Fraction}, \text{LEV2}) \times EF^{LEV2}_{NMOG} \end{aligned} \tag{2.18}$$

$$\begin{aligned} \mathrm{EF}_{\mathrm{NMOG}}^{\mathrm{fleet}} &= 0.07 \times 4.5 \text{ g NMOG } (\mathrm{L-gas})^{-1} \\ &+ 0.36 \times 1.3 \text{ g NMOG } (\mathrm{L-gas})^{-1} \\ &+ 0.57 \times 0.4 \text{ g NMOG } (\mathrm{L-gas})^{-1} \end{aligned} \tag{2.19}$$

$$\mathrm{EF}_{\mathrm{NMOG}}^{\mathrm{fleet}} = 1.01 \text{ g NMOG } (\mathrm{L-gas})^{-1} \tag{2.20}$$

The total NMOG emission factor for the LDGV fleet reported by *Gordon et al.* (2013) (equation 20) is similar to the value reported in *McDonald et al.* (2013), and is roughly a factor of ∼2 higher than that reported by *Gentner et al.* (2012). These differences in emission factors are most likely attributable to the differences in LDGV driving conditions in each study.

In a similar manner, we calculate a fleet-average LDGV CO emission factor based on the values reported by *Gordon et al.* (2013) (see Table 2.7):

$$\mathrm{EF}_{\mathrm{CO}}^{\mathrm{fleet}} = 21.6 \text{ g CO } (\mathrm{L-gas})^{-1} \tag{2.21}$$

The fleet-average CO emission factor given by equation (21) is ∼50% larger than the value reported by *Gentner et al.* (2012) (equation 3).

To facilitate a consistent comparison with the analysis presented in *Gentner et al.* (2012), the SOA mass yields presented in *Gordon et al.* (2013) have been rescaled based on the total NMOG tail-pipe emissions and not the fraction of NMOG emissions that is expected to be comprised of SOA precursors. Therefore, the SOA mass yields reported in Table 2.7 are roughly half as large as

those reported in Figure 7 of *Gordon et al.* (2013).

$$\mathrm{Y_{preLEV}} = (2\%) \times (0.38 \text{ g SOA Prec /g NMOG}) = 0.8\% \tag{2.22}$$

$$\mathrm{Y_{LEV1}} = (6\% - 33\%) \times (0.51 \text{ g SOA Prec /g NMOG}) = 10\% \ ((3\% + 17\%)/2) \tag{2.23}$$

$$\mathrm{Y_{LEV2}} = (15\% - 50\%) \times (0.49 \text{ g SOA Prec /g NMOG}) = 16\% \ ((7\% + 25\%)/2) \tag{2.24}$$

where the (SOA Prec/NMOG) conversion factors are taken directly from Figure 3 of *Gordon et al.* (2013). Using these values, a fleet-average SOA emission factor can also be approximated:

$$\begin{aligned}\mathrm{EF_{SOA}^{fleet}} &= (\mathrm{Fleet-Fraction, preLEV}) \times \mathrm{Y_{preLEV}^{SOA}} \times \mathrm{EF_{NMOG}^{preLEV}} \\ &+ (\mathrm{Fleet-Fraction, LEV1}) \times \mathrm{Y_{LEV1}^{SOA}} \times \mathrm{EF_{NMOG}^{LEV1}} \\ &+ (\mathrm{Fleet-Fraction, LEV2}) \times \mathrm{Y_{LEV2}^{SOA}} \times \mathrm{EF_{NMOG}^{LEV2}}\end{aligned} \tag{2.25}$$

$$\begin{aligned}\mathrm{EF_{SOA}^{fleet}} &= 0.07 \times 4.5 \times 0.008 \times \text{g NMOG (L} - \text{gas})^{-1} \\ &+ 0.36 \times 1.3 \times 0.10 \times \text{g NMOG (L} - \text{gas})^{-1} \\ &+ 0.57 \times 0.4 \times 0.16 \times \text{g NMOG (L} - \text{gas})^{-1}\end{aligned} \tag{2.26}$$

Dividing equation (26) by equation (20) gives an approximate, experimentally derived fleet-averaged SOA mass yield:

$$\mathrm{Y_{LDGV,fleet}^{SOA}} = \mathrm{EF_{SOA}^{fleet}/EF_{NMOG}^{fleet}} \times 100\% \tag{2.27}$$

$$\mathrm{Y_{LDGV,fleet}^{SOA}} = 9\% \tag{2.28}$$

The SOA mass yield given in equation (28) is ∼4 times larger than the yield for pure gasoline reported by *Gentner et al.* (2012) ($\mathrm{Y_{gas}} = 2.3\%$). With respect to diesel-fueled vehicle emissions, *Jathar et al.* (2013) showed that unburned diesel fuel and combustion tail-pipe exhaust from diesel-

fueled vehicles have similar SOA formation potentials. As shown in Figure 4 of *Jathar et al.* (2013), the experimentally derived aggregate SOA mass yields for diesel exhaust are very similar to the value reported by *Gentner et al.* (2012) ($Y_{dies} = 15\%$), which suggests that this value is representative of diesel-fueled vehicles in California. However, in this analysis we reduce the $EF_{NMOG,dies}$ to 0.69 g NMOG $(L - dies)^{-1}$ to account for the fraction of non-diesel-particulate-filter-equipped heavy-duty diesel vehicles in the South Coast Air Basin, based on discussions in *May et al.* (2014).

To determine the impact of partial combustion and incomplete catalytic conversion on ambient SOA formation, the analysis presented in Figure 2.3A has been redone using the experimentally derived LDGV EF_{NMOG}, EF_{CO}, and the SOA mass yield given in equations 20, 21, and 28, respectively (see Figure 2.5A). As shown in Figure 2.5A, using the values reported by *Gordon et al.* (2013) produces results that are qualitatively identical to those shown in Figure 2.3. As discussed in the next paragraph, the impact of predicted yield uncertainty is demonstrated via sensitivity analyses. Therefore, the predicted-yield error bars are excluded from Figure 2.5A.

To account for the uncertainty associated with the SOA yield scaling technique used above, and to determine the upper limit of the SOA formation potential of gasoline vehicles, we have conducted similar analyses assuming $Y_{gas} = 16\%$ and $Y_{gas} = 25\%$, which are the upper limits of the LEV1 and LEV2 vehicle classes, respectively, reported by *Gordon et al.* (2013). As shown in Figures B.1, although increasing Y_{gas} to its upper limit does improve agreement to some extent, the predicted and required yields still differ by more than a factor of 3 even when using the highest yields reported by *Gordon et al.* (2013). To account for the uncertainty associated with calculating the fraction of emitted SOA precursors that have undergone chemical reaction after 0.45 days of photochemical aging, an additional sensitivity analysis was conducted in which 100% of the emitted NMOG is assumed to have reacted (see Figure B.2). As shown in Figure B.2, assuming 100% conversion of NMOG effectively reduces the required SOA mass yields by a factor of 2. The predicted yields shown in Figure B.2C are still lower than the required yields by a factor of $\sim$1.7. We emphasize that there is a significant lack of closure between expected and observed organic aerosol concentrations attributable to fossil-fuel emissions even when assuming 100% NMOG conversion and an LDGV

fleet-averaged SOA mass yield of 25%. Both assumptions are expected to be very unrepresentative of ambient conditions in California.

A more straightforward way to assess the impact of partial combustion and incomplete catalytic conversion on SOA formation from gasoline exhaust is to compare the SOA/ΔCO enhancement ratios measured by *Gordon et al.* (2013) directly to the SV-OOA/ΔCO enhancement ratios measured at the Pasadena ground site during the CalNex field campaign (see Figure 2.5B). As shown in Figure 2.5B, the SOA/ΔCO enhancements for all three LDGV vehicle classes are lower than the CalNex measured value at 0.14 days of photochemical aging. Average SOA/ΔCO enhancement slopes (units μg m^{-3}/ppmvCO/day) are calculated for each vehicle class by extending a straight line from the origin through the measured data points. As shown in Figure 2.5B, the average SV-OOA/ΔCO enhancement slope (57 μg m^{-3}/ppmvCO/day) is $\sim$7 times larger than the fleet-average SOA/ΔCO enhancement slope (8 μg m^{-3}/ppmvCO/day), and $\sim$ 3.5 times larger than the LEV2 vehicle class slope. Note that the results presented in Figure 2.5B are self consistent, and therefore are not influenced by the uncertainty associated with the emission factors and aggregate SOA mass yields reported by *Gordon et al.* (2013) and *Gentner et al.* (2012), but they are susceptible to other factors. For instance, *Gordon et al.* (2013) do not account for loss of organic vapors directly to chamber walls (*Matsunaga and Ziemann*, 2010). Although highly uncertain, as acknowledged by *Gordon et al.* (2013), accounting for vapor-phase wall loss would increase their estimated SOA production.

To our knowledge, there is currently no combination of published vehicular emission factors and SOA mass yields derived from laboratory experiments, or measured SOA/ΔCO enhancements based on tail-pipe exhaust emissions that can explain the measurements presented in Figure 2.1. Based on the analysis presented in this section, a robust conclusion is that either the SOA mass yields for vehicular tail-pipe exhaust are significantly higher than what has been recently reported, or non-vehicular source categories contribute significantly to the anthropogenic fossil OOA budget measured at the Pasadena ground site. For the latter possibility to be true, the non-vehicular fossil emissions must be comprised of compounds other than those listed in Table 2.6.

2.4.2.5 Off-road Vehicular Emissions

A large part of this analysis is based on on-road gasoline/diesel fuel sales, and accounting for off-road use of diesel may increase the fraction of total diesel fuel use by several percentage points. However, this is not expected to influence our conclusions because, as shown in Figures 2.5, B.1, and B.2, significant discrepancies exist at virtually all gasoline/diesel fuel usage ratios. In addition, looking at the TOTAL MOBILE SOURCES category of Table 5, which represents the sum of all on-road and off-road mobile emissions, we calculate the emission factor ratio for Los Angeles and SoCAB both to be ∼145 μg ROG m^{-3} $(ppmvCO)^{-1}$ (still using the 1250 μg CO sm^{-3} $(ppmv\ CO)^{-1}$ conversion factor). Assuming that ∼50% of the ROG has reacted after 0.45 days of photochemical aging, and that the aggregate SOA mass yield is 10%, we calculate an SOA enhancement ratio of 7.25 μg SOA m^{-3} $(ppmvCO)^{-1}$. This value is well below the 25 μg SV-OOA m^{-3} $(ppmvCO)^{-1}$ measured during CalNex (Figure 1). Although this result is consistent with the other results presented in this study, there is considerable uncertainty associated with this calculation, and future work should focus on obtaining detailed speciation profiles and expected SOA mass yields for all major anthropogenic ROG sources in Southern California.

2.5 Conclusions

Using the best available laboratory-derived SOA mass yields, the SV-OOA/ΔCO enhancements attributable to anthropogenic fossil activity (Figure 2.1) cannot be explained by the measured and predicted NMOG/CO vehicular emission ratios or the measured ambient NMHC/ΔCO ratios. This conclusion is based on the following observations:

- Emission factors and estimated yields reported in *Gentner et al.* (2012), *Fujita et al.* (2012), *McDonald et al.* (2013), and calculated using EMFAC2011 significantly underpredict OOA/ΔCO enhancements when compared to CalNex observations.
- Accounting for emissions from all drive-cycle phases (e.g. start, idle, evaporative, running, etc.) does not improve agreement between predicted and required SOA mass yields significantly.

- Accounting for all upwind sources of single-ring aromatics and light alkanes (C_6,C_9-C_{11}) does not improve agreement between predicted and required SOA mass yields significantly.

- Accounting for products of incomplete combustion and products of incomplete catalytic converter oxidation does not improve agreement between predicted and required SOA mass yields significantly.

With respect to the applicability of these results to other major urban areas, ratios of OOA/ΔCO for Mexico City and the Northeast US are similar or smaller by about a factor of 2 than those observed in Los Angeles, as reported by *Hayes et al.* (2013). Ratios of NMHC/ΔCO for emissions in the Northeast United States are very similar to those in the Los Angeles area (*Borbon et al.*, 2013), while those in Mexico City are higher by about a factor of 2 (*Bon et al.*, 2011). Therefore similar qualitative discrepancies between predicted and required yields, albeit of somewhat lower magnitude, may exist in these urban areas as well.

We return to the question: "Is it more likely that (1) ambient SOA mass yields are substantially larger than what has been derived experimentally, or (2) vehicular emissions do not dominate SOA concentrations attributable to anthropogenic fossil activity in Southern California?". Neither possibility can be categorically ruled out; therefore, both options should be explored further, particularly since their implications for SOA control strategies are markedly different.

Acknowledgements

The authors would like to thank Roya Bahreini, Drew Gentner, Arthur Chan, Allen Goldstein, and two anonymous reviewers for providing valuable comments. This study was supported by NOAA Climate Program Office's AC4 program, award # NA13OAR4310058. PLH and JLJ thank CARB 08-309 & 11-305, DOE (BER/ASR) DE-SC0006035, and a CIRES Visiting Fellowship.

Bibliography

Aiken, A. C., DeCarlo, P. F., Kroll, J. H., Worsnop, D. R., Huffman, J. A., Docherty, K. S., Ulbrich, I. M., Mohr, C., Kimmel, J. R., Sueper, D., Sun, Y., Zhang, Q., Trimborn, A., Northway, M., Ziemann, P. J., Canagaratna, M. R., Onasch, T. B., Alfarra, M. R., Prevot, A. S. H., Dommen, J., Duplissy, J., Metzger, A., Baltensperger, U., and Jimenez, J. L.: O/C and OM/OC ratios of primary, secondary, and ambient organic aerosols with high-resolution time-of-flight aerosol mass spectrometry, *Environ. Sci. Technol.*, *42(12)*, 4478–4485, 2008.

Allan, J. D., P. I. Williams, W. T. Morgan, C. L. Martin, M. J. Flynn, J. Lee, E. Nemitz, G. J. Phillips, M. W. Gallagher, and H. Coe: Contributions from transport, solid fuel burning and cooking to primary organic aerosols in two UK cities, *Atmos. Chem. Phys.*, *10(2)*, 647-668, 2010.

Atkinson, R. J. : Gas-Phase Tropospheric Chemistry of Volatile Organic Compounds: 1. Alkanes and Alkenes, *Phys. Chem. Ref. Data*, *26*, 215–290, 1997.

Bahreini, R., Middlebrook, A. M., de Gouw, J. A., Warneke, C., Trainer, M., Brock, C. A., Stark, H., Brown, S. S., Dube, W. P., Gilman, J. B., Hall, K., Holloway, J. S., Kuster, W. C., Perring, A. E., Prevot, A. S. H., Schwarz, J. P., Spackman, J. R., Szidat, S., Wagner, N. L., Weber, R. J., Zotter, P., and Parrish D. D.: Gasoline emissions dominate over diesel in formation of secondary organic aerosol mass, *Geophys. Res. Lett.*, *39*, L06805, 2012.

Bon, D. M., Ulbrich, I. M., de Gouw, J. A., Warneke, C., Kuster, W. C., Alexander, M. L., Baker, A., Beyersdorf, A. J., Blake, D., Fall, R., Jimenez, J. L., Herndon, S. C., Huey, L. G., Knighton, W. B., Ortega, J., Springston, S., and Vargas, O.: Measurements of volatile organic compounds at a suburban ground site (T1) in Mexico City during the MILAGRO 2006 campaign: measurement comparison, emission ratios, and source attribution, *Atmos. Chem. Phys.*, *11*, 2399-2421, doi:10.5194/acp-11-2399-2011, 2011.

Borbon, A., Gilman, J. B., Kuster, W. C., Grand, N., Chevaillier, S., Colomb, A., Dolgorouky, C., Gros, V., Lopez, M., Sarda-Esteve, R., Holloway, J. S., Stutz, J., Petetin,H., McKeen, S.,

Beekmann, M., Warneke, C., Parrish, D. D., and de Gouw, J. A. : Emission ratios of anthropogenic volatile organic compounds in northern mid-latitude megacities: Observations versus emission inventories in Los Angeles and Paris, *J. Geophys. Res.-Atmos.*, *118*, 2041–2057, 2013.

Calvert, J. G., Atkinson, R., Becker, K. H., Kamens, R. M., Seinfeld, J. H., Wallington, T. J., and Yarwood, G. : The Mechanisms of Atmospheric Oxidation of Aromatic Hydrocarbons, *Oxford University Press*, New York, 556pp., 2002.

DeCarlo, P. F., Kimmel, J. R., Trimborn, A., Northway, M. J., Jayne, J. T., Aiken, A. C., Gonin, M., Fuhrer, K., Horvath, T., Docherty, K. S., Worsnop, D. R., and Jimenez, J. L. : Field-Deployable, High-Resolution, Time-of-Flight Aerosol Mass Spectrometer, *Anal. Chem.*, *78*, 8281-8289, 2006.

de Gouw, J. A., Middlebrook, A. M., Warneke, C., Goldan, P. D., Kuster, W. C., Roberts, J. M., Fehsenfeld, F. C., Worsnop, D. R., Canagaratna, M. R., Pszenny, A. A. P., Keene, W. C., Marchewka, M., Bertman, S. B., and Bates T. S.: Budget of organic carbon in a polluted atmosphere: Results from the New England Air Quality Study in 2002, *J. Geophys. Res.-Atmos.*, *110*, D16305, 2005.

de Gouw, J. A., Brock, C. A., Atlas, E. L., Bates, T. S., Fehsenfeld, F. C., Goldan, P. D., Holloway, J. S., Kuster,Lerner, B. M., Matthew, B. M., Middlebrook, A. M., Onasch, T. B., Peltier, R. E., Quinn, P. K., Senff, C. J., Stohl, A., Sullivan, A. P., Trainer, M., Warneke, C., Weber, R. J., and Williams, E. J. : Sources of particulate matter in the northeastern United States: 1. Direct emissions and secondary formation of organic matter in urban plumes, *J. Geophys. Res.-Atmos.*, *113*, D08301, 2008.

de Gouw, J. A., Gilman, J. B., Borbon, A., Warneke, C., Kuster, W. C., Goldan, P. D., Holloway, J. S., Peischl, J., Ryerson, T. B., Parrish, D. D., Gentner, D. R., Goldstein, A. H., and Harley, R. A. : Increasing atmospheric burden of ethanol in the United States, *Geophys. Res. Lett.*, *39*, L15803, 2012.

Dusanter, S., Vimal, D., Stevens, P. S., Volkamer, R., and Molina, L. T. : Measurements of OH and

HO2 concentrations during the MCMA-2006 field campaign – Part 1: Deployment of the Indiana University laser-induced fluorescence instrument, *Atmos. Chem. Phys.*, *9(5)*, 1665-1685, 2009.

California Air Resources Board, Motor Vehicle Emission Factor/Emission Inventory Model - EMFAC 2011 (`http://www.arb.ca.gov/msei/msei.htm`)

Fujita, E. M., Campbell, D. E., Zielinska, B., Chow, J. C., Lindhjem, C. E., DenBleyker, A., Bishop, G. A., Schuchmann, B. G., Stedman, D. H., and Lawson, D. R., : Comparison of the MOVES2010a, MOBILE6.2, and EMFAC2007 mobile source emission models with on-road traffic tunnel and remote sensing measurements, *J. Air and Waste Manag.*, *62*, 1134-1149, 2012.

D. R. Gentner,Isaacman, G., Worton, D. R., Chan, A. W. H., Dallmann, T. R., Davis, L., Liu, S., Day, D. A., Russell, L. M., Wilson,Weber, R., uha, A., Harley, R. A., and Goldstein A. H.: Elucidating secondary organic aerosol from diesel and gasoline vehicles through detailed characterization of organic carbon emissions, *PNAS*, *109*, 18318–18323, 2012.

Gerbig, C., Schmitgen, S., Kley, D., Volz-Thomas, A., Dewey, K., and Haaks, D. : An improved fast-response vacuum-UV resonance fluorescence CO instrument, *J. Geophys. Res.-Atmos.*, *104(D1)*, 1699-1704, 1999.

Gilman, J. B., Kuster, W. C., Goldan, P. D., Herndon, S. C., Zahniser, M. S., Tucker, S. C., Brewer, W. A., Lerner, B. M., Williams, E. J., Harley, R. A., Fehsenfeld, F. C., Warneke, C., and de Gouw J. A.: Measurements of volatile organic compounds during the 2006 TexAQS/GoMACCS campaign: Industrial influences, regional characteristics, and diurnal dependencies of the OH reactivity, *J. Geophys. Res.-Atmos.*, *114*, D00F06, 2009.

Gordon, T. D., Presto, A. A., May, A. A., Nguyen, N. T., Lipsky, E. M., Donahue, N. M., Gutierrez, A., Zhang, M., Maddox, C., Rieger, P., Chattopadhyay, S., Maldonado, H., Maricq, M. M., and Robinson, A. L.: Secondary organic aerosol formation exceeds primary particulate matter emissions for light-duty gasoline vehicles, *Atmos. Chem. Phys.*, *13*, 23173-23216, doi:10.5194/acpd-13-23173-2013, 2013.

Griffin, R. J., J. Chen, K. Carmody, S. Vutukuru, and D. Dabdub: Contribution of gas phase oxidation of volatile organic compounds to atmospheric carbon monoxide levels in two areas of the United States, *J. Geophys. Res.-Atmos.*, *112*, D10S17, 2007.

Hayes, P. L., Ortega, A. M., Cubison, M. J., Froyd, K. D., Zhao, Y., Cliff, S. S, Hu, W. W., Toohey, D. W, Flynn, J. H., Lefer, B. L., Grossberg, N., Alvarez, S., Rappengluck, B., Taylor, J. W., Allan, J. D., Holloway, J. S., Gilman, J. B., Kuster, W. C., de Gouw, J. A., Massoli, P., Zhang, X., Liu, J., Weber, R. J., Corrigan, A. L., Russell, L. M., Isaacman, G., Worton, D. R., Kreisberg, N. M., Goldstein, A. H., Thalman, R., Waxman, E. M., Volkamer, R., Lin, Y. H., Surratt, J. D., Kleindienst, T. E., Offenberg, J. H., Dusanter, S., Griffith, S., Stevens, P. S., Brioude, J., Angevine, W. M., Jimenez, J. L. : Organic Aerosol Composition and Sources in Pasadena, California during the 2010 CalNex Campaign , *J. Geophys. Res.-Atmos.*, *118*, 2013.

Hodzic, A., Jimenez, J. L., Madronich, S., Canagaratna, M. R., DeCarlo, P. F., Kleinman, L., and Fast J.: Modeling organic aerosols in a megacity: potential contribution of semi-volatile and intermediate volatility primary organic compounds to secondary organic aerosol formation, *Atmos. Chem. Phys.*, *10*, 5491–5514, 2010.

Jathar, S. H., Miracolo, M. A., Tkacik, D. S., Donahue, N. M., Adams, P. J., Robinson, A. L.: Secondary Organic Aerosol Formation from Photo-Oxidation of Unburned Fuel: Experimental Results and Implications for Aerosol Formation from Combustion Emissions, *Environ. Sci. Technol.*, *47(22)*, 12886-12893, 2013.

Johnson, D., Utembe, S. R., Jenkin, M. E., Derwent, R. G., Hayman, G. D., Alfarra, M. R., Coe, H., and McFiggans, G. : Simulating regional scale secondary organic aerosol formation during the TORCH 2003 campaign in the southern UK, *Atmos. Chem. Phys.*, *6*, 403-418, 2006.

Jimenez, J. L., Canagaratna, M. R., Donahue, N. M., Prevot, A. S. H., Zhang, Q., Kroll, J. H., DeCarlo, P. F., Allan, J. D., Coe, H., Ng, N. L., Aiken, A. C., Docherty, K. S., Ulbrich, I. M., Grieshop, A. P., Robinson, A. L., Duplissy, J., Smith, J. D., Wilson, K. R., Lanz, V. A., Hueglin, C., Sun, Y. L., Tian, J., Laaksonen, A., Raatikainen, T., Rautiainen, J., Vaattovaara, P., Ehn,

M., Kulmala, M., Tomlinson, J. M., Collins, D. R., Cubison, M. J., Dunlea, E. J., Huffman, J. A., Onasch, T. B., Alfarra, M. R., Williams, P. I., Bower, K., Kondo, Y., Schneider, J., Drewnick, F., Borrmann, S., Weimer, S., Demerjian, K., Salcedo, D., Cottrell, L., Griffin, R., Takami, A., Miyoshi, T., Hatakeyama,S., Shimono, A., Sun, J. Y., Zhang, Y. M., Dzepina, K., Kimmel, J. R., Sueper, D., Jayne, J. T., Herndon, S. C., Trimborn, A. M., Williams, L. R., Wood, E. C., Middlebrook, A. M., Kolb, C. E., Baltensperger, U., and Worsnop, D. R. : Evolution of Organic Aerosols in the Atmosphere, *Science*, *326(5959)*, 1525–1529, 2009.

Kleinman, L. I., Springston, S. R., Daum, P. H., Lee, Y. N., Nunnermacker, L. J., Senum, G. I., Wang, J., Weinstein-Lloyd, J., Alexander, M. L., Hubbe, J., Ortega, J., Canagaratna, M. R., and Jayne, J. : The time evolution of aerosol composition over the Mexico City plateau, *Atmos. Chem. Phys.*, *8*, 1559–1575, 2008.

Matsunaga, A., and Ziemann, P. J.: Gas-Wall Partitioning of Organic Compounds in a Teflon Film Chamber and Potential Effects on Reaction Product and Aerosol Yield Measurements, *Aerosol Sci. Technol.*, *44*, 881–892, 2010.

Matsui, H., Koike, M., Takegawa, N., Kondo, Y., Griffin, R. J., Miyazaki, Y., Yokouchi, Y., and Ohara, T.: Secondary organic aerosol formation in urban air: Temporal variations and possible contributions from unidentified hydrocarbons, *J. Geophys. Res.-Atmos.*, *114*, D04201, 2009.

May, A. A., Nguyen, N. T., Presto, A. A., Gordon, T. D., Lipsky, E. M., Karve, M., Gutierrez, A., Robertson, W. H., Zhang, M., Chang, O., Chen, S., Cicero-Fernandez, P., Fuentes, M., Huang, S.-M., Ling, R., Long, J., Maddox, C., Massetti, J., McCauley, E., Na, K., Pang, Y., Rieger, P., Sax, T., Truong, T., Vo, T., Chattopadhyay, S., Chattopadhyay, S., C, H., Maricq, M., Robinson, A. L.: Gas- and particle-phase primary emissions from in-use, on-road gasoline. *Atmos. Environ.*, *Submitted*.

McDonald, B. C., Gentner, D. R., Goldstein, A. H., and Harley, R., A. : Long-Term Trends in Motor Vehicle Emissions in U.S. Urban Areas, *Environ. Sci. Technol.*, *Just Accepted*, doi:10.1021/es401034z, 2013.

Odum, J. R., Jungkamp, T. P. W., Griffin, R. J., Flagan, R. C., and Seinfeld, J. H.: The atmospheric aerosol-forming potential of whole gasoline vapor, *Science*, *276(5309)*, 96-99, 1997.

Odum, J. R., Hoffmann, T., Bowman, F., Collins, D., Flagan, R. C., and Seinfeld, J. H.: Gas/particle partitioning and secondary organic aerosol yields, *Environ. Sci. Technol.*, *30(8)*, 2580-2585, 1996.

Paatero, P. and Tapper, U. : Positive matrix factorization - a nonnegative factor model with optimal utilization of error-estimates of data values, *Environmetrics*, *5(2)*, 111-126, 1994.

Parrish, D. D., Stohl, A., Forster, C., Atlas, E. L., Blake, D. R., Goldan, P. D., Kuster, W. C., and de Gouw, J. A. : Effects of mixing on evolution of hydrocarbon ratios in the troposphere, *J. Geophys. Res.-Atmos.*, *112(D10)*, D10S34, 2007.

Ryerson, P. L., Andrews, A. E., Angevine, W. M., Bates, T. S., Brock, C. A., Cairns, B., Cohen, R. C., Cooper, O. R., de Gouw, J. A., Fehsenfeld, F. C., Ferrare, R. A., Fischer, M. L., Flagan, R. C., Goldstein, A. H., Hair, J. W., Hardesty, R. M., Hostetler, C. A., Jimenez, J. L., Langford, A. O., McCauley, E., McKeen, S. A., Molina, L. T., Nenes, A., Oltmans, S. J., Parrish, D. D., Pederson, J. R., Pierce, R. B., Prather, K., Quinn, P. K., Seinfeld, J. H., Senff, C. J., Sorooshian, A., Stutz, J., Surratt, J. D., Trainer, M., Volkamer, R., Williams, E. J., and Wofsy, S. C. : The 2010 California research at the Nexus of air quality and climate change (CalNex) field study, *J. Geophys. Res.-Atmos.*, *In Press.*, 2013.

Thalman, R., and Volkamer, R. : Inherent calibration of a blue LED-CE-DOAS instrument to measure iodine oxide, glyoxal, methyl glyoxal, nitrogen dioxide, water vapour and aerosol extinction in open cavity mode, *Atmos. Meas. Tech.*, *3(6)*, 1797-1814, 2010.

Ulbrich, I. M., Canagaratna, M. R., Zhang, Q., Worsnop, D. R., and Jimenez, J. L. : Interpretation of organic components from Positive Matrix Factorization of aerosol mass spectrometric data, *Atmos. Chem. Phys.*, *9(9)*, 2891–2918, 2009.

Volkamer, R., Jimenez, J. L., San Martini, F., Dzepina, K., Zhang, Q., Salcedo, D., Molina, L. T.,

Worsnop, D. R., and Molina, M. J. : Secondary organic aerosol formation from anthropogenic air pollution: Rapid and higher than expected, *Geophys. Res. Lett.*, *33*, L17811, 2006.

Warneke, C., deGouw, J. A., Holloway, J. S., Peischl, J., Ryerson, T. B., Atlas, E., Blake, D., Trainer, M., and Parrish, D. D.: Multiyear trends in volatile organic compounds in Los Angeles, California: Five decades of decreasing emissions, *J. Geophys. Res.-Atmos.*, *117*, D00V17, 2012.

Zhang, Q., Jimenez, J. L., Canagaratna, M. R., Allan, J. D., Coe, H., Ulbrich, I., Alfarra, M. R., Takami, A., Middlebrook, A. M., Sun, Y. L., Dzepina, K., Dunlea, E., Docherty, K., DeCarlo, P. F., Salcedo, D., Onasch, T., Jayne, J. T., Miyoshi, T., Shimono, A., Hatakeyama, S., Takegawa, N., Kondo, Y., Schneider, J., Drewnick, F., Borrmann, S., Weimer, S., Demerjian, K., Williams, P., Bower, K., Bahreini, R., and Cottrell, L., R. J. Griffin,J. Rautiainen,J. Y. Sun,Y. M. Zhang, D. R. Worsnop : Ubiquity and Dominance of Oxygenated Species in Organic Aerosols in Anthropogenically–Influenced Northern Hemisphere Mid-latitudes, *Geophys. Res. Lett.*, *34*, L13801, 2007b.

Zotter, P., El-Haddad, I., Zhang, Y., Hayes, P. L., Zhang, X., Lin, Y., Wacker, L., Schnelle-Kreis, J., Abbaszade, G., Zimmermann, R., Surratt, J. D., Weber, R., Jimenez, J. L., Szidat, S., Baltensperger, U., and Prevot A. S. H.: Diurnal cycle of fossil and non-fossil carbon using radiocarbon analyses during CalNex, *J. Geophys. Res.-Atmos.*, *submitted*, 2013.

Table 2.1: Fraction of hydrocarbon reacted for an OH-exposure = 58.3×10^9 molec cm^{-3} s at 298 K and 1 atm. Hydrocarbons shown are abundant in a typical mixture of liquid gasoline and diesel fuel. Fraction reacted = 1 - exp(- $k_{OH} \times [OH] \times t$).

Hydrocarbon	Fraction Reacted	OH reaction-rate constant (cm^3 molec^{-1} s^{-1})
benzene[a]	0.069	1.22×10^{-12}
toluene[a]	0.280	5.63×10^{-12}
m-xylene[a]	0.740	2.31×10^{-11}
n-hexane[b]	0.272	5.45×10^{-12}
n-octane[b]	0.398	8.71×10^{-12}
n-dodecane[b]	0.555	1.39×10^{-11}

[a]Reaction rate constants from *Calvert et al.* (2002)
[b]Reaction rate constants from *Atkinson* (1997)

Table 2.2: Measured fleet-averaged fuel-based CO and NMHC emission factors (g/kg of fuel) reported by *Fujita et al.* (2012); *Gentner et al.* (2012). Numerical values in the right-most column are calculated using the conversion factor 1250 μg CO sm^{-3} (ppmv CO)$^{-1}$.

Date Values from *Fujita et al.* (2012)	Temperature °F	EF_{CO} $\frac{\text{g CO}}{\text{kg fuel}}$	EF_{NMHC} $\frac{\text{g NMHC}}{\text{kg fuel}}$	EF_{NMHC}/EF_{CO} $\frac{\text{g NHMC}}{\text{g CO}}$	EF_{NMHC}/EF_{CO} $\frac{\mu\text{g NMHC sm}^{-3}}{\text{ppmv CO}}$
Aug 21, Sat PM	95	23.0	1.59	0.069	86.3
Aug 22, Sun PM	92	25.4	1.98	0.078	97.5
Aug 24, Tue AM	92	16.7	1.40	0.084	105
Aug 24, Tue PM	101	19.1	2.51	0.131	164
Aug 25, Wed AM	92	18.9	1.35	0.071	88.8
Aug 25, Wed PM	102	30.4	3.05	0.100	125
Aug 28, Sat AM	72	25.9	1.09	0.042	52.5
Aug 29, Sun AM	70	10.7	0.51	0.048	60.0
Mean		21.3	1.69	0.078	97.5
Median		21.1	1.50	0.075	93.8
Values from *Gentner et al.* (2012)				0.039	48.8

Table 2.3: Gasoline vehicle-specific emission ratios, EF_{NMHC}/EF_{CO}, predicted by EMFAC2011 (`http://www.arb.ca.gov/emfac/`) for the South Coast Air Basin in Summer 2010. Emission ratios are based on daily CO and NMHC emission rates calculated by EMFAC2011. Emission ratios include all drive-cycle components (i.e. running, idle, start, diurnal evaporative, hot-soak evaporative, running evaporative, and resting evaporative). Rows are ordered in descending population. Numerical values in $\frac{\mu g\ NMHC\ m^{-3}}{ppmv\ CO}$ columns are calculated using the conversion factor 1250 μg CO sm^{-3} $(ppmv\ CO)^{-1}$. Note that the values predicted by EMFAC are higher than what is reported by *Gentner et al.* (2012) because they include products of incomplete combustion, evaporative emissions, and start emissions.

Veh. Class[a]	$\frac{g\ NHMC}{g\ CO}$	$\frac{\mu g\ NMHC\ sm^{-3}}{ppmv\ CO}$	Population
Values from *Gentner et al.* (2012)	0.031	38.3	Caldecott Tunnel
LDA	0.116	145	5,566,383
LDT2	0.093	116	1,806,334
MDV	0.081	101	1,474,925
LDT1	0.112	140	655,343
LHD1	0.115	144	257,882
MCY	0.161	201	213,296
MH	0.035	43.8	58,258
LHD2	0.112	140	27,933
T6TS	0.096	120	22,177
OBUS	0.088	110	7,278
UBUS	0.100	125	1,766
T7IS	0.051	63.8	1,501
SBUS	0.068	85.0	1,491

[a] See `http://www.arb.ca.gov/msei/emfac2011-pl-users-guide-122112.pdf` for a detailed description of each vehicle class.

Table 2.4: Diesel vehicle-specific emission ratios, EF_{NMHC}/EF_{CO}, predicted by EMFAC2011 (`http://www.arb.ca.gov/emfac/`) for the South Coast Air Basin in Summer 2010. Emission ratios are based on daily CO and NMHC emission rates calculated by EMFAC2011. Emission ratios include all drive-cycle components (i.e. running, idle, start, diurnal evaporative, hot-soak evaporative, running evaporative, and resting evaporative). Rows are ordered in descending population. Numerical values in $\frac{\mu g\ NMHC\ m^{-3}}{ppmv\ CO}$ columns are calculated using the conversion factor 1250 μg CO sm^{-3} $(ppmv\ CO)^{-1}$.

Veh. Class[a]	$\frac{g\ NHMC}{g\ CO}$	$\frac{\mu g\ NMHC\ m^{-3}}{ppmv\ CO}$	Population
Values from *Gentner et al.* (2012)	0.224	280.0	Caldecott Tunnel
LHD1	0.204	255	80,690
T6 instate small	0.256	320	37,131
LHD2	0.203	254	27,901
LDA	0.225	281	19,184
T6 instate heavy	0.275	344	15,303
T7 tractor	0.219	274	11,037
MH	0.261	326	10,110
T7 POLA	0.198	248	9,818
T7 Single	0.220	275	8,951
UBUS	0.217	271	7,084
T6 instate construction small	0.256	320	5,410
T7 NNOOS	0.224	280	5,372
T7 CAIRP	0.227	284	5,325
T6 Public	0.272	340	5,282
T7 SWCV	0.232	290	4,839
SBUS	0.314	393	4,388
T7 Public	0.267	334	3,579
All Other Buses	0.278	348	3,178
T7 single construction	0.220	275	3,176
T7 tractor construction	0.221	276	2,306

Continued on next page

Table 2.4 – *Continued from previous page*

Veh. Class[a]	$\frac{\text{g NHMC}}{\text{g CO}}$	$\frac{\mu\text{g NMHC m}^{-3}}{\text{ppmv CO}}$	Population
T6 instate construction heavy	0.275	344	2,242
T7 NOOS	0.231	289	1,939
MDV	0.205	256	1,504
Motor Coach	0.232	290	1,313
LDT1	0.236	295	953
T6 utility	0.238	298	890
LDT2	0.245	306	861
T7 utility	0.243	304	423
T7 CAIRP construction	0.227	284	392
T7 Ag	0.217	271	231
T6 Ag	0.291	364	187
T6 CAIRP small	0.244	305	136
T6 OOS small	0.244	305	78
T6 CAIRP heavy	0.258	323	44
T6 OOS heavy	0.258	323	25

[a] See `http://www.arb.ca.gov/msei/emfac2011-pl-users-guide-122112.pdf` for a detailed description of each vehicle class.

Table 2.5: CARB 2010 Estimated daily emission rates (annual average). Units are (metric-tons day^{-1}).

Source	Los Angeles County		South Coast Air Basin	
	CO	ROG[a]	CO	ROG[a]
STATIONARY SOURCES				
FUEL COMBUSTION	24.1 (1.3%)	4.3 (1.1%)	34.1 (1.1%)	5.8 (0.9%)
WASTE DISPOSAL	0.8 (0%)	0.9 (0.2%)	1.1 (0%)	9.1 (1.4%)
CLEANING AND SURFACE COATINGS	0.0 (0%)	25.8 (6.6%)	0.1 (0%)	40.7 (6.1%)
PETROLEUM PRODUCTION AND MARKETING	8.9 (0.5%)	25.1 (6.4%)	8.9 (0.3%)	33.2 (5.0%)
INDUSTRIAL PROCESSES	1.3 (0%)	11.6 (3.0%)	2.5 (0%)	20.2 (3.0%)
TOTAL STATIONARY SOURCES	35.0 **(1.9%)**	67.7 **(17.3%)**	46.8 **(1.5%)**	109.0 **(16.5)**
AREAWIDE SOURCES				
SOLVENT EVAPORATION	0 (0%)	82.7 (21.2%)	0 (0%)	129.4 (19.5%)
MISCELLANEOUS PROCESSES	51.2 (2.8%)	5.4 (1.4%)	112.3 (3.6%)	14.7 (2.2%)
TOTAL AREAWIDE SOURCES	51.2 **(2.8%)**	88.0 **(22.5%)**	112.3 **(3.6%)**	144.1 **(21.8%)**
MOBILE SOURCES				
ON-ROAD MOTOR VEHICLES	1096.3 (60.0%)	113.1 (29.0%)	1817.6 (58.4%)	182.8 (27.6%)
OTHER MOBILE SOURCES	579.5 (31.7%)	81.0 (20.7%)	973.2 (31.3%)	140.1 (21.1)
TOTAL MOBILE SOURCES	1675.8 **(91.7%)**	194.1 **(49.7%)**	2790.8 **(89.6%)**	322.9 **(48.7%)**
NATURAL (NON-ANTHROPOGENIC) SOURCES				
NATURAL SOURCES	65.0 (3.6%)	40.5 (10.4%)	164.2 (5.3%)	86.5 (13.1%)
TOTAL NATURAL SOURCES	65.0 **(3.6%)**	40.5 **(10.4%)**	164.2 **(5.3%)**	86.5 **(13.1%)**

(http://www.arb.ca.gov/app/emsinv/emssumcat.php)

[a]CARB reports ROG emission rates, which are similar to NMHC but do not include several low-reactive organic compounds such as ethane, acetone, CFCs, and HCFCs.

Table 2.6: Chemical constituents of lumped species shown in Figure 2.4.

Alkanes (C_6,C_9-C_{11})	Single-ring aromatics
n-hexane	benzene
n-nonane	toluene
n-decane	o-xylene
n-undecane	m-xylene
	p-xylene
	1-ethyl benzene
	styrene
	isopropyl benzene
	npropyl benzene
	1-ethyl 2-methyl benzene
	1-ethyl 3-methyl benzene
	1-ethyl 4-methyl benzene
	1,2,3-trimethylbenzene
	1,2,4-trimethylbenzene
	1,3,5-trimethylbenzene

Table 2.7: Median emission factors and SOA mass yields reported in *Gordon et al.* (2013). These values include products of incomplete combustion and products of incomplete catalytic converter oxidation.

	preLEV	LEV1	LEV2
Median EF_{CO} (gCO L-gas^{-1})	210	25	9
Median EF_{NMOG} (gNMOG L-gas^{-1})	4.5	1.3	0.40
LDGV-Fleet Fraction	0.07	0.36	0.57
Effective SOA Mass Yield[a] (g/g)	0.008 (0.008)	0.03-0.17 (0.10)	0.07-0.25 (0.16)

[a] Values in parentheses are the arithmetic mean of the reported SOA mass yield range.

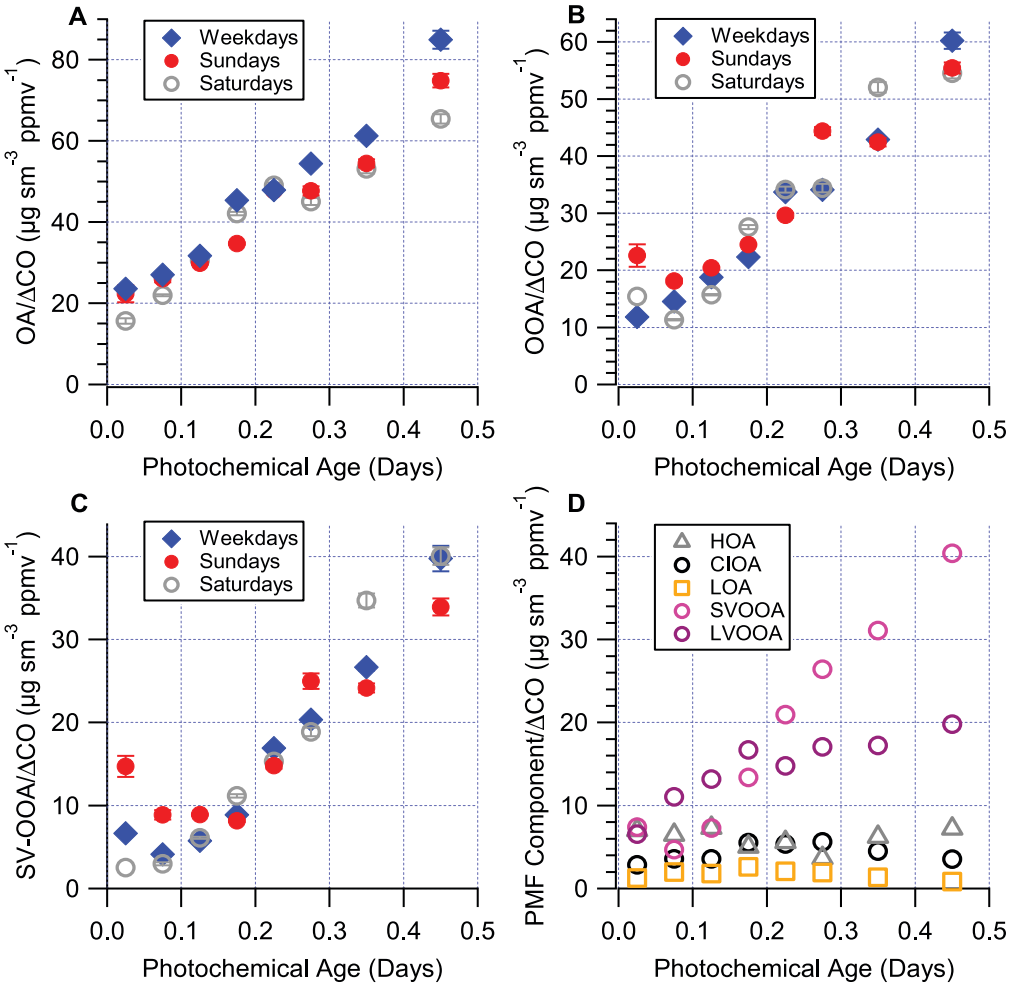

Figure 2.1: Measured AMS PMF factor concentrations normalized by CO enhancement (ΔCO is the ambient CO minus the estimated background CO (105 ppb) as functions of photochemical age (see (*Hayes et al.*, 2013) for a detailed description of how this figure was constructed). (A) The evolution of OA/ΔCO versus photochemical age for Pasadena during CalNex separated by day of the week. Error bars indicate the standard errors. Photochemical age is determined using the method of *Parrish et al.* (2007). Also shown are the analogous plots for (B) OOA and (C) SV-OOA. (D) Evolution of the PMF component concentrations normalized to ΔCO versus photochemical age.

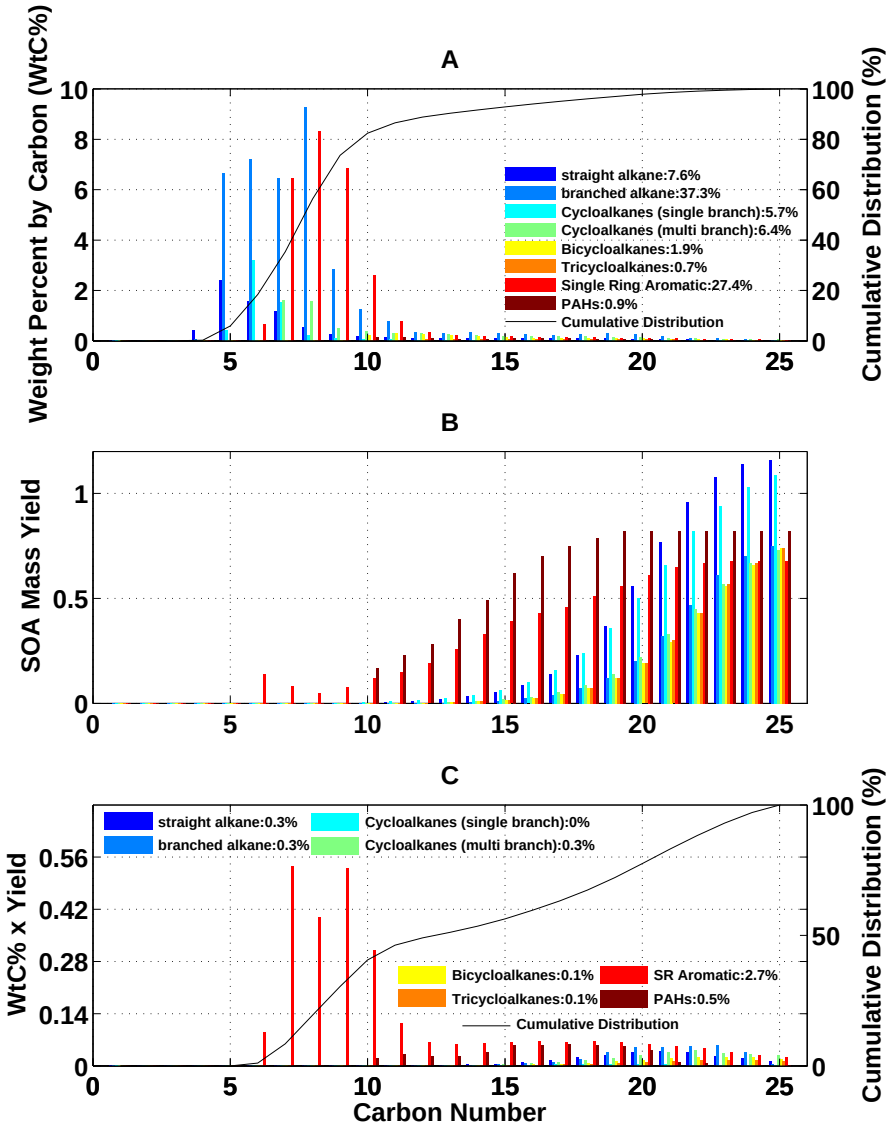

Figure 2.2: Distribution of mass by chemical class based on California fuel-sale data comprising 13% diesel and 87% gasoline, by volume (top panel). Distribution of compound specific SOA mass yields (middle panel). Relative contributions of each group of species to predicted SOA, calculated as the yields multiplied by weight percent (by carbon) in liquid fuel (bottom panel). Data are from Tables S5, S6, and S8 of *Gentner et al.* (2012).

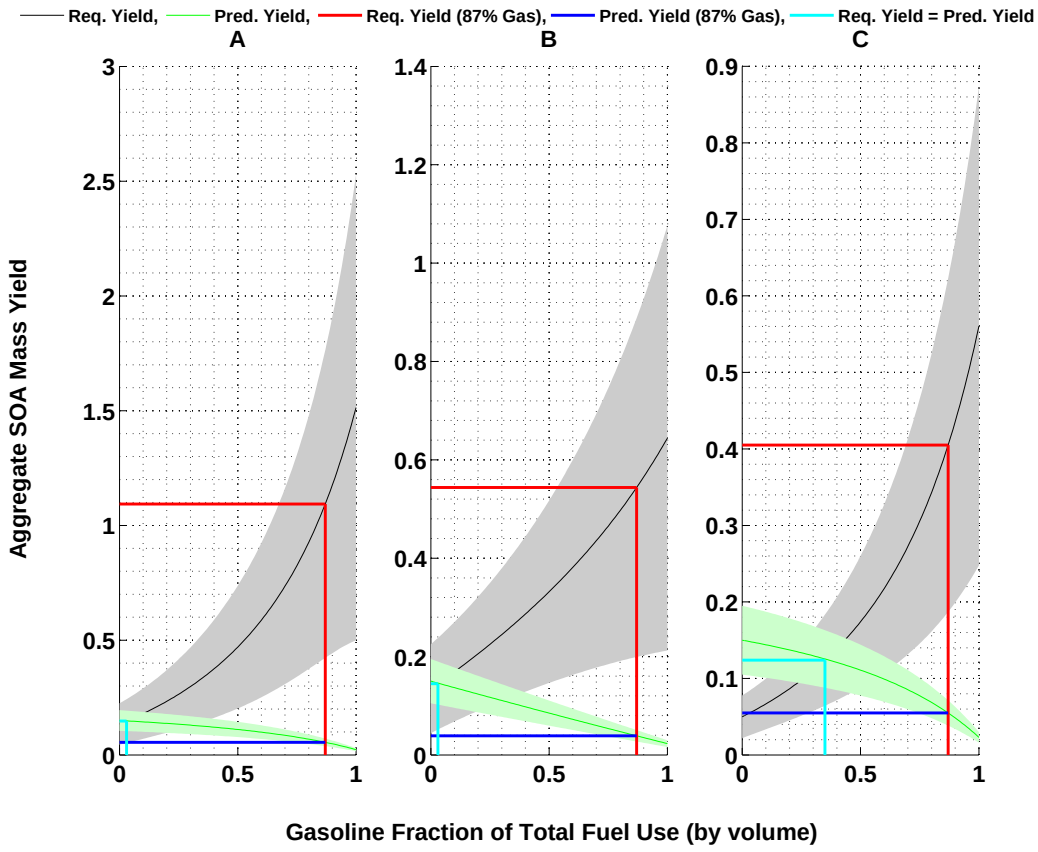

Figure 2.3: Vehicular SOA mass yields compared to ambient SV-OOA mass yields assuming all fossil SV-OOA is attributable to vehicular emissions. (A) Black Line: Aggregate SOA mass yield required to match observations at the Pasadena ground site assuming all fossil SOA is attributable to vehicular emissions. Green Line: SOA mass yield of unburned fuel (gasoline/diesel) components reported by *Gentner et al.* (2012). Red Line: yield required for 87% gasoline and 13% diesel fuel (state-average). Blue Line: SOA mass yield of liquid fuel for 87% gasoline and 13% diesel fuel (state-average). Cyan Line: point at which the black line crosses the green line. (B) Same as (A) except $EF_{GPOM,gas}$ have been increased by a factor of 2.35. (C) Same as (A) except $EF_{GPOM,gas}$ and $EF_{GPOM,dies}$ have both been increased by a factor of 2.7 (*McDonald et al.*, 2013). Error-bars correspond to propagated uncertainties, and all plots have been adjusted to account for partial reaction of hydrocarbons at 0.45 days of photochemical aging. Required yields are based on SV-OOA measurements and ^{14}C measurements reported in *Zotter et al.* (2013); *Hayes et al.* (2013). All quantities are plotted as functions of gasoline and diesel fuel sales (by volume).

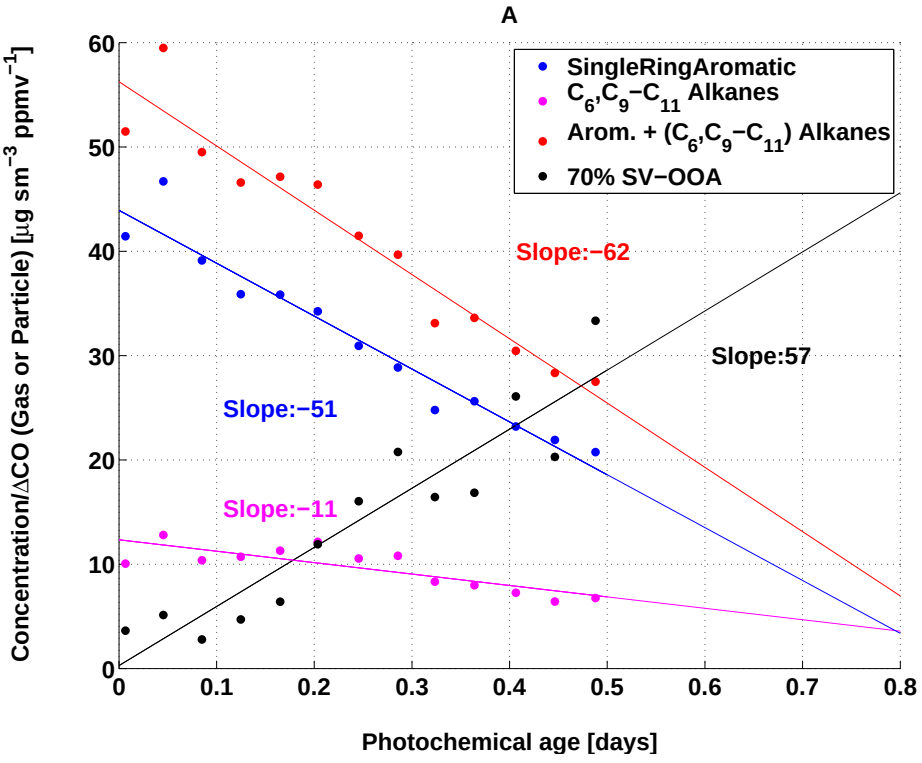

Figure 2.4: Measured PMF OOA factor concentrations normalized by CO enhancement (ΔCO is the ambient CO minus the estimated background CO (105 ppb)) as functions of photochemical age. Also shown are lumped gas-phase VOC concentrations normalized by ΔCO. See Table 2.6 for the chemical speciation of each lumped species.

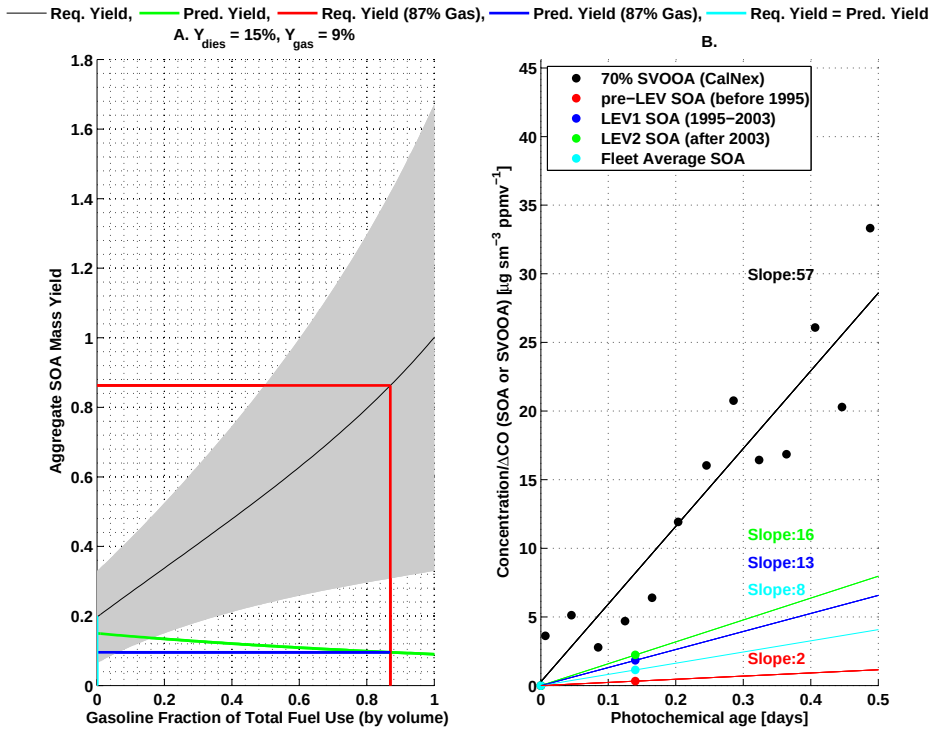

Figure 2.5: Same as Figure 2.3, except emission factors for gasoline-fueled vehicles and aggregate SOA mass yields are based on the experimentally derived values reported in *Gordon et al.* (2013). (A) Aggregate SOA mass yield for gasoline exhaust is 9%, which is considered representative of the California LDGV fleet. (B) Measured PMF SV-OOA factor concentrations normalized by CO enhancement (ΔCO is the ambient CO minus the estimated background CO (105 ppb)) as functions of photochemical age. Also shown are experimentally derived SOA/ΔCO enhancements resulting from photooxidation of tail-pipe emissions from 15 light-duty gasoline vehicles (LDGVs) recruited from the California in-use fleet. All LDGV experiments were conducted in a portable chamber under urban-like conditions, and all LDGV data are taken directly from *Gordon et al.* (2013).

Chapter 3

Insight into the Numerical Challenges of Implementing 2-Dimensional SOA Models in Atmospheric Chemical Transport Models

3.1 Abstract

The new generation of secondary organic aerosol (SOA) models that represent gas- and particle-phase chemistry and thermodynamic partitioning using discrete two-dimensional grids (e.g. SOM, 2D-VBS) cannot be efficiently implemented into three-dimensional atmospheric chemical transport models (CTMs) due to the large number of bins (tracers) required. In this study, we introduce a novel mathematical framework, termed the Oxidation State/Volatility Moment Method, that is designed to address these computational burdens so as to allow the new generation of SOA models to be implemented into CTMs. This is accomplished by mapping the two-dimensional grids onto probability distributions that conserve carbon and oxygen mass. Assessment of the Moment Method strengths (speed, carbon and oxygen conservation) and weaknesses (numerical drift) provide valuable insight that can guide future development of SOA modules for atmospheric CTMs.

3.2 Introduction

Secondary organic aerosol (SOA) formation ensues with homogeneous gas-phase reactions between volatile organic compounds (VOCs) and oxidants (OH, O_3, NO_3), leading to products of sufficiently low volatility to condense into the particle phase. For most VOCs, the initial oxidant attack is followed by several generations of gas-phase reactions, involving functionalization or fragmentation reactions of the products (*Jimenez et al.*, 2009). Heterogeneous and particle-phase reactions may also play a significant role in certain systems (*Cappa and Wilson*, 2012; *Zhang and Seinfeld*, 2012). Whereas it is desirable to embody within a model describing SOA formation as much basic understanding as possible of the formation and evolution process, a key goal of SOA model development is a computational module that can be included in 3-dimensional atmospheric chemical transport models (CTMs). Consequently, the challenge is to balance the desire for chemical fidelity with the need for computational feasibility.

Aerosol Mass Spectrometer (AMS) measurements of organic aerosols, now a routine component of atmospheric measurements and chamber experiments, enable derivation of the atomic O:C and

H:C ratios of SOA, from which one can infer overall aerosol oxidation state (*Kroll et al.*, 2011). The volatility of the organic mixture is related to the molecular properties of its components, as embodied, for example, in carbon number and oxidation state. The relationship between oxidation state and volatility is not unique; that is, molecular mixtures with the same overall oxidation state do not necessarily exhibit the same overall volatility. Therefore, an essential characteristic of an SOA model is the representation of volatility and oxidation state.

The new generation of SOA models represents SOA formation and evolution in terms of the competition between functionalization and fragmentation, particle-phase chemistry, the extent of oxidation, and the change of volatility. For instance, *Pankow and Barsanti* (2009) introduced the "carbon number - polarity grid" (CNPG) framework, which expands the traditional "2-product" concept of *Odum et al.* (1996) to the "np+mP", in which n products with m possible types of low volatility compounds represent the lumped oxidation and accretion products. The carbon number and polarity of each product need to be evaluated according to the current understanding of gas-phase SOA formation. SOA growth is computed based on equilibrium partitioning theory (*Barsanti et al.*, 2011; *Pankow and Barsanti*, 2009).

Donahue et al. (2011) developed the two-dimensional Volatility Basis Set (2D-VBS) employing saturation mass concentration, C^*, and the mean oxidation state, $\overline{OS}$, of the aerosol to describe the coupled aging and phase partitioning of SOA. A bin in the 2D space represents a suite of molecules; an ensemble of molecules with the same C^* and $\overline{OS}$ is assumed to behave similarly in the aggregate. When chamber data are available, the volatility distribution of the products is obtained by SOA mass yield fitting. A gas-phase photooxidation mechanism for a parent VOC provides the functionalization and fragmentation channels leading to products that map onto the 2D-VBS grid. A key issue is to assign the SOA yield of each bin that potentially comprises a suite of compounds sharing similar C^* and $\overline{OS}$ (*Donahue et al.*, 2012a, 2011).

Cappa and Wilson (2012) formulated the Statistical Oxidation Model (SOM) that describes SOA formation as a statistical evolution in the space of numbers of carbon and oxygen atoms, n_C and n_O, respectively, with fitted parameters that govern the probability of fragmentation vs.

functionalization, the number of oxygen atoms added per functionalization reaction, and the decrease in vapor pressure accompanying addition of an oxygen atom. An advantage of SOM is that the functionalization channel is fully represented by several free parameters so that no adjustment (e.g., molar yields for each bin of 2-D VBS, distribution of functional groups in FGOM) is required before optimal fitting of the free parameters to chamber-generated SOA. A disadvantage is that predicted products do not necessarily correspond to actual molecules (*Cappa and Wilson*, 2012).

Zhang and Seinfeld (2012) developed the Functional Group Oxidation Model (FGOM), which is based on explicit functional groups that result from the oxidation of a parent VOC, but also characterized by a set of parameters that are determined by fitting to chamber data. The progressive gas-phase oxidation channel leading to a distribution of different functional groups is generated according to specific VOC photooxidation mechanisms. The fragmentation channel, particle-phase oxidative and non-oxidative channels are represented by a set of adjustable parameters. The distribution and evolution of a set of functional groups that can sufficiently represent the gas-phase photochemistry of a certain hydrocarbon is required (*Zhang and Seinfeld*, 2012).

In short, significant progress has been made in the development of next-generation models to represent the formation and evolution of SOA. However, the gap between the new class of 2D SOA models and the computational requirements of 3D CTMs has not been bridged. Specifically, each of the SOA models described above, except the FGOM, represents the evolution of the SOA-forming chemistry via a matrix of properties. Simulating the physio-chemical evolution of such a matrix within a box-model does not present a computational problem. However, in a 3D CTM, the advection-diffusion equation requires each matrix to be defined over the entire 3D grid so that matrices can be transported between grid cells. Since a typical 3D grid may contain thousands of grid cells, this poses a severe computational burden. Consequently, the Odum 2-product model (*Odum et al.*, 1996), although now out of date, has remained the most commonly used SOA parameterization in state-of-the-art 3D CTMs (*Barsanti et al.*, 2013). Therefore, computational simplifications need to be devised to implement any of the 2D SOA models in a 3D model. Here we describe a new computational approach, termed the Oxidation State/Volatility Moment Method (hereafter referred

to as the Moment Method). We focus on the 2D-VBS as exemplary of the new class of SOA models for demonstrating the strengths and limitations of the new approach.

3.3 Discrete 2D-VBS

In the 2-Dimensional Volatility Basis Set (2D-VBS) (*Donahue et al.*, 2012a, 2011), SOA formation and evolution is represented by lumping species into discrete bins according to their oxidation state and the pure component saturation concentration (C^*) of the molecule. *Donahue et al.* (2011) originally used O:C ratio as the 2D-VBS ordinate, whereas *Donahue et al.* (2012a) use the mean oxidation state of carbon, $\overline{OS}$. Since O:C ratio and $\overline{OS}$ are intimately linked, we use the O:C ratio as a measure of oxidation because, as will be shown later, this allows the Moment Method to conserve oxygen mass. At any instant in time, the 2D-VBS predicts the probability of finding carbon atoms associated with molecules that have a given discrete O:C and C^*, defined here as $F_{g,p}(O{:}C,C^*)$ (g = gas, p = particle). The 2D probability distributions are such that:

$$\sum_{O:C}\sum_{C^*} F_g(O:C,C^*) = 1 \tag{3.1}$$

$$\sum_{O:C}\sum_{C^*} F_p(O:C,C^*) = 1 \tag{3.2}$$

These probability distributions are combined with the total carbon concentrations (C-atoms m^{-3}) in the gas and particle phases, denoted by $NC_{tot,g}$ and $NC_{tot,p}$, respectively,

$$\mathrm{NC_g(O:C, C^*) = NC_{tot,g} F_g(O:C, C^*)} \qquad [\text{C-atom m}^{-3}] \tag{3.3}$$

$$\mathrm{NC_p(O:C, C^*) = NC_{tot,p} F_p(O:C, C^*)} \qquad [\text{C-atom m}^{-3}] \tag{3.4}$$

$$\sum_{\mathrm{O:C}} \sum_{\mathrm{C^*}} \mathrm{NC_g(O:C, C^*) = NC_{tot,g}} \qquad [\text{C-atom m}^{-3}] \tag{3.5}$$

$$\sum_{\mathrm{O:C}} \sum_{\mathrm{C^*}} \mathrm{NC_p(O:C, C^*) = NC_{tot,p}} \qquad [\text{C-atom m}^{-3}] \tag{3.6}$$

where, for example, $\mathrm{C^*}$ may range from 10^{-5} to 10^{9} μg m^{-3}, separated by powers of 10, and O:C may range from 0 to 1, in increments of 0.1. $\mathrm{NC_g(O:C, C^*)}$ and $\mathrm{NC_p(O:C, C^*)}$ are the portions of the carbon atom concentration associated with molecules that have the specified values of O:C and $\mathrm{C^*}$ in the gas and the particle phases, respectively. As will be shown later, the average number of carbon atoms per molecule can be determined from the total carbon atom concentration, $\mathrm{C^*}$, and the O:C ratio in each grid cell.

These gas- and particle-phase probability distributions are updated continuously according to the gas-phase oxidation/fragmentation mechanism and absorptive partitioning framework of the 2D-VBS (*Donahue et al.*, 2012a). At any instant in time, the 2D probability distributions given by equations (3.3)–(3.4) can be collapsed into 1D probability distributions:

$$\mathrm{NC_{O:C,g}(O:C) = \sum_{C^*} NC_g(O:C, C^*)} \tag{3.7}$$

$$\mathrm{NC_{C^*,g}(C^*) = \sum_{O:C} NC_g(O:C, C^*)} \tag{3.8}$$

$$\mathrm{NC_{O:C,p}(O:C) = \sum_{C^*} NC_p(O:C, C^*)} \tag{3.9}$$

$$\mathrm{NC_{C^*,p}(C^*) = \sum_{O:C} NC_p(O:C, C^*)} \tag{3.10}$$

where $\mathrm{NC_{O:C,g}(O:C)}$, $\mathrm{NC_{O:C,p}(O:C)}$, $\mathrm{NC_{C^*,g}(\ C^*)}$, and $\mathrm{NC_{C^*,p}(\ C^*)}$ are the 1D probability distributions for gas- and particles-phase carbon atoms associated with the specified O:C ratio, and gas-

and particles-phase carbon atoms associated with the specified C^*, respectively. The n^{th} moment, M_n, of each of these four distributions is:

$$M_n^{O:C,g} = \sum_{O:C} (O:C)^n NC_{O:C,g}(O:C) \tag{3.11}$$

$$M_n^{C^*,g} = \sum_{C^*} (C^*)^n NC_{C^*,g}(C^*) \tag{3.12}$$

$$M_n^{O:C,p} = \sum_{O:C} (O:C)^n NC_{O:C,p}(O:C) \tag{3.13}$$

$$M_n^{C^*,p} = \sum_{C^*} (C^*)^n NC_{C^*,p}(C^*) \tag{3.14}$$

Note that the zeroth moments of these distributions are equal to the total carbon atom concentrations in the gas and particle phases, and the first moments of $NC_{O:C,g}(O:C)$ and $NC_{O:C,p}(O:C)$ are equal to the total oxygen atom concentrations in the gas and particle phases, respectively.

To determine average molecular quantities, such as the average number of carbon atoms per molecule, one begins with the following equation that was derived to relate pure component vapor pressure to n_C and n_O (*Donahue et al.*, 2011):

$$\log_{10} C^* = (n_C^o - n_C) b_C - n_O b_O - 2 \frac{n_C n_O}{n_C + n_O} b_{CO} \tag{3.15}$$

where C^* is the pure component saturation concentration (μg m^{-3}), $b_C \simeq 0.475$, $b_O \simeq 2.3$, $b_{CO} \simeq -0.3$, $n_C^o = 25$, n_C = average number of carbon atoms per molecule, n_O = average number of oxygen atoms per molecule. On the 2D-VBS grid, the values of C^*, O:C, and total carbon concentration, $NC(O:C,C^*)$, are specified for each grid cell. Therefore, the left hand side of equation (3.15) is known, and n_O on the right hand side of equation (3.15) can be replaced with $(O:C)n_C$:

$$\log_{10} C^* = (n_C^o - n_C) b_C - (O:C) n_C b_O - 2 \frac{(O:C) n_C}{1 + (O:C)} b_{CO} \tag{3.16}$$

Solving for n_C, one obtains:

$$n_C(O:C, C^*) = \frac{n_C^o b_C - \log_{10} C^*}{(b_C + (O:C) b_O + 2\frac{(O:C)}{1+(O:C)} b_{CO})} \qquad [\text{C-atoms molecule}^{-1}] \qquad (3.17)$$

$$n_O(O:C, C^*) = (O:C) \times n_C(O:C, C^*) \qquad [\text{O-atoms molecule}^{-1}] \qquad (3.18)$$

With the average number of carbon atoms per molecule and the total carbon atom concentration specified, the total molecular concentration in each 2D-VBS grid is:

$$N(O:C, C^*)[\text{molecules m}^{-3}] = \frac{NC(O:C, C^*)\ [\text{C-atoms m}^{-3}]}{n_C(O:C, C^*)\ [\text{C-atoms molecule}^{-1}]} \qquad (3.19)$$

where N(O:C,C^*) is the total number of molecules within a given 2D-VBS grid cell. The average molecular mass for a given grid cell is:

$$MW(O:C, C^*) = MW_C \times n_C(O:C, C^*) + MW_O \times n_O(O:C, C^*) \qquad (3.20)$$

where MW_C and MW_O are the molecular masses of carbon and oxygen, respectively. These quantities are necessary for simulating any physio-chemical transformations (e.g. gas-phase chemistry, thermodynamic partitioning).

3.4 Derivation of a Continuous 2D-VBS

3.4.1 Transforming discrete distributions into continuous distributions

The main challenge in using the 2D-VBS, or any of the recently developed discrete 2D-SOA models, is that a large number of species must be tracked explicitly (e.g. discretization of the [O:C,C^*] space for 2 phases×15 C^* bins ×11 O:C bins = 330 tracers). To put this into perspective, the Community Multiscale Air Quality (CMAQ) model currently simulates all alkane SOA using four tracers (one parent hydrocarbon, one species to track how much of the parent has reacted in a given time step, one semi-volatile particle-phase species, and one semi-volatile gas-phase species) (*Carlton et al.*, 2012).

Therefore, implementing the discrete 2D-VBS grid increases the number of tracers by a factor of 82.5, which is computationally challenging. The Moment Method overcomes these computational obstacles by approximating the discrete probability distribution given by equations (3.3)–(3.4) using a continuous 2D probability distribution such that:

$$\mathrm{dF(O:C, C^*) = f(O:C, C^*)d(O:C)d(C^*)} \tag{3.21}$$

$$\iint \mathrm{f(O:C, C^*)d(O:C)d(C^*)} = 1 \tag{3.22}$$

$$\iint \mathrm{NC_{tot} f(O:C, C^*)d(O:C)d(C^*)} = \mathrm{NC_{tot}} \tag{3.23}$$

Where f is defined as the probability density at a given [O:C,C^*] on the continuous probability distribution. Note that dF(O:C,C^*) now represents the probability that a portion of the total carbon number concentration comprises molecules having O:C ratios between O:C and O:C + d(O:C) and C^* values between C^* and C^* + d(C^*).

For mathematical convenience, the continuous 2D probability distributions are assumed to be separable:

$$\mathrm{f_g(O:C, C^*) = f_{O:C,g}(O:C) f_{C^*,g}(C^*)} \tag{3.24}$$

$$\mathrm{f_p(O:C, C^*) = f_{O:C,p}(O:C) f_{C^*,p}(C^*)} \tag{3.25}$$

This assumption presupposes that at any instant in time, the general shape of the probability distributions in a particular phase are "ellipse-like" with the major and minor axes being aligned with the axes of the 2D space. Fig. 3.1 depicts a hypothetical 2D distribution as represented by this approach. From equations (3.24)–(3.25) it follows that:

$$\mathrm{NC_{tot,g} = NC_{tot,g} \int f_{O:C,g}(O:C)d(O:C) \int f_{C^*,g}(C^*)d(C^*)} \tag{3.26}$$

$$\mathrm{NC_{tot,p} = NC_{tot,p} \int f_{O:C,p}(O:C)d(O:C) \int f_{C^*,p}(C^*)d(C^*)} \tag{3.27}$$

We are now free to choose a functional form for each 1D probability distribution ($f_{O:C,g}$, $f_{C^*,g}$, $f_{O:C,p}$, $f_{C^*,p}$). We choose to represent all continuous 1D O:C probability distributions as gamma probability distributions and all continuous 1D C^* probability distributions as log-normal distributions:

$$f_{gamma}(x) = \frac{1}{\Gamma(k)(\theta)^k}(x)^{k-1}e^{(-\frac{x}{\theta})} \tag{3.28}$$

$$f_{log-normal}(x) = \frac{1}{\sqrt{2\pi}\ln(\sigma)x}e^{-\left(\frac{\ln(\frac{x}{x_{ave}})}{\sqrt{2}\ln(\sigma)}\right)^2} \tag{3.29}$$

where $\Gamma(\bullet)$ is the gamma function, and k, θ, σ, and x_{ave} are free parameters. These probability distributions are chosen because of their mathematical convenience, the compact number of parameters required to describe each distribution, and the fact that the distributions are defined on the appropriate domains. This technique is similar to representing a binned aerosol population number distribution using continuous functions such as the log-normal probability distribution with D_p as the independent variable (*Binkowski and Roselle*, 2003). Here we assume that the binned SOA carbon concentration distribution in both phases can be represented as the product of two 1D probability distributions, which have O:C and C^* as their respective independent variables. A graphical example of the Moment Method is shown Fig. 3.1

Therefore, the assumed probability distributions in the gas and the particle phases are:

$$f_{O:C,g}(O:C) = \frac{1}{\Gamma(k_g)(\theta_g)^{k_g}}(O:C)^{k_g-1}e^{(-\frac{O:C}{\theta_g})} \tag{3.30}$$

$$f_{C^*,g}(C^*) = \frac{1}{\sqrt{2\pi}\ln(\sigma_g)C^*}e^{-\left(\frac{\ln\left(\frac{C^*}{C^*_{avg,g}}\right)}{\sqrt{2}\ln(\sigma_g)}\right)^2} \tag{3.31}$$

$$f_{O:C,p}(O:C) = \frac{1}{\Gamma(k_p)(\theta_p)^{k_p}}(O:C)^{k_p-1}e^{(-\frac{O:C}{\theta_p})} \tag{3.32}$$

$$f_{C^*,p}(C^*) = \frac{1}{\sqrt{2\pi}\ln(\sigma_p)C^*}e^{-\left(\frac{\ln\left(\frac{C^*}{C^*_{avg,p}}\right)}{\sqrt{2}\ln(\sigma_p)}\right)^2} \tag{3.33}$$

Notice that each of the four probability distributions requires two parameters, k and θ for the gamma distributions, and C^*_{avg} and σ for the log-normal distributions. Therefore, the total number

of parameters that need to be specified for each phase is 5 (k, θ, σ, C^*_{avg}, and NC_{tot}). The moment-generating functions for the general gamma distribution and the general log-normal distributions are:

$$M_n = \int_0^\infty (x)^n \frac{1}{\Gamma(k)(\theta)^k}(x)^{k-1}e^{-\frac{x}{\theta}}dx = (\theta)^n \frac{\Gamma(k+n)}{\Gamma(k)} \tag{3.34}$$

$$M_n = \int_0^\infty (x)^n \frac{1}{\sqrt{2\pi}\ln(\sigma)x}e^{-\left(\frac{\ln(\frac{x}{x_{ave}})}{\sqrt{2}\ln(\sigma)}\right)^2}dx = (x_{ave})^n e^{\left(\frac{n^2}{2}\ln^2\sigma\right)} \tag{3.35}$$

Using the continuous $f_{O:C,g}$ and $f_{C^*,g}$ as examples, the moment-generating functions become:

$$M_n^{O:C,g} = NC_{tot,g}\int_0^\infty (O:C)^n f_{O:C,g}(O:C)d(O:C) = NC_{tot,g}(\theta_g)^n \frac{\Gamma(k_g+n)}{\Gamma(k_g)} \tag{3.36}$$

$$M_n^{C^*,g} = NC_{tot,g}\int_0^\infty (C^*)^n f_{C^*,g}(C^*)d(C^*) = NC_{tot,g}(C^*_g)^n e^{\left(\frac{n^2}{2}\ln^2\sigma_g\right)} \tag{3.37}$$

The first three moments of $NC_{C^*,g}$ are:

$$M_0^{C^*,g} = NC_{tot,g}(C^*_{ave,g})^0 e^{\left(\frac{0^2}{2}\ln^2\sigma_g\right)} \tag{3.38}$$

$$M_1^{C^*,g} = NC_{tot,g}(C^*_{ave,g})^1 e^{\left(\frac{1^2}{2}\ln^2\sigma_g\right)} \tag{3.39}$$

$$M_2^{C^*,g} = NC_{tot,g}(C^*_{ave,g})^2 e^{\left(\frac{2^2}{2}\ln^2\sigma_g\right)} \tag{3.40}$$

The values of $NC_{tot,g}$, σ_g, and $C^*_{avg,g}$ are constrained by the first three moments of $NC_{C^*,g}(C^*)$. Solving equations (3.38)–(3.40) explicitly for $NC_{tot,g}$, σ_g, and $C^*_{avg,g}$, one obtains:

$$N_{tot,g} = M_0^{C^*,g} \tag{3.41}$$

$$\sigma_g = \exp\left(\sqrt{\ln\left(\frac{M_2^{C^*,g}M_0^{C^*,g}}{\left(M_1^{C^*,g}\right)^2}\right)}\right) \tag{3.42}$$

$$C^*_{ave,g} = \frac{M_1^{C^*,g}}{M_0^{C^*,g}}\sqrt{\frac{(M_1^{C^*,g})^2}{M_0^{C^*,g}M_2^{C^*,g}}} \tag{3.43}$$

The parameters given by (3.41)–(3.43) can be used as initial guesses in a nonlinear least-squares regression to find the optimal log-normal parameters for describing the discrete 1D distributions. By optimal, we mean that upon rediscretizing the continuous 1D C* distribution (see next section), the appropriate amount of mass is placed into the correct C^* bins. This is necessary because the parameters given by equations (3.41)–(3.43) are defined for a continuous log-normal C^* distribution that is consistent with the moments of the discrete 1D distributions given by equations (3.12) and (3.14). However, the discrete 1D C^* probability distributions given by (3.8) and (3.10) may not be exactly log-normal, and small differences between the original discrete 1D distribution and the 1D distribution created from discretizing the continuous 1D distribution defined by (3.41)–(3.43) may incorrectly shift mass between phases during thermodynamic gas-particle equilibration. Determining the optimal log-normal parameters via least-squares regression mitigates this issue to some extent, and once the optimal log-normal parameters have been determined, the moments that correspond to these parameters can be determined via equations (3.38)–(3.40). As will be discussed later, inexact fitting of a continuous C^* distribution to a discretized C^* distribution is the dominant limitation of the Moment Method in its current form.

The first three moments of $NC_{O:C,g}$ are:

$$M_0^{O:C,g} = NC_{tot,g}(\theta_g)^0 \frac{\Gamma(k_g + 0)}{\Gamma(k_g)} \tag{3.44}$$

$$M_1^{O:C,g} = NC_{tot,g}(\theta_g)^1 \frac{\Gamma(k_g + 1)}{\Gamma(k_g)} \tag{3.45}$$

$$M_2^{O:C,g} = NC_{tot,g}(\theta_g)^2 \frac{\Gamma(k_g + 2)}{\Gamma(k_g)} \tag{3.46}$$

For any positive real k_g, the following relations hold:

$$\Gamma(1) = 1 \tag{3.47}$$

$$\Gamma(k_g + 1) = k_g \Gamma(k_g) \tag{3.48}$$

Using this property of the gamma function, equations (3.44)–(3.46) can be simplified to:

$$M_0^{O:C,g} = NC_{tot,g} \tag{3.49}$$

$$M_1^{O:C,g} = NC_{tot,g}(\theta_g)^1 k_g \tag{3.50}$$

$$M_2^{O:C,g} = NC_{tot,g}(\theta_g)^2 k_g(k_g + 1) \tag{3.51}$$

Therefore, the values of $NC_{tot,g}$, k, and θ are constrained by the first three moments of each 1D probability distribution. Solving equations (3.49)–(3.51) explicitly for N_{tot}, k, and θ, we get:

$$NC_{tot,g} = M_0^{O:C,g} \tag{3.52}$$

$$k_g = \frac{(M_1^{O:C,g})^2}{(M_o^{O:C,g})(M_2^{O:C,g}) - (M_1^{O:C,g})^2} \tag{3.53}$$

$$\theta_g = \frac{(M_0^{O:C,g})(M_2^{O:C,g}) - (M_1^{O:C,g})^2}{(M_0^{O:C,g})(M_1^{O:C,g})} \tag{3.54}$$

Since thermodynamic gas-particle partitioning is much less sensitive to O:C ratio than it is to C^*, the least-squares procedure used for the 1D C^* distributions is not necessary for 1D O:C distributions, and the parameters given by equations (3.52)–(3.54) can be used to constrain the continuous 1D O:C distributions.

We are now in a position to transform a discretized O:C by C^* probability distribution to a continuous O:C by C^* probability distribution. The steps of the process are summarized as follows:

1. Begin with the discretized O:C by C^* grids in the gas phase and particle phase predicted by the 2D-VBS at any instant in time.

2. Calculate the four 1D probability distributions of the discretized O:C by C^* grid using equations (3.7)–(3.10).

3. Calculate the first three moments of each 1D probability distribution using equations (3.11)–(3.14).

4. Use each three-moment set ($M_0^{C^*}$, $M_1^{C^*}$, $M_2^{C^*}$) to determine the three parameters (NC_{tot}, σ,

C^*_{ave}) for the continuous 1D C^* probability distribution using equations (3.41)–(3.43). Using these as initial guesses, use nonlinear least-squares regression to determine the optimal log-normal parameters for describing the discrete 1D C^* distributions. Using equations (3.38)–(3.40), calculate a new three-moment set ($M_0^{C^*}$, $M_1^{C^*}$, $M_2^{C^*}$) that corresponds to the optimal log-normal parameters.

5. Use each three-moment set ($M_0^{O:C}$, $M_1^{O:C}$, $M_2^{O:C}$) to determine the three parameters (NC_{tot}, k, θ) needed to constrain each continuous 1D O:C probability distribution using equations (3.52)–(3.54).

6. Once all four continuous 1D probability distributions have been determined, calculate the continuous 2D probability distributions in the gas and particle phases using equations (3.24)–(3.25)

Using this approach, any discretized O:C by C^* grid can be transformed to a continuous O:C by C^* probability distribution such that total carbon number concentration ($M_0^{O:C}$) and total oxygen number ($M_1^{O:C}$) are conserved. The next step is to develop a methodology by which the continuous O:C by C^* probability distributions can be mapped back to the discretized O:C by C^* probability distributions.

3.4.2 Transforming continuous distributions into discrete distributions

Representing [O:C, C^*] probability distributions as the product of two continuous 1D probability distributions is ideal for implementing the 2D-VBS into a 3D CTM because only the 10 moments needed to constrain the four 1D distributions are tracked (as compared to the 330 grid boxes in the original 2D-VBS). However, the gas-phase oxidation/fragmentation mechanism and the absorptive partitioning framework of the 2D-VBS requires that the continuous probability distribution be mapped onto a discretized O:C by C^* grid prior to any physio-chemical transformation. This is accomplished using the cumulative gamma distribution function and the cumulative log-normal

distribution function H(x) = CDF(x):

$$H(x) = \int_0^x F(x)dx = \int_0^x \frac{1}{\Gamma(k)(\theta)^k}(x)^{k-1}e^{-\frac{x}{\theta}}dx \tag{3.55}$$

$$H(x) = \int_0^x F(x)dx = \int_0^x \frac{1}{\sqrt{2\pi}\ln(\sigma)x}e^{-\left(\frac{\ln(\frac{x}{x_{avg}})}{\sqrt{2}\ln(\sigma)}\right)^2}dx \tag{3.56}$$

Using the continuous $F_{O:C,g}(O:C)$ as an example, the probability of a molecule having carbon number between $O:C_{min}$ and $O:C_{max}$ is:

$$F^{disc}_{O:C,g}(O:C) = \int_{O:C_{min}}^{O:C_{max}} f^{cont}_{O:C,g}(O:C)d(O:C) = H(O:C_{max}) - H(O:C_{min}) \tag{3.57}$$

where the superscripts "disc" and "cont" stand for discretized and continuous, respectively. The value of $f^{cont}_{O:C,g}(O:C_{min} < O:C < O:C_{max})$ derived from the continuous probability distribution will be assigned to the discrete $F^{disc}_{O:C,g}(O:C)$ bin. For example, assume $O:C_{min}$ is 0.45, $O:C_{C,max}$ is 0.55, and O:C is the discrete bin value 0.5. Therefore, the probability of finding a molecule using the continuous probability distribution, $F_{O:C,g}(O:C)$, that should be assigned to the discrete bin O:C = 0.5 is:

$$F^{disc}_{O:C,g}(0.5) = H(0.5 + 0.05) - H(0.5 - 0.05) \tag{3.58}$$

Note that in equation (3.58) we have arbitrarily chosen ±0.05 as the integration offsets. However, the integration offsets are not free parameters, but instead are chosen such that total oxygen number is conserved upon integration of the new discretized probability distribution. Since we will apply equation (3.58) to all discrete O:C values (i.e. O:C = 0.0, 0.1, 0.2, 0.3,...), which are separated by 0.1, then $O:C_{min}$ and $O:C_{max}$ should differ by 0.1 ($O:C_{max}$ - $O:C_{min}$ = 0.1). Let the integration offset (OS) be defined as OS = $O:C_{max}$ – O:C. Combining the definition of OS with the 0.1 difference between $O:C_{max}$ and $O:C_{min}$, equation (3.58) becomes:

$$F^{disc}_{O:C,g}(O:C) = H(O:C + OS) - H(O:C - (0.1 - OS)) \tag{3.59}$$

If we equate the 1st moment of equation (3.59) with the 1st moment given by equation (3.11), we end up with one equation and one unknown:

$$M_1^{O:C,g} = \sum_{O:C} (O:C)(H(O:C + OS) - H(O:C - (0.1 - OS)))NC_{tot,g} \tag{3.60}$$

Equation (3.60) guarantees that total oxygen number is conserved upon mapping the continuous 1D probability distribution, $F_{O:C,g}^{cont}$, back to the discrete 1D probability distribution, $F_{O:C,g}^{disc}$. OS can be solved for in equation (3.60) using standard numerical techniques (e.g., bisection). Once OS is known, equation (3.59) can be used to populate the entire discretized 1D probability distribution for gas-phase O:C.

The equations in this section have been developed using $F_{O:C,g}$ as an example, and the identical process can be repeated for $F_{O:C,p}$. For discretizing F_{C^*}, the OS is set to half the C^* bin width ($10^{0.5}$ in this study). This is necessary because the continuous F_{C^*} distributions are determined via least-squares regression based on the centers of the discrete 1D C^* distribution bins.

We are now in a position to transform a continuous O:C by C^* probability distribution to a discretized O:C by C^* probability distribution. The steps of the process are summarized as follows:

1. Begin with the four continuous 1D probability distributions ($F_{O:C,g}$, $F_{C^*,g}$, $F_{O:C,p}$, and $F_{C^*,p}$) given by equations (3.30)–(3.33)

2. For each 1D O:C probability distribution, solve equation (3.60) for the integration offset, OS, needed to ensure conservation of total carbon and total oxygen

3. Once the OS is known for each 1D O:C probability distribution, populate each 1D O:C probability distribution using equation (3.59).

4. For the 1D C^* distributions, set the OS to half the discrete C^* bin width, and populate each 1D C^* probability distribution using equation (3.59).

5. Once all four continuous 1D probability distributions have been determined, calculate the discretized 2D probability distributions in the gas and particle phases using equations (3.24)–

(3.25)

In this section, we have presented the derivation of the mathematical framework of the Moment Method. In the following section, we present four numerical experiments to demonstrate the strengths and limitations of the Moment Method.

3.5 Results and Discussion

In this section, four numerical experiments are conducted to evaluate the behavior and performance of the Moment Method using the fully-explicit discretized 2D-VBS grid as a basis for comparison. The four tests are summarized as follows:

1. **Basic characterization:** Construct an initial discretized 2D distribution (e.g., Fig. 3.1), allow it to equilibrate, and reform it using the Moment Method.

2. **Air Mass Mixing:** Mix two discrete grids to obtain a third, and mix the moments of two discrete grids to obtain the moments of the third. Compare the mixed grids to see how well the Moment Method handles air mass mixing.

3. **Semi-scattered Data:** Determine how well equilibration of a semi-randomized distribution is approximated by the Moment Method.

4. **Numerical Drift:** Repeat the basic-characterization test 100 times to demonstrate how error from the fitting procedure propagates.

These tests are designed to illustrate the behavior of the Moment Method as it pertains to transforming discrete grids to continuous grids, transforming continuous grids back to discrete grids, and distributing mass between the gas and particle phases via thermodynamic partitioning. Addressing the Moment Method limitations identified in this work, as well as adding gas- and particle-phase oxidation/fragmentation chemistry remain as future work.

3.5.1 Basic characterization

In this section, we apply the Moment Method approach, in its entirety, to a synthetic data set. First, a synthetic, continuous 2D distribution is constructed by multiplying a log-normal distribution with a gamma distribution. The system is then initialized with 10^{17} C-atoms m^{-3}, which correspond to $\sim$4 μg m^{-3} of total (gas + particle) organic material. Then the continuous distribution is discretized using the mathematical relations presented in Section 3 (Fig. 3.2A). This grid is then equilibrated between the gas and particle phases (Fig. 3.2B,C) via the thermodynamic partitioning algorithm presented in Appendix A. Once the discrete grids have been equilibrated, distributions in each phase are then refit, rediscretized, and re-equilibrated to obtain new grids (Fig. 3.2D,E). Note that although the initial distribution given in Fig. 3.2A is a product of a gamma and log-normal function, the distributions given in Fig. 3.2B,C and Fig. 3.2D,E are not due to the equilibration. Finally, the discrete grids presented in Fig. 3.2D,E are combined (Fig. 3.2F) and compared to the original distribution (Fig. 3.2A).

The shapes and positions of the four phase-specific equilibrated distributions (Fig. 3.2B-E) and the two total distributions (Fig. 3.2A,F) are qualitatively identical. As given in Table 3.1, the O:C ratios in each phase are very similar with differences in O:C ratio being $\sim$0.5%, and differences in total mass being $\sim$3%. We conclude that, for these conditions, the Moment Method is able to reproduce a 2D-VBS grid with high fidelity; the discretizing-equilibrating-fitting (DEF) procedure behaves as expected.

3.5.2 Air Mass Mixing

In this section, the ability of the Moment Method to simulate air mass mixing is explored. Air mass mixing occurs continuously in the real atmosphere, and is represented within 3D CTMs via solution of the advection-diffusion equation. Therefore, it is imperative that any SOA model candidate represent air mass mixing as accurately as possible.

We begin with two air masses, each of which is initially represented by a single (gas+particle) discrete 2D-VBS grid (see Fig. 3.3A,B). These air masses are mixed by combining the individual grid

cells of the respective 2D-VBS grids, resulting in a third discrete grid (not shown). The third grid is then equilibrated, resulting in new 2D distributions in the gas and particle phase (Fig. 3.3C,D). In this analysis, Fig. 3.3C,D represent the "correct" air mass mixing solution.

To represent the same phenomenon using the Moment Method, the 2D grids shown in Fig. 3.3A,B are equilibrated individually prior to mixing. This results in four 2D distributions (Fig. 3.3EFHI). We then determine the moments of each phase in each air mass and combine them to form the moments of the third air mass (i.e. $M_n^{Cell1} + M_n^{Cell2} = M_n^{Cell3}$). Once the moments of the third air mass have been determined, we then rediscretize the continuous distributions in each phase (Fig. 3.3G for gas phase and Fig. 3.3J for particle phase). Finally, the discrete distributions of the third air mass are equilibrated (Fig. 3.3M,N) and compared to the "correct" air mass mixing solution (Fig. 3.3C,D). Note that air mass mixing was conducted by combining the moments of each respective phase, as opposed to combining the individual grid cells. As given in Table 3.2, the Moment Method predicts mass concentrations and O:C ratios in each phase that are within 5% of the correct answer.

The same analysis was conducted for initial conditions with varying degrees of diagonal separation (Fig. 3.4). The initial conditions in Fig. 3.3A,B correspond to a medium degree of separation (Fig. 3.4B). Table 3.2 contains the resulting data for the Moment Method applied to initial total (Air Mass 1 + Air Mass 2) distributions given in Fig. 3.4. As shown in Table 3.2, the absolute and relative errors of both total mass and O:C ratio are fairly independent of the diagonal separation shown in Fig. 3.4. This makes sense because if the two air masses have a significant diagonal separation, then one air mass will be predominately in the gas phase and one will be in the particle phase. On the other hand, if the air masses have minimal diagonal separation, then the correct solution resembles that of Fig. 3.2A, which we showed could be represented accurately by the Moment Method (see Basic Characterization).

3.5.3 Semi-scattered Data

The starting initial distributions so far have been discretizations of gamma and log-normal functions. We now assess how well the Moment Method performs with a more scattered distribution. Such an assessment is necessary because gas-phase oxidation/fragmentation chemistry will produce distributions that are not necessarily gamma-log-normal products. To begin, a standard (gamma-lognormal) distribution of total organic mass was altered via randomized scaling factors (Fig. 3.5A), and the Moment Method was implemented exactly as in the Basic Characterization test. The correct 2D distributions shown in Fig. 3.5B,C are very similar (i.e. within 5%) to those given in Fig. 3.5D,E. Therefore, even when the initial 2D distribution is not exactly a gamma-lognormal product, at thermodynamic equilibrium, the 2D distributions in each phase can be approximated well by the Moment Method.

We note that the absolute and relative errors will depend on both the initial distributions and the total (gas + particle) concentration of organic mass in the system. Nevertheless, this test suggests that the Moment Method may be able to represent other scattered distributions well. Future work is necessary to characterize how well the Moment Method handles distributions created by realistic gas-phase chemical mechanisms that include both fragmentation and functionalization pathways.

3.5.4 Numerical Drift

In this section we discuss the primary numerical limitation of the Moment Method in its current form. As given in Table 3.1, the DEF procedure introduces some nonzero error with each iteration. Were the Moment Method to be implemented into a 3D CTM, the DEF procedure will be executed hundreds of times for a given simulation. Therefore, it is necessary to characterize the extent to which this error propagates throughout a simulation. We begin with a discrete 1D C^* log-normal distribution (black line in Fig. 3.6A). This distribution is then allowed to equilibrate between the gas and particle phases (red and blue lines, respectively, in Fig. 3.6A). Ideally, the DEF procedure should not alter the distributions shown in Fig. 3.6. However, the partitioning equation skews the correct distributions in the gas and particle phase to the left and right, respectively. When

continuous 1D log-normal distributions (which are symmetric) are then refit, some non-zero fraction of mass is inevitably shifted between grid cells. As shown in Figure Fig. 3.6B, C, this mass shifting can become substantial after several iterations. This numerical limitation suggests that the Moment Method is not yet an adequate solution for combining 2D SOA models with 3D CTMS. Potential strategies for overcoming this limitation are discussed in the next section.

3.6 Moment-Bin Hybrid & Grid Coarsening

One approach to overcome the numerical drift is to use a bin-moment-hybrid framework in which the 1D C^* distributions always remain binned and the 1D O:C distributions are still assumed to be continuous gamma distributions. Shown graphically in Figure 3.7B, a bin-moment-hybrid approach removes the error introduced by inaccurately shifting mass between bins when discretizing the continuous lognormal distributions in the original Moment Method approach. The main challenge with the hybrid approach is that it requires many more tracers. Specifically, 6 moments are required for each C^* bin (3 moments to constrain $NC^i_{tot,g}$, k^i_g, θ^i_g, and 3 moments to constrain $NC^i_{tot,p}$, k^i_p, θ^i_p, where i corresponds to C^* bin "i"). This approach is still computationally advantageous as compared to the original 2D-VBS framework with a 70% reduction in the number of tracers (10 O:C bins per C^* bin $\rightarrow$ 3 O:C moments per C^* bin), but may still be too computationally expensive to be used in a 3D model such as CMAQ.

An alternative approach would be to deliberately coarsen the 2D grid such that only a few fixed grid boxes are retained. In theory, the grid boxes would be identified by running the explicit 2D-VBS and then determining which grid boxes contribute most significantly to the measurable particle-phase properties (e.g. total mass concentration, O:C ratio). Once these grid boxes, and their grid-box precursors, are identified, all other grid boxes can be discarded. The grid coarsening approach is basically a systematic way to optimize the chemical characteristics (O:C ratio and saturation concentration) of a 1D VBS. This approach is shown graphically in Figure 3.7C. Although this method requires a fair amount of tuning, it does remove the numerical drift limitation of the Moment Method approach, and requires far fewer tracers than the bin-moment hybrid approach.

3.7 Implementing the Moment Method into a 3D CTM

In the event that the numerical drift limitation can be overcome, the Moment Method can be implemented into a 3D CTM via the following steps. As shown above, the O:C and C^* distributions can be constrained in both phases by tracking 10 moments (M_0^g, M_0^p, $M_1^{O:C,g}$, $M_1^{C^*,g}$, $M_1^{O:C,p}$, $M_1^{C^*,p}$, $M_2^{O:C,g}$, $M_2^{C^*,g}$, $M_2^{O:C,p}$, $M_2^{C^*,p}$). These 10 moments would be added to a CTM as tracers and tracked (i.e. emitted, transported, and deposited) at all locations within the Eulerian 3D grid at all times. If a specific cell in the 3D grid meets certain criteria (e.g. $M_0^g + M_0^p \geq M_0^{min}$), the moments can be converted into the discretized O:C by C^* grids. Once the discretized O:C by C^* grids in both phases have been populated, they can then be updated during the model time step according to the gas-phase oxidation/fragmentation mechanism and absorptive partitioning framework of the original 2D-VBS. After the O:C by C^* grids undergo oxidation, fragmentation, and equilibration, the 10 moments can be updated, and the discretized O:C by C^* grids can be discarded. In this study, continuous distributions are discretized to form grids that contain 330 grid boxes (165 in each phase). However, the resolution of the discretized grids can be increased or decreased to address factors such as mitigating numerical drift due to the DEF procedure, accurately representing gas- and particle-phase chemical reactions, and the computational requirements of the computer on which the 3D CTM is running.

3.8 Conclusions

Significant progress has been made in using box models to represent the formation and evolution of SOA. However, little work has focused on bridging the gap between the advanced chemical mechanisms of 2D SOA box models and the strict computational requirements of 3D CTMs. In this study, we have presented a novel mathematical framework, termed the Oxidation State/Volatility Moment Method, that addresses this issue. Specifically, when applied to the 2D-VBS, the Moment Method reduces the number of tracers required from 330 to 10. This is accomplished by describing the 2D grids using certain probability distributions, which can reproduce a variety of data while conserving

carbon and oxygen masses.

Various numerical experiments were conducted to characterize the behavior and performance of the Moment Method. The Basic Characterization Test, Air Mass Mixing Test, and Semi-scattered Test all suggest that the Moment Method is a promising mathematical framework for combining 2D SOA models with 3D CTMS. However, the Numeric Drift Test revealed that inexact fitting of symmetric distributions to skewed distributions introduces an unacceptable amount of error when the DEF procedure is repeated several times. Two strategies (Moment-Bin Hybrid & Grid Coarsening) for overcoming this numerical drift limitation were discussed qualitatively.

Future work should focus on (1) removing the error introduced by inexact fitting followed by thermodynamic partitioning, (2) assessing how the Moment Method performs when gas-phase oxidation/fragmentation chemistry is included, (3) testing alternative 1D probability distributions (not just log-normal and gamma distributions), and (4) quantitatively assessing the Moment-Bin Hybrid & Grid Coarsening approaches as compared to the explicit 2D-VBS.

Acknowledgements

This work was supported by U.S. Department of Energy grant DE-SC 0006626.

Bibliography

Barsanti, K. C., Smith, J. N., and Pankow, J. F. (2011), Application of the np+mP modeling approach for simulating secondary organic particulate matter formation from /alpha-pinene oxidation, *Atmos. Environ.*, *45*, 6812-6819.

Barsanti, K. C., Carlton, A. G., and Chung, S. H. (2013), Analyzing experimental data and model parameters: implications for predictions of SOA using chemical transport models, *Atmos. Chem. Phys.*, *13*, 12073-12088.

Binkowski, F. and Roselle, S. (2003), Models-3 community multiscale air quality (CMAQ) model aerosol component - 1. Model description, *J. Geophys. Res.-Atmos.* , *108*.

Cappa, C. D. and Wilson, K. R. (2011), Evolution of organic aerosol mass spectra upon heating: implications for OA phase and partitioning behavior, *Atmos. Chem. Phys.*, *11*, 1895-1911.

Cappa, C. and Wilson, K. R. (2012), Multi-generation gas-phase oxidation, equilibrium partitioning, and the formation and evolution of secondary organic aerosol, *Atmos. Chem. Phys.*, *12*, 9505-9528.

Annmarie G. Carlton, Prakash V. Bhave, Sergey L. Napelenok, Edward O. Edney, Golam Sarwar, Robert W. Pinder, George A. Pouliot, and Marc Houyoux (2012), Model Representation of Secondary Organic Aerosol in CMAQv4.7, *Environ. Sci. Technol.*, *44(22)*, 8553–8560.

Donahue, N. M., Epstein, S. A., Pandis, S. N., and Robinson, A. L. (2011), A two-dimensional volatility basis set: 1. organic-aerosol mixing thermodynamics, *Atmos. Chem. Phys.*, *11*, 3303-3318.

Donahue, N. M., Kroll, J. H., Pandis, S. N., and Robinson, A. L. (2012a), A two-dimensional volatility basis set – Part 2: Diagnostics of organic-aerosol evolution, *Atmos. Chem. Phys.*, *12*, 615-634.

Donahue, N. M., Henry, K. M., Mentel, T. F., Kiendler-Scharr, A., Spindler, C., Bohn, B., Brauers, T., Dorn, H. P., Fuchs, H., Tillmann, R., Wahner, A., Saathoff, H., Naumann, K.-H., Mhler, O., Leisner, T., Mller, L., Reinning, M.-C., Hoffman, T., Salo, K., Hallquist, M., Frosch, M., Bilde, M., Tritscher, T., Barmet, P., Praplan, A. P., DeCarlo, P. F., Domenn, J., Prvt, A. S. H., and Baltensperger, U. (2012b), Aging of biogenic secondary organic aerosol via gas-phase OH radical reactions, *Proc. Natl. Acad. Sci.*, *109*, 13503-13508.

Jimenez, J. L., et al. (2009), Evolution of Organic Aerosols in the Atmosphere, *Science*, *326(5959)*, 1525–1529

Kroll, J. H., Donahue, N. M., Jimenez, J. L., Kessler, S. H., Canagaratna, M. R., Wilson, K. R., Altieri, K. E., Mazzoleni, L. R., Wozniak, A. S., Bluhm, H., Mysak, E. R., Smith, J. D., Charles, E. K., and Worsnop, D. R. (2011), Carbon oxidation state as a metric for describing the chemistry of atmospheric organic aerosol, *Nature Chem.*, *3*, 133-139.

Murphy, B. N., Donahue, N. M., Fountoukis, C., and Pandis, S. N. (2012), Simulating the oxygen content of ambient organic aerosol with the 2D volatility basis set, *Atmos. Chem. Phys.*, *11*, 7859-7873.

Murphy, B. N., Donahue, N. M., Fountoukis, C., DallOsto, M., ODowd, C., Kiendler-Scharr, A., and Pandis, S. N. (2012), Functionalization and fragmentation during ambient organic aerosol aging: application of the 2-D volatility basis set to field studies, *Atmos. Chem. Phys. Discuss.*, *12*, 9857-9901.

Nguyen, K., and Dabdub, D. (2001), Two-level time-marching scheme using splines for solving the advection equation, *Atmos. Environ.*, *35*, 1627–1637.

Odum, J. R., Hoffmann, T.,Bowman, F., Collins, D., Flagan, R. C., Seinfeld, J. H. (1996), Gas/Particle Partitioning and Secondary Organic Aerosol Yields, *Environ. Sci. Technol.*, *30*, 2580–2585.

Pankow, J. F., and Barsanti, K. C. (2009), The carbon number-polarity grid: A means to manage the complexity of the mix of organic compounds when modeling atmospheric organic particulate matter, *Atmos. Environ.*, *43*, 2829-2835.

Shiraiwaa, M., Ammannb, M., Koopc, T., Pschl, U. (2011), Gas uptake and chemical aging of semisolid organic aerosol particles, *Proceedings of the National Academy of Sciences*, *108*, 11003-11008.

Zhang, X., and Seinfeld, J. H. (2012), A Functional Group Oxidation Model (FGOM) for SOA formation and aging, *Atmos. Chem. Phys. Discuss.*, *12*, 32565-32611.

Table 3.1: Statistical performance of the Moment Method during the Basic Characterization Test (Fig. 3.2).

Subfigure*	Mass (μg m^{-3})	Abs. Error (μg m^{-3})	Rel. Error (%)	O:C$_{ave}$	Abs. Error (O:C)	Rel. Error (%)
3.2b	1.58			0.41		
3.2c	2.40			0.40		
3.2d(b)	1.64	0.06	3.77	0.41	0.00	0.45
3.2e(c)	2.34	-0.06	-2.48	0.40	0.00	-0.36

*In the subfigure column, "m(n)" indicates m is the fitted solution predicted by the Moment Method and n is the benchmark (correct) solution.
Abs. Error = (Moment Method Value) - (Benchmark Value)
Rel. Error = (Moment Method Value) - (Benchmark Value) / (Benchmark Value) × 100%

Table 3.2: Gas and particle-phase concentrations from Air Mass Mixing Test presented in Fig. 3.3 using initial conditions from Fig. 3.4. "Fit" refers to air masses mixed via the Moment Method.

Quantity	Fig. 3.4a (close)	Fig. 3.4b (medium)	Fig. 3.4c (far)
Gas Mass (μg m^{-3})	3.79	3.00	2.66
Gas Mass Fit (μg m^{-3})	3.80	3.08	2.68
Gas Mass Abs. Error (μg m^{-3})	0.01	0.08	0.01
Gas Mass Rel. Error (%)	0.28	2.66	0.55
Particle Mass (μg m^{-3})	3.29	4.39	5.35
Particle Mass Fit (μg m^{-3})	3.28	4.31	5.33
Particle Mass Abs. Error (μg m^{-3})	-0.01	-0.08	-0.02
Particle Mass Rel. Error (%)	-0.32	-1.82	-0.29
Gas O:C	0.26	0.25	0.24
Gas O:C Fit	0.26	0.26	0.25
Gas O:C Abs. Error	0.01	0.01	0.01
Gas O:C Rel. Error (%)	2.16	3.91	3.20
Particle O:C	0.30	0.37	0.52
Particle O:C Fit	0.29	0.37	0.51
Particle O:C Abs. Error	-0.01	-0.01	-0.01
Particle O:C Rel. Error (%)	-2.28	-1.68	-1.04

Table 3.3: Statistical performance of the Moment Method during the Semi-scattered Test (Fig. 3.5).

Subfigure*	Mass (μg m^{-3})	Abs. Error (μg m^{-3})	Rel. Error (%)	O:C$_{ave}$	Abs. Error (O:C)	Rel. Error (%)
3.5b	1.80			0.41		
3.5c	2.17			0.39		
3.5d(b)	1.72	-0.08	-4.39	0.41	-0.00	-0.37
3.5e(c)	2.25	0.08	3.65	0.39	0.00	0.51

*In the subfigure column, "m(n)" indicates m is the fitted solution predicted by the Moment Method and n is the benchmark (correct) solution.
Abs. Error = (Moment Method Value) - (Benchmark Value)
Rel. Error = (Moment Method Value) - (Benchmark Value) / (Benchmark Value) × 100%

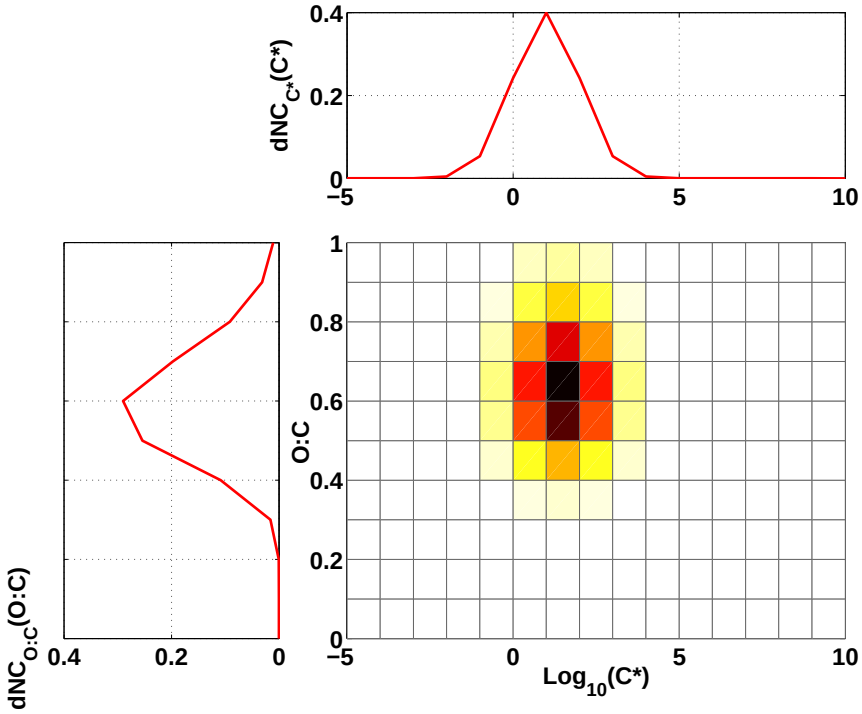

Figure 3.1: The Moment Method: 2D probability distributions are represented as products of 1D probability distributions.

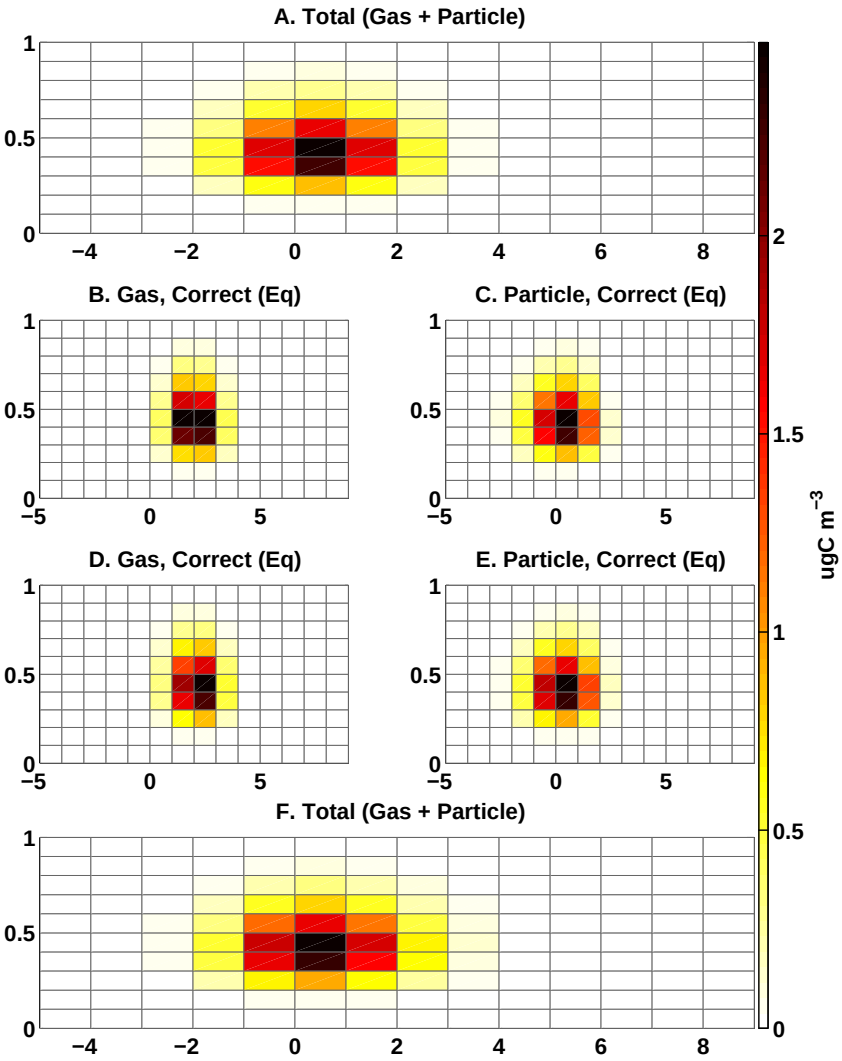

Figure 3.2: Application of the Moment Method to a hypothetical O:C vs C^* distribution: (A) Organic material is distributed on the grid. This material is then equilibrated between the gas (B) and particle phases (C). Using the equations in the text, continuous distributions are then fit to each phase, rediscretized, and re-equilibrated to form updated gas (D) and particle phase (E) distributions. These distributions are then added together (F).

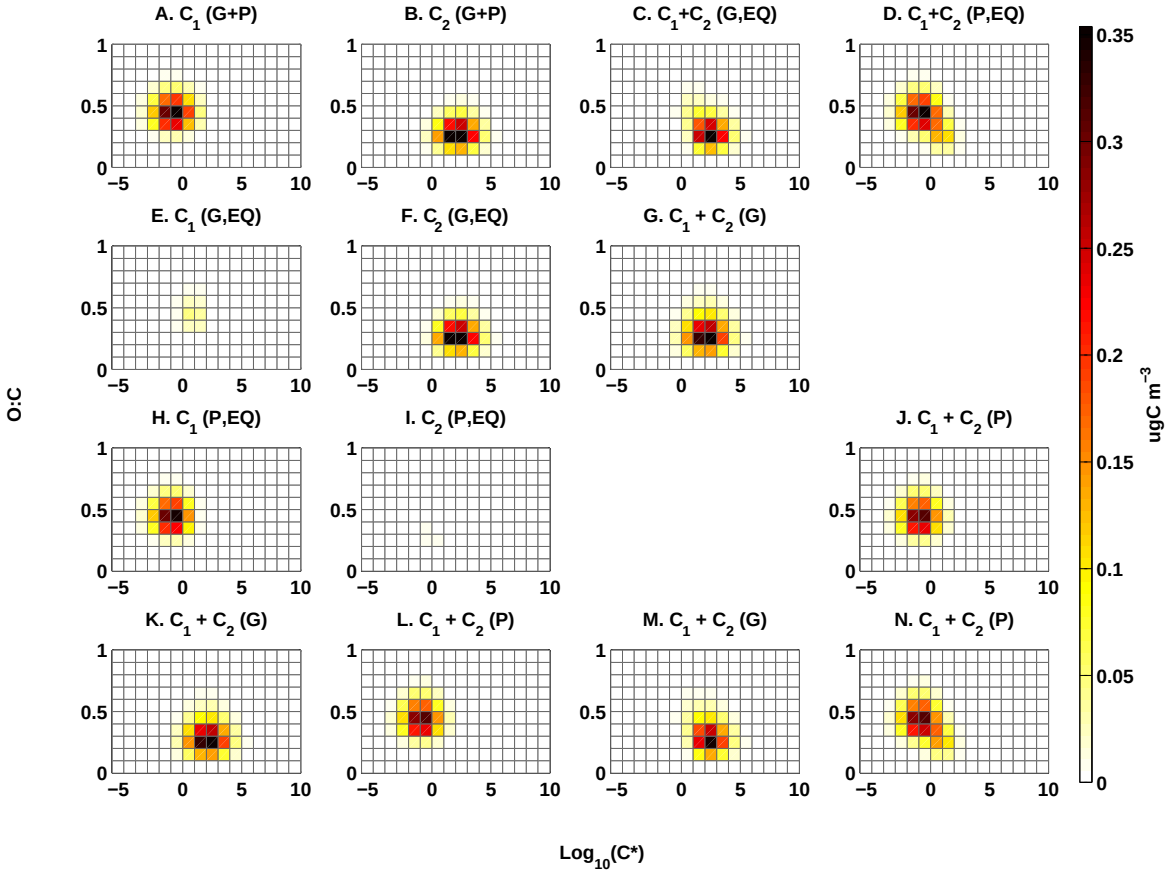

Figure 3.3: Grid Cell Mixing: (A) Total (gas+particle) mass is distributed in Cell 1 (C1). (B) Total (gas+particle) mass is distributed in Cell 2 (C2). (C) Gas-phase portion of C1+C2 after equilibration. (D) Particle-phase portion of C1+C2 after equilibration. (E) Gas-phase portion of C1 after equilibration, but prior to mixing. (F) Gas-phase portion of C2 after equilibration, but prior to mixing. (G) Gas-phase grid created from the combined moments of subfigures E and F. (H) Particle-phase portion of C1 after equilibration, but prior to mixing. (I) Particle-phase portion of C2 after equilibration, but prior to mixing. (J) Particle-phase grid created from the combined moments of subfigures H and I. (K) Same as (G). (L) Same as (J). (M) Gas-phase grid created from the combined moments of subfigures E and F after equilibration. (N) Particle-phase grid created from the combined moments of subfigures E and F after equilibration. (M) and (N) should be compared to (C) and (D), respectively.

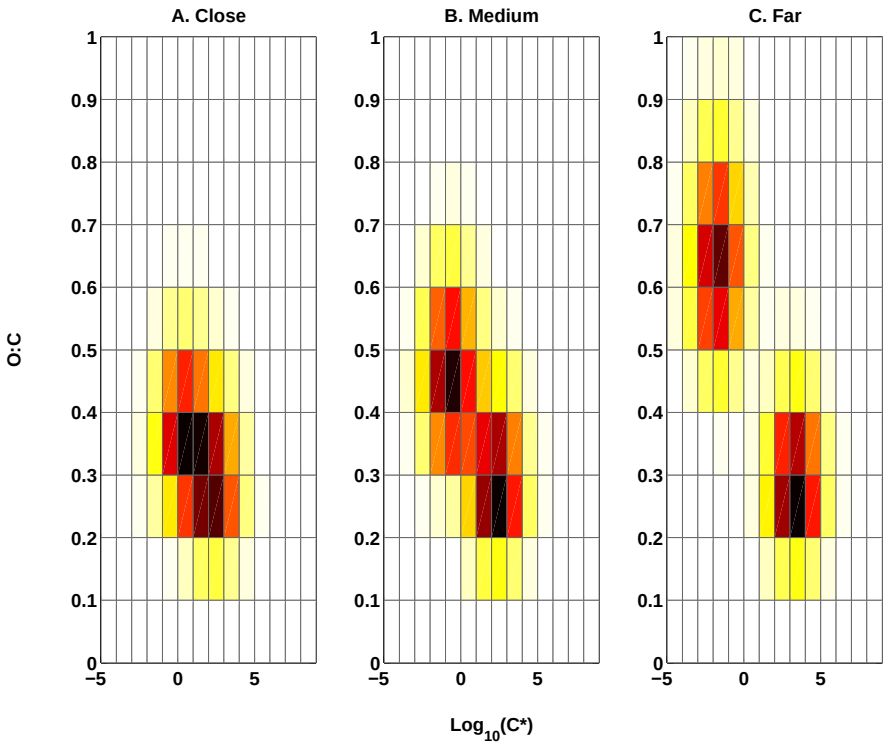

Figure 3.4: Combining cells that occupy different parts of the O:C vs C^* grid. The analysis shown in Figure 3.3 was conducted for initial conditions with varying degrees of diagonal separation (Fig. 3.4A,B,C). The initial conditions in Fig. 3.3A,B correspond to a medium degree of separation (Fig. 3.4B).

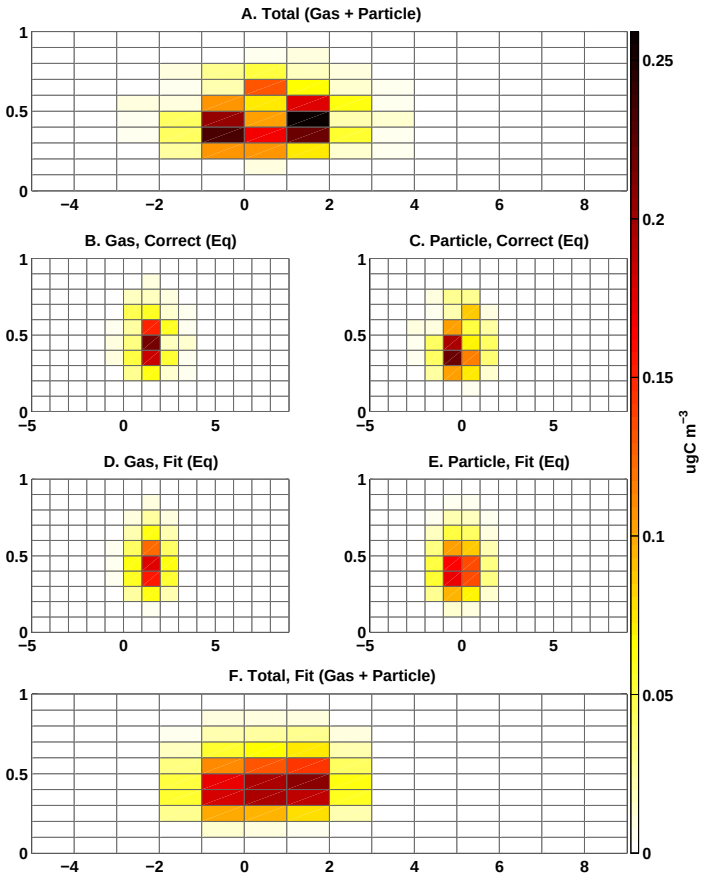

Figure 3.5: Same as Figure 3.2, except using semi-scattered data for the initial 2D distribution. Semi-scattered means beginning with a lognormal-gamma product and then altering specific grid cells via randomized scaling factors. The initial distribution in Fig. 3.5A is then renormalized to ensure all probability distributions sum to unity.

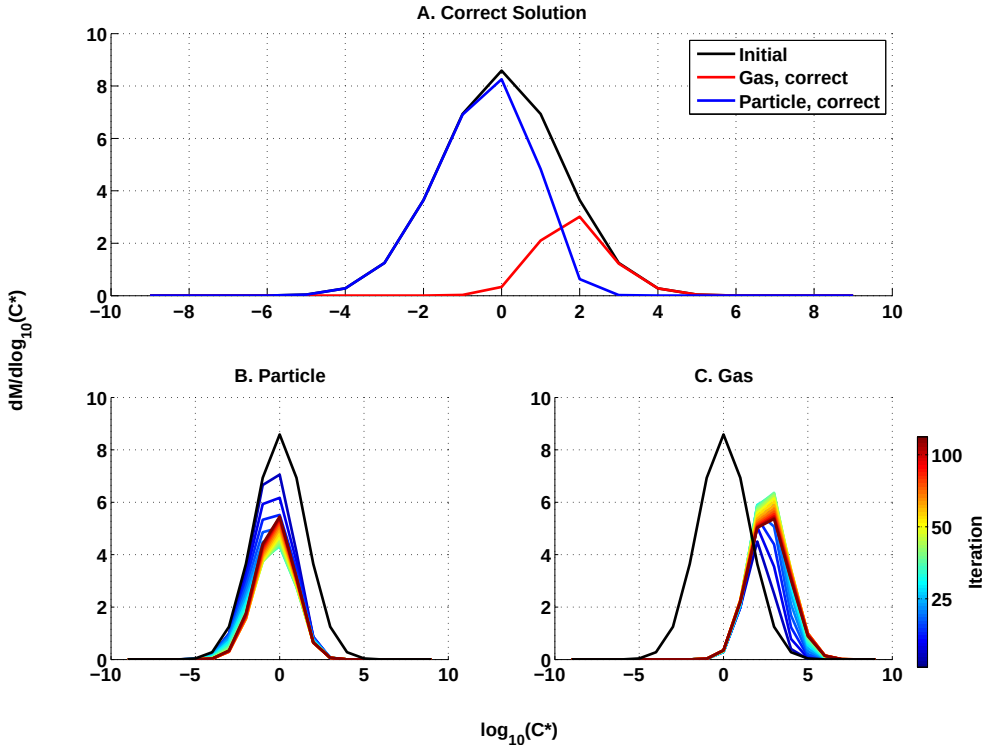

Figure 3.6: Susceptibility of the Moment Method to numerical drift: (A) An initial 1D log-normal distribution (black line) is equilibrated between the gas (red line) and particle phase (blue line). Continuous 1D log-normal distributions are then fit to the distributions in each phase, discretized, and equilibrated. The process is repeated for 100 iterations. (B) Evolution of the particle-phase distributions as a function of iteration. (C) Evolution of the gas-phase distributions as a function of iteration. The initial distribution (black line) is plotted in (B) and (C) for reference.

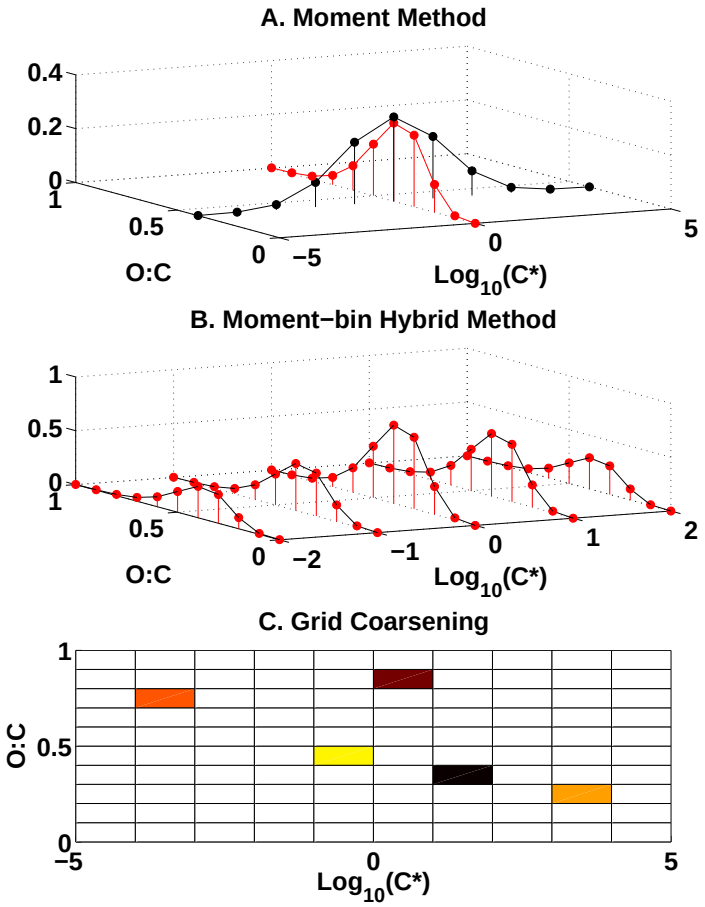

Figure 3.7: Illustration of the conceptual differences between (A) the Moment Method approach, (B) the Bin-Moment Hybrid approach, and (C) the grid-coarsening approach.

3.9 SOA Partitioning Algorithm

3.9.1 Definitions

G^{i}_{mol} = gas – phase molar concentration of species i

P^{i}_{mol} = particle – phase molar concentration of species i

$C^{i}_{tot,mol} = G^{i}_{mol} + P^{i}_{mol}$ = total (gas + particle) molar concentration of species i

$C^{i}_{sat,mol}$ = molar saturation concentration of species i

$M_{tot,mol}$ = total particle – phase molar concentration

Small Number $\simeq$ 0 (e.g. 10^{-10})

3.9.2 Initial guess

$M_{tot,mol} = \Sigma_i P^{i}_{mol}$

3.9.3 Algorithm to find correct $M_{tot,mol}$

If $\left(\Sigma_i \left(\frac{C^i_{tot,mol}}{C^i_{sat,mol}}\right) < 1\right)$ Then

Everything evaporates, $M_{tot,mol} = 0$

Else

Do

$$Y = \Sigma_i \frac{(C^i_{tot,mol})}{(C^i_{sat,mol} + M_{tot,mol})} - 1$$

$$dY = -\Sigma_i \frac{(C^i_{tot,mol})}{(C^i_{sat,mol} + M_{tot,mol})^2}$$

If ($\|Y\|$ < Small Number) Then

$M_{tot,mol}$ is correct, exit the Do loop before the next iteration

End If

If ($Y < 0$) Then

Update $M_{tot,mol}$ guess, $M_{tot,mol} = M_{tot,mol} \times 0.5$

Else

Update $M_{tot,mol}$ guess, $M_{tot,mol} = M_{tot,mol} - \frac{Y}{dY}$

End If

End Do

EndIf

3.9.4 Update gas-phase and particle-phase concentrations

$$P^{i}_{mol} = C^{i}_{tot,mol} \times \left(\frac{M_{tot,mol}}{C^{i}_{sat,mol} + M_{tot,mol}} \right)$$

$$G^{i}_{mol} = C^{i}_{tot,mol} \times \left(1 - \frac{M_{tot,mol}}{C^{i}_{sat,mol} + M_{tot,mol}} \right)$$

Chapter 4

Inorganic and black carbon aerosols in the Los Angeles Basin during CalNex *

*Reproduced by permission of American Geophysical Union from "Inorganic and black carbon aerosols in the Los Angeles Basin during CalNex" by J. J. Ensberg, J. S. Craven, A. R. Metcalf, J. D. Allan, W. M. Angevine, R. Bahreini, J. Brioude, C. Cai, H. Coe, J. A. de Gouw, R. A. Ellis, J. H. Flynn, C. L. Haman, P. L. Hayes, J. L. Jimenez, B. L. Lefer, A. M. Middlebrook, J. G. Murphy, J. A. Neuman, J. B. Nowak, J. M. Roberts, J. Stutz, J. W. Taylor, P. R. Veres, J. M. Walker, J. H. Seinfeld, *Journal of Geophysical Research–Atmospheres, 118*, 1777–1803, doi:10.1029/2012JD018136.

4.1 Abstract

We evaluate predictions from the Community Multiscale Air Quality (CMAQ version 4.7.1) model against a suite of airborne and ground-based meteorological measurements, gas- and aerosol-phase inorganic measurements, and black carbon (BC) measurements over Southern California during the CalNex field campaign in May/June 2010. Ground-based measurements are from the CalNex Pasadena ground site, and airborne measurements took place onboard the Center for Interdisciplinary Remotely-Piloted Aircraft Studies (CIRPAS) Navy Twin Otter and the NOAA WP-3D aircraft. BC predictions are in general agreement with observations at the Pasadena ground site and onboard the WP-3D, but are consistently overpredicted when compared to Twin Otter measurements. Adjustments to predicted inorganic mass concentrations, based on predicted aerosol size distributions and the AMS transmission efficiency, are shown to be significant. Owing to recent shipping emission reductions, the dominant source of sulfate in the L.A. Basin may now be long-range transport. Sensitivity studies suggest that severely underestimated ammonia emissions, and not the exclusion of crustal species (Ca^{2+}, K^{+}, and Mg^{2+}), are the single largest contributor to measurement/model disagreement in the eastern part of the L.A. Basin. Despite overstated NO_x emissions, total nitrate concentrations are underpredicted, which suggests a missing source of HNO_3 and/or overprediction of deposition rates. Adding gas-phase NH_3 measurements and size-resolved measurements, up to 10 μm, of nitrate and various cations (e.g. Na^{+}, Ca^{2+}, K^{+}) to routine monitoring stations in the L.A. Basin would greatly facilitate interpreting day-to-day fluctuations in fine and coarse inorganic aerosol.

4.2 Introduction

The Los Angeles mega-city has consistently experienced among the highest particulate matter levels in the United States and the highest ozone levels (`http://www.stateoftheair.org/2012/city-rankings/most-polluted-cities.html`). Several measurement campaigns have focused on characterizing particulate air quality in the Los Angeles Basin (e.g. *Appel et al.* (1982); *Turpin and*

Huntzicker (1991); *Chow et al.* (1994); *Watson et al.* (1994); *Eldering et al.* (1994); *Liu et al.* (2000); *Hughes et al.* (2002); *Pastor et al.* (2003); *Croes and Fujita* (2003); *Neuman et al.* (2003); *Jacob et al.* (2010); *Docherty et al.* (2011)), and in other urban areas, such as Pittsburgh, PA (Pittsburgh Air Quality Study, PAQS; e.g. *Wittig et al.* (2004); *Cabada et al.* (2004); *Modey et al.* (2004); *Pekney et al.* (2006); *Bein et al.* (2006)), Mexico City, Mexico (Mega-city Initiative: Local and Global Research Observations, MILAGRO; e.g. *Salcedo et al.* (2006); *DeCarlo et al.* (2008); *Querol et al.* (2008); *Molina et al.* (2010)), Houston, Texas (2006 Texas Air Quality Study, TexAQS; e.g. *Parrish et al.* (2009); *Nowak et al.* (2010); *Washenfelder et al.* (2010)), and Beijing, China (Campaign of Air Quality Research in Beijing, CAREBEIJING; e.g. *van Pinxteren et al.* (2009); *Yue et al.* (2009, 2010); *Ianniello et al.* (2011); *Zheng et al.* (2011)). Many studies have used data gathered during these field campaigns to evaluate the fidelity of three-dimensional atmospheric chemical transport models (CTMs) (e.g. *Sarwar and Bhave* (2007); *Fountoukis and Nenes* (2007); *Nolte et al.* (2008); *Matsui et al.* (2009); *Fountoukis et al.* (2009); *McKeen et al.* (2009); *Fast et al.* (2009); *Foley et al.* (2010); *Renner and Wolke* (2010); *Zhang and Ying* (2010); *Karydis et al.* (2010); *Kelly et al.* (2010); *Lee et al.* (2011); *Huang et al.* (2011); *Pfister et al.* (2011)).

The California Research at the Nexus of Air Quality and Climate Change (CalNex) study was conducted during May–June 2010 to address both air quality and climate change through coordination and collaboration between several government agencies, such as the California Air Resources Board (CARB), the National Oceanic and Atmospheric Administration (NOAA), and academic institutions (`www.esrl.noaa.gov/csd/calnex/`). During CalNex, state-of-the-art airborne, ship-based, and ground-based measurements of atmospheric species, and of their transport over and off the coast of California, were conducted with the goal of understanding the impact of airborne pollutants on air quality and climate.

The motivation for the present work is to evaluate the extent to which we understand the observed behavior of inorganic aerosols in the Los Angeles airshed, one of the world's most important urban areas from the point of view of air quality. The suite of ground-level and airborne measurements made during CalNex represent, by far, the most complete characterization of Los Angeles air quality

yet carried out. Such a complex suite of measurements, gas and particle, surface and aloft, can only be placed in a unified context through the integration of chemistry and physics provided by a state-of-the-science atmospheric chemical transport model, driven by appropriate meteorology for the days of the experiment and operating on the emissions inventory of the region assembled by the relevant governmental agencies. In many respects, the current work can be seen as a parallel to the Mexico City MILAGRO study (*Molina et al.*, 2010).

To evaluate the extent to which predictions of a state-of-the-science CTM, driven by current emission inventories and resolved meteorological fields, agree with measured concentrations, we employ the Community Multiscale Air Quality (CMAQ) model version 4.7.1 (`http://www.cmaq-model.org/`, *Foley et al.* (2010)) to simulate the three-dimensional distribution of aerosols and gases over Southern California during the CalNex field campaign. Predictions are compared to a suite of airborne and ground-based meteorological measurements, gas- and aerosol-phase inorganic measurements, and black carbon (BC) measurements over Southern California during the CalNex field campaign. Airborne measurements took place onboard the Center for Interdisciplinary Remotely-Piloted Aircraft Studies (CIRPAS) Navy Twin Otter aircraft (hereafter referred to as the Twin Otter) and the NOAA WP-3D (hereafter referred to as the P3) aircraft during May and June 2010. A Lagrangian particle dispersion model, FLEXPART (`http://transport.nilu.no/flexpart`, *Stohl et al.* (2005)), is used to track the origins of measured and predicted species in the Los Angeles Basin during CalNex by calculating back trajectories based on advection and turbulent mixing processes. Our goal is to identify the major sources of measurement/model disagreement for BC and various inorganic aerosol species and to suggest additional measures that address these sources of error. The organic component of the particulate matter will be addressed in a future study.

4.3 Model description and application

4.3.1 CMAQ

In this study, we use CMAQ version 4.7.1 (*Foley et al.*, 2010) on a domain that includes a large portion of Southern California as well as parts of Mexico (Figure 4.1), covering the area from (31.83°N, 121.43°W) to (35.69°N, 114.43°W) with 4 km by 4 km horizontal grid cells (102 x 156 grid points). Simulations cover the time period of May 2010. All simulations include a minimum spin-up period of four days to mitigate the influence of initial conditions, except for the P3 flight during 4 May 2012 which included only three days of spin up due to lack of MM5 meteorology for 30 April 2010. The meteorological fields used to drive the model were generated by the 5th generation Penn State/National Center for Atmospheric Research Meso-scale Model (MM5 version 3.7.4; *Grell et al.* (1995)). Three nested grids, with horizontal resolutions of 36, 12, and 4 km, were used to generate meteorological fields at the desired resolution (Figure C.1). Nesting is the process by which a model simulation is run over a certain domain (the parent domain) at a given resolution. From the predicted concentrations within the parent domain, boundary conditions are extracted and used to drive a separate finer-resolution model simulation that is run over a portion of the parent domain (the nested domain). The MM5 model was initialized from NARR analysis data (`http://nomads.ncdc.noaa.gov/data/narr/`) with analysis nudging option, but observational nudging was not used. The 36 km and 12 km grids were first run together, via two-way nesting, using the Grell cumulus, simple ice microphysics, NOAH soil scheme, MRF PBL, and RRTM radiation options. The 4 km grid was then run, via one-way nesting, using boundary conditions derived from the 12 km grid with all options identical to the coarse domain simulations, except that the cumulus parameterization was turned off since the sufficiently fine horizontal resolution of the 4 km grid is expected to capture the smaller cloud scale atmospheric motions. CMAQ-compatible meteorological fields were then generated by processing MM5 output using the Meteorology-Chemistry Interface Program (MCIP) version 3.6 (*Otte and Pleim*, 2010). Vertically, the meteorological fields extend from the surface to 100 mb (∼18 km above sea level) using 30 layers. This vertical resolution is

typical for regional-scale and meso-scale modeling studies such as this. For instance, *Kelly et al.* (2010) configured CMAQ to use 30 vertical layers for the coast of Florida. Similarly, *Foley et al.* (2010) tested CMAQ4.7 over the eastern United States using 12, 24, and 34 vertical layers. In the present study, there are 11 layers in the lowest 1000 m, and the surface layer is ∼30 m deep.

The emission inventory used in this study is a modified version of the day-specific ARCTAS-CARB inventory from June 2008. The modification consists of averaging June emissions to produce emissions for one representative week-day and one representative weekend-day for use during May 2010. In so doing, it is implicitly assumed that emissions did not change appreciably from 2008 to 2010. This assumption may be in question due to the recent emissions control programs, such as the diesel truck rules and ocean going vessel (OGV) fuel regulations (`http://www.arb.ca.gov/msprog/operators.htm`). As a result, emissions of BC and sulfur containing compounds may have decreased significantly from 2008 to 2010 (*Dallmann et al.*, 2011; *Lack et al.*, 2011). The CARB recognizes this limitation and is working toward releasing a newer version of the emission inventory. Daily total emission rates for each species are given in Tables C.4 and C.5, and the emission inventory used in this study is available from the authors upon request. The limitations of the current CARB inventory are expected to impact agreement between observations and predictions of anthropogenic BC and sulfur containing compounds, but not sea-salt emissions of SO_4^{2-} which are modeled interactively in CMAQ (*Sarwar and Bhave*, 2007; *Kelly et al.*, 2010). All meteorological fields and gridded emission inventories were prepared and provided by CARB.

Gas-phase predictions are based on a modified version of the Statewide Air Pollution Research Center (SAPRC) chemical mechanism (version SAPRC07TC, *Carter* (2010)) implemented in CMAQ with the Rosenbrock numerical solver. The main modification consists of using an updated isoprene photooxidation mechanism based on *Paulot et al.* (2009a,b). Atmospheric mass distributions of particulate matter by size are represented in CMAQ as the superposition of three log-normal distributions, referred to as modes. These are the Aitken mode (typical D_p range is 20 nm to 90 nm), the accumulation mode (typical D_p range is 90 nm to 1-2.5 μm), and the coarse aerosol mode (typical D_p range is 1-2.5 to 10 μm) (*Binkowski and Roselle*, 2003). Each mode is defined by its geometric

standard deviation, geometric mean diameter, and the magnitude of mass within the mode. All particles are assumed to be spherical and each mode is assumed to be internally mixed chemically. Aerosol processes such as evaporation, condensation, coagulation, nucleation, advection, and wet and dry deposition affect the total number of particles, total surface area, and total mass within each mode. The majority of primary $PM_{2.5}$ emissions (99.9% by mass), including BC, are assigned to the accumulation mode, and a small fraction (0.1% by mass) is assigned to the Aitken mode according to Section 1.3 of *Binkowski and Roselle* (2003).

The thermodynamic model ISORROPIA-II (*Fountoukis and Nenes*, 2007) is used in CMAQ to compute the thermodynamic equilibrium of the NH_4^+-Na^+-SO_4^{2-}-NO_3^--Cl^--H_2O aerosol system. The assumption of thermodynamic equilibrium between fine inorganic particulate nitrate and ammonium with gas-phase nitric acid and ammonia is commonly invoked in atmospheric CTMs. The validity of this assumption for fine particles (D_p typically < 2.5 μm) was confirmed on the basis of data obtained during the 1999 Atlanta Supersite Experiment (*Zhang et al.*, 2002). *Karydis et al.* (2010) used the PMCAMx model with ISORROPIA-II to model inorganic aerosol measured during the Mexico City MILAGRO campaign. They concluded that explicitly treating mass transfer to and from coarse aerosol as a dynamic process is essential for capturing the competition between small and large particles for condensible inorganic vapors. To account for this competition, CMAQ partitions mass between the gas and aerosol phases according to the hybrid method (*Capaldo et al.*, 2000), in which instantaneous equilibrium is assumed between the gas and aerosol phases in the two fine modes, and dynamic mass transfer governs the coarse aerosol mode. Since ISORROPIA-II is capable of simulating aerosol systems that include K^+-Ca^{2+}-Mg^{2+}, we conduct an additional sensitivity simulation on the impact of dust emissions and crustal species on inorganic aerosol concentrations in the L.A. Basin.

4.3.2 GEOS-Chem

Dynamic chemical boundary conditions (1-h temporal resolution) used in the CMAQ simulations were generated from the GEOS-Chem global chemical transport model (version 9-01-01, `http://`

acmg.seas.harvard.edu/geos/) via one-way nesting. GEOS-Chem was used to simulate global gas- and aerosol-phase concentrations at 2° latitude x 2.5° longitude horizontal resolution, with 47 vertical levels. Boundary conditions were extracted from the global simulation and used to drive a nested GEOS-Chem simulation over North America at 0.5° latitude x 0.667° longitude horizontal resolution, with 47 vertical levels. Finally, CMAQ-consistent boundary conditions were then extracted from the nested GEOS-Chem simulations for the domain shown in Figure 4.1. All three domains are shown on a single map in Figure C.2. The coarse GEOS-Chem parent grid simulation spin-up period was 1 year, and the spin-up period for the nested GEOS-Chem grid simulation was 4 months (Jan-Apr 2010). Goddard Earth Observing System (GEOS-5) assimilated meteorological data from the NASA Global Modeling and Assimilation Office (GMAO) were used for all GEOS-Chem model simulations, which included ozone-NO_x-hydrocarbon chemistry (*Bey et al.*, 2001), coupled with sulfate-nitrate-ammonium aerosol chemistry (*Park et al.*, 2004). Outside North America, global emissions used in the coarse simulations are from the Emissions Database for Global Atmospheric Research (EDGAR) inventory (*Olivier and Berdowski*, 2001). Anthropogenic emissions data for the United States, used in GEOS-Chem, were from the EPA National Emissions Inventory (NEI) 2005, scaled to the simulation period according to trends in the EPA Acid Rain Program (http://camddataandmaps.epa.gov/gdm/) and the NEI Air Pollutant Emissions Trends Data (http://www.epa.gov/ttn/chief/trends/). The nested GEOS-Chem simulation also includes aircraft, biofuel, and natural emissions of inorganic aerosol precursors, as described by *Park et al.* (2004).

Since the nested GEOS-Chem horizontal grid resolution of 0.5° latitude x 0.667° longitude (∼55 km x ∼60 km at latitude 33°N) is considerably coarser than the 4 km x 4 km resolution of CMAQ, and the domain shown in Figure 4.1 is relatively small compared to the North American continent, the potential double-counting of species in the L.A. Basin was taken into consideration. Coarse resolution acts to smooth concentration gradients via dilution, thereby reducing peak values within the region and increasing species concentrations at the boundaries. These species can then partially reenter the L.A. Basin as boundary conditions, while simultaneously being emitted within the L.A. Basin via the ARCTAS-CARB emission inventory, which is physically unrealistic. However, it is

possible for species emitted in the L.A. Basin to be transported outside the domain (Figure 4.1), and then reenter via recirculation. To determine the impacts of both of these potential issues, additional sensitivity simulations have been conducted with CMAQ using two sets of boundary conditions: (1) one set is derived from a nested GEOS-Chem simulation over North America that includes emissions in the L.A. Basin, and (2) one set is derived from the same nested GEOS-Chem simulation over North America with emissions in the domain shown in Figure 4.1 set to zero (the latter set was used in the results to be presented). The results (not shown) indicate that the impact of turning off emissions in the L.A. Basin in the nested GEOS-Chem simulation has virtually no impact on black carbon concentrations, and only a very slight impact on the boundary inflow of sulfate. Therefore recirculation and the potential double-counting of species are not issues in the current model configuration, although this may not be true for modeling configurations with different domain sizes and different grid-cell sizes, or if there are significant emissions sources near the boundaries of the nested domain.

4.3.3 FLEXPART

To trace the origins of measured and predicted species during CalNex, a modified version of the FLEXPART Lagrangian particle dispersion model (*Stohl et al.*, 2005) is used to calculate back trajectories of air masses. FLEXPART has been used extensively to quantify the impacts of meteorological processes on pollution transport (e.g., *de Foy et al.* (2006); *Palau et al.* (2006); *Ding et al.* (2009); *Brioude et al.* (2009)). A detailed description of the FLEXPART model used in this study can be found in the Supplementary Material.

4.4 Observations

4.4.1 Pasadena Ground-Site Data

Planetary boundary layer (PBL) heights were measured at the Pasadena ground site with a Vaisala Ceilometer CL31, which uses the minimum-gradient method to determine aerosol backscatter profiles

(*Emeis and Schafer*, 2006; *Schafer et al.*, 2004). Observed PBL heights are compared to predicted PBL heights in Figure 4.2. Previous studies have shown overall agreement between this technique as compared to radiosonde and sonic detection and ranging estimates of PBL height (*Haman*, 2011; *van der Kamp et al.*, 2010; *Martucci et al.*, 2007; *Münkel et al.*, 2006). For this study, the average PBL height uncertainty and the minimum detection limit are ±5m and ∼80 m, respectively. A detailed description of the instruments and settings used in this study can be found in *Haman* (2011).

Refractory black carbon (BC) aerosol mass was measured at the Pasadena ground-site with a Droplet Measurement Technologies (DMT, Boulder, CO, USA) Single Particle Soot Photometer (SP2). Briefly, the SP2 detects refractory BC mass by measuring the incandescence signal emitted from single BC-containing particles heated to their boiling point when passing through an intense Nd:YAG laser beam (λ =1064 nm). BC volume-equivalent diameter (VED) is calculated from the detected mass assuming a spherical particle with density of 1.8 g cm^{-3} (*Bond and Bergstrom*, 2006). The SP2 incandescence channels were calibrated in the same way as described in Section 2 of the Supplemental Material to *McMeeking et al.* (2010), with the main difference being that Alfa Aesar glassy carbon spheres were used instead of Aquadag. The data have been corrected for mass above and below the detection limit of the instrument by fitting a log-normal distribution to the primary mode in the BC mass distribution and another log-normal distribution to the residual of this fit (i.e. a secondary mode). The two fits were then added together, and the fraction of the fits above and below the SP2 detection limit were calculated as 8.0% of BC mass below the detection limit and 1.9% above. The measured BC mass concentrations have been divided by (1- 0.099). Based on *Shiraiwa et al.* (2008) and *Schwarz et al.* (2008b), the uncertainty in the determination of the mass of a single BC particle measured at the Pasadena ground site is estimated to be ∼30%. All BC measurements from the Pasadena ground site are shown in Figure 4.3

Inorganic aerosol measurements were made by the University of Colorado-Boulder Aerodyne high-resolution time-of-flight aerosol mass spectrometer (Aerodyne HR-ToF-AMS, Aerodyne Research, Inc., Billerica, MA USA, (*DeCarlo et al.*, 2008)) at the CalNex Pasadena ground site. The inlet is designed to transmit particles with aerodynamic diameters (D_{va}) of 60 to 600 nm with unit

transmission efficiency, although particles with D_{va} above 600 nm are also detected (*Canagaratna et al.*, 2007; *DeCarlo et al.*, 2004). A composition-dependent collection efficiency (CE) was applied to the AMS data based on recent work (*Middlebrook et al.*, 2012). The composition based method for collection efficiency addresses the issue of particle bounce in the AMS and that particle bounce is a function of particle phase. The technique presented by *Middlebrook et al.* (2012) encompasses the four main factors influencing particle phase: relative humidity in the sampling line, acidity/neutralization of the sulfate content, ammonium nitrate content, and organic liquid content. For this data set, there were several instances where ammonium nitrate dominated the aerosol mass, and as shown in Figure 3 in *Middlebrook et al.* (2012), when the ammonium nitrate fraction exceeds 0.4, the CE for the aerosol increases from 0.45 to 1. Using a constant CE value during these periods would cause an overprediction of aerosol mass. The ground-site AMS measurements are reported as 5-min averages and have an uncertainty <30%. NH_3 was measured at 1 Hz by quantum cascade tunable infrared laser differential absorption spectroscopy (QC-TILDAS from Aerodyne Inc.) with an overall uncertainty during the CalNex campaign of 10% + 0.42 ppb. (*Ellis et al.*, 2010). HNO_3 measurements were made with the acetate ion CIMS described by *Roberts et al.* (2010). Data were acquired every 10 seconds, and were averaged to one minute. The calibrations were performed with permeation tubes calibrated as described by *Neuman et al.* (2002). The time constant for transmission of HNO_3 through the inlet was found to be several minutes. The overall uncertainty of the HNO_3 measurement was 34% + 0.05ppbv. SO_2 mixing ratios were measured at the Pasadena site with a commercial pulsed fluorescence detector (Model 43i-TL, Thermo Electron Corp) operated as described in *Luke* (1997). All inorganic species measurements from the Pasadena ground site are shown in Figure 4.4. Hourly measurements of NO_x and SO_2 at three ground sites in the L.A. Basin are also reported by the CARB ground network (`http://www.arb.ca.gov/aqmis2/aqmis2.php`) and shown in Figure 4.5.

4.4.2 CIRPAS Twin Otter

BC aerosol mass was measured onboard the Twin Otter aircraft with a Droplet Measurement Technologies (DMT, Boulder, CO, USA) Single Particle Soot Photometer (SP2). The major findings from this SP2 during CalNex, including calibration of the instrument, are detailed elsewhere (*Metcalf et al.*, 2012). In *Metcalf et al.* (2012), 1-min average data are reported, but in this study, we have re-sampled the dataset at 1 Hz to take advantage of the highest time-resolution available. To account for the BC mass outside the SP2 detection range, a single log-normal function is fit to each 1-s histogram of single-particle BC mass between 0.48 and 290 fg (50-675 nm VED, assuming a spherical particle density of 1.8 g cm^{-3}), and integrated to give bulk BC mass concentrations. Unlike the SP2 measurements at the Pasadena ground site, a single log-normal mode is sufficient to adjust the measured BC size distributions for mass above and below the Twin Otter SP2 detection limits (*Metcalf et al.*, 2012). As discussed in *Metcalf et al.* (2012), this adjustment increases bulk BC mass concentrations by 15–20%. Based on the calibration standards available, uncertainty in single-particle BC mass determination and bulk mass concentrations is estimated to be ∼40%.

Non-refractory particle mass and composition measurements were made by an Aerodyne compact time-of-flight aerosol mass spectrometer (C-ToF-AMS, Aerodyne Research, Inc., Billerica, MA USA) (*Drewnick et al.*, 2005; *Murphy et al.*, 2009). The AMS onboard the Twin Otter measures submicron, non-refractory, size-resolved aerosol composition. The inlet and collection efficiency of the AMS onboard the Twin Otter were similar to those of the AMS at the Pasadena ground site. In an effort to measure aerosol mass distributions, the AMS onboard the Twin Otter was periodically run in particle-time-of-flight (PToF) mode. Due to relatively low aerosol loadings, the signal-to-noise ratio was not of sufficient quality for a meaningful comparison to size distributions predicted by CMAQ. Instead, we focus on bulk particulate ammonium (NH_4^+), particulate nitrate (NO_3^-), and particulate sulfate (SO_4^{2-}) mass concentrations reported as 10-s averages. We note that due to the attempted size-resolved measurements, narrow plumes may have been missed by the AMS onboard the Twin Otter.

All Twin Otter measurements reported here are from instruments inside an unpressurized cabin.

All instruments sampled downstream of a two-stage diffusion inlet with a transmission efficiency near unity for particle diameters up to about 3.5 μm (*Hegg et al.*, 2005). Sampling lines inside the cabin are kept reasonably uniform to all instruments, so further corrections for diffusional losses in these lines have not been made. The Twin Otter conducted 18 research flights from Ontario, CA between 4 May and 28 May 2010 during CalNex. The AMS was onboard during 8 of the flights, three of which were to San Joaquin Valley, which is outside the domain shown in Figure 4.1. Therefore, this analysis makes use of 5 Twin Otter flights during which inorganic aerosol concentrations were measured within the L.A. Basin.

4.4.3 NOAA P3

The P3 aircraft conducted 18 research flights from Ontario, CA between 4 May and 20 June 2010 during CalNex 2010 (esrl.noaa.gov/csd/calnex/). This study uses daytime measurements from 5 P3 flights that focused on sampling L.A. Basin emissions and the resulting photochemical products. NH_3, HNO_3, NH_4^+, NO_3^-, and SO_4^{2-}, and various meteorological parameters were measured onboard the P3 aircraft. NH_3 was measured at 1 Hz (equivalent to 100 m spatial resolution) by chemical ionization mass spectrometry (CIMS) with typical uncertainties of (30% + 0.2 ppbv) and a 1σ imprecision of 0.08 ppbv (*Nowak et al.*, 2010). HNO_3 was measured at 1 Hz by a separate CIMS instrument with an uncertainty of (15% + 0.040 ppbv) and a 1σ imprecision of 0.012 ppbv (*Neuman et al.*, 2012). CO measurements were made by a vacuum ultraviolet fluorescence instrument with 5% uncertainty and 1 ppbv imprecision (*Holloway et al.*, 2000). SO_4^{2-}, NH_4^+, and NO_3^- were measured from a pressure-controlled region downstream of a low turbulence inlet using a compact time-of-flight aerosol mass spectrometer (Aerodyne, Billerica, Massachusetts) (*Bahreini et al.*, 2009). The AMS data are reported as 10-s averages with 2σ uncertainty (1-σ imprecision) of 34% (0.06 μg m^{-3}), 34% (0.01 μg m^{-3}), and 36% (0.01 μg m^{-3}) for ammonium, nitrate, and sulfate, respectively. BC measurements in the size range of 95-720 nm VED (still assuming a BC void-free density of 1.8 g cm^{-3}) were made by an SP2 similar to that used onboard the Twin Otter (*Schwarz et al.*, 2006). As with the SP2 measurements onboard the Twin Otter, a single log-normal function is sufficient to

account for mass above and below the P3 SP2 detection limits, and this adjustment increases bulk BC mass concentrations by 10–25%. As described in detail in *Metcalf et al.* (2012), due to differences in calibration, measurements from the SP2 onboard the Twin Otter are potentially biased low by ∼12%, as compared to those from the SP2 onboard the P3 (e.g., if the P3 measurement is 1 μg m^{-3}, the Twin Otter measurement would be 0.88 μg m^{-3}).

The AMSs used in this study, both ground-based and airborne, measured only particles with vacuum aerodynamic diameters between 60 nm and 600 nm diameter with 100% efficiency. Particles with aerodynamic diameters above 600 nm were also measured, but with reduced collection efficiency. However, since the predicted Aitken, accumulation, and coarse aerosol modes are expressed in CMAQ in terms of log-normal functions, each mode is defined for particle diameters ranging from zero to infinity. Therefore, all aerosol predictions are adjusted to match the transmission efficiency of the AMS based on the following piece-wise defined transmission function:

1. 0% transmission below D_{va} = 40 nm;
2. linear increase in transmission vs ln(D_{va}), from 0% at D_{va} = 40 nm to 100% at D_{va} = 100 nm;
3. 100% transmission from D_{va} = 100 nm up to D_{va} = 550 nm;
4. linear decrease in transmission vs ln(D_{va}), from 100% at D_{va} = 550 nm to 0% at D_{va} = 2 μm.
5. 0% transmission above D_{va} = 2 μm;

This transmission function is an average of the transmission curves used in several AMS studies as described in *Knote et al.* (2011) and references therein, and is applied to all inorganic aerosol predictions (CMAQ) that are compared to AMS measurements from the Pasadena site, the Twin Otter aircraft, and the P3 aircraft. We note that due to variation between specific aerodynamic lenses in different instruments, the exact transmission efficiencies of the AMS at the Pasadena site, onboard the Twin Otter, and onboard the P3 will be slightly different than the one used in this study. Appendix A presents the equations used to modify CMAQ predictions based on the AMS

transmission window and efficiencies, and a derivation of these equations is given in the Supplemental Material. Measured BC concentrations from all platforms, adjusted for mass above and below the SP2 detection limits, are compared directly to the unmodified predicted BC concentrations in all results to be presented.

4.5 Results and discussion

The Aerosol Modeling Testbed analysis toolkit (*Fast et al.*, 2011) was used to map three-dimensional CMAQ meteorological parameters, predicted gas-phase concentrations, and predicted aerosol-phase concentrations onto each flight path (as well as for various ground sites). The temporal resolution of the CARB emission inventory and MM5 meteorology is 1-h. In this work, CMAQ predicted species concentration fields, averaged over the previous hour, are compared to observations according to observational time-stamps (i.e. observational points with time-stamps of 12:20 and 12:40 would both be compared to predictions averaged between the hours of 12:00-13:00). The discrepancy between measured and simulated species concentration fields and meteorological parameters is quantitatively assessed using the following four statistical metrics:

$$\mathrm{ME} = \frac{1}{\mathrm{N}} \sum_{\mathrm{i}=1}^{\mathrm{N}} |\mathrm{P_i} - \mathrm{M_i}| \qquad \textit{(mean error)} \tag{4.1}$$

$$\mathrm{MB} = \frac{1}{\mathrm{N}} \sum_{\mathrm{i}=1}^{\mathrm{N}} (\mathrm{P_i} - \mathrm{M_i}) \qquad \textit{(mean bias)} \tag{4.2}$$

$$\mathrm{NME} = \frac{\sum_{\mathrm{i}=1}^{\mathrm{N}} |\mathrm{P_i} - \mathrm{M_i}|}{\sum_{\mathrm{i}=1}^{\mathrm{N}} \mathrm{M_i}} \qquad \textit{(normalized mean error)} \tag{4.3}$$

$$\mathrm{NMB} = \frac{\sum_{\mathrm{i}=1}^{\mathrm{N}} (\mathrm{P_i} - \mathrm{M_i})}{\sum_{\mathrm{i}=1}^{\mathrm{N}} \mathrm{M_i}} \qquad \textit{(normalized mean bias)} \tag{4.4}$$

where N, P, and M stand for the number of data points, predicted quantity, and measured quantity, respectively.

4.5.1 Meteorological variables

4.5.1.1 Ground Site

Observed and predicted temperature, relative humidity (RH), and planetary boundary layer (PBL) height from the Pasadena ground site are shown in Figure 4.2 and statistical metrics are given in Table 4.1. Overall, the agreement between observed and predicted PBL height in Pasadena has a 15-day average bias of -80 m (-9%). Agreement between observed and predicted temperature has a 15-day average bias of 1.01°C. The agreement between observed and predicted RH has a 15-day average bias of -10.4%. The discrepancies in RH are most likely a combination of underpredicted water vapor mixing ratios and of the exponential dependence of saturation-vapor pressure on errors in temperature (1°C temperature error leads to approximately 5% RH error). Additional ground-site comparisons of predicted and observed meteorology are given in the Supplemental Material. The results show that temperature and RH are consistently overpredicted and underpredicted, respectively, during the first week of May, with much better agreement during the last three weeks. Predicted wind speeds and wind directions agree to within 2 m/s and 60°, respectively, at all surface sites.

4.5.1.2 Twin Otter and P3

The Twin Otter and P3 flight paths and altitudes are shown in Figures 4.6–4.11 and Figures 4.13–4.16. Temperature and relative humidity (RH) measurements from the Twin Otter and P3 flights are compared to MM5 predictions in Table 4.2. Observed and predicted temperatures (averaged over each flight) typically agree to within 4°C, while observed and predicted RH (averaged over each flight) typically agree to within 15%. *Zhang et al.* (2006) evaluated MM5 meteorology coupled with CMAQ against measurements taken during the Southern Oxidants Study, and found similar levels of agreement between predicted and observed temperature and RH. In the present study, the largest disagreement occurred during the 21 May Twin Otter flight and the 14 May P3 flight, during which predicted RH was biased low by 26.6% and 22.1%, respectively. Wind speed and wind directions measurements onboard the Twin Otter and the P3 are shown in Table 4.3. Predicted and observed

wind speeds generally agree to within ∼50% when averaged over each flight. Although the mean discrepancy between predicted and observed wind direction ranges between 22-65°, the average predicted and observed wind direction is that of the daytime southwesterly sea breeze which advects emissions towards the north and northeast, exiting the Basin through passes in the San Gabriel and San Bernardino mountain ranges (*Lu and Turco*, 1995). However, it is difficult to quantify errors in species concentrations attributable to discrepancies between measured and observed wind vectors.

4.5.2 Black Carbon

4.5.2.1 Pasadena ground site

Measured and predicted BC concentrations at the Pasadena ground site are shown in Figure 4.3. The overall agreement between predicted and observed BC concentrations is very good, with a CalNex-average NME and NMB of 47.8% and 6.6%, respectively (Table 4.1). This NME of 47.8% is slightly higher than the measurement error inherent to the SP2 (∼30–40%) owing mostly to large missing peaks in predicted BC on specific days (e.g., 27 and 28 May). Because predicted BC is chemically inert, the Pasadena ground-site is fixed, and all weekday emissions are assumed to be identical, day-to-day variations in BC predictions at the Pasadena ground site can only be caused by variations in the predicted meteorological fields (e.g., wind fields). For instance, May 20 and May 27 were both Thursdays. However, the 1-h average BC predictions on 27 May did not get above 0.4 μg^{-3}, while BC predictions on 20 May were up to 1.1 μg^{-3}. Since the predicted PBL heights on these days were comparable (Figure 4.2), variation in the predicted wind fields is the primary cause of the day-to-day variation in predicted BC concentrations. Therefore, if the differences between the predicted and observed wind fields on any given day are comparable to the day-to-day differences in the predicted wind fields, large errors in BC predictions may occur at any given point (e.g., Pasadena ground site). However, the overall agreement between predicted and observed BC at the Pasadena ground site (NMB = 6.6%) suggests that on average, both wind fields and upwind BC sources are represented well by CMAQ.

4.5.2.2 Twin Otter and P3

Measured and predicted BC concentrations from the Twin Otter flights and the P3 flights during May 2010 are shown in Figures 4.6–4.11 and Figures 4.13–4.16. The illusory differences in noise levels of the Twin Otter BC measurements and the P3 BC measurements exist because (1) the P3 aircraft transitioned between high and low altitudes many times during each flight, which creates the appearance of less noise due to very low BC concentrations at high altitudes, and (2) the average P3 flight was roughly 1.5 times longer than the average Twin Otter flight, but the x-axes in all time-series plots are the same length. Therefore, the P3 time-series are more compressed and the true level of noise in the measurements is somewhat obscured. To illustrate this, all measurements from both aircraft made above 1000 m a.s.l. have been removed and the resulting data-set is plotted as a function of data-point number, as opposed to time, so that the series plots are continuous (Figure C.3). In addition, the x-axis limits for all subplots in Figure C.3, regardless of the length of the flight, are identical. Figure C.3 shows that the actual noise for both instruments is essentially comparable during most flights.

A statistical comparison, at all altitudes and below 1000 m above sea level (a.s.l.) where local emissions influence BC concentrations most, between BC predictions and observations is given in Table 4.4. Although the extent of agreement between observations and predictions varies from flight to flight, the overall agreement (i.e. the 5-flight average) indicates that predicted BC concentrations have a slight positive bias (19.2%) when compared to P3 measurements below 1000 m a.s.l., and a significant positive bias (78.2%) when compared to Twin Otter measurements. Visual inspection of Figures 4.6–4.11 and Figures 4.13–4.16 suggests that the CMAQ predictions capture the spatial distribution of BC during many flights, although the predicted concentration range is biased by 53 to 116% as compared to Twin Otter measurements below 1000 m a.s.l., and biased by -27% to 52% as compared to P3 measurements below 1000 m a.s.l. FLEXPART back trajectory analyses indicate that highest predicted BC concentrations exist in air masses influenced by emissions in the Long Beach industrial area. For example, the trajectory paths shown in Figure C.4 suggest that during the 24 May flight, both observed and predicted concentrations of BC, at 11:21 (downtown Los

Angeles) and 14:59 (Fontana), occurred in air masses that were influenced by emissions near Long Beach and downtown Los Angeles. We note that since WRF meteorological fields were used to drive FLEXPART, whereas MM5 meteorological fields were used to drive CMAQ, potential inconsistencies may exist between between the two sets of meteorology. Nevertheless, both the FLEXPART back trajectories and the extent of agreement between observed and predicted BC concentrations from both aircraft suggests that the locations of the BC sources are accurately accounted for in the CARB BC inventory used in this study.

As mentioned previously, the calibration of the SP2 onboard the Twin Otter biased BC measurements low by 12% as compared to those of the SP2 onboard the P3 (*Metcalf et al.*, 2012). Since the normalized statistical metrics used in this study are nonlinear functions of observed concentrations, the 12% measurement bias will cause higher than 12% bias when compared to predictions. As an example, in a 1-point data set, if the predicted BC concentration is 1 μg m^{-3} and the observed BC concentration is 0.568 μg m^{-3}, the NMB will be 76.1%. However, if the measured concentration is reduced to 0.5 μg m^{-3} due to the 12% instrument bias (88% of 0.568 is 0.5), the NMB becomes 100%, which is a difference in NMB of 23.9%. Taking this difference into account brings the NMBs from several of the Twin Otter flights into closer agreement with the higher NMBs from the P3 flight. For instance, dividing all Twin Otter measurements by 0.88 reduces the NMBs from the May 25, 27, and 28 Twin Otter flights (below 1000 m a.s.l.) to 56.5%, 34.6%, and 40.6%, respectively, which are comparable to the NMBs measured during the May 8 and 16 P3 flights, which are 52.3% and 39.5%, respectively. The precise reason for Twin Otter observations being a factor $\sim$2 lower than predictions during the May 21 and 24 flights cannot be pinpointed at this time.

Additional results showing measured and predicted CO mixing ratios (available only for P3 flights), as well as predicted and observed ΔBC/ΔCO ratios (Figure C.5), are included in the Supplemental Material. For the comparison shown in Figure C.5, ΔBC/ΔCO values are calculated by subtracting the minimum BC and CO measurements (background values) below 1000 m a.s.l. from all BC and CO measurements, respectively, below 1000 m a.s.l. Data points for which ΔCO < 1 ppbv are also removed. Note that, owing to data points lying on top of each other in Figure

C.5, the average $\Delta BC/\Delta CO$ ratios (horizontal lines) can appear lower than the spread of individual data points may suggest. Since the accuracy of the ARCTAS-CARB CO emissions has already been established by *Wunch et al.* (2009), using measured and observed ratios of $\Delta BC/\Delta CO$ reduces the impact of inaccuracies in meteorology at locations other than Pasadena. As shown in Figure C.5, the comparisons of $\Delta BC/\Delta CO$ are in general agreement with observations, with ratios being overpredicted during the May 8 and 16 flights, and underpredicted during the May 4, 14, and 16 flights. The agreement between surface measurements and the P3 measurements suggests that no systematic bias exists in the ARCTAS-CARB emission inventory, or the MM5 meteorology used in this study.

4.5.3 Sulfate

To characterize the sources of the predicted sulfate, the CMAQ sulfate tracking system was employed, in which separate tracers are used to keep track of the sulfate contributions from the formation pathways listed in Table C.1. Due to the transmission window of the AMS, the mass contributions from the Aitken mode and the coarse mode sulfate are a negligible fraction of the total predicted sulfate aerosol mass ($< 1\%$) in the applicable size range and are not shown in Figure 4.4. Sulfate predicted to be formed by aqueous-phase oxidation by methyl hydrogen peroxide (MHP) and peroxyacetic acid (PAA) is also predicted to be negligible. However, *Stein and Saylor* (2012) show that the relative contributions of sulfate formation pathways depend critically on the chemical mechanism used. Specifically, during the ICARTT 2004 campaign, up to 30% of the sulfate in certain locations is attributable to the aqueous phase oxidation of MHP when using CMAQv4.6 with the CBIV mechanism, and very little sulfate is attributable to PAA oxidation. However, this is likely an overestimation since the MHP concentrations were overpredicted by an order of magnitude with that mechanism. Furthermore, when using the CB05 or SAPRC99 mechanisms, very little sulfate is attributable to MHP oxidation, and up to 20% is attributable to PAA oxidation. However, this is also likely an overestimation since the PAA was overpredicted by up to a factor of 4 when using the CB05 or SAPRC99. We are not aware of any sulfate tracking assessments based

on the SAPRC07 mechanism combined with the ARCTAS-CARB inventory. Although Fe^{3+} and Mn^{2+} are not model-predicted species in CMAQv4.7.1 (although they are in CMAQv5.0), prescribed background concentrations of 0.01 μg m^{-3} Fe^{3+} and 0.005 μg m^{-3} Mn^{2+} still lead to a small, but non-negligible, portion (up to 5%) of accumulation mode sulfate forming via these routes (*Walcek and Taylor*, 1986; *Chang et al.*, 1987). The predominant predicted accumulation mode sulfate comes from four sources (no particular order): the inflow of sulfate from the boundaries (e.g., Asian inflow (*Lin et al.*, 2012)), aqueous-phase oxidation of S(IV) by H_2O_2 and O_3, gas-phase photooxidation of SO_2, and direct sulfate emission.

4.5.3.1 Pasadena Ground Site

Observed and predicted sulfate and sulfur dioxide concentrations from the CalNex Pasadena ground site are shown in Figure 4.4, and statistical metrics are given in Table 4.1. In addition, ground-site SO_2 measurements from three locations within the L.A. Basin, taken from the CARB AQMIS are compared to CMAQ predictions in Figure 4.5. As at the Pasadena ground site, SO_2 mixing ratios are over-predicted at all locations within the L.A. Basin.

Despite over-predictions in SO_2, predicted sulfate concentrations are actually biased low compared to sulfate measurements at the Pasadena ground site, mostly due to underestimations during the first few days of comparison. The relative sulfate contributions are listed in Table 4.5. Few clouds are present during daylight hours, but an MM5 predicted nighttime coastal marine layer facilitates aqueous-phase conversion of S(IV) to S(VI) in CMAQ. The predicted marine layer evaporates during the day, but the cloud-processed sulfate remains airborne. At the Pasadena ground site, enhancements in the relative sulfate contributions from aqueous-phase oxidation of SO_2 are not directly proportional to over-predictions in SO_2 emissions owing partially to the nonlinear pH dependence of the rate of S(IV) oxidation by O_3. More specifically, the second-order reaction rate constant for the S(IV)-O_3 reaction varies by up to four orders of magnitude for aerosol pH ranging from 1 to 6 (*Seinfeld and Pandis*, 2006). Production of sulfate via this reaction lowers the pH and slows down the reaction. In addition, if the oxidants H_2O_2 and O_3 are the limiting reactants,

the impacts of overestimated SO_2 emissions will also be lessened. Sulfate formation via gas-phase oxidation of SO_2 should respond more linearly to increases in SO_2 concentrations. However, the lifetime of SO_2 against the hydroxyl radical is relatively long (∼1 week, *Seinfeld and Pandis* (2006)) and only represents 7% of the average predicted sulfate at the Pasadena ground site. Long-range transport of sulfate is predicted (CMAQ) to account for 26% of the sulfate measured at the Pasadena ground-site.

4.5.3.2 Twin Otter and P3

Observed and predicted sulfate concentrations from the Twin Otter and P3 flights are shown in Figures 4.6–4.11 and Figures 4.13–4.16. A statistical comparison between sulfate predictions and observations is given in Table 4.6. The average predicted sulfate concentration is biased high by 55% to 268% as compared to Twin Otter measurements, and biased by 0% to 71% as compared to P3 measurements (Table 4.6). Moreover, the relative contributions predicted from each sulfate source vary considerably for both aircraft depending on the individual flight path.

A significant fraction of the predicted sulfate (airborne and ground-based) comes from direct sulfate emission and boundary inflow of sulfate, both of which are independent of SO_2 concentrations (Table 4.5 and Figures 4.6–4.11). That direct sulfate emission contributes a significant fraction of the predicted sulfate in the L.A. Basin can be understood via analysis of the CARB sulfur emission inventory (Tables C.4 and C.5). The CARB sulfur emission inventory includes gas-phase SO_2 emissions, gas-phase H_2SO_4 emissions, and particle-phase SO_4^{2-} emissions (i.e. direct sulfate emission). Since, sulfuric acid is highly water-soluble and has an extremely low vapor pressure, it is assumed to enter the particle-phase immediately upon emission. Therefore, direct sulfate emissions include both direct emission of sulfate and direct emission of sulfuric acid. The ratio (by mass) of the different sulfur emissions in the CARB inventory, $(H_2SO_4 + SO_4^{2-})/(H_2SO_4 + SO_4^{2-} + SO_2)$ within the Basin is ∼5%. However, since only a fraction of the SO_2 emitted is converted to sulfate, the sulfate from primary emissions will account for more than 5% of the total sulfate measured at the ground site and by the aircraft (*Dominguez et al.*, 2008). As shown in Figure 4.10 and 4.11,

sharp increases in predicted sulfate were predicted but not measured by the P3 near Long Beach (e.g., 8 May just before 13:00 and 14 May just after 13:00). Similarly, FLEXPART back trajectories suggest that during the 21 May flight (at 11:23 and 13:57, specifically), the Twin Otter intercepted air masses that had been influenced by emissions near Long Beach (Figure C.6) and should have contained high concentrations of primary sulfate. Since such hot spots of primary sulfate near Long Beach were generally not observed by the Twin Otter (Figures 4.13, 4.6, and 4.7), one concludes that the major source of disagreement between predicted and observed sulfate is most likely attributable to the emission inventory.

Sulfate concentrations measured onboard the Twin Otter were below 1 μg m^{-3} on 21, 24, and 25 May and showed little spatial variation. For these three flights, the predicted sulfate attributable to the GEOS-Chem boundary conditions represents 43-58% of the total predicted sulfate and accounts for almost the entire measured sulfate. Boundary inflow of sulfate affects predicted sulfate concentrations along P3 flight paths in a similar manner. That the sulfate boundary conditions exert a noticeable impact on sulfate concentrations within the basin is not totally unexpected. For instance, *Huang et al.* (2011) evaluated the inflow of sulfur oxides ($SO_x = SO_2 + SO_4^{2-}$) to the South Coast (SC) of California by comparing predictions from the STEM atmospheric chemical transport model against aircraft measurements during the ARCTAS-CARB campaign (*Jacob et al.*, 2010) in June 2008. They estimated that elevated SO_x levels at altitudes between 1-4 km enhanced SO_4^{2-} surface levels by a maximum of $\sim$0.13 ppb (0.13 ppb $SO_4^{2-} \simeq 0.5$ μg m^{-3} at 1 atmosphere and 300 K) during this time period. Despite the influence of long-range SO_x transport, *Huang et al.* (2011) found that near-surface SO_x concentrations were mostly influenced by local emissions and estimated that the 2005 CARB sulfur emissions were low by about a factor of two. This is in contrast to our findings which suggest that the 2008 CARB SO_2 emissions are overestimated (Figure 4.5). Since the sulfur emission inventory used in *Huang et al.* (2011) is similar to that used in this study, the most likely explanation is that SO_2 emissions have decreased from 2008 to 2010, which is consistent with sulfur emission regulations that went into effect during those two years.

The CMAQ sulfate source apportionment presented in this study suggests that, with the cur-

rent sulfur emission inventory based on emission factors from 2008, long-range transport of sulfate accounts for 22-82% of the sulfate in the L.A. Basin. However, if the reductions in sulfur emission factors reported by *Lack et al.* (2011) (∼90%) were to be included in the simulations, unlike the results presented in *Huang et al.* (2011), the boundary inflow of sulfate would become the single largest contributor to predicted sulfate concentrations in the L.A. Basin. Future work should continue to quantify the impact of foreign and domestic emissions on Southern California air quality as this is crucial for determining the potential efficacy of emission control strategies, and establishing the necessity for international collaboration.

4.5.4 Ammonium and Nitrate

Ammonium nitrate aerosol is semivolatile and continuously partitions between the gas- and aerosol-phase. The distributions of total ammonium (NH_3 + NH_4^+) and total nitrate (NO_3^- + HNO_3) between the gas- and aerosol-phases are sensitive to the relative concentrations of other ions such as sulfate, sodium, and chloride, as well as meteorological factors such as temperature and relative humidity.

4.5.4.1 Pasadena Ground Site

Particulate ammonium and nitrate predictions are generally biased low at the Pasadena ground site (Table 4.1). Aside from the large over-prediction on 24 May, NH_3 concentrations are well predicted (average bias of 22%), and predicted HNO_3 concentrations have a 15-day average bias of -38%. *Nowak et al.* (2012) used observations from the P3 aircraft during CalNex to show that the NH_3 emissions from automobiles in the CARB inventory are fairly accurate and contribute ∼60 metric tons day^{-1} to the NH_3 budget within the L.A. Basin. *Nowak et al.* (2012) also found the NH_3 emissions from dairy facilities in the eastern part of the L.A. Basin are likely understated by up to a factor of 20. Since, strictly during the daytime, the Pasadena ground site is downwind of downtown L.A., but upwind of the dairy facilities, the predicted and observed NH_3 at this location is represented well within CMAQ.

Ground-site NO_x ($NO + NO_2$) measurements taken from the CARB AQMIS are compared to CMAQ predictions in Figure 4.5. NO_x mixing ratios are over-predicted by a factor of ∼2 at the three locations (North Long Beach, L.A. Westchester, and L.A. North Main Street location). Although slight over-predictions of temperature and under-predictions of RH artificially shift particulate ammonium and nitrate to the gas-phase, both particulate nitrate and nitric acid concentrations are underpredicted from 15-20 May. Since SO_4^{2-}, HNO_3, NO_3^-, and NH_4^+ are underpredicted during the first week of comparison, but are in better agreement with predictions during the second week, and since these species have different upwind sources, it is likely that errors in predicted wind fields, as opposed to uncertainties in the CARB emission inventory, are responsible for disagreement during the first week of comparison. Uncertainties/inaccuracies in predicted sea-salt emissions may also influence the agreement between predictions and observations at the Pasadena ground site, as will be discussed in the next section.

4.5.4.2 Twin Otter and P3

Observed and predicted particulate nitrate and ammonium concentrations from the Twin Otter and P3 flights are shown in Figures 4.6–4.11 and Figures 4.13–4.16. Statistical metrics for inorganic aerosol species from both aircraft are given in Table 4.6. The fraction of simulated mass the AMS would measure is determined by taking the ratio of predictions that have been modified to match the AMS transmission efficiency to the total, unmodified inorganic aerosol concentration predictions. As shown in Figures 4.6–4.11 and Figures 4.13–4.16, application of the AMS transmission efficiency results in the removal of ∼35% of the total predicted particulate sulfate and ammonium, and 20-100% (higher removal at low altitudes where sea-salt is present) of the total predicted nitrate during all flights. Since all predicted inorganic components are assumed to be in a metastable state (i.e. an aqueous electrolyte solution), predicted coarse mode particulate nitrate forms when HNO_3 reversibly condenses onto coarse NaCl particles via solution thermodynamics (*Kelly et al.*, 2010). This causes a significant fraction of the predicted particulate nitrate to reside in the coarse aerosol mode, while ammonium and sulfate reside primarily within the accumulation mode. Since sea-salt emissions are

modeled online in CMAQv4.7.1, variations in wind speed lead to fluctuations in sea-salt emissions, and therefore different distributions of nitrate between the accumulation mode and the coarse mode. As shown in Figure C.7, the day-to-day differences in sodium emissions can be substantial. Therefore, the differences in the fraction of nitrate removed by the AMS transmission curve along somewhat similar flight paths is likely attributable to the amount of sea-salt emitted. For instance, the amount of predicted nitrate removed as a result of the AMS transmission efficiency curve is ∼40% on the 27 May flight and ∼55% on the 28 May flight, which is consistent with the sea-salt emissions on May 28 being much greater than on May 27 (Figure C.7). Adding size-resolved sodium and nitrate measurements, up to 10 μm, at various monitoring sites in the L.A. Basin would help unravel the impacts of anthropogenic and natural emissions on inorganic aerosol formation.

Gas-phase measurements of HNO_3 and NH_3 were not conducted on the Twin Otter, so one cannot determine based on that data set alone if discrepancies between particulate ammonium and nitrate observations and predictions are the result of errors in the NO_x ($NO + NO_2$) emissions, NH_3 emissions, or predictions of HNO_3 within the SAPRC07TC chemical mechanism. However, HNO_3 and NH_3 measurements were conducted onboard the P3 aircraft (Figures 4.10–4.11 and Figures 4.14–4.16 and Table 4.7). As stated previously, *Nowak et al.* (2012) estimated, via mass balance, that the NH_3 emissions from automobiles in the CARB inventory are consistent with their measurements (∼60 metric tons day^{-1}), but that the CARB inventory underestimates NH_3 emissions from dairy facilities by a factor of 3-20. By conducting a formal 3-D simulation, we not only corroborate the conclusions of *Nowak et al.* (2012), but also show that NH_3 mixing ratios can be under-predicted by factors as high as 10^2–10^3 (Figure 4.16). Moreover, sharp increases in submicrometer ammonium and nitrate measurements downwind of dairy facilities (e.g., Figure 4.11 just before 14:00) can be attributed entirely to point-source dairy NH_3 emissions. As these sharp increases in ammonium and nitrate are consistently missed by predictions, severely underpredicted NH_3 emissions from dairy facilities is identified as the dominant source of measurement/model disagreement in the eastern L.A. Basin. Upwind of dairies, predicted NH_3 mixing ratios are in better agreement with observations (see "no dairy" metrics in Table 4.7). Similarly, HNO_3 mixing ratios are generally predicted well

during the P3 flights (NME typically ∼0.5) with the most notable exception being 14 May between 11:00 and 12:00 when the aircraft flew off the coast. HNO_3 and NO_x contour maps (not shown) suggest that the over-predictions on 14 May are caused by overstated coastal NO_x emissions (Figure 4.5).

Even though gas-phase measurements were not taken onboard the Twin Otter, the impact of understated ammonia emissions and underpredicted total nitrate concentrations can be seen in the particulate ammonium and nitrate measurements (Figures 4.6–4.8). For instance, as shown in Figures 4.6 and 4.7, particulate ammonium and nitrate concentrations are significantly under-predicted in the eastern part of the L.A. Basin before the Twin Otter flew into the outflow regions at 12:30 and 14:30 during the 21 May flight. These under-predictions are exacerbated by an under-prediction of RH by 26.6% (flight average, Table 4.2). Particulate ammonium and nitrate concentrations are also under-predicted in the eastern part of the L.A. Basin during the 24 (between 13:00 and 15:00), 25 (between 13:30 and 15:30), and 27 (just after every hour) flights. Both predicted and observed nitrate concentrations are ∼2 times higher in the eastern part of the L.A. Basin on 25 May as compared to 24 May. The differences in nitrate concentrations are potentially attributable to warmer temperatures and lower RHs (predicted and observed) that shift both predicted and observed particulate nitrate to the gas-phase during the 24 May flight.

Given that surface-level NO_x concentrations are generally over-predicted (Figure 4.5), one might expect the total nitrate mixing ratios to be over-predicted. However, as shown in Figure C.8 and given in Table C.2, the predicted total nitrate mixing ratios (within the AMS transmission window) agree with observations to within 50% NME, but tend to be under-predicted. There are several potential explanations for this. (1) Since the daytime production of HNO_3 occurs via gas-phase oxidation of NO_2 ($OH + NO_2 \rightarrow HNO_3$), the predicted OH concentration, which is highly dependent on the concentrations of hydrocarbons and other oxidants, may be too low. (2) The rate of conversion of NO to NO_2, which is also highly dependent on the concentrations of hydrocarbons and other oxidants, may be limiting. (3) The nighttime heterogeneous reaction of N_2O_5 ($N_2O_5(g) + H_2O(s) \rightarrow 2HNO_3$) may be understated. (4) If the predicted particulate nitrate mass concentrations are

correct, but the size distributions predicted by CMAQ are inaccurate, the amount of predicted particulate nitrate could be biased low once predictions are adjusted to match the size-dependent transmission efficiency of the AMS. (5) Inaccurate shifting of total nitrate from the particle phase to the gas phase for various potential reasons (e.g., over-predicted temperature, under-predicted RH, over-predicted SO_4^{2-} concentrations, under-predicted NH_3 emissions) may artificially enhance the removal of total nitrate from the system due to faster dry deposition rates for gas-phase HNO_3 (*Dzepina et al.*, 2009). (6) Coarse cations (either from sea-salt particles or crustal species from dust emissions) may significantly reduce HNO_3 concentrations via condensation of HNO_3 onto deliquesced particles to form non-refractory coarse nitrate (*Fountoukis et al.*, 2009; *Hsu et al.*, 2007; *Moya et al.*, 2002; *Jacobson*, 1999).

We focus on the possibilities (4) and (6) regarding total nitrate underpredictions and defer a detailed analysis regarding the extent to which the other four sources of inaccuracy/uncertainty impact the amount of total nitrate predicted as the subject of future work. We note, however, that positive temperature biases and negative RH biases (Table 4.2), as well as positive sulfate biases (Table 4.6) and negative ammonia biases (Table 4.7), suggest that several of these possible factors contribute to shifting of predicted particulate nitrate to the gas-phase, thereby artificially enhancing total nitrate removal via dry deposition. To examine the hypothesis that total nitrate concentrations are underpredicted during most flights due to inaccurate distribution of total nitrate between the gas-phase, the fine aerosol-phase, and the coarse aerosol-phase, we present statistical metrics for all five P3 flights (Table C.2) with and without the AMS transmission curve applied to predictions. When the AMS transmission efficiency is taken into consideration, total nitrate concentrations are underpredicted during four of the five P3 flights by 0-42% (Table C.2). However, when full transmission (i.e. all predicted particulate nitrate and gas-phase nitric acid) is assumed, total nitrate concentrations are still underpredicted by up to 33% during the 4, 16, and 19 May flights. Since coarse particles were not measured onboard the Twin Otter or P3, the accuracy of the coarse mode nitrate predictions cannot be assessed. However, by comparing predicted and observed concentrations of total nitrate, assuming full transmission (Table C.2), we show that regardless of

whether nitrate is predicted to form ammonium nitrate, nitric acid, or coarse nitrate (e.g., sodium nitrate, calcium nitrate, potassium nitrate, etc.), on most days predicted total nitrate concentrations are simply not high enough. We deduce that the two likeliest causes of this are: (1) there is a missing source of HNO_3, or (2) the inaccurate distribution of total nitrate between the gas-phase and the two aerosol modes artificially enhances the removal of nitrate via dry deposition.

4.5.4.3 Impact of crustal species on ammonium and nitrate

Several studies have shown that crustal species (Mg^{2+}, K^{+}, Ca^{2+}), from both anthropogenic emissions and fugitive dust, can potentially influence the thermodynamic partitioning of ammonium and nitrate aerosol between the gas-phase and both fine and coarse aerosol modes (*Fountoukis et al.*, 2009; *Moya et al.*, 2002; *Jacobson*, 1999). Dominant sources of crustal species include unpaved and paved roads, agricultural tilling, construction dust, and sand and gravel from mining and quarry operations (*Reff et al.*, 2009). Assessing the impacts of crustal species requires representation of fugitive dust emissions, anthropogenic dust emissions, and chemical speciation profiles to determine the mass fraction of crustal elements within the dust. All three of these inputs are not well constrained on regional and global scales. For example, in a modeling study of the April 2001 dust storm episode over the trans-Pacific domain, *Wang et al.* (2012) assume that 10% of emitted crustal species reside in the fine mode and 90% reside in the coarse mode based on results presented in *Midwest Research Institute* (2005), and use a static speciation profile based on *Van Pelt and Zobeck* (2007) to map 0.10%, 0.17%, and 0.071% of fugitive dust to K^{+}, Ca^{2+}, and Mg^{2+}, respectively. In contrast, in CMAQv5.0, 80% of fugitive dust emissions are assumed to reside in the coarse mode and 20% in the fine mode. In CMAQv5.0, a static speciation profile is used to map 3.8%, 7.9%, and 0.0% of all windblown dust to K^{+}, Ca^{2+}, and Mg^{2+}, respectively (`http://www.cmaq-model.org/cmaqwiki/index.php?title=CMAQv5.0_PMother_speciation`), while fine mode soil dust requires source specific speciation profiles available from the EPA SPECIATE database (`http://www.epa.gov/ttnchie1/software/speciate/`). One concludes that simulating dust emissions of crustal species is quite uncertain. Despite this high uncertainty, the potential influence of

crustal species on aerosol formation suggests that this be addressed, if only approximately.

Crustal species are not represented explicitly in the standard CMAQv4.7.1 model, and the ARCTAS-CARB emission inventory does not contain speciated crustal emission rates. However, the ARCTAS-CARB emission inventory does include two species, PM_{fine} and PM_{coarse}, which represent primary, unspeciated, fine and coarse mode particulate emissions, respectively. Within CMAQv4.7.1, 90% of PM_{coarse} emissions are assigned to the inert species ASOIL, which represents all coarse-mode, soil-derived, fugitive dust emissions, and 10% are assigned to the inert species ACORS, which represents non-fugitive dust emissions from anthropogenic sources such as diesel trucks. All fine dust emissions are assigned to the unspeciated accumulation-mode species A25J (A = aerosol, 25 = PM2.5, J = accumulation mode). Long-range transport of fine and coarse dust is accounted for via nested GEOS-Chem simulations of chemically inert dust species (`http://wiki.seas.harvard.edu/geos-chem/index.php/Mineral_dust_aerosols`).

Due to a lack of information, we use static speciation profiles to assign the fractions of ACORS, ASOIL, and A25J to coarse and fine mode crustal species, respectively (Table 4.8). Fine mode speciation profiles listed in Table 4.8 are taken directly from Figure 3 of *Reff et al.* (2009), and are based on average speciation profiles from the U.S. National Emission Inventory (2001). Coarse mode speciation profiles listed in Table 4.8 are taken directly from the static speciation profiles used in CMAQv5.0, which are based on a combination of speciation profiles from the EPA SPECIATE database. We have modified CMAQv4.7.1 to use ISORROPIAII, which allows for the inclusion of crustal species in thermodynamic calculations. We have not modified any other simulated processes (e.g., dry deposition, wet deposition, sea-salt emissions, aqueous-phase chemistry) to account for the chemical speciation of dust aerosol. As in the unmodified CMAQv4.7.1 model, mass is partitioned between the gas- and aerosol-phases according to the hybrid method (*Capaldo et al.*, 2000)

For the sake of brevity, we restrict our analysis of crustal species to the P3 flights. Figure 4.12 shows particulate (still corrected for AMS transmission window) predicted along P3 flight paths, with and without crustal species. The results suggest that, with the inclusion of crustal species, ammonium concentrations consistently decrease, while nitrate concentrations can increase, decrease,

or remain virtually unchanged. *Jacobson* (1999) showed that, depending on the environment (e.g., ammonia limited, nitric acid limited), coarse crustal species can increase, decrease, or have virtually no effect on the predicted amount of coarse-mode nitrate. Nitrate concentration increases are caused by crustal cations driving nitric acid into the particle phase to maintain charge balance. Nitrate concentration decreases are caused by crustal cations increasing mixed activity coefficients and driving ammonium nitrate aerosol into the gas phase. When these two effects roughly cancel each other, nitrate concentrations remain unchanged and ammonium also gets shifted to the gas phase, or to a different aerosol mode (e.g. coarse aerosol phase). Figure C.9 shows time-series plots of Ca^{2+}, K^{+}, and Mg^{2+} concentrations predicted along the five P3 flight paths, as well as the amount of additional fine and coarse mode nitrate that could potentially be neutralized by the crustal cations. Using the speciation profile listed in Table 4.8, predicted coarse mode Ca^{2+} concentrations are typically higher than fine mode concentrations, fine and coarse mode K^{+} concentrations are comparable, and Mg^{2+} is present only in the fine aerosol mode. Since crustal species are predicted to be present in both fine and coarse modes, it is difficult to decouple the impacts aerosol modes have on each other. Overall, the inclusion of crustal species tends to decrease submicrometer ammonium aerosol, and increase or decrease submicrometer nitrate aerosol depending on the relative concentrations of dust. However, other than the May 4 P3 flight, the results presented in Figure 4.12 indicate that the impact of crustal species is not very substantial, most likely due to low crustal species concentrations predicted along the P3 flight paths. Moreover, these results would be even less pronounced if the speciation factors from *Van Pelt and Zobeck* (2007) were to be used since they are roughly an order of magnitude lower than those listed in Table 4.8. These results suggest that the exclusion of crustal species in thermodynamic calculations is not the dominant source of error between predicted and observed fine ammonium and nitrate concentrations. Future work should focus on acquiring chemically-resolved and size-resolved (up to 10 μm) measurements of crustal species, sea-salt, and nitrate.

4.6 Summary and Conclusions

A detailed three-dimensional chemical transport model (CMAQ version 4.7.1), which contains state-of-the-science gas-phase chemistry and aerosol thermodynamics, was applied during the May 2010 CalNex campaign in the Los Angeles Basin. Boundary conditions were extracted from a nested global-scale GEOS-Chem model (version 9.1.1) simulation. Input meteorology and emission inventories were provided by the CARB. Inorganic and BC aerosol predictions were compared against the suite of ground-based and airborne measurements taken from various CIRPAS Twin Otter and WP-3D flights. The FLEXPART Lagrangian particle dispersion model is used to determine the trajectories of air parcels that reached the aircraft.

Comparisons of predicted and observed BC measurements at the Pasadena ground site suggest that potentially large peaks in measured BC concentrations may be missed on any given day, owing most likely to inaccuracy in the predicted wind fields, but are generally represented well by CMAQ. BC predictions are consistently higher than observations onboard the Twin Otter, which is at least partially due to a systematic bias inherent to the SP2 onboard. However, predicted and observed BC concentrations and $\Delta BC/\Delta CO$ ratios along P3 flight paths suggests that no systematic bias exists in the ARCTAS-CARB BC emission inventory or the MM5 meteorology.

SO_2 concentrations are consistently overpredicted at surface sites, while the agreement between predicted and observed sulfate concentrations is variable. Sulfate is over-predicted by 55%-268% as compared to Twin Otter measurements, 0%-71% as compared to P3 measurements, and is actually under-predicted by 17% as compared to observations at the Pasadena ground site. The sulfate source apportionment presented in this study suggests that, with the current sulfur emission inventory based on emission factors from 2008, long-range transport of sulfate accounts for a substantial fraction (22-82%) of the sulfate in L.A. Basin. However, if the reductions in sulfur emission factors reported by *Lack et al.* (2011) ($\sim$90%) were to be included in simulations, unlike the results presented in *Huang et al.* (2011), the boundary inflow of sulfate would become the single largest contributor to predicted sulfate concentrations in the L.A. Basin.

Severely underpredicted NH_3 emissions from dairy facilities are identified as the dominant source

of measurement/model disagreement in the eastern L.A. Basin. By comparing predicted and observed concentrations of total nitrate, with and without applying the AMS transmission window, we show that, regardless of whether nitrate is predicted to form ammonium nitrate, nitric acid, or coarse nitrate (e.g. sodium nitrate, calcium nitrate, potassium nitrate, etc.), on most days predicted total nitrate concentrations are simply not high enough. We deduce that the two likeliest causes of this are: (1) there is a missing source of HNO_3, or (2) the inaccurate distribution of total nitrate between the gas-phase and the two aerosol modes artificially enhances the removal of nitrate via dry deposition. We estimate that, for most P3 flights, the exclusion of crustal species in thermodynamic calculations is not the dominant source of error between predicted and observed fine ammonium and nitrate concentrations. However, as stated previously, there is considerable uncertainty in all parameters used in the crustal sensitivity simulation, and we are reluctant to draw conclusions based on this study alone.

This work, as part of the CalNex campaign, provides an up-to-date characterization of the inorganic and black carbon fraction of the Los Angeles Basin particulate matter. Adding gas-phase NH_3 measurements and size-resolved measurements, up to 10 μm, of nitrate and various cations (e.g. Na^+, Ca^{2+}, K^+, Mg^{2+}) to routine monitoring stations in the L.A. Basin would facilitate interpreting day-to-day fluctuations in fine and coarse inorganic aerosol greatly. Future work will focus on improving and assessing the treatment of anthropogenic and fugitive dust emissions, as well as characterizing the nature of organic aerosol formation and evolution in the Los Angeles Basin.

4.7 Additional Flights

Section 4.7 contains Figures 4.13–4.16.

4.8 AMS Transmission Efficiencies

The AMS transmission curve used in this study is piece-wise defined for three diameter ranges: (a) linear increase in transmission vs $\ln(D_{va})$, from 0% at D_{va} = 40 nm to 100% at D_{va} = 100 nm, (b)

100% transmission from D_{va} = 100 nm up to D_{va} = 550 nm, (c) linear decrease in transmission vs ln(D_{va}), from 100% at D_{va} = 550 nm to 0% at D_{va} = 2 μm, and zero elsewhere. This transmission curve can be applied analytically to any log-normal mass distribution:

40 nm $< D_{va} <$ 100 nm:

$$f(D_{va}) = \frac{\ln(D_{va}/40\text{ nm})}{\ln(100\text{ nm}/40\text{ nm})} \tag{4.5}$$

$$M(40\ \text{nm} < D_{va} < 100\text{ nm}) = \tag{4.6}$$

$$M(40\ \text{nm}/\rho_{dry} < D_p < 100\ \text{nm}/\rho_{dry}) =$$

$$\frac{M_{tot}}{2} \times \frac{\ln(\overline{D}_{pgV}^{dry}/(40\text{ nm}/\rho_{dry}))}{\ln(100\text{ nm}/40\text{ nm})} \times \left[\text{erf}\left(\frac{\ln\left((100\text{ nm}/\rho_{dry})/\overline{D}_{pgV}^{dry}\right)}{\sqrt{2}\times\ln(\sigma_{dry})}\right) - \text{erf}\left(\frac{\ln\left((40\text{ nm}/\rho_{dry})/\overline{D}_{pgV}^{dry}\right)}{\sqrt{2}\times\ln(\sigma_{dry})}\right)\right] +$$

$$\frac{M_{tot}}{2} \times \frac{\ln(\sigma_{dry})}{\ln(100\text{ nm}/40\text{ nm})\times\sqrt{\frac{\pi}{2}}} \times \left\{\exp\left[-\left(\frac{\ln\left(40\text{ nm}/\overline{D}_{pgV}^{dry}\right)}{\sqrt{2}\times\ln(\sigma_{dry})}\right)^2\right] - \exp\left[-\left(\frac{\ln\left(100\text{ nm}/\overline{D}_{pgV}^{dry}\right)}{\sqrt{2}\times\ln(\sigma_{dry})}\right)^2\right]\right\}$$

100 nm $< D_{va} <$ 550 nm:

$$f(D_{va}) = 1 \tag{4.7}$$

$$M(100\ \text{nm} < D_{va} < 550\ \text{nm}) = \tag{4.8}$$

$$M(100\ \text{nm}/\rho_{dry} < D_p < 550\ \text{nm}/\rho_{dry}) =$$

$$\frac{M_{tot}}{2} \times \left[\text{erf}\left(\frac{\ln\left((550\text{ nm}/\rho_{dry})/\overline{D}_{pgV}^{dry}\right)}{\sqrt{2}\times\ln(\sigma_{dry})}\right) - \text{erf}\left(\frac{\ln\left((100\text{ nm}/\rho_{dry})/\overline{D}_{pgV}^{dry}\right)}{\sqrt{2}\times\ln(\sigma_{dry})}\right)\right]$$

$550\ \text{nm} < D_{va} < 2000\ \text{nm}$:

$$f(D_{va}) = \frac{\ln(D_{va}/2000\ \text{nm})}{\ln(550\ \text{nm}/2000\ \text{nm})} \tag{4.9}$$

$$M(550\ \ \text{nm} < D_{va} < 2000\ \ \text{nm}) = \tag{4.10}$$

$$M(550\ \ \text{nm}/\rho_{dry} < D_p < 2000\ \ \text{nm}/\rho_{dry}) =$$

$$\frac{M_{tot}}{2} \times \frac{\ln(\overline{D}_{pgV}^{dry}/(2000\ \text{nm}/\rho_{dry}))}{\ln(550\ \text{nm}/2000\text{nm})} \times \left[\text{erf}\left(\frac{\ln\left((2000\ \text{nm}/\rho_{dry})/\overline{D}_{pgV}^{dry}\right)}{\sqrt{2} \times \ln\left(\sigma_{dry}\right)}\right) - \text{erf}\left(\frac{\ln\left((550\ \text{nm}/\rho_{dry})/\overline{D}_{pgV}^{dry}\right)}{\sqrt{2} \times \ln\left(\sigma_{dry}\right)}\right)\right] +$$

$$\frac{M_{tot}}{2} \times \frac{\ln(\sigma_{dry})}{\ln(550\ \text{nm}/2000\ \text{nm}) \times \sqrt{\frac{\pi}{2}}} \times \left\{\exp\left[-\left(\frac{\ln\left((550\ \text{nm}/\rho_{dry})/\overline{D}_{pgV}^{dry}\right)}{\sqrt{2} \times \ln\left(\sigma_{dry}\right)}\right)^2\right] - \exp\left[-\left(\frac{\ln\left((2000\ \text{nm}/\rho_{dry})/\overline{D}_{pgV}^{dry}\right)}{\sqrt{2} \times \ln\left(\sigma_{dry}\right)}\right)^2\right]\right\}$$

where f is the transmission efficiency as a function of D_{va}, M_{tot} is the unmodified, total amount of predicted species mass (e.g. nitrate, sulfate, ammonium) in the mode, and $M(D_{va,min} < D_{va} < D_{va,max})$ is the modified amount of species mass, within the mode, in the given vacuum-aerodynamic diameter range. The vacuum-aerodynamic diameter limits of the AMS transmission curve are converted to particle (Stokes) diameters for each data point by using $D_p = (\frac{\rho_o}{\rho_{dry}})D_{va}$ (*DeCarlo et al.*, 2004), where D_p is the physical (Stokes) diameter of the particle, D_{va} is the vacuum-aerodynamic diameter, ρ_o is the standard density (1 g cm^{-3}), and ρ_{dry} is the density of the particle predicted by CMAQ not including water. The total mass from each mode (using this specific AMS transmission efficiency curve) is then:

$$M_{mode}^{AMS} = M(40\ \ \text{nm} < D_{va} < 100\ \ \text{nm}) + M(100\ \ \text{nm} < D_{va} < 550\ \ \text{nm}) + M(550\ \ \text{nm} < D_{va} < 2000\ \ \text{nm}) \tag{4.11}$$

where M_{mode}^{AMS} is the total amount of predicted species mass in the mode that has been adjusted to match the transmission curve of the AMS. The total amount of predicted species mass that should be compared to the AMS is then the sum of all three adjusted modes ($M = M_I^{AMS} + M_J^{AMS} + M_K^{AMS}$), where I, J, and K are the Aitken mode, the accumulation mode, and the coarse mode,

respectively. The derivation of the equations for transmission curve adjustment are presented in the supplementary section.

Acknowledgments

This work was funded by NOAA grant NA09OAR4310128 and by the State of California Air Resources Board (CARB) Agreement 10-328. NOAA's Climate and Air Quality programs supported the NOAA-P3 deployment. PLH and JLJ were supported by CARB-319 and DOE (BER, ASR program) DE-SC0006035, and PLH acknowledges a CIRES Visiting Postdoctoral Fellowship. This work was supported in part by the NOAA Health of the Atmosphere Program and the NOAA Climate Goal. We acknowledge four anonymous reviewers for their thorough and insightful comments. The authors would like to thank Nehzat Motallebi, Havala O. T. Pye, and Andreas Zuend for useful discussions, Ying Xie and Rob Pinder at the Environmental Protection Agency (EPA) for providing the SAPRC07TC chemical mechanism, Anne Perring, Joshua Schwartz, and David Fahey for the use of the SP2 measurements from the NOAA P3 aircraft and for useful discussion, John Holloway at NOAA for CO measurements from the NOAA P3 aircraft, Kemal Gurer for MM5 modeled data, and Jerome Fast for providing the Aerosol Modeling Testbed analysis toolkit. The statements and conclusions in this paper are those of the researchers (contractor) and not necessarily those of CARB. The mention of commercial products, their source, or their use in connection with material reported herein is not to be construed as actual or implied endorsement of such products.

Bibliography

Angevine., W. M., Eddington, L., Durkee, K., Fairall, C., Bianco, L., Brioude, J. (2012), Meteorological model evaluation for CalNex 2010, *Mon. Wea. Rev.*, *In Press*, doi:10.1175/MWR-D-12-00042. 1.

Appel, B., Hoffer, E., Tokiwa, Y., and Kothny, E. (1982), Measurement of sulfuric-acid and par-

ticulate strong acidity in the Los-Angeles basin, *Atmos. Environ.*, *16*, 589–593, doi:10.1016/0004-6981(82)90168-8.

Bahreini, R., Ervens, B., Middlebrook, A. M., Warneke, C., de Gouw, J. A., DeCarlo, P. F., Jimenez, J. L., Brock, C. A., Neuman, J. A., Ryerson, T. B., Stark, H., Atlas, E., Brioude, J., Fried, A., Holloway, J. S., Peischl, J., Richter, D., Walega, J., Weibring, P., Wollny, A. G., and Fehsenfeld, F. C. (2009), Organic aerosol formation in urban and industrial plumes near Houston and Dallas, Texas, *J. Geophys. Res.-Atmos.*, *114*, doi:{10.1029/2008JD011493}.

Bein, K. J., Zhao, Y., Pekney, N. J., Davidson, C. I., Johnston, M. V., and Wexler, A. S.: Identification of sources of atmospheric PM at the Pittsburgh Supersite - Part II (2006), Quantitative comparisons of single particle, particle number, and particle mass measurements, *Atmos. Environ.*, *40*, S424–S444, doi:{10.1016/j.atmosenv.2006.01.064}.

Bey, I., Jacob, D., Yantosca, R., Logan, J., Field, B., Fiore, A., Li, Q., Liu, H., Mickley, L., and Schultz, M.: Global modeling of tropospheric chemistry with assimilated meteorology (2001), Model description and evaluation, *J. Geophys. Res.-Atmos.* , *106*, 23 073–23 095, doi:{10.1029/2001JD000807}.

Binkowski, F. and Roselle, S. (2003), Models-3 community multiscale air quality (CMAQ) model aerosol component - 1. Model description, *J. Geophys. Res.-Atmos.* , *108*, doi:10.1029/2001JD001409.

Bond, T. and Bergstrom, R. (2006), Light absorption by carbonaceous particles: An investigative review, *Aerosol. Sci. Tech.*, *40*, 27–67, doi:{10.1080/02786820500421521}.

Brioude, J., Cooper, O. R., Feingold, G., Trainer, M., Freitas, S. R., Kowal, D., Ayers, J. K., Prins, E., Minnis, P., McKeen, S. A., Frost, G. J., and Hsie, E. Y. (2009), Effect of biomass burning on marine stratocumulus clouds off the California coast, *Atmos. Chem. Phys.*, *9*, 8841–8856.

Cabada, J., Rees, S., Takahama, S., Khlystov, A., Pandis, S., Davidson, C., and Robinson, A. (2004),

Mass size distributions and size resolved chemical composition of fine particulate matter at the Pittsburgh supersite, *Atmos. Environ.*, *38*, 3127–3141, doi:{10.1016/j.atmosenv.2004.03.004}.

Canagaratna, M. R., Jayne, J. T., Jimenez, J. L., Allan, J. D., Alfarra, M. R., Zhang, Q., Onasch, T. B., Drewnick, F., Coe, H., Middlebrook, A., Delia, A., Williams, L. R., Trimborn, A. M., Northway, M. J., DeCarlo, P. F., Kolb, C. E., Davidovits, P., and Worsnop, D. R. (2007), Chemical and microphysical characterization of ambient aerosols with the aerodyne aerosol mass spectrometer, *Mass Spectrom. Rev.*, *26*, 185–222, doi:{10.1002/mas.20115}.

Capaldo, K., Pilinis, C., and Pandis, S. (2000), A computationally efficient hybrid approach for dynamic gas/aerosol transfer in air quality models, *Atmos. Environ.*, *34*, 3617–3627.

Carter, W. P. L. (2010), Development of a condensed SAPRC-07 chemical mechanism, *Atmos. Environ.*, *44*, 5336–5345, doi:{10.1016/j.atmosenv.2010.01.024}, 2nd Biennial Conference on Atmospheric Chemistry Mechanisms, Air Quality Res Ctr, Davis, CA, DEC, 2008.

Chang, J., Brost, R., Isaksen, I., Madronich, S., Middleton, P., Stockwell, W., and Walcek, C. (1987), A 3-dimensional eulerian acid deposition model - physics concepts and formulation, *J. Geophys. Res.-Atmos.*, *92*, 14 681–14 700, doi:{10.1029/JD092iD12p14681}.

Chow, J., Fujita, E., Watson, J., Lu, Z., Lawson, D., and Asbaugh, L. (1994), Evaluation of filter-based aerosol measurements during the 1987 Southern California Air-Quality Study, *Env. Monit. Assess.*, *30*, 49–80,doi:{10.1007/BF00546199}.

Clarke, A., Shinozuka, Y., Kapustin, V., Howell, S., Huebert, B., Doherty, S., Anderson, T., Covert, D., Anderson, J., Hua, X., Moore, K., McNaughton, C., Carmichael, G., and Weber, R. (2004), Size distributions and mixtures of dust and black carbon aerosol in Asian outflow: Physiochemistry and optical properties, *J. Geophys. Res.-Atmos.*, *109*, doi:{10.1029/2003JD004378}.

Croes, B. and Fujita, E. (2003), Overview of the 1997 Southern California Ozone Study (SCOS97-NARSTO), *Atmos. Environ.*, *37*, S3–S26, doi:10.1016/S1352-2310(03)00379-0.

Dallmann, T., Harley, R., and Kirchstetter, T. (2011), Effects of diesel particle filter retrofits and accelerated fleet turnover on drayage truck emissions at the port of oakland, *Environ. Sci. Technol.*, *45*,10773-10779, doi:10.1021/es202609q.

de Foy, B., Varela, J., Molina, L., and Molina, M. (2006), Rapid ventilation of the Mexico City basin and regional fate of the urban plume, *Atmos. Chem. Phys.*, *6*, 2321–2335.

de Leeuw, G., Neele, F., Hill, M., Smith, M., and Vignali, E. (2000), Production of sea spray aerosol in the surf zone, *J. Geophys. Res.-Atmos.*, *105*, 29 397–29 409,doi:10.1029/2000JD900549.

DeCarlo, P., Slowik, J., Worsnop, D., Davidovits, P., and Jimenez, J. (2004), Particle morphology and density characterization by combined mobility and aerodynamic diameter measurements. Part 1: Theory, *Aerosol. Sci. Tech.*, *38*, 1185–1205, doi:{10.1080/027868290903907}.

DeCarlo, P. F., Dunlea, E. J., Kimmel, J. R., Aiken, A. C., Sueper, D., Crounse, J., Wennberg, P. O., Emmons, L., Shinozuka, Y., Clarke, A., Zhou, J., Tomlinson, J., Collins, D. R., Knapp, D., Weinheimer, A. J., Montzka, D. D., Campos, T., and Jimenez, J. L. (2008), Fast airborne aerosol size and chemistry measurements above Mexico City and Central Mexico during the MILAGRO campaign, *Atmos. Chem. Phys.*, *8*, 4027–4048.

Ding, A., Wang, T., Xue, L., Gao, J., Stohl, A., Lei, H., Jin, D., Ren, Y., Wang, X., Wei, X., Qi, Y., Liu, J., and Zhang, X. (2009), Transport of north China air pollution by midlatitude cyclones: Case study of aircraft measurements in summer 2007, *J. Geophys. Res.-Atmos.*, *114*, doi:{10.1029/2008JD011023}.

Docherty, K. S., Aiken, A. C., Huffman, J. A., Ulbrich, I. M., DeCarlo, P. F., Sueper, D., Worsnop, D. R., Snyder, D. C., Peltier, R. E., Weber, R. J., Grover, B. D., Eatough, D. J., Williams, B. J., Goldstein, A. H., Ziemann, P. J., and Jimenez, J. L. (2011), The 2005 Study of Organic Aerosols at Riverside (SOAR-1): instrumental intercomparisons and fine particle composition , *Atmos. Chem. Phys.*, *11*, 12387-12420, doi:10.5194/acp-11-12387-2011,2011.

Dominguez, G., Jackson, T., Brothers, L., Barnett, B., Nguyen, B., and Thiemens, M. H. (2008),

Discovery and measurement of an isotopically distinct source of sulfate in Earth's atmosphere, *Proc. Nat. Acad. Sci. USA*, *105*, 12 769–12 773, doi:{10.1073/pnas.0805255105}.

Drewnick, F., Hings, S., DeCarlo, P., Jayne, J., Gonin, M., Fuhrer, K., Weimer, S., Jimenez, J., Demerjian, K., Borrmann, S., and Worsnop, D. (2005), A new time-of-flight aerosol mass spectrometer (TOF-AMS) - Instrument description and first field deployment, *Aerosol. Sci. Tech.*, *39*, 637–658,doi:{10.1080/02786820500182040}.

Dzepina, K., Volkamer, R. M., Madronich, S., Tulet, P., Ulbrich, I. M., Zhang, Q., Cappa, C. D., Ziemann, P. J., and Jimenez, J. L. (2009), Evaluation of recently-proposed secondary organic aerosol models for a case study in Mexico City, *Atmos. Chem. Phys.*, *9*, 5681–5709, doi:10.5194/acp-9-5681-2009.

Eldering, A., Cass, G., and Moon, K. (1994), An air monitoring network using continuous particle-size distribution monitors - connecting pollutant properties to visibility via mie scattering calculations, *Atmos. Environ.*, *28*, 2733–2749,doi:10.1016/1352-2310(94)90445-6.

Ellis, R. A., Murphy, J. G., Pattey, E., van Haarlem, R., O'Brien, J. M., and Herndon, S. C. (2010),Characterizing a Quantum Cascade Tunable Infrared Laser Differential Absorption Spectrometer (QC-TILDAS) for measurements of atmospheric ammonia, *Atmos. Meas. Tech.*, *3*, 397–406, doi:10.5194/amt-3-397-2010.

Emeis, S. and Schafer, K. (2006), Remote sensing methods to investigate boundary-layer structures relevant to air pollution in cities, *Bound.-Lay. Meteorol.*, *121*, 377385, doi::10.1007/s10546-006-9068-2.

Fast, J., Aiken, A. C., Allan, J., Alexander, L., Campos, T., Canagaratna, M. R., Chapman, E., DeCarlo, P. F., de Foy, B., Gaffney, J., de Gouw, J., Doran, J. C., Emmons, L., Hodzic, A., Herndon, S. C., Huey, G., Jayne, J. T., Jimenez, J. L., Kleinman, L., Kuster, W., Marley, N., Russell, L., Ochoa, C., Onasch, T. B., Pekour, M., Song, C., Ulbrich, I. M., Warneke, C., Welsh-Bon, D., Wiedinmyer, C., Worsnop, D. R., Yu, X.-Y., and Zaveri, R. (2009), Evaluating simulated

primary anthropogenic and biomass burning organic aerosols during MILAGRO: implications for assessing treatments of secondary organic aerosols, *Atmos. Chem. Phys.* , *9*, 6191-6215, doi: 10.5194/acp-9-6191-2009.

Fast, J. D., Gustafson, Jr., W. I., Chapman, E. G., Easter, R. C., Rishel, J. P., Zaveri, R. A., Grell, G. A., and Barth, M. C. (2011), The Aerosol Modeling Testbed: A community tool to objectively evaluate aerosol process modules, *Bull. Amer. Meteor. Soc.*, *92*, 343–360, doi:10.1175/2010BAMS2868.1.

Foley, K. M., Roselle, S. J., Appel, K. W., Bhave, P. V., Pleim, J. E., Otte, T. L., Mathur, R., Sarwar, G., Young, J. O., Gilliam, R. C., Nolte, C. G., Kelly, J. T., Gilliland, A. B., and Bash, J. O. (2010), Incremental testing of the Community Multiscale Air Quality (CMAQ) modeling system version 4.7, *Geosci. Mod. Devel.*, *3*, 205–226.

Fountoukis, C. and Nenes, A. (2007), ISORROPIA II: a computationally efficient thermodynamic equilibrium model for K^+-Ca^{2+}-Mg^{2+}-NH_4^+-Na^+-SO_4^{2-}-NO_3^--Cl^--H_2O aerosols, *Atmos. Chem. Phys.*, *7*, 4639–4659.

Fountoukis, C., Nenes, A., Sullivan, A., Weber, R., Van Reken, T., Fischer, M., Matias, E., Moya, M., Farmer, D., and Cohen, R. C. (2009), Thermodynamic characterization of Mexico City aerosol during MILAGRO 2006, *Atmos. Chem. Phys.*, *9*, 2141–2156.

Gong, S. (2003), A parameterization of sea-salt aerosol source function for sub- and super-micron particles, *Glo. Biogeochem. Cyc.*, *17*, doi:10.1029/2003GB002079.

Grell, G. A., Dudhia, J., and Stauffer, D. R. (1995), A description of the fifth-generation Penn State/NCAR mesoscale model (MM5). NCAR Technical Note NCAR/TN-398+STR, Note TN398 STR, p. 138.

Haman, C. L. (2011), Seasonal and daily variability of the boundary layer and the impact of synoptic controls and micrometeorological processes on surface ozone evolution at an urban site, Ph.D. thesis, University of Houston, Texas, USA.

Hegg, D., D. Covert, H. Jonsson, and P. Covert (2005), Determination of the transmission efficiency of an aircraft aerosol inlet, *Aerosol Sci. Technol.*, *39*(10), 966–971, doi:10.1080/02786820500377814.

Holloway, J. S., R. O. Jakoubek, D. D. Parrish, C. Gerbig, A. Volz-Thomas, S. Schmitgen, A. Fried, B. Wert, B. Henry, and J. R. Drummond (2000), Airborne intercomparison of vacuum ultraviolet fluorescence and tunable diode laser absorption measurements of tropospheric carbon monoxide, *J. Geophys. Res.*, *105*(D19), 24,25124,261, doi::10.1029/2000JD900237.

Hsu, S.-C., Liu, S. C., Kao, S.-J., Jeng, W.-L., Huang, Y.-T., Tseng, C.-M., Tsai, F., Tu, J.-Y., and Yang, Y. (2007),Water-soluble species in the marine aerosol from the northern South China Sea: High chloride depletion related to air pollution, *J. Geophys. Res.*, *112*, D19304, doi: 10.1029/2007JD008844.

Huang, M., Carmichael, G. R., Spak, S. N., Adhikary, B., Kulkarni, S., Cheng, Y., Wei, C., Tang, Y., D'Allura, A., Wennberg, P. O., Huey, G. L., Dibb, J. E., Jimenez, J. L., Cubison, M. J., Weinheimer, A. J., Kaduwela, A., Cai, C., Wong, M., Pierce, R. B., Al-Saadi, J. A., Streets, D. G., and Zhang, Q. (2011), Multi-scale modeling study of the source contributions to near-surface ozone and sulfur oxides levels over California during the ARCTAS-CARB period, *Atmos. Chem. Phys.*, *11*, 3173–3194, doi:{10.5194/acp-11-3173-2011}.

Hughes, L., Allen, J., Salmon, L., Mayo, P., Johnson, R., and Cass, G. (2002), Evolution of nitrogen species air pollutants along trajectories crossing the Los Angeles area, *Environ. Sci. Technol.*, *36*, 3928–3935, doi:10.1021/es0110630.

Ianniello, A., Spataro, F., Esposito, G., Allegrini, I., Hu, M., and Zhu, T. (2011), Chemical characteristics of inorganic ammonium salts in PM(2.5) in the atmosphere of Beijing (China), *Atmos. Chem. Phys.*, *11*, 10 803–10 822,doi:{10.5194/acp-11-10803-2011}.

Jacob, D. J., Crawford, J. H., Maring, H., Clarke, A. D., Dibb, J. E., Emmons, L. K., Ferrare, R. A., Hostetler, C. A., Russell, P. B., Singh, H. B., Thompson, A. M., Shaw, G. E., McCauley,

E., Pederson, J. R., and Fisher, J. A. (2010), The Arctic Research of the Composition of the Troposphere from Aircraft and Satellites (ARCTAS) mission: design, execution, and first results, *Atmos. Chem. Phys.*, *10*, 5191–5212, doi:{10.5194/acp-10-5191-2010}.

Jacobson, M. Z. (1999), Studying the effects of calcium and magnesium on size-distributed nitrate and ammonium with EQUISOLV II, *Atmos. Environ.*, *33*, 36353649, doi::10.1016/S1352-2310(99) 00105-3.

Jayne, J., Leard, D., Zhang, X., Davidovits, P., Smith, K., Kolb, C., and Worsnop, D. (2000), Development of an aerosol mass spectrometer for size and composition analysis of submicron particles, *Aerosol. Sci. Tech.*, *33*, 49–70,doi:{10.1080/027868200410840}.

Jiang, W., Smyth, S., Giroux, E., Roth, H., and Yin, D. (2006), Differences between CMAQ fine mode particle and PM2.5 concentrations and their impact on model performance evaluation in the lower Fraser valley, *Atmos. Env.*, *40*, 4973–4985, doi:{10.1016/j.atmonsenv.2005.10.069}

Karydis, V. A., Tsimpidi, A. P., Fountoukis, C., Nenes, A., Zavala, M., Lei, W., Molina, L. T., and Pandis, S. N. (2010), Simulating the fine and coarse inorganic particulate matter concentrations in a polluted megacity, *Atmos. Environ.*, *44*, 608–620, doi:10.1016/j.atmosenv.2009.11.023.

Kelly, J. T., Bhave, P. V., Nolte, C. G., Shankar, U., and Foley, K. M. (2010), Simulating emission and chemical evolution of coarse sea-salt particles in the Community Multiscale Air Quality (CMAQ) model, *Geosci. Mod. Devel.*, *3*, 257–273, doi:10.5194/gmd-3-257-2010.

Knote, C., Brunner, D., Vogel, H., Allan, J., Asmi, A., Äijälä, M., Carbone, S., van der Gon, H. D., Jimenez, J. L., Kiendler-Scharr, A., Mohr, C., Poulain, L., Prévôt, A. S. H., Swietlicki, E., and Vogel, B. (2011), Towards an online-coupled chemistry-climate model: evaluation of trace gases and aerosols in COSMO-ART, *Geosci. Model Dev.*, *4*, 1077–1102, doi:10.5194/gmd-4-1077-2011.

Lack, D. A., Cappa, C. D., Langridge, J., Bahreini, R., Buffaloe, G., Brock, C., Cerully, K., Coffman, D., Hayden, K., Holloway, J., Lerner, B., Massoli, P., Li, S.-M., McLaren, R., Middlebrook, A. M., Moore, R., Nenes, A., Nuaaman, I., Onasch, T. B., Peischl, J., Perring, A., Quinn, P. K., Ryerson,

T., Schwartz, J. P., Spackman, R., Wofsy, S. C., Worsnop, D., Xiang, B., and Williams, E. (2011), Impact of fuel quality regulation and speed reductions on shipping emissions: implications for climate and air quality, *Environ. Sci. Technol.*, *45*, 9052–9060, doi:10.1021/es2013424.

Lee, S. H., Kim, S. W., Angevine, W. M., Bianco, L., McKeen, S. A., Senff, C. J., Trainer, M., Tucker, S. C., and Zamora, R. J. (2011), Evaluation of urban surface parameterizations in the WRF model using measurements during the Texas Air Quality Study 2006 field campaign, *Atmos. Chem. Phys.*, *11*, 2127–2143,doi:{10.5194/acp-11-2127-2011}.

Lin, M., Fiore, A. M., Horowitz, L. W., Cooper, O. R., Naik, V., Holloway, J., Johnson, B. J., Middlebrook, A. M., Oltmans, S. J., Pollack, I. B., Ryerson, T. B., Warner, J. X., Wiedinmyer, C., Wilson, J., and Wyman, B. (2012), Transport of Asian ozone pollution into surface air over the western United States in spring, *J. Geophys. Res.-Atmos.*, *117*, doi:{10.1029/2011JD016961}.

Liu, D., Prather, K., and Hering, S. (2000), Variations in the size and chemical composition of nitrate-containing particles in Riverside, CA, *Aerosol. Sci. Tech.*, *33*, 71–86,doi:10.1080/027868200410859.

Lu, R. and Turco, R. (1995), Air pollutant transport in a coastal environment -II. 3-Dimensional simulations over Los-Angeles Basin, *Atmos. Environ.*, *29*, 14991518, doi:10.1016/1352-2310(95) 00015-Q.

Luke, W. T. (1997), Evaluation of a commercial pulsed fluorescence detector for the measurement of low-level SO2 concentrations during GASIE. *J. Geophys. Res. 102*, 16, 25516, doi:10.1029/ 96JD03347.

Martucci, G., Matthey, R., Mitev, V., and Richner, H. (2007), Comparison between backscatter lidar and radiosonde measurements of the diurnal and nocturnal stratification in the lower troposphere, *J. Atmos. Ocean. Technol.*, *24*, 12311244, doi::10.1175/JTECH2036.1.

Matsui, H., Koike, M., Kondo, Y., Takegawa, N., Kita, K., Miyazaki, Y., Hu, M., Chang, S. Y., Blake, D. R., Fast, J. D., Zaveri, R. A., Streets, D. G., Zhang, Q., and Zhu, T. (2009), Spatial

and temporal variations of aerosols around Beijing in summer 2006: Model evaluation and source apportionment, *J. Geophys. Res.-Atmos.*, *114*,doi:{10.1029/2008JD010906}.

McKeen, S., Grell, G., Peckham, S., Wilczak, J., Djalalova, I., Hsie, E. Y., Frost, G., Peischl, J., Schwarz, J., Spackman, R., Holloway, J., de Gouw, J., Warneke, C., Gong, W., Bouchet, V., Gaudreault, S., Racine, J., McHenry, J., McQueen, J., Lee, P., Tang, Y., Carmichael, G. R., and Mathur, R. (2009), An evaluation of real-time air quality forecasts and their urban emissions over eastern Texas during the summer of 2006 Second Texas Air Quality Study field study, *J. Geophys. Res.-Atmos.*, *114*, doi:{10.1029/2008JD011697}.

McMeeking, G. R., Hamburger, T., Liu, D., Flynn, M., Morgan, W. T., Northway, M., Highwood, E. J., Krejci, R., Allan, J. D., Minikin, A., and Coe, H. (2010), Black carbon measurements in the boundary layer over western and northern Europe, *Atmos. Chem. Phys.*, *10*, 9393-9414, doi::10.5194/acp-10-9393-2010.

Metcalf, A. R., J. S. Craven, J. J. Ensberg, J. Brioude, W. M. M. Angevine, A. Sorooshian, H. T. Duong, H. H. Jonsson, R. C. Flagan, and J. H. Seinfeld (2012), Black carbon aerosol over the Los Angeles Basin during CalNex, *J. Geophys Res.*, *117*, doi::10.1029/2011JD017255.

Middlebrook, A. M., Bahreini, R., Jimenez, J. L., and Canagaratna, M. R. (2012), Evaluation of composition-dependent collection efficiencies for the Aerodyne Aerosol Mass Spectrometer using field data, *Aerosol. Sci. Tech.*, *46*, 258–271,doi:{10.1080/02786826.2011.620041}.

Midwest Research Institute: Analysis of fine fraction of particulate matter in fugitive dust, Report to the WRAP by Midwest Research Institute, Project No. 110397, 2005.

Modey, W., Eatough, D., Anderson, R., Martello, D., Takahama, S., Lucas, L., and Davidson, C. (2004), Ambient fine particulate concentrations and chemical composition at two sampling sites in metropolitan Pittsburgh: a 2001 intensive summer study, *Atmos. Environ.*, *38*, 3165–3178, doi:{10.1016/j.atmosenv.2004.03.005}.

Molina, L. T., Madronich, S., Gaffney, J. S., Apel, E., de Foy, B., Fast, J., Ferrare, R., Hern-

don, S., Jimenez, J. L., Lamb, B., Osornio-Vargas, A. R., Russell, P., Schauer, J. J., Stevens, P. S., and Zavala, M. (2010), An overview of the MILAGRO 2006 Campaign: Mexico City emissions and their transport and transformation, *Atmos. Chem. Phys.* , *10*, 8697-8760, doi: 10.5194/acp-10-8697-2010.

Moteki, N., Kondo, Y., Miyazaki, Y., Takegawa, N., Komazaki, Y., Kurata, G., Shirai, T., Blake, D. R., Miyakawa, T., and Koike, M. (2007), Evolution of mixing state of black carbon particles: Aircraft measurements over the western Pacific in March 2004, *Geophys. Res. Lett.*, *34*, doi: {10.1029/2006GL028943}.

Moya, M., Pandis, S. N., and Jacobson, M. Z. (2002), Is the size distribution of urban aerosols determined by thermodynamic equilibrium?: An application to Southern California, *Atmos. Environ.*, *36*, 23492365, doi:10.1016/S1352-2310(01)00549-0.

Münkel, C., E. Noora, J. Räsänen, and A. Karppinen (2006), Retrieval of mixing height and dust concentration with lidar ceilometer. *Bound.-Lay. Meteorol.*, doi:10.1007/s10546-006-9103-3.

Murphy, S. M., Agrawal, H., Sorooshian, A., Padro, L. T., Gates, H., Hersey, S., Welch, W. A., Jung, H., Miller, J. W., Cocker, III, D. R., Nenes, A., Jonsson, H. H., Flagan, R. C., and Seinfeld, J. H. (2009), Comprehensive simultaneous shipboard and airborne characterization of exhaust from a modern container ship at sea, *Environ. Sci. Technol.*, *43*, 4626–4640,doi:{10.1021/es802413j}.

Nehrkorn, T., Eluszkiewicz, J., Wofsy, S. C., Lin, J. C., Gerbig, C., Longo, M., and Freitas, S. (2010): Coupled weather research and forecasting-stochastic time-inverted lagrangian transport (WRF-STILT) model, *Met. Atmos. Phys*, *107*, 51–64,doi:{10.1007/s00703-010-0068-x}.

Neuman, J., Huey, L., Dissly, R., Fehsenfeld, F., Flocke, F., Holecek, J., Holloway, J., Hubler, G., Jakoubek, R., Nicks, D., Parrish, D., Ryerson, T., Sueper, D., and Weinheimer, A. (2002), Fast-response airborne in situ measurements of HNO3 during the Texas 2000 Air Quality Study, *J. Geophys. Res.-Atmos.*, *107*, doi:{10.1029/2001JD001437}.

Neuman, J., Nowak, J., Brock, C., Trainer, M., Fehsenfeld, F., Holloway, J., Hubler, G., Hudson, P.,

Murphy, D., Nicks, D., Orsini, D., Parrish, D., Ryerson, T., Sueper, D., Sullivan, A., and Weber, R. (2003), Variability in ammonium nitrate formation and nitric acid depletion with altitude and location over California, *J. Geophys. Res.-Atmos.*, *108*,doi:{10.1029/2003JD003616}.

Neuman, J. A., Trainer, M., Aikin, K. C., Angevine, W. M., Brioude, J., Brown, S. S., de Gouw, J. A., Dube, W. P., Flynn, J. H., Graus, M., Holloway, J. S., Lefer, B. L., Nedelec, P., Nowak, J. B., Parrish, D. D., Pollack, I. B., Roberts, J. M., Ryerson, T. B., Smit, H., Thouret, V., and Wagner, N. L. (2012), Observations of ozone transport from the free troposphere to the Los Angeles basin, *J. Geophys. Res.-Atmos.*, *117*, doi:{10.1029/2011JD016919}.

Nolte, C. G., Bhave, P. V., Arnold, J. R., Dennis, R. L., Zhang, K. M., and Wexler, A. S. (2008), Modeling urban and regional aerosols - Application of the CMAQ-UCD Aerosol Model to Tampa, a coastal urban site, *Atmos. Environ.*, *42*, 3179–3191,doi:10.1016/j.atmosenv.2007.12.059.

Nowak, J. B., Neuman, J. A., Bahreini, R., Brock, C. A., Middlebrook, A. M., Wollny, A. G., Holloway, J. S., Peischl, J., Ryerson, T. B., and Fehsenfeld, F. C. (2010), Airborne observations of ammonia and ammonium nitrate formation over Houston, Texas, *J. Geophys. Res.-Atmos.*, *115*, doi:{10.1029/2010JD014195}.

Nowak, J. B., J. A. Neuman, R. Bahreini, A. M. Middlebrook, J. S. Holloway, S. A. McKeen, D. D. Parrish, T. B. Ryerson, and M. K. Trainer (2012), Ammonia sources in the California South Coast Air Basin and their impact on ammonium nitrate formation, *J. Geophys. Res.-Lett.*, *39*, doi:{10.1029/2012GL051197}.

Olivier, J.G.J. and J.J.M. Berdowski (2001), Global emissions sources and sinks. In: Berdowski, J., Guicherit, R. and B.J. Heij (eds.) The Climate System, pp. 33-78. A. A. Balkema Publishers/Swets and Zeitlinger Publishers, Lisse, The Netherlands., 2001.

Otte, T. L., and Pleim, J. E. (2010), The Meteorology-Chemistry Interface Processor (MCIP) for the CMAQ modeling system: updates through MCIPv3.4.1, *Geosci. Model Dev.*, *3*, 243–256, doi:10.5194/gmd-3-243-2010

Palau, J., Perez-Landa, G., Melia, J., Segarra, D., and Millan, M. (2006), A study of dispersion in complex terrain under winter conditions using high-resolution mesoscale and Lagrangian particle models, *Atmos. Chem. Phys.*, *6*, 1105–1134.

Park, R., Jacob, D., Field, B., Yantosca, R., and Chin, M.: Natural and transboundary pollution influences on sulfate-nitrate-ammonium aerosols in the United States (2004), Implications for policy, *J. Geophys. Res.-Atmos.*, *109*,doi:{10.1029/2003JD004473}.

Parrish, D. D., Allen, D. T., Bates, T. S., Estes, M., Fehsenfeld, F. C., Feingold, G., Ferrare, R., Hardesty, R. M., Meagher, J. F., Nielsen-Gammon, J. W., Pierce, R. B., Ryerson, T. B., Seinfeld, J. H., and Williams, E. J. (2009), Overview of the Second Texas Air Quality Study (TexAQS II) and the Gulf of Mexico Atmospheric Composition and Climate Study (GoMACCS), *J. Geophys. Res.-Atmos.*, *114*,doi:{10.1029/2009JD011842}.

Pastor, S., Allen, J., Hughes, L., Bhave, P., Cass, G., and Prather, K. (2003), Ambient single particle analysis in Riverside, California by aerosol time-of-flight mass spectrometry during the SCOS97-NARSTO, *Atmos. Environ.*, *37*, S239–S258,doi:10.1016/S1352-2310(03)00393-5.

Paulot, F., Crounse, J. D., Kjaergaard, H. G., Kroll, J. H., Seinfeld, J. H., and Wennberg, P. O. (2009a), Isoprene photooxidation: new insights into the production of acids and organic nitrates, *Atmos. Chem. Phys.*, *9*, 1479–1501.

Paulot, F., Crounse, J. D., Kjaergaard, H. G., Kuerten, A., St Clair, J. M., Seinfeld, J. H., and Wennberg, P. O. (2009b), Unexpected epoxide formation in the gas-phase photooxidation of isoprene, *Science*, *325*, 730–733, doi:10.1126/science.1172910.

Pekney, N. J., Davidson, C. I., Bein, K. J., Wexler, A. S., and Johnston, M. V.: Identification of sources of atmospheric PM at the Pittsburgh Supersite, Part I (2006), Single particle analysis and filter-based positive matrix factorization, *Atmos. Environ.*, *40*, S411–S423, doi:10.1016/j.atmosenv.2005.12.072.

Pfister, G. G., Parrish, D. D., Worden, H., Emmons, L. K., Edwards, D. P., Wiedinmyer, C.,

Diskin, G. S., Huey, G., Oltmans, S. J., Thouret, V., Weinheimer, A., and Wisthaler, A. (2011), Characterizing summertime chemical boundary conditions for airmasses entering the US West Coast, *Atmos. Chem. Phys.*, *11*, 1769–1790,doi:{10.5194/acp-11-1769-2011}.

Pueschel, R. F., D. F. Blake, K. G. Snetsinger, A. D. A. Hansen, S. Verma, and K. Kato (1992), Black carbon (soot) aerosol in the lower stratosphere and upper troposphere, *Geophys. Res. Lett.*, *19*(16), 1659–1662,doi:10.1029/92GL02478.

Pun, B. K., Seigneur, C., Bailey, E. M., Gautney, L. L., Douglas, S. G., Haney, J. L., and Kumar, N. (2008), Response of atmospheric particulate matter to changes in precursor emissions: A comparison of three air quality models, *Environ. Sci. Technol.*, *42*, 831–837, doi:10.1021/es702333d.

Querol, X., Pey, J., Minguillon, M. C., Perez, N., Alastuey, A., Viana, M., Moreno, T., Bernabe, R. M., Blanco, S., Cardenas, B., Vega, E., Sosa, G., Escalona, S., Ruiz, H., and Artinano, B. (2008), PM speciation and sources in Mexico during the MILAGRO-2006 Campaign, *Atmos. Chem. Phys.*, *8*, 111–128.

Ramanathan, V. and Carmichael, G. (2008), Global and regional climate changes due to black carbon, *Nat. Geosci.*, *1*, 221–227,doi:{10.1038/ngeo156}.

Reff, A., Bhave, P.V., Simon, H., Pace, T.G., Pouliot, G.A., Mobley, J.D., Houyoux, M. (2009), Emissions inventory of PM2.5 trace elements across the United States, *Environ. Sci. Technol.*, *43*, 5790-5796, doi::10.1021/es802930x.

Renner, E. and Wolke, R. (2010), Modelling the formation and atmospheric transport of secondary inorganic aerosols with special attention to regions with high ammonia emissions, *Atmos. Environ.*, *44*, 1904–1912, doi:{10.1016/j.atmosenv.2010.02.018}.

Roberts, J. M.,Veres, P.,Warneke, C.,Neuman, J. A., Washenfelder, R. A., Brown, S. S., Baasandorj, M., Burkholder, J. B., Burling, I. R., Johnson, T. J., Yokelson, R. J., de Gouw, J. (2010), Measurement of HONO, HNCO, and other inorganic acids by negative-ion proton-transfer chemical-

ionization mass spectrometry (NI-PT-CIMS): Application to biomass burning emissions, *Atmos. Meas. Tech.*, *3*, 981-990, doi:{10.5194/amt-3-981-2010}.

Salcedo, D., Onasch, T., Dzepina, K., Canagaratna, M., Zhang, Q., Huffman, J., DeCarlo, P., Jayne, J., Mortimer, P., Worsnop, D., Kolb, C., Johnson, K., Zuberi, B., Marr, L., Volkamer, R., Molina, L., Molina, M., Cardenas, B., Bernabe, R., Marquez, C., Gaffney, J., Marley, N., Laskin, A., Shutthanandan, V., Xie, Y., Brune, W., Lesher, R., Shirley, T., and Jimenez, J. (2006), Characterization of ambient aerosols in Mexico City during the MCMA-2003 campaign with Aerosol Mass Spectrometry: results from the CENICA Supersite, *Atmos. Chem. Phys.*, *6*, 925–946.

Sarwar, G. and Bhave, P. V. (2007), Modeling the effect of chlorine emissions on ozone levels over the eastern United States, *J. Appl. Met. Clim.*, *46*, 1009–1019,doi:{10.1175/JAM2519.1}.

Schafer, K., Emeis, S. M., Rauch, A., and Vogt, C. (2004), Determination of mixing layer heights from ceilometer data, *Remote Sens. Clouds Atmos.*, *5571*, 248–259,doi:10.1117/12.565592.

Schwarz, J. P., Gao, R. S., Fahey, D. W., Thomson, D. S., Watts, L. A., Wilson, J. C., Reeves, J. M., Darbeheshti, M., Baumgardner, D. G., Kok, G. L., Chung, S. H., Schulz, M., Hendricks, J., Lauer, A., Kaercher, B., Slowik, J. G., Rosenlof, K. H., Thompson, T. L., Langford, A. O., Loewenstein, M., and Aikin, K. C. (2006), Single-particle measurements of midlatitude black carbon and light-scattering aerosols from the boundary layer to the lower stratosphere, *J. Geophys. Res.-Atmos.*, *111*, doi:{10.1029/2006JD007076}.

Schwarz, J. P., Spackman, J. R., Fahey, D. W., Gao, R. S., Lohmann, U., Stier, P., Watts, L. A., Thomson, D. S., Lack, D. A., Pfister, L., Mahoney, M. J., Baumgardner, D., Wilson, J. C., and Reeves, J. M. (2008), Coatings and their enhancement of black carbon light absorption in the tropical atmosphere, *J. Geophys. Res.-Atmos.*, *113*, doi:{10.1029/2007JD009042}.

Shiraiwa, M., Kondo, Y., Moteki, N., Takegawa, N., Sahu, L. K., Takami, A., Hatakeyama, S., Yonemura, S., and Blake, D. R. (2008), Radiative impact of mixing state of black carbon aerosol in Asian outflow, *J. Geophys. Res.-Atmos.*, *113*, D24210, doi:10.1029/2008JD010546.

Seinfeld, J. and Pandis, S. (2006), Atmospheric chemistry and physics: from air pollution to climate change (Second Edition), John Wiley and Sons, Inc..

Stein, A. F., Saylor, R. D. (2012), Sensitivities of sulfate aerosol formation and oxidation pathways on the chemical mechanism employed in simulations *Atmos. Chem. Phys.*, *12*, 8567–8574, doi: 10.5194/acp-12-8567-2012.

Stephens, M., Turner, N., and Sandberg, J. (2003), Particle identification by laser-induced incandescence in a solid-state laser cavity, *Appl. Optics.*, *42*, 3726–3736,doi:{10.1364/AO.42.003726}.

Stohl, A., Forster, C., Frank, A., Seibert, P., and Wotawa, G. (2005), Technical note: The Lagrangian particle dispersion model FLEXPART version 6.2, *Atmos. Chem. Phys.*, *5*, 2461–2474.

Turpin, B. and Huntzicker, J. (1991), Secondary formation of organic aerosol in the Los Angeles Basin - A descriptive analysis of organic and elemental carbon concentrations, *Atmos. Environ.*, *25*, 207–215,doi:10.1016/0960-1686(91)90291-E.

van der Kamp, D. and McKendry, I.: Diurnal and seasonal trends in convective mixed-layer heights estimated from two years of continuous ceilometer observations in Vancouver, BC (2010), *Bound.-Lay. Meteorol.*, *137*, 459475, doi:10.1007/s10546-010-9535-7.

Van Pelt, R. S. and Zobeck, T. M. (2007), Chemical constituents of fugitive dust, *Environ. Monit. Assess.*, *130*, 3–16, doi::10.1007/s10661-006-9446-8.

van Pinxteren, D., Brueggemann, E., Gnauk, T., Iinuma, Y., Mueller, K., Nowak, A., Achtert, P., Wiedensohler, A., and Herrmann, H. (2009), Size- and time-resolved chemical particle characterization during CAREBeijing-2006: Different pollution regimes and diurnal profiles, *J. Geophys. Res.-Atmos.*, *114*,doi:{10.1029/2008JD010890}.

Wang, K., Zhang, Y., Nenes, A., and Fountoukis, C. (2012), Implementation of dust emission and chemistry into the Community Multiscale Air Quality modeling system and initial application to an Asian dust storm episode *Atmos. Chem. Phys. Disc.*, `http://www.atmos-chem-phys-discuss.net/12/13457/2012/acpd-12-13457-2012-discussion.html`

Walcek, C. and Taylor, G. (1986), A theoretical method for computing vertical distributions of acidity and sulfate production within cumulus clouds, *J. Atmos. Sci.*, *43*, 339–355, doi:{10.1175/1520-0469(1986)043⟨0339:ATMFCV⟩2.0.CO;2}.

Washenfelder, R. A., Trainer, M., Frost, G. J., Ryerson, T. B., Atlas, E. L., de Gouw, J. A., Flocke, F. M., Fried, A., Holloway, J. S., Parrish, D. D., Peischl, J., Richter, D., Schauffler, S. M., Walega, J. G., Warneke, C., Weibring, P., and Zheng, W. (2010), Characterization of NO(x), SO(2), ethene, and propene from industrial emission sources in Houston, Texas, *J. Geophys. Res.-Atmos.*, *115*,doi:{10.1029/2009JD013645}.

Watson, J., Chow, J., LU, Z., Fujita, E., Lowenthal, D., Lawson, D., and Ashbaugh, L. (1994), Chemical mass-balance source apportionment of pm(10) during the Southern California air-quality study, *Aerosol. Sci. Tech.*, *21*, 1–36,doi:10.1080/02786829408959693.

Wittig, A., Anderson, N., Khlystov, A., Pandis, S., Davidson, C., and Robinson, A. (2004), Pittsburgh air quality study overview, *Atmos. Environ.*, *38*, 3107–3125,doi:{10.1016/j.atmosenv.2004.03.003}.

Wunch, D., P. O. Wennberg, G. C. Toon, G. Keppel-Aleks, and Y. G. Yavin (2009), Emissions of greenhouse gases from a North American megacity, *Geophys. Res. Lett.*, *36*, L15810, doi:10.1029/2009GL039825.

Yue, D., Hu, M., Wu, Z., Wang, Z., Guo, S., Wehner, B., Nowak, A., Achtert, P., Wiedensohler, A., Jung, J., Kim, Y. J., and Liu, S. (2009), Characteristics of aerosol size distributions and new particle formation in the summer in Beijing, *J. Geophys. Res.-Atmos.*, *114*, doi:{10.1029/2008JD010894}.

Yue, D. L., Hu, M., Zhang, R. Y., Wang, Z. B., Zheng, J., Wu, Z. J., Wiedensohler, A., He, L. Y., Huang, X. F., and Zhu, T. (2010), The roles of sulfuric acid in new particle formation and growth in the mega-city of Beijing, *Atmos. Chem. Phys.*, *10*, 4953–4960, doi:{10.5194/acp-10-4953-2010}.

Zhang, Y., Liu, P., Pun, B., Seigneur, C. (2006), A comprehensive performance evaluation

of MM5-CMAQ for the Summer 1999 Southern Oxidants Study episode - Part I: Evaluation protocols, databases, and meteorological predictions, *Atmos. Environ.*, *40*, 4825-4838, doi: :10.1016/j.atmosenv.2005.12.043.

Zhang, H. and Ying, Q. (2010), Source apportionment of airborne particulate matter in Southeast Texas using a source-oriented 3D air quality model, *Atmos. Environ.*, *44*, 3547–3557,doi:{10.1016/ j.atmosenv.2010.06.004}.

Zhang, J., Chameides, W., Weber, R., Cass, G., Orsini, D., Edgerton, E., Jongejan, P., and Slanina, J.: An evaluation of the thermodynamic equilibrium assumption for fine particulate composition (2002), Nitrate and ammonium during the 1999 Atlanta Supersite Experiment, *J. Geophys. Res.-Atmos.*, *108*,doi:10.1029/2001JD001592.

Zheng, J., Hu, M., Zhang, R., Yue, D., Wang, Z., Guo, S., Li, X., Bohn, B., Shao, M., He, L., Huang, X., Wiedensohler, A., and Zhu, T. (2011), Measurements of gaseous H(2)SO(4) by AP-ID-CIMS during CAREBeijing 2008 Campaign, *Atmos. Chem. Phys.*, *11*, 7755–7765, doi:{10. 5194/acp-11-7755-2011}.

Table 4.1: Statistical metrics based on measurements and predictions at the Pasadena ground site during May 2010.

Parameter	N	ME	MB	NME	NMB
PBL Height (m)	1179	129	-80	0.14	-0.09
Temperature (k)	24697	1.88	1.06		
RH (%)	24697	11.6	-10.3		
BC (μg m^{-3})	3918	0.190	0.0261	0.478	0.0660
SO_4^{2-} (μg m^{-3})	1860	0.93	-0.36	0.44	-0.17
NO_3^- (μg m^{-3})	1860	2.15	-1.50	0.72	-0.50
NH_4^+ (μg m^{-3})	1860	1.07	-0.76	0.35	-0.25
SO_2 (ppbv)	22491	0.72	0.64	2.50	2.01
HNO_3 (ppbv)	22761	0.98	-0.38	0.85	-0.38
NH_3 (ppbv)	366	1.51	0.45	0.74	0.22

ME = Mean Error, MB = Mean Bias, NME = Normalized Mean Error, NMB = Normalized Mean Bias. N is the number of data points collected during May 2010.

Table 4.2: Statistical metrics based on measured and predicted temperature and relative humidity for Twin Otter and P3 flights during May 2010.

Flight Date	N	ME [°C]	MB [°C]
Temperature (Twin Otter)			
21	189	3.89	3.88
24	167	3.33	3.32
25	334	2.21	2.21
27	219	1.55	-1.23
28	239	0.75	-0.23
Temperature (P3)			
4	17219	2.12	0.60
8	25439	2.10	1.60
14	22258	3.77	3.33
16	27899	2.17	0.92
19	24239	1.67	0.71
Flight Date	N	ME [%]	MB [%]
Relative Humidity (Twin Otter)			
21	189	26.7	-26.6
24	167	9.99	-9.13
25	334	5.76	-5.12
27	219	10.5	5.67
28	239	7.16	-0.33
Relative Humidity (P3)			
4	17219	12.3	-0.47
8	25439	14.6	-1.00
14	22258	24.9	-22.1
16	27899	16.1	-7.91
19	24239	8.89	-2.49

ME = Mean Error, MB = Mean Bias. N is the number of data points collected during a given flight.

Table 4.3: Statistical metrics based on measured and predicted wind magnitudes and directions for Twin Otter and P3 flights during May 2010.

Flight Date	N	ME [m/s]	MB [m/s]	NME	NMB
Wind Magnitudes (Twin Otter)					
21	180	1.89	1.19	0.38	0.23
24	167	1.79	-0.61	0.36	-0.12
25	334	1.89	0.49	0.37	0.10
27	219	2.04	0.98	0.56	0.27
28	239	2.00	2.11	0.55	0.52
Wind Magnitudes (P3)					
4	17219	2.33	-0.48	0.48	-0.10
8	25439	2.15	1.06	0.27	0.14
14	22258	1.69	0.57	0.55	0.19
16	27899	2.10	-0.26	0.41	-0.05
19	24239	4.03	-2.63	0.48	-0.31

Flight Date	N	ME [deg]	$\overline{\theta}_{\mathrm{obs}}$ [deg]	$\overline{\theta}_{\mathrm{mod}}$ [deg]
Wind Directions (Twin Otter)				
21	180	23.8	242	254
24	167	40.7	228	253
25	334	28.8	209	223
27	219	36.9	225	242
28	239	22.5	240	246
Wind Directions (P3)				
4	17219	64.0	263	239
8	25439	24.2	263	276
14	22258	65.1	203	206
16	27899	54.5	224	230
19	24239	25.2	278	267

ME = Mean Error, MB = Mean Bias, NME = Normalized Mean Error, NMB = Normalized Mean Bias, and $\overline{\theta}$ = average wind direction. N is the number of data points collected during a given flight. The wind directions θ_{obs} and θ_{mod} are the observed and modeled wind directions, respectively, in units of degrees ($0° \leq \theta \leq 360°$). Wind direction, θ, is defined as the direction from which the wind is blowing, and is measured in degrees clockwise from true north.

Table 4.4: Statistical metrics based on measured and predicted black carbon concentrations, at all altitudes and below 1000 m above sea level, for Twin Otter flights and P3 flights during May 2010.

Flight Date	N	ME [μg m^{-3}]	MB [μg m^{-3}]	NME	NMB
Black Carbon (Twin Otter, all altitudes)					
21	8537	0.23	0.19	1.08	0.90
24	6503	0.13	0.13	1.16	1.04
25	8256	0.13	0.11	0.84	0.70
27	8133	0.12	0.09	0.73	0.53
28	8700	0.14	0.11	0.79	0.60
5-flight average	40129	0.15	0.12	0.91	0.74
Black Carbon (Twin Otter, below 1000 m a.s.l.)					
21	6794	0.27	0.25	1.20	1.09
24	4117	0.17	0.16	1.26	1.16
25	5406	0.16	0.14	0.89	0.78
27	8133	0.12	0.09	0.73	0.53
28	8656	0.14	0.11	0.80	0.60
5-flight average	33106	0.171	0.14	0.936	0.782
Black Carbon (P3, all altitudes)					
4	16923	0.07	0.00	0.58	0.01
8	25257	0.08	0.04	0.74	0.32
14	18974	0.14	0.05	0.83	0.30
16	21273	0.10	0.07	1.32	1.01
19	23610	0.08	-0.03	0.47	-0.12
5-flight average	106037	0.09	0.03	0.79	0.31
Black Carbon (P3, below 1000 m a.s.l.)					
4	3527	0.13	-0.04	0.48	-0.13
8	11184	0.13	0.09	0.75	0.52
14	10803	0.16	0.02	0.62	0.09
16	9791	0.08	0.06	0.60	0.40
19	7518	0.17	-0.12	0.40	-0.27
5-flight average	42823	0.13	0.02	0.60	0.19

ME = Mean Error, MB = Mean Bias, NME = Normalized Mean Error, NMB = Normalized Mean Bias. N is the number of data points collected during a given flight.

Table 4.5: Relative contributions to predicted sulfate concentrations at the Pasadena ground site averaged over 15-30 May 2010.

Sulfate Pathway	Predicted contribution (%)
Boundary inflow	26
Aq, O_3	6
Aq, H_2O_2	29
Aq, O_2 (FEMN)	4
Gas, OH	7
Primary SO_4^{2-}	28

"Boundary inflow" refers to sulfate attributable to boundary conditions, "(Aq,Gas),O_x" refers to secondary sulfate produced by aqueous-phase (Aq) or gas-phase (Gas) oxidation of SO_2 by oxidant O_x. "Primary SO_4^{2-}" refers to sulfate emitted within the basin. "FEMN" refers to catalysts Fe^{3+} and Mn^{2+}.

Table 4.6: Statistical metrics based on measured and predicted particulate sulfate, ammonium, and nitrate concentrations for Twin Otter and P3 flights during May 2010.

Twin Otter						**P3**					
Flight Date	N	ME [μg m^{-3}]	MB [μg m^{-3}]	NME	NMB	Flight Data	N	ME [μg m^{-3}]	MB [μg m^{-3}]	NME	NMB
Sulfate						**Sulfate**					
21	185	1.30	1.30	2.68	2.68	4	1722	0.26	0.24	0.79	0.71
24	172	0.28	0.27	0.84	0.82	8	2544	0.41	0.20	0.65	0.32
25	337	0.39	0.39	1.11	1.11	14	2226	0.47	0.16	0.59	0.20
27	224	0.50	0.44	0.62	0.55	16	2790	0.33	0.00	0.33	0.00
28	244	0.53	0.46	0.77	0.65	19	2424	0.20	0.02	0.33	0.02
Ammonium						**Ammonium**					
21	185	0.92	-0.77	0.62	-0.52	4	1722	0.23	-0.11	0.77	-0.36
24	172	0.29	-0.14	0.68	-0.33	8	2544	0.27	-0.17	0.65	-0.42
25	337	0.54	-0.51	0.60	-0.56	14	2226	0.33	-0.15	0.64	-0.28
27	224	0.59	-0.47	0.46	-0.36	16	2790	0.47	-0.38	0.65	-0.52
28	244	0.42	-0.20	0.46	-0.22	19	2424	0.70	-0.65	0.71	-0.65
Nitrate						**Nitrate**					
21	185	1.64	-1.47	0.73	-0.65	4	1722	0.50	-0.31	0.99	-0.62
24	172	0.80	-0.50	0.84	-0.52	8	2544	0.51	-0.38	0.93	-0.68
25	337	1.17	-0.94	0.72	-0.58	14	2226	0.62	-0.37	0.91	-0.55
27	224	1.24	-0.85	0.52	-0.35	16	2790	0.94	-0.77	0.94	-0.76
28	244	0.93	-0.37	0.61	-0.24	19	2424	2.03	-1.99	0.80	-0.78

Table 4.7: Statistical metrics based on measured and predicted ammonia and nitric acid mixing ratios for P3 flights during May 2010.

P3					
Flight Date	N	ME [ppbv]	MB [ppbv]	NME	NMB
Nitric Acid					
4	17219	0.92	-0.54	0.46	-0.27
8	25439	0.86	0.15	0.56	0.09
14	22258	2.50	2.32	1.96	1.82
16	27899	0.60	0.09	0.41	0.06
19	24239	0.96	-0.31	0.46	-0.15
Ammonia					
4	17219	2.96	-2.00	0.81	-0.55
8	25439	3.37	-3.00	0.98	-0.60
14	22258	3.80	-3.11	0.72	-0.59
16	27899	2.78	-2.05	0.86	-0.63
19	24239	12.38	-12.31	0.91	-0.90
Ammonia (no dairy)					
4	17219	1.39	-0.15	0.78	-0.09
8	25439	2.17	-1.98	0.60	-0.55
14	22258	1.25	-0.83	0.47	-0.31
16	27899	0.82	-0.34	0.77	-0.32
19	24239	2.80	-2.73	0.67	-0.68

Statistical metrics based on ammonia measurements in the "no dairy" column are calculated excluding all data points east of longitude 117.7°W.

Table 4.8: Speciation of primary PM_{fine} and PM_{coarse} emissions into Ca^{2+}, K^{+}, and Mg^{2+}.

Fine Mode Species	*Reff et al.* (2009)
Ca^{2+}	0.0386×A25J
K^{+}	0.0309×A25J
Mg^{2+}	0.00368×A25J
Coarse Mode Species	**CMAQv5.0[a]**
Ca^{2+}	0.0838×ASOIL + 0.0562×ACORS
K^{+}	0.0242×ASOIL + 0.0176×ACORS
Mg^{2+}	0.0000×ASOIL + 0.0032×ACORS

[a] ASOIL = $0.9 \times PM_{coarse}$, ACORS = $0.1 \times PM_{coarse}$, A25J = PM_{fine}

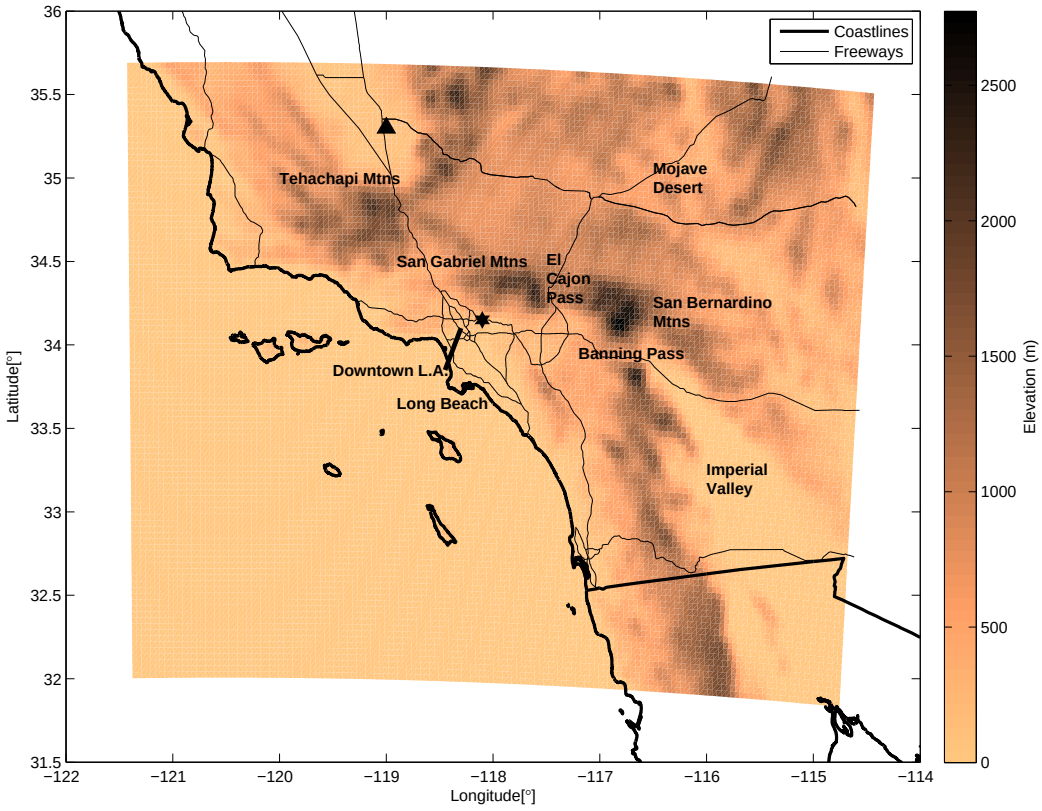

Figure 4.1: CMAQ modeling domain (colored area) used for simulations during the CalNex Field Campaign. The domain covers the area from (31.83°N, 121.43°W) to (35.69°N, 114.43°W) with 4 km x 4 km horizontal grid cells (102 x 156 grid points). The star represents the Pasadena ground site and the triangle represents Bakersfield.

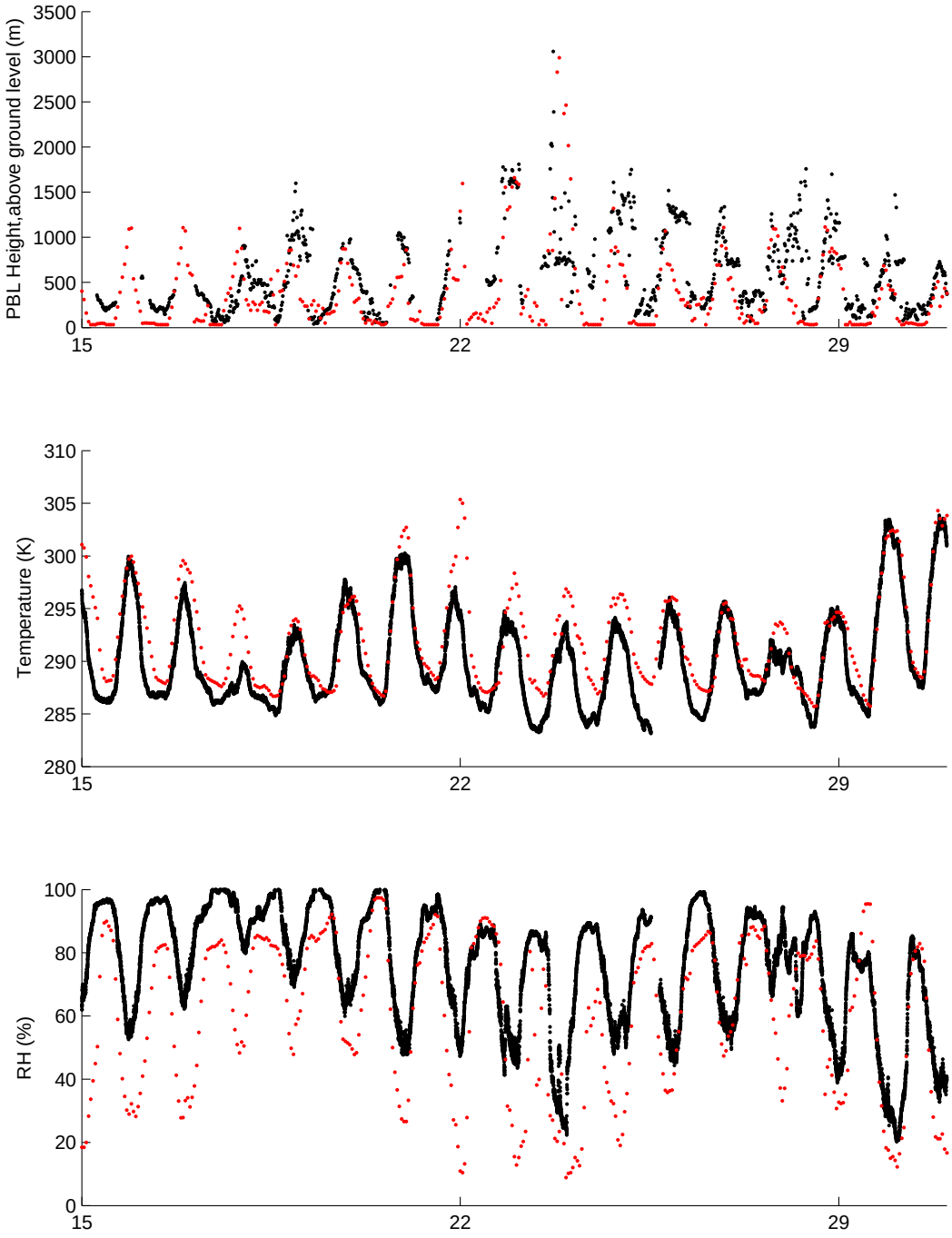

Figure 4.2: Observed (black) and predicted (red) planetary boundary layer (PBL) heights, temperature, and relative humidity (RH) from the Pasadena ground site.

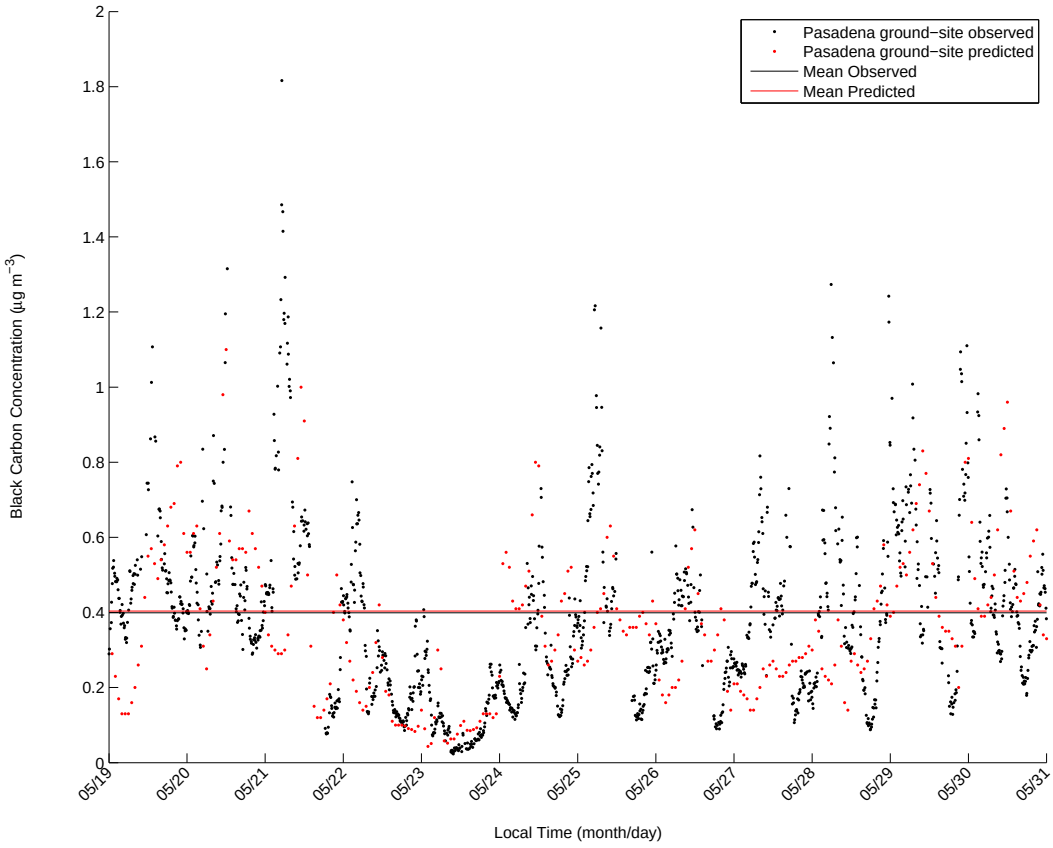

Figure 4.3: Measured (black dots) and predicted (red dots) BC concentrations at the Pasadena ground site from 19 May – 31 May 2010.

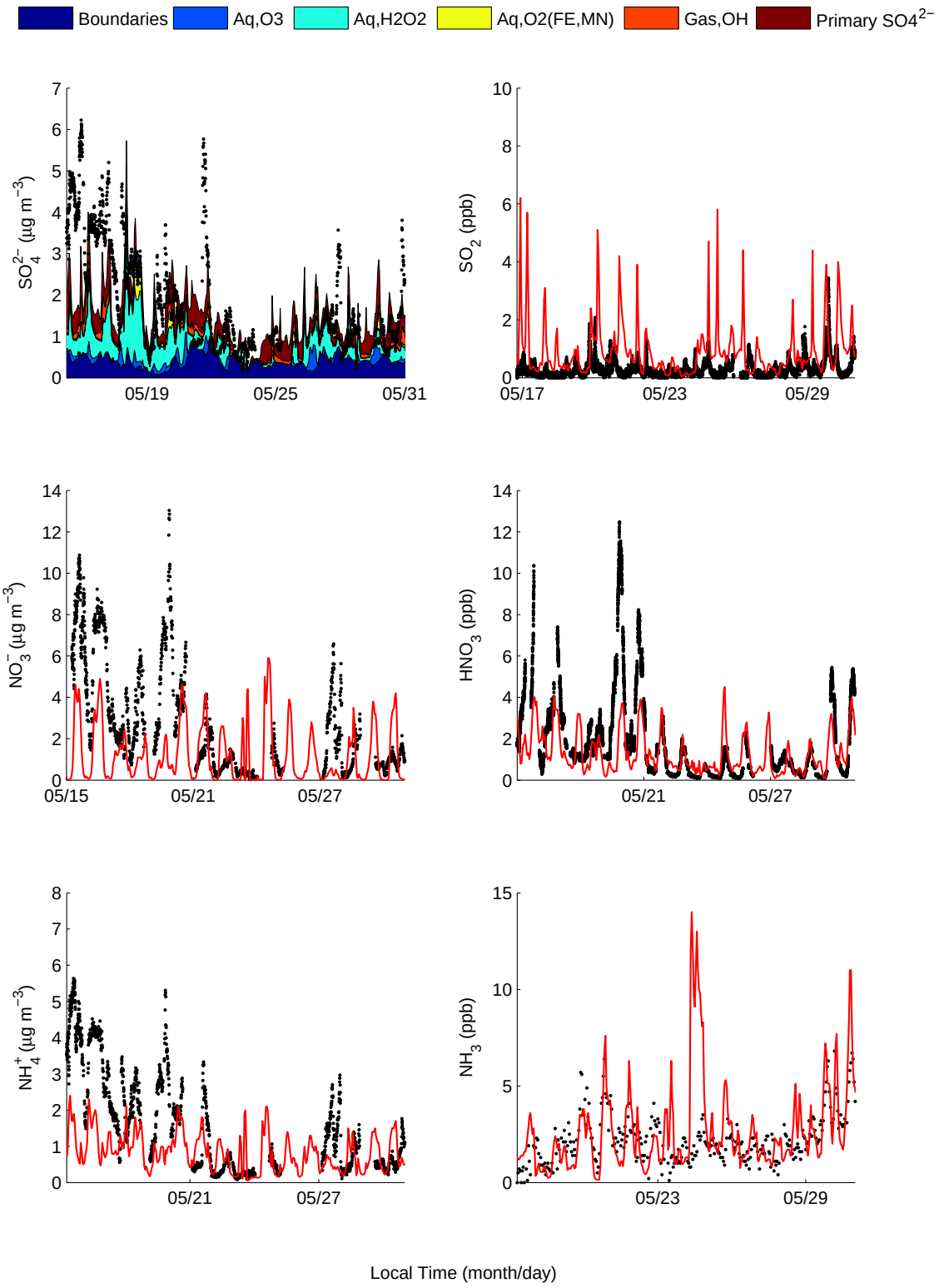

Figure 4.4: Observed (black) and predicted (red) particulate sulfate, nitrate, ammonium, sulfur dioxide, nitric acid, and ammonia concentrations from the CalNex Pasadena ground site. In the legend, "Boundaries" refers to sulfate attributable to boundary conditions, "(Aq,Gas),O_x" refers to secondary sulfate produced by aqueous-phase (Aq) or gas-phase (Gas) oxidation of SO_2 by oxidant O_x. "Primary SO_4^{2-}" refers to sulfate emitted within the basin.

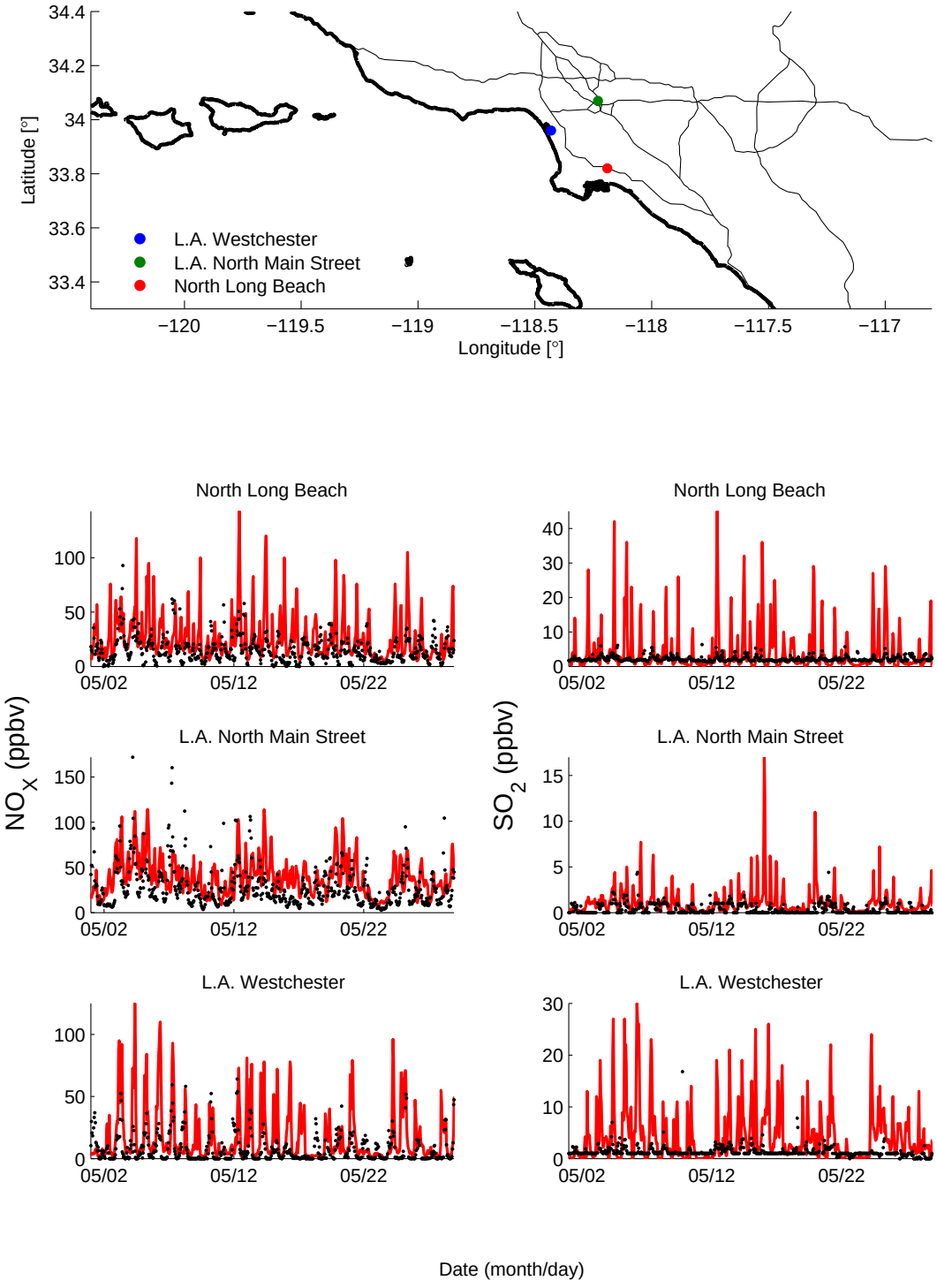

Figure 4.5: Measured (black) and predicted (red) NO_x and SO_2 mixing ratios for May 2010 at three locations in the Los Angeles Basin. Gaseous measurements were taken from the Air Quality and Meteorological Information System (AQMIS, `http://www.arb.ca.gov/aqmis2/aqmis2.php`).

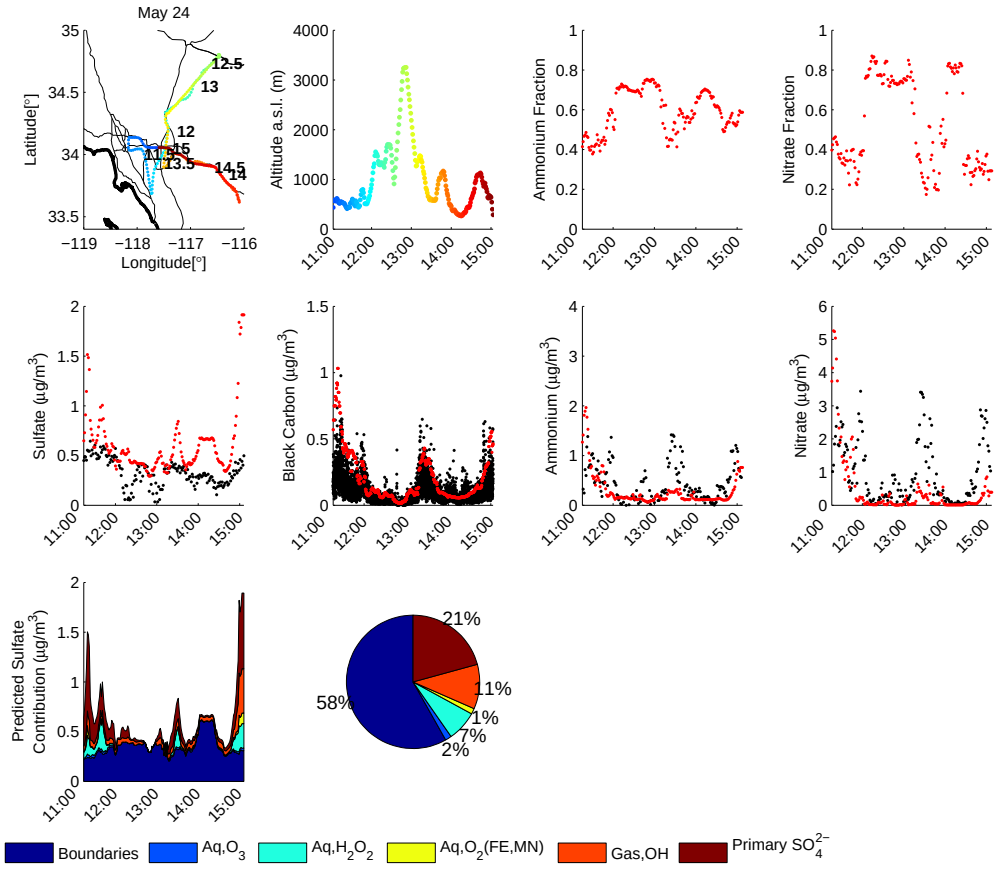

Figure 4.6: From left to right and top to bottom: Twin Otter aircraft flight path for May 24, Twin Otter altitudes (with respect to sea level) with the flight track and altitude trace are colored by the time (Pacific Standard Time) of day and time-stamps printed along each flight path in 30 min increments, Fraction of predicted particulate ammonium within the AMS transmission window, Fraction of predicted particulate nitrate within the AMS transmission window, predicted (red) and observed (black) sulfate concentrations, predicted (red) and observed (black) black carbon concentrations, predicted (red) and observed (black) nitrate concentrations, predicted (red) and observed (black) ammonium concentrations, predicted sulfate source apportionment, Pie chart indicating the relative contribution from routes to sulfate averaged over a given flight. In the bottom legend, "Boundaries" refers to sulfate attributable to boundary conditions, "(Aq,Gas),O_x" refers to secondary sulfate produced by aqueous-phase (Aq) or gas-phase (Gas) oxidation of SO_2 by oxidant O_x. "Primary SO_4^{2-}" refers to sulfate emitted within the basin.

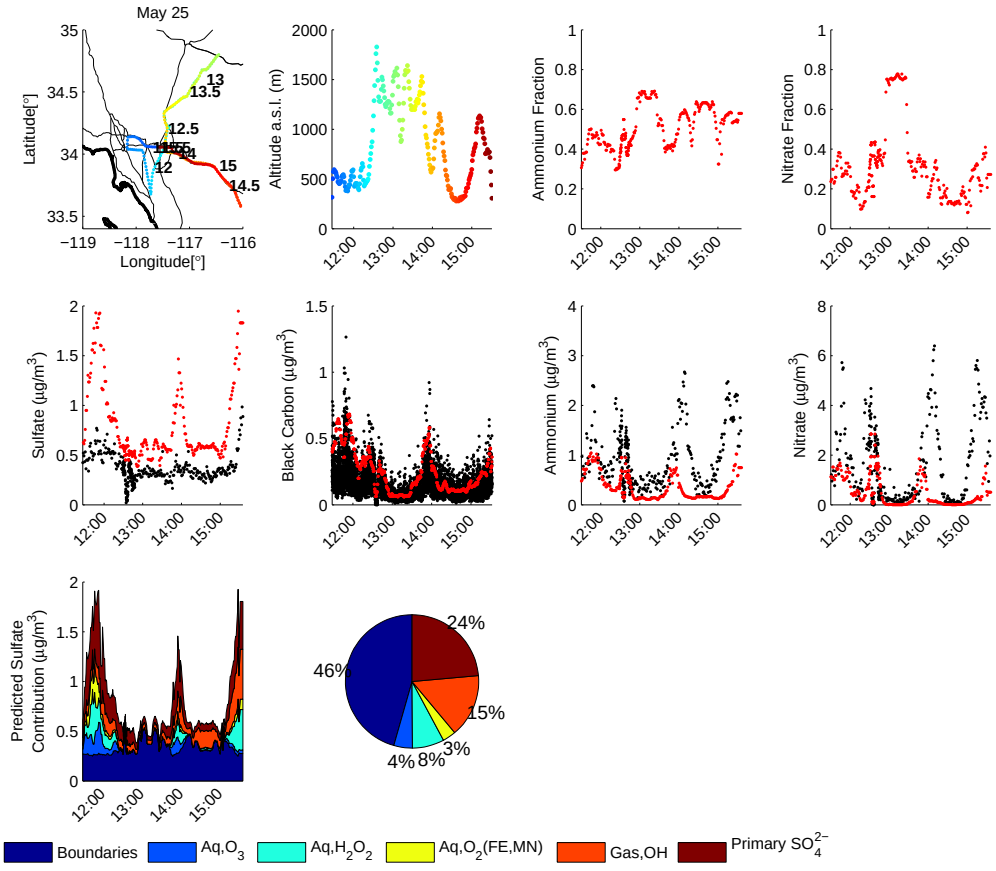

Figure 4.7: Same as Figure 4.6, but for the Twin Otter May 25 flight.

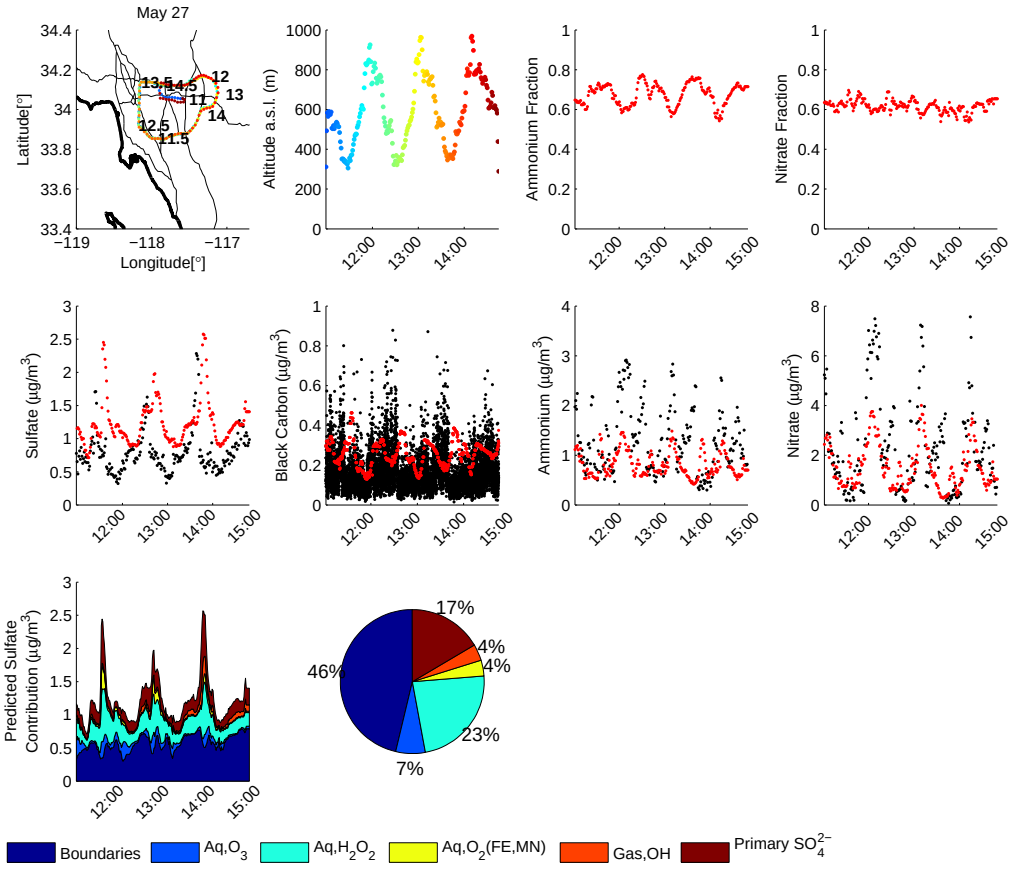

Figure 4.8: Same as Figure 4.6, but for the Twin Otter May 27 flight.

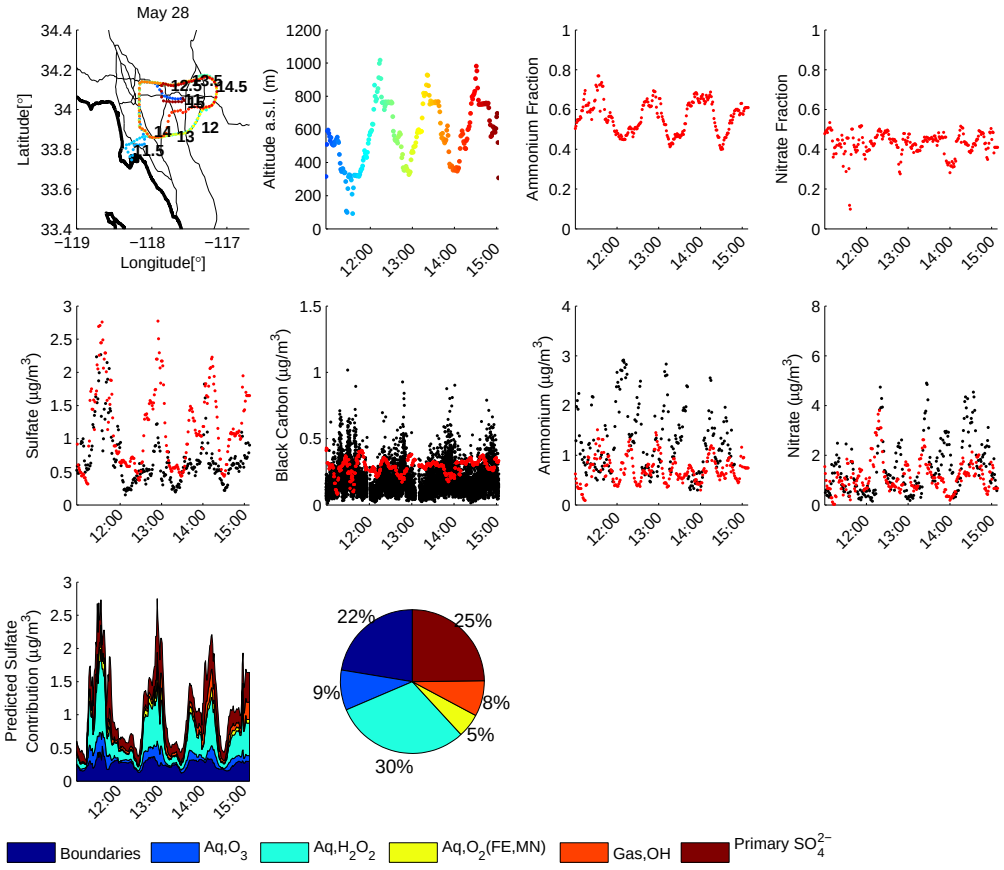

Figure 4.9: Same as Figure 4.6, but for the Twin Otter May 28 flight.

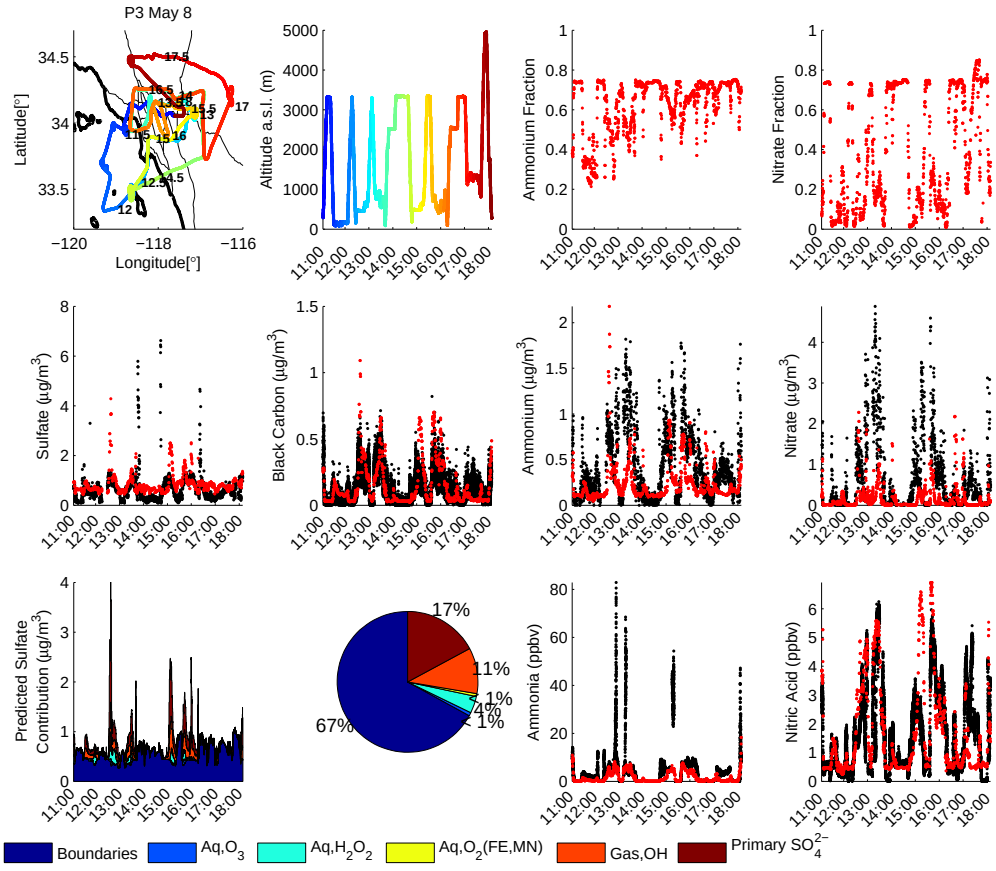

Figure 4.10: From left to right and top to bottom: P3 aircraft flight path for May 8, P3 altitudes (with respect to sea level) with the flight track and altitude trace are colored by the time (Pacific Standard Time) of day and time-stamps printed along each flight path in 30 min increments, Fraction of predicted particulate ammonium within the AMS transmission window, Fraction of predicted particulate nitrate within the AMS transmission window, predicted (red) and observed (black) sulfate concentrations, predicted (red) and observed (black) black carbon concentrations, predicted (red) and observed (black) nitrate concentrations, predicted (red) and observed (black) ammonium concentrations, predicted sulfate source apportionment, Pie chart indicating the relative contribution from routes to sulfate averaged over a given flight. In the bottom legend, "Boundaries" refers to sulfate attributable to boundary conditions, "(Aq,Gas),O_x" refers to secondary sulfate produced by aqueous-phase (Aq) or gas-phase (Gas) oxidation of SO_2 by oxidant O_x. "Primary SO_4^{2-}" refers to sulfate emitted within the basin.

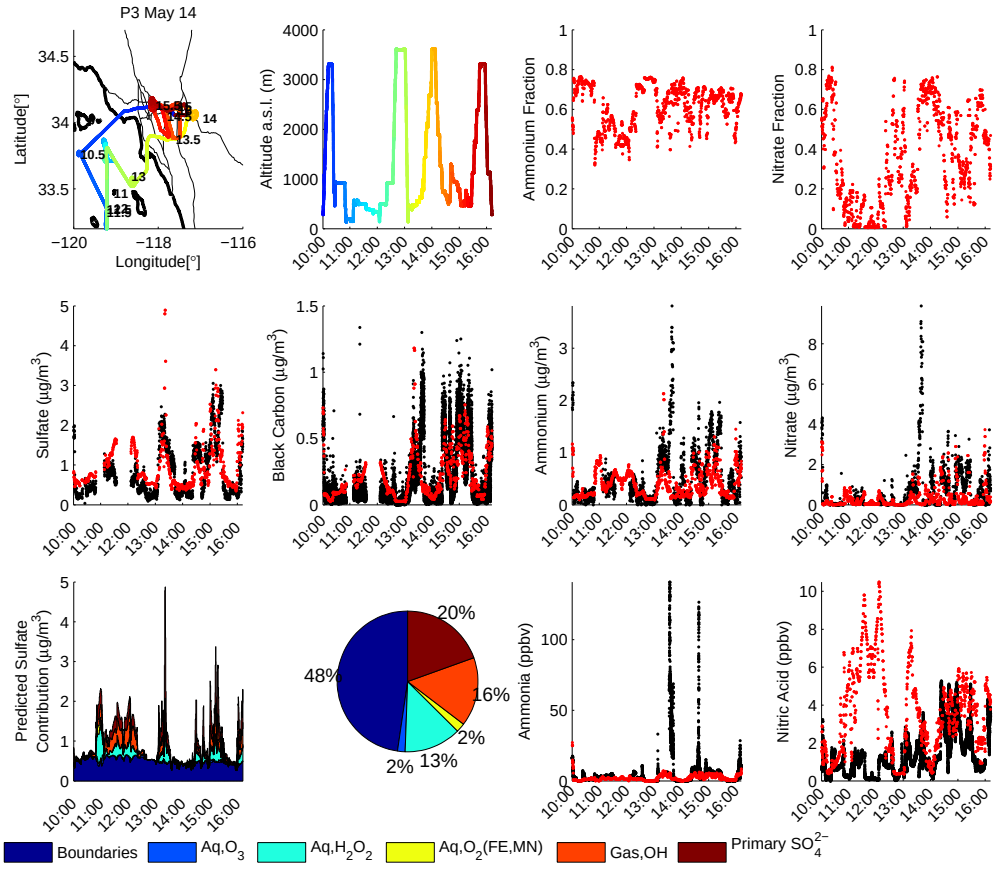

Figure 4.11: Same as Figure 4.10, but for the P3 May 14 flight.

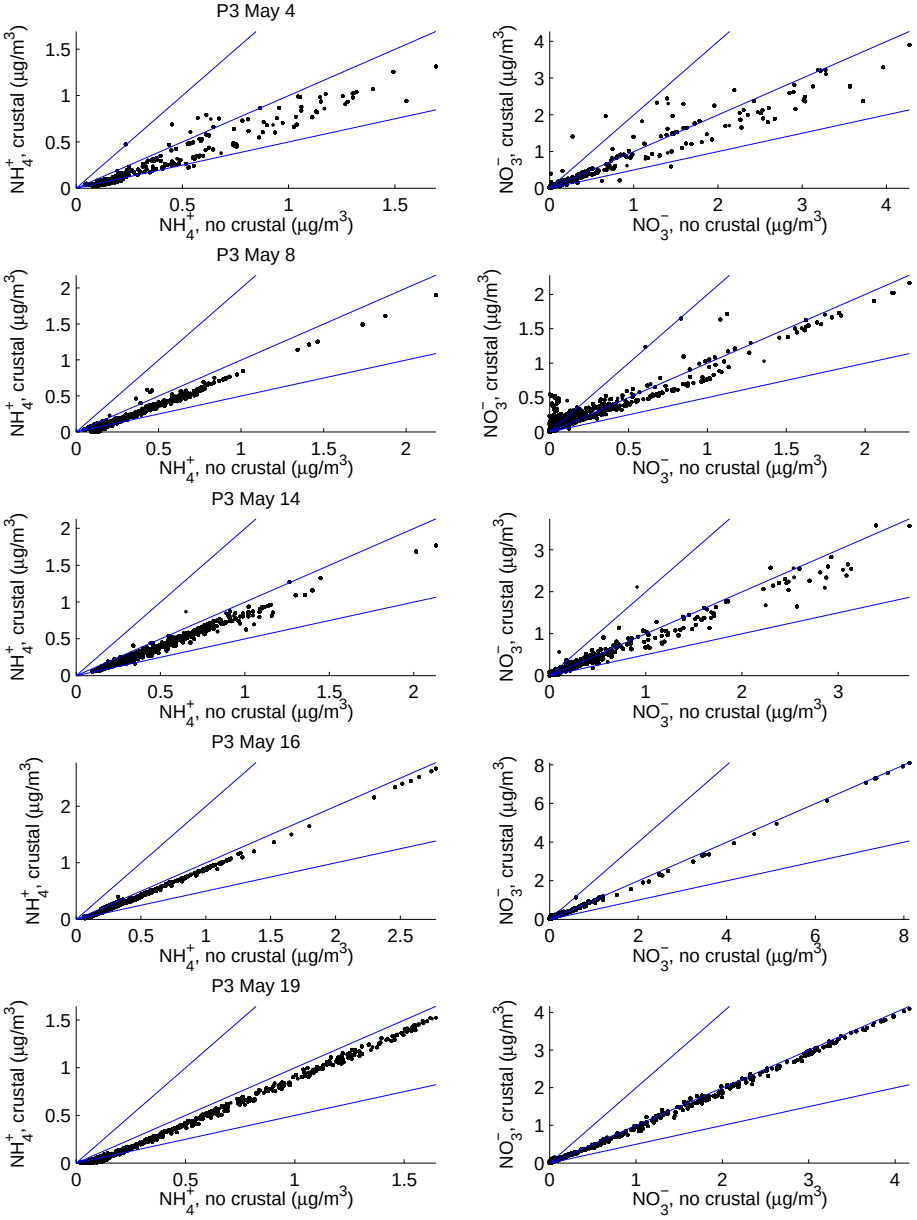

Figure 4.12: Scatter plots showing predicted ammonium and nitrate concentrations, with and without crustal species, along five P3 flight paths. Ammonium and nitrate predictions have been corrected to account for the transmission window of the AMS. The 1–1, 1–2, and 2–1 lines are included for reference.

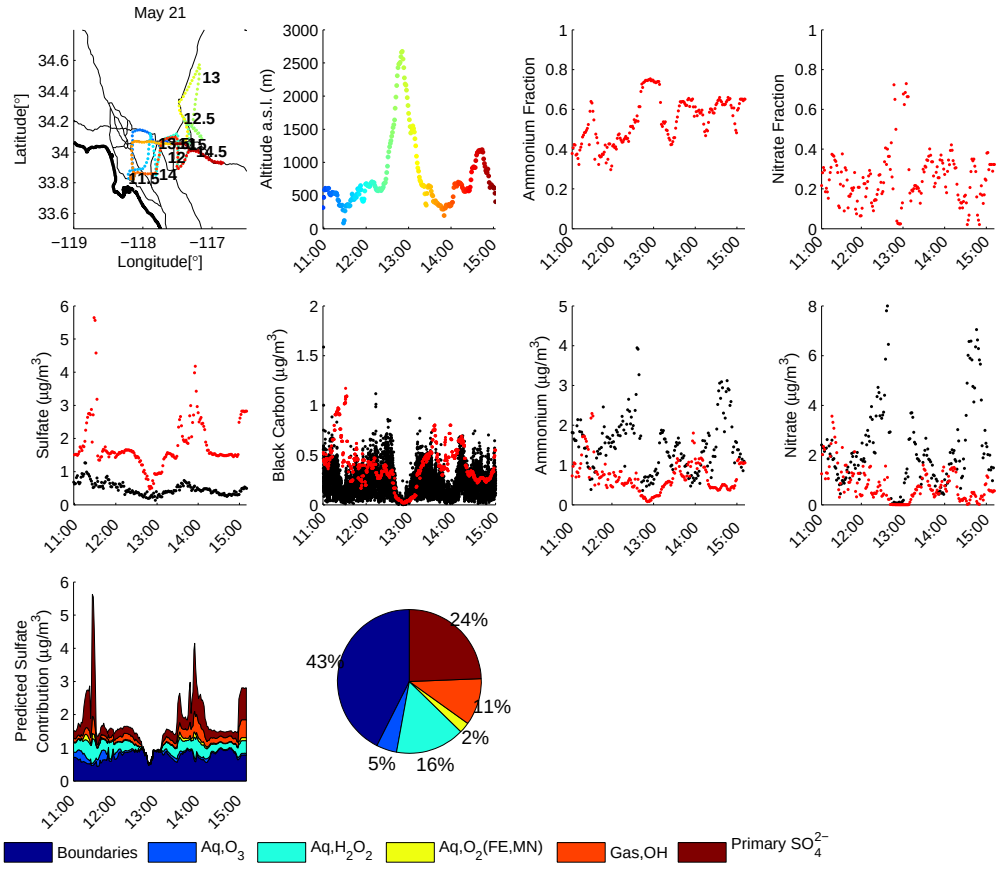

Figure 4.13: Same as Figure 4.6, but for the Twin Otter May 21 flight.

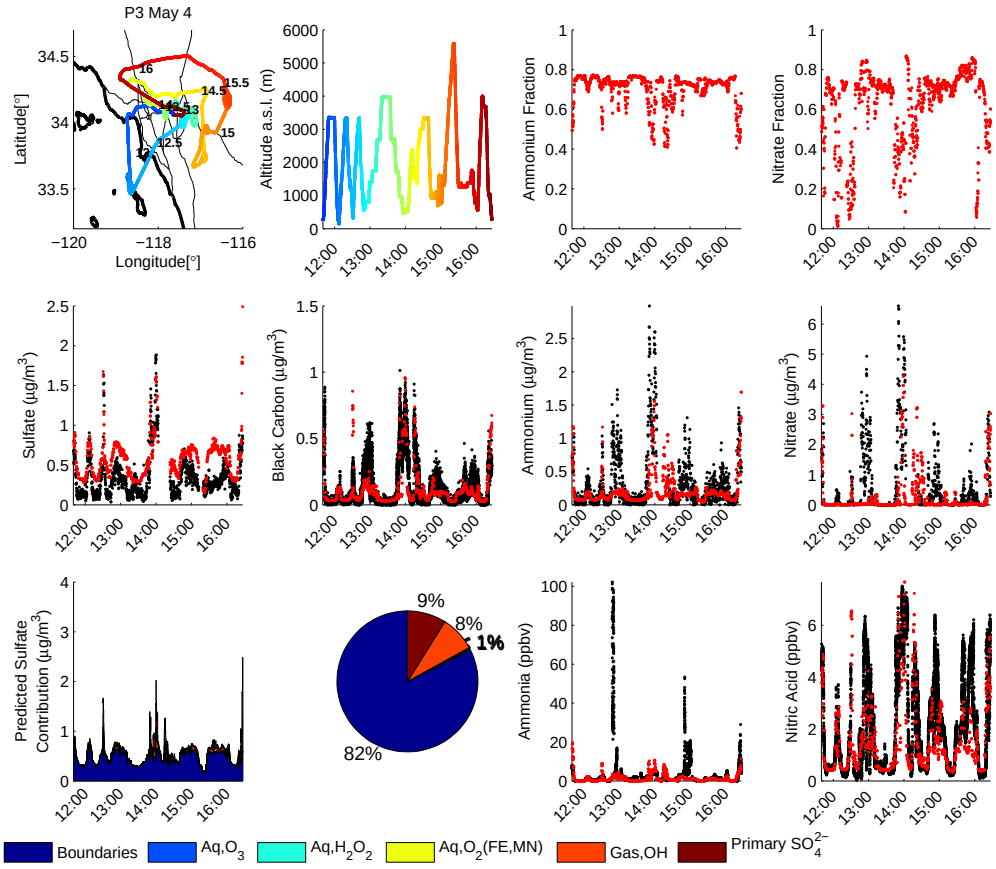

Figure 4.14: Same as Figure 4.10, but for the P3 May 4 flight.

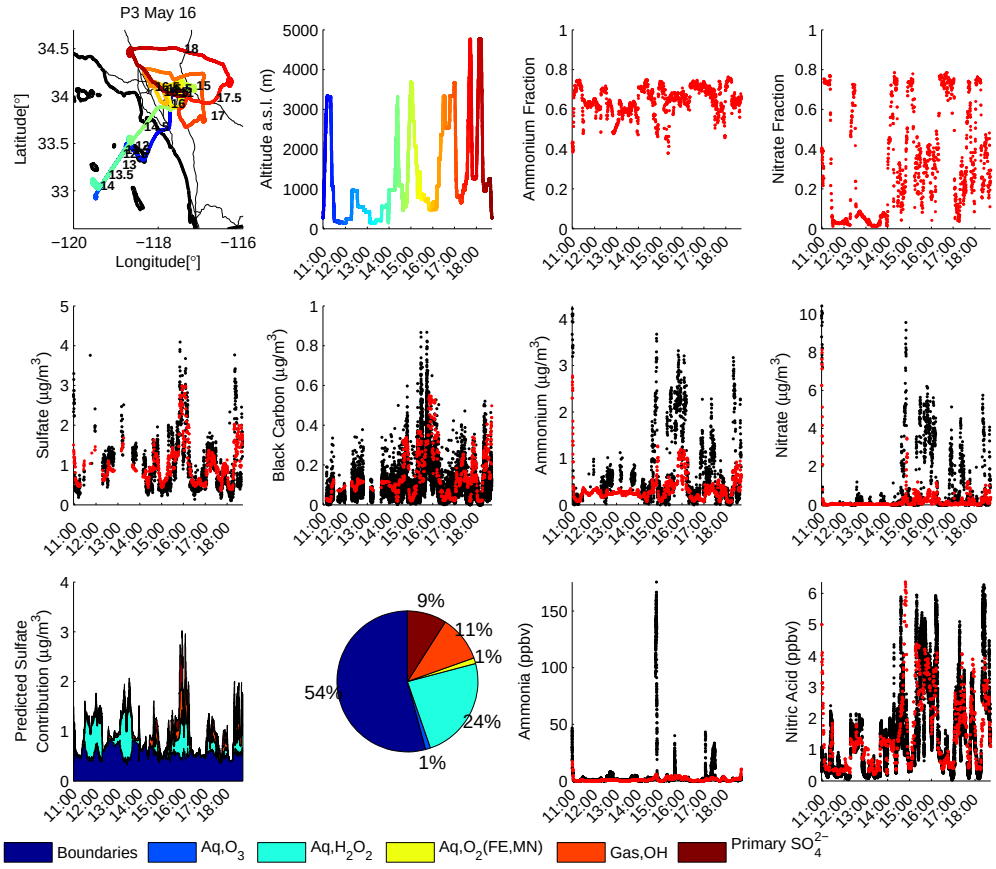

Figure 4.15: Same as Figure 4.10, but for the P3 May 16 flight.

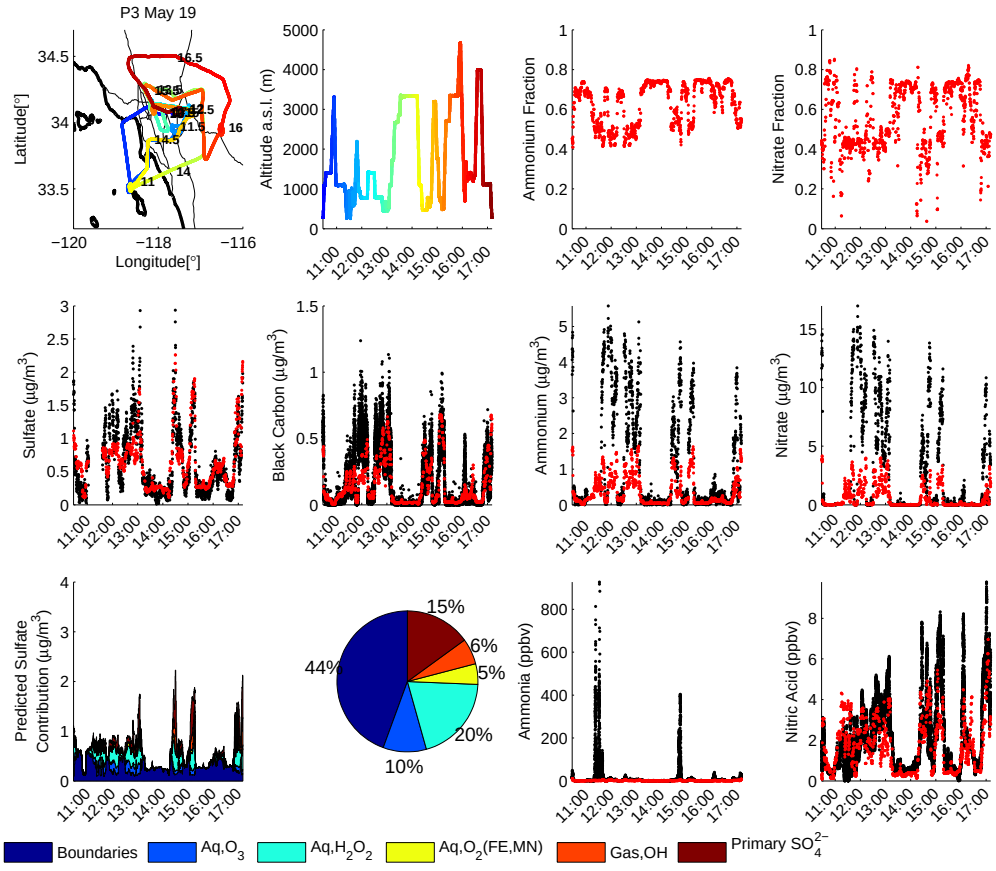

Figure 4.16: Same as Figure 4.10, but for the P3 May 19 flight.

Chapter 5

Conclusions and Future Work

Unless derived from first principles, numerical models are only as accurate as the experiments on which they are based. Results presented in Chapter 2 and Appendix A suggest that, owing to loss of vapors directly to laboratory chamber walls, SOA mass yields derived from laboratory chamber experiments are biased low by up to a factor of 4. Furthermore, predictions from the Statistical Oxidation Model of *Cappa and Wilson* (2012) suggest that this bias could be as high as a factor of ∼8, provided the influence of the chamber walls could be removed entirely. This finding likely explains the persistent underprediction of ambient SOA concentrations by current atmospheric models in urban areas, which are based on chamber experiments, as well as recent contradictory findings regarding the relative contribution of emissions from gasoline- and diesel-fueled vehicles to the formation of SOA in Southern California. Specifically, since the conclusions of *Bahreini et al.* (2012) and *Hayes et al.* (2013) are not based on SOA mass yields derived from chamber experiments, whereas the conclusions of *Gentner et al.* (2012) and *Gordon et al.* (2013) are, it is likely the gasoline-fueled vehicles are the dominant source of anthropogenic SOA attributable attributable of fossil activity. However, the results presented in Appendix A include toluene only. Therefore, future work should most certainly include a comprehensive reevaluation of SOA yields from all anthropogenic VOC classes (e.g. single-ring aromatics, polycyclic aromatics, alkanes, alkenes, and oxygenated compounds) using the new experimental protocols. SOA mass yields for biogenic species (e.g. isoprene, monoterpenes, and sesquiterpenes) should also be reevaluated.

Although the traditional Odum 2-product SOA parameterization will likely perform better when

based on updated chamber data, a growing body of evidence suggests that the assumptions on which the Odum 2-product framework is based are simply not valid under ambient conditions (e.g. instantaneous, reversible thermodynamic equilibration, lack of multigenerational oxidation pathways, lack of fragmentation pathways, and lack of particle-phase reaction pathways). Therefore, once vapor-phase wall loss has been accounted for in a new suite of laboratory chamber experiments, the SOA parameterizations within atmospheric chemical transport models should also be updated. Specifically, significant progress has been made in using box models to represent the formation and evolution of SOA. However, little work has focused on bridging the gap between the advanced chemical mechanisms of 2D SOA box models and the strict computational requirements of 3D CTMs. In Chapter 3, a novel mathematical framework, termed the Oxidation State/Volatility Moment Method, designed to address this issue is presented. Various numerical experiments suggest that the Moment Method is a promising mathematical framework for combining 2D SOA models with 3D CTMS. However, the Numeric Drift Test revealed that inexact fitting of symmetric distributions to skewed distributions introduces an unacceptable amount of error when the DEF procedure is repeated several times. Two strategies (Moment-Bin Hybrid & Grid Coarsening) for overcoming this numerical drift limitation were discussed qualitatively. Future work should focus on (1) removing the error introduced by inexact fitting followed by thermodynamic partitioning, (2) assessing how the Moment Method performs when gas-phase oxidation/fragmentation chemistry is included, (3) testing alternative 1D probability distributions (not just log-normal and gamma distributions), and (4) quantitatively assessing the Moment-Bin Hybrid & Grid Coarsening approaches as compared to the explicit 2D-VBS.

Finally, a detailed comparison of predictions from the Community Multiscale Air Quality (CMAQ version 4.7.1) model to a suite of airborne and ground-based meteorological measurements, gas- and aerosol-phase inorganic measurements, and black carbon (BC) measurements revealed the following:

- BC predictions are consistently higher than observations onboard the Twin Otter, which is at least partially due to a systematic bias inherent to the SP2 onboard. However, predicted and observed BC concentrations and $\Delta BC/\Delta CO$ ratios along P3 flight paths suggests that no

systematic bias exists in the ARCTAS-CARB BC emission inventory or the MM5 meteorology.

- With the current sulfur emission inventory based on emission factors from 2008, long-range transport of sulfate accounts for a substantial fraction (22-82%) of the sulfate in Los Angeles Basin. This suggests that targeting sulfur emissions with the hopes of reducing ambient PM concentrations is not the most effective strategy for Southern California.

- Severely underpredicted NH_3 emissions from dairy facilities, and not the exclusion of crustal species, are the dominant source of measurement/model disagreement in the eastern Los Angeles Basin. Targeting dairy emissions is an effective strategy for reducing ammonium nitrate concentrations in the eastern part of the Los Angeles Basin.

- Despite overstated NO_x emissions, total nitrate concentrations are generally too low. This is most likely attributable to a missing source of HNO_3, or the inaccurate distribution of total nitrate between the gas-phase and the two aerosol modes artificially enhances the removal of nitrate via dry deposition.

Adding gas-phase NH_3 measurements and size-resolved measurements, up to 10 μm, of nitrate and various cations (e.g., Na^+, Ca^{2+}, K^+, Mg^{2+}) to routine monitoring stations in the Los Angeles Basin would facilitate interpreting day-to-day fluctuations in fine and coarse inorganic aerosol greatly. Future work should focus on improving and assessing the treatment of anthropogenic and fugitive dust emissions, as well as continuing to characterize the fraction of ambient particulate matter attributable to local emissions versus long-range transport.

Bibliography

Bahreini, R., Middlebrook, A. M., de Gouw, J. A., Warneke, C., Trainer, M., Brock, C. A., Stark, H., Brown, S. S., Dube, W. P., Gilman, J. B., Hall, K., Holloway, J. S., Kuster, W. C., Perring, A. E., Prevot, A. S. H., Schwarz, J. P., Spackman, J. R., Szidat, S., Wagner, N. L., Weber, R. J., Zotter, P., and Parrish D. D.: Gasoline emissions dominate over diesel in formation of secondary organic aerosol mass, *Geophys. Res. Lett.*, *39*, L06805, 2012.

Cappa, C. and Wilson, K. R. (2012), Multi-generation gas-phase oxidation, equilibrium partitioning, and the formation and evolution of secondary organic aerosol, *Atmos. Chem. Phys.*, *12*, 9505-9528.

Gentner, D. R., Isaacman, G., Worton, D. R., Chan, A. W. H., Dallmann, T. R., Davis, L., Liu, S., Day, D. A., Russell, L. M., Wilson,Weber, R., uha, A., Harley, R. A., and Goldstein A. H.: Elucidating secondary organic aerosol from diesel and gasoline vehicles through detailed characterization of organic carbon emissions, *PNAS*, *109*, 18318–18323, 2012.

Gordon, T. D., Presto, A. A., May, A. A., Nguyen, N. T., Lipsky, E. M., Donahue, N. M., Gutierrez, A., Zhang, M., Maddox, C., Rieger, P., Chattopadhyay, S., Maldonado, H., Maricq, M. M., and Robinson, A. L.: Secondary organic aerosol formation exceeds primary particulate matter emissions for light-duty gasoline vehicles, *Atmos. Chem. Phys.*, *13*, 23173-23216, doi:10.5194/acpd-13-23173-2013, 2013.

Hayes, P. L., Ortega, A. M., Cubison, M. J., Froyd, K. D., Zhao, Y., Cliff, S. S, Hu, W. W., Toohey, D. W, Flynn, J. H., Lefer, B. L., Grossberg, N., Alvarez, S., Rappengluck, B., Taylor, J. W., Allan, J. D., Holloway, J. S., Gilman, J. B., Kuster, W. C., de Gouw, J. A., Massoli, P., Zhang, X., Liu, J., Weber, R. J., Corrigan, A. L., Russell, L. M., Isaacman, G., Worton, D. R., Kreisberg, N. M., Goldstein, A. H., Thalman, R., Waxman, E. M., Volkamer, R., Lin, Y. H., Surratt, J. D., Kleindienst, T. E., Offenberg, J. H., Dusanter, S., Griffith, S., Stevens, P. S., Brioude, J., Angevine, W. M., Jimenez, J. L. : Organic Aerosol Composition and Sources in Pasadena, California during the 2010 CalNex Campaign , *J. Geophys. Res.-Atmos.*, *118*, 2013.

Appendix A

Influence of vapor wall-loss in laboratory chambers on yields of secondary organic aerosol

Title: Influence of vapor wall-loss in laboratory chambers on yields of secondary organic aerosol

Short Title: Vapor wall loss and secondary organic aerosol

Authors: Xuan Zhang[a,1], Christopher D. Cappa[b,1,2], Shantanu Jathar[b], Renee C. McVay[c], Joseph J. Ensberg[c], Michael J. Kleeman[b], and John H. Seinfeld[a,c,2]

Affiliations:

[a] Division of Engineering and Applied Science, California Institute of Technology, Pasadena, CA, USA

[b] Department of Civil and Environmental Engineering, University of California at Davis, Davis, CA, USA

[c] Division of Chemistry and Chemical Engineering, California Institute of Technology, Pasadena, CA, USA

[1]These authors contributed equally to this work.

To whom correspondence should be addressed: cdcappa@ucdavis or seinfeld@caltech.edu

Author contributions: C.D.C., X.Z., J.J.E. and J.H.S. designed research; X. Z. designed and performed the experiments; C.D.C., S. J., R.C.M. and M.J.K. analyzed data; C.D.C., X.Z. and J.H.S. wrote the supplement; and C.D.C. and J.H.S. wrote the paper.

Classification: Physical Sciences – Earth, Atmospheric and Planetary Sciences

Keywords: Secondary organic aerosol; particulate matter; air quality; climate

Abstract

Secondary organic aerosol (SOA) constitutes a major fraction of sub-micrometer atmospheric particulate matter. Quantitative simulation of SOA within air quality and climate models—and its resulting impacts—depends on the translation of SOA formation observed in laboratory chambers into robust parameterizations. Worldwide data have been accumulating indicating that model predictions of SOA are substantially lower than ambient observations. While possible explanations for this mismatch have been advanced, none has addressed the laboratory chamber data themselves. Losses of particles to the walls of chambers are routinely accounted for, but there has been little evaluation of the effects on SOA formation of losses of semi-volatile vapors to chamber walls. Here, we experimentally demonstrate that such vapor losses can lead to substantially underestimated SOA formation, by factors as much as 4. Accounting for such losses has the clear potential to bring model predictions and observations of organic aerosol levels into much closer agreement.

Significance Statement

Atmospheric **s**econdary organic aerosol (SOA) has important impacts on climate and air quality, yet models continue to have difficulty in accurately simulating SOA concentrations. Nearly all SOA models are tied to observations of SOA formation in laboratory chamber experiments. Here, a comprehensive analysis of new experimental results demonstrates that the formation of SOA in laboratory chambers may be substantially suppressed due to losses of SOA-forming vapors to chamber walls, leading to underestimates of SOA in air quality and climate models, especially in urban areas where anthropogenic SOA precursors dominate. This analysis provides a new time-dependent framework for the interpretation of laboratory chamber experiments that will allow for development of parameterized models of SOA formation that are appropriate for use in atmospheric models.

Most of the understanding concerning the formation of secondary organic aerosol (SOA) from atmospheric oxidation of volatile organic compounds (VOCs) over the past 30 years has been developed from data obtained in laboratory chambers (1). SOA is a major component of particulate matter smaller than 1 μm (2) and consequently has important impacts on regional and global climate and human health and welfare. Accurate simulation of SOA formation and abundance within 3D models is critical to quantifying its atmospheric impacts. Measurements of SOA formation in laboratory chambers provide the basis for the parameterizations of SOA formation (3) in regional air quality models and global climate models (4). A number of studies indicate that ambient SOA concentrations are underpredicted within models, often substantially so, when these traditional parameterizations are used (e.g. 5, 6). Some of this bias has been attributed to missing SOA precursors in emissions inventories, such as so-called intermediate volatility organic compounds (IVOCs), to ambient photochemical aging of semi-volatile compounds occurring beyond that in chamber experiments (7) or to aerosol water/cloud processing (8). The addition of a more complete spectrum of SOA precursors into models has not, however, closed the measurement/prediction gap robustly. For example, recent analysis of organic aerosol (OA) concentrations in Los Angeles revealed that observed OA levels, which are dominated by SOA, exceed substantially those predicted by current atmospheric models (9), in accord with earlier findings in Mexico City (10).

Here, we demonstrate that losses of SOA-forming vapors to chamber walls during photooxidation experiments can lead to substantial and systematic underestimation of SOA. Recent experiments have demonstrated that losses of organic vapors to the typically Teflon walls of a laboratory chamber can be substantial (11), but the effects on SOA formation have not yet been quantitatively established. In essence, the walls serve as a large reservoir of equivalent OA mass that compete with the particulate SOA for SOA-forming compounds.

Toluene Photooxidation Experiments

The effect of vapor wall loss on SOA formation has been comprehensively assessed based on results from a series of 18-h toluene photooxidation experiments conducted in the Caltech environmental chamber under both high- and low-NO_x conditions (SI Materials and Methods, Toluene photooxidation experiments, Table S1). Toluene is a component of motor vehicle emissions and an important SOA precursor (1). Initial [VOC]/[NO_x] ratios were 5.4 ± 0.3 ppbC/ppb, similar to current conditions in Los Angeles, CA. In these experiments, the

ratio of initial seed particle surface area (SA) to chamber wall SA was systematically varied by changing the concentration and diameter of $(NH_4)_2SO_4$ seed aerosol while keeping all other conditions the same (i.e. hydroxyl radical (OH) and toluene concentration). In this manner, the influence of seed SA on SOA formation can be isolated.

Figure 1 shows the observed time-dependent SOA yields, defined as the mass of SOA formed per mass of VOC reacted, determined from the evolution of the particle size distributions (Fig. S1) as a function of initial seed SA for the high- and low-NO_x experiments. The SOA concentrations have been corrected for physical deposition of particles to the walls (SI Materials and Methods, Particle wall-loss correction), which is the appropriate correction to use here as our analysis explicitly accounts for loss of vapors to the walls, discussed further below. Except for the unseeded experiment, the SOA yield for each low-NO_x experiment is reasonably constant with time (from 4 to 18 h) and C_{OA} at any given SA. For each high-NO_x experiment there is a clear increase in the yield with C_{OA} and time. The toluene SOA yield at a given C_{OA} is generally lower for high-NO_x than for low-NO_x conditions at a comparable initial seed SA. These differences in the time-dependent yields indicate differences in the chemical pathways leading to SOA formation between low and high-NO_x conditions. Most importantly, the absolute amount of SOA formed for the same initial conditions increases with seed SA, with an indication of a plateau being reached at the highest seed SA. The SOA formed in the unseeded experiments is particularly small. Typical laboratory chamber experiments use initial seed SA < 10^3 μm^2 cm^{-3}, which corresponds to seed-to-wall ratios of <1 x 10^{-3} in most chambers. These experiments definitively demonstrate that SOA yields vary with seed SA. This variability may partially explain some of the differences in SOA yields reported in the literature.

SOA Modeling and the Influence of Vapor Wall-Loss

The increase in yield with seed SA is consistent with loss of vapors to the chamber walls and likely results from an increase in the rate of mass transfer of vapor species to the particles relative to the walls. Quantitative understanding of the role of vapor wall-loss is necessary to characterize the extent to which SOA yields in chamber experiments are underestimated relative to the atmosphere. The loss of "extremely low volatility" organic compounds (EVLOCs) to chamber walls has recently been implicated as important for understanding SOA formation for a different chemical system, α-pinene + O_3 (12, 13). The competition

between vapor condensation to particles versus to chamber walls is quantitatively examined here using a time-dependent, parameterizable model of SOA formation, the statistical oxidation model (SOM) (14, 15) (SI Materials and Methods, The Statistical Oxidation Model). The SOM accounts for vapor wall-losses based on observations showing that wall-losses of semi-volatile species in Teflon chambers are reversible (11). Such wall-loss is modelled dynamically and depends on the equivalent OA mass of the chamber walls (C_w, mg m^{-3}), the first-order vapor wall-loss rate coefficient (k_w, s^{-1}), and the vapor saturation concentration of compounds i (C_i^*, μg m^{-3}). k_w reflects the combined effects of turbulent mixing in the chamber, molecular diffusion of vapor molecules through the near-wall boundary layer, and any penetration into chamber walls. k_w is likely to be chamber-specific, as the extent of turbulent mixing depends on specific chamber operating conditions, but is reasonably independent of compound identity (11). Values of k_w for a range of gases were estimated in one study (16) to range from ~ 2 x 10^{-5} - 10^{-3} s^{-1}, corresponding to timescales of many hours to 10 minutes. The largest k_w values are appropriate only for chambers with active mixing, which the Caltech chamber does not have (SI Materials and Methods, Vapor wall-loss). Observations (11) suggest that C_w varies somewhat with compound identity, ranging from ~2-24 mg m^{-3}, compared to chamber OA concentrations that are usually 1-3 orders of magnitude smaller; a value of 10 mg m^{-3} is used here as the base-case. Gas-particle partitioning is modelled dynamically assuming absorptive partitioning, including correction for noncontinuum effects and imperfect accommodation, the latter of which is characterized by the mass accommodation coefficient, α. The accommodation coefficient reflects the overall transfer of vapor molecules into the particle bulk, and is likely dependent on the chemical make-up of both the vapor and particle phases and processes that occur at the particle surface. This formulation is more general than most previous analyses of SOA formation in environmental chambers, which typically assume instantaneous gas-particle equilibrium.

Optimal values for k_w and α have been determined for the sets of low- and high-NO_x experiments by comparing observed and simulated best-fit time-dependent C_{OA} profiles for a wide range of k_w and α. The k_w/α pair that provides for the best overall agreement with the time-dependent SOA formation observed across all experiments at a given NO_x condition, excluding the nucleation experiments, is considered the optimal solution (Fig. 2a-b) (SI Materials and Methods, Optimizing k_w and α, Fig. S3). For low-NO_x experiments, the

optimal k_w = 2.5 x 10^{-4} s^{-1} and α = 2 x 10^{-3}. The independently determined values for high-NO_x experiments are similar: k_w = 2.5 x 10^{-4} s^{-1} and α = 1 x 10^{-3}. The simulations provide good overall agreement with the observed seed SA dependence only for a combination of a small α and a $k_w \sim O(10^{-4})$ s^{-1}, indicating that both parameters are important to describing chamber SOA formation. (It should be noted that a reasonable fit for an individual experiment can be obtained for many k_w/α pairs, including when instantaneous gas-particle equilibrium is assumed, i.e. when α = 1. This is not meant to imply that the absolute values of these parameters are not important, but that only in analyzing the combined data sets at multiple seed SA can optimal k_w and α values be uniquely established.) The determined optimal k_w values are consistent with theoretical estimates SI Materials and Methods, Vapor wall-loss, Fig. S4) and some observations (11), but larger than some previous observations in the Caltech chamber (17), most likely reflecting the limited time resolution of those observations, which might not have allowed for separation of filling and mixing of the chamber from wall-loss, but potentially also reflecting differences between chemical systems.

The small optimal α values required to reproduce the observed seed SA dependence likely reflect mass-transfer limitations within the particle phase, which can occur for highly viscous SOA particles (18). When $\alpha \sim 10^{-3}$, mass accommodation is relatively slow and the vapors and particles cannot be assumed to be in instantaneous equilibrium. The timescale associated with reaching gas-particle equilibrium ($\tau_{g\text{-}p,eqm}$) varies with seed SA and size (SI Materials and Methods, Gas-particle partitioning timescales, Fig. S5). Given $\alpha = 10^{-3}$, $\tau_{g\text{-}p,eqm}$ ranges from ~230 min for the smallest seed SA to only ~30 min for the largest seed SA. Thus, at the smallest seed SA $\tau_{g\text{-}p,eqm}$ is similar to the timescale determined for gas wall-loss ($1/k_w$ = 67 min) and the influence of gas wall-loss is more pronounced.

Importantly, loss of condensable vapors to the chamber walls leads to a low-bias in the observed SOA formed even for the experiments with the highest seed SA. To quantitatively assess this bias, simulations have been performed using the best-fit SOM parameters determined for the optimal k_w/α pair above, but with k_w = 0 (no wall-loss). The ratio $R_{wall} = C_{SOA}(k_w=0)/C_{SOA}(k_{w,optimal})$ has been calculated for each experiment and quantifies the bias in the SOA yield due to traditionally unaccounted for vapor wall-losses. The magnitude of R_{wall} depends on the experiment considered, decreasing with increasing seed SA and reaching a plateau at large seed SA (Fig. 2c). For the seeded experiments, R_{wall} averaged over the period

when C_{OA} > 0.5 μg m^{-3} varied from 3.6 (±0.6) to 2.1 (±0.2) for low-NO_x and from 4.2 (±0.9) to 2.1 (±0.2) for high-NO_x in going from lowest to highest seed SA, and where the uncertainties are one standard deviation over the averaging period. These ratios correspond to end-of-experiment corrected mass yields of 1.6 (low-NO_x) and 0.93 (high-NO_x), substantially exceeding the values currently used in chemical transport models for toluene (~0.47 for low-NO_x and ~0.12 for high-NO_x (4)). Given an O:C ratio for toluene + OH SOA of ~0.7 (19), the carbon yields would be 0.94 (low-NO_x) and 0.55 (high-NO_x). (The calculated end of experiment O:C are 0.67 (low-NO_x) and 0.91 (high-NO_x).) This implies that ~6% and ~55% of the product carbon mass remains in the gas-phase for low and high-NO_x conditions, respectively. The oxidation process is a balance between functionalization and fragmentation. In the absence of fragmentation, the carbon yield would asymptote to 100%. The low-NO_x carbon yield in the absence of vapor wall loss is close to 100% and the SOA yield is approximately independent of the total OA mass, which together indicate that fragmentation plays only a minor role. Fragmentation is comparably more important under high-NO_x conditions.

Interestingly, R_{wall} values similar to those determined for the optimal k_{wall}/α pair are obtained when vapor wall-loss is accounted for (i.e. $k_w \neq 0$) but when it is assumed that $\alpha = 1$ (i.e. that gas-particle equilibration is effectively instantaneous) during fitting of each individual experiment (Fig. 2c), This indicates that the magnitude of α is not key to fitting of an individual experiment, but when the experiments are taken together as a combined dataset α is indeed key to matching the observed dependence on seed surface area. Related, α is not key to there being an influence of vapor wall-loss on the overall SOA yield, which is controlled more-so by the magnitude of k_w. The finding that large R_{wall} values are obtained even when $\alpha = 1$ indicates that the general conclusions here regarding vapor wall-loss are robust with respect to knowledge of α. This is important because other chemical systems might not exhibit as slow mass accommodation but could still be affected by vapor wall-loss. Clearly, loss of condensable vapors to the chamber walls can suppress SOA yields relative to those that are relevant for the atmosphere.

Dependence on Experimental Conditions

For a given chamber the extent to which vapor wall loss affects SOA yield will depend on the combination of (i) the rate of oxidation and duration of a given experiment, (ii) the

precursor VOC concentration, (iii) the particular chemical pathways associated with oxidation of a given species, i.e. the precursor identity, and (iv) the seed SA. This is illustrated for the toluene low-NO_x system by carrying out a series of 18 h simulations where [OH] is varied from 1-100 x 10^6 molecules cm^{-3} and $[toluene]_{initial}$ from 1-300 ppb for a seed SA = 1000 μm^2 cm^{-3} using the SOM parameters and optimal k_w/α determined above. The calculated R_{wall} varies with oxidant and precursor concentration (actually, VOC loss rate), with smaller R_{wall} when oxidation is faster and at larger precursor VOC concentration (Fig. 3 and Fig. S6). (Note that these calculations do not account for differences that might result from changes in the relative importance of RO_2+HO_2 versus RO_2+RO_2 reactions as $[VOC]_{initial}$ and [OH] are varied.) Such "rate effects" have been observed for SOA produced in aromatic systems (20). The seed SA dependence is substantially reduced when the $[VOC]_{initial}$ is large, especially at high [OH]. Overall, these dependencies, along with differences in the initial seed SA, may help explain some of the differences (and similarities) in historical aerosol yields measured in different chambers.

Vapor losses and Sensitivity to C_w

The observed time-dependent C_{OA} to which the SOM was fit were corrected to account for physical deposition of the particles to the walls. Loss of vapors, excluding growth of suspended particles, was separately accounted for assuming that the vapors continuously interact with the Teflon chamber walls, with C_w = 10 mg m^{-3} (11). Some previous studies (21, 22) have alternatively assumed that vapors interact only with particles that have deposited to the walls during that experiment, as opposed to with the walls directly, and further that the time-scales associated with partitioning between vapors and suspended or wall-deposited particles are the same (SI Materials and Methods, Particle wall-loss correction). In this alternative scenario, the effective C_w is time-dependent (and zero at the start of an experiment) and related to the suspended particle concentration and the particle wall-loss rate. Most chamber experiments aim to limit the extent of particle deposition, and thus it is reasonable to assume that, in general, the concentration of wall-deposited particles is less than the suspended particle concentration. Further, most modern experiments limit the observed C_{OA} to < 0.1 mg m^{-3}, and thus the effective C_w in this alternative case will be substantially smaller than when vapors are assumed to partition into the chamber walls.

It is therefore useful to examine the dependence of the calculated R_{wall} on the assumed C_w, where an assumed C_w < ~0.1 mg m^{-3} corresponds approximately to the wall-deposited particle alternative scenario (21, 22). This has been done for the low-NO_x experiments where the SOM was fit to the observations for different assumed C_w, with good fits obtained for all C_w. Above C_w = 0.2 mg m^{-3} (= 200 μg m^{-3}) the calculated R_{wall} is constant. Below 0.2 mg m^{-3} the calculated R_{wall} falls off, reaching a second plateau at small C_w that is still above unity (Fig. 4). The plateaus at high and low C_w result from the best-fit SOM parameters varying with C_w to compensate for the differing amounts of loss of vapors to the walls while still maintaining the same suspended C_{OA} time-profile (Fig. S7). Since measurements demonstrate that vapors are lost directly to Teflon walls (11), this indicates that when vapor wall-loss is accounted for assuming that the vapors interact only with wall-deposited particles the extent of the vapor loss is underestimated. That R_{wall} is constant above C_w = 0.2 mg m^{-3} demonstrates that our conclusions are robust with respect to the assumption regarding the exact value of C_w.

Consideration of Historical Experiments

To estimate the potential influence of vapor wall-losses for systems other than toluene, we calculated SOA yield biases for a variety of other VOCs (15, 19, 20, 22, 23) (SI Materials and Methods, Fitting of historical chamber data). It should be noted that the experimental conditions in the historical experiments are not identical to those for the toluene experiments, especially for high-NO_x conditions (SI Materials and Methods, Historical Experiments). Although k_w for a given chamber is reasonably independent of the precursor compound, α may depend on the precursor identity. The results for the toluene experiments indicate that smaller α values generally correspond to larger R_{wall}. Therefore, a conservative, likely lower-bound estimate of R_{wall} has been obtained for each precursor assuming that α = 1 during fitting and using $k_w = 1 \times 10^{-4}$ s^{-1} (instead of 2.5×10^{-4}) to account for potential differences in the chamber used for these historical experiments (Figs. S8-S10). The use of a smaller k_w will decrease R_{wall}, all other factors being equal. Calculated R_{wall} values range from as small as 1.1 to as large as 4.1 (Table 1 and Fig. S11). The typically smaller values for the high-NO_x vs. low-NO_x experiments reflect the much shorter reaction timescales and higher oxidant and NO_x concentrations in the historical high-NO_x experiments, as compared to the current experiments with toluene. Evidently, the extent to which vapor wall-loss will have influenced

historical experiments is variable, yet potentially substantial and deserving of further investigation through new experiments and consideration of other datasets. Importantly, the results here indicate that quantitative analysis of SOA formation in chambers requires use of an explicitly time-dependent model that accounts for the simultaneous and competing condensation of vapors onto particles versus onto the chamber walls, representing a major shift from most historical analyses, which did not take time explicitly into account.

Implications

Our results show that the effect of vapor wall loss on SOA yields can be substantial. If reported SOA yields are low by factors of ~ 1.1-4.2, as our results suggest they may be, then SOA concentrations simulated in 3D models will be correspondingly low. While the analysis presented here for the toluene SOA system needs to be comprehensively expanded to other main classes of SOA precursors, beyond the assessment above, it is likely that a lack of proper accounting for vapor wall-losses that suppress chamber-derived SOA yields contribute substantially to the underprediction of ambient SOA concentrations in atmospheric models.

Materials and Methods

Chamber Experiments. Toluene photooxidation experiments were carried out in the new 24 m^3 Teflon environmental reaction chambers at Caltech. Liquid toluene was evaporated into the chamber to achieve a concentration of ~38 ppb gas-phase mixing ratio (= 143 μg m^{-3}). Hydroxyl radicals were generated from photolysis of H_2O_2 either with (high-NO_x) or without (low-NO_x) addition of NO to the chamber. Dried ammonium sulfate seed particles were added via atomization of an aqueous solution of ammonium sulfate solution until the desired seed concentration was obtained. The toluene, seed particles, H_2O_2 and NO_x were allowed to mix in the chamber for 1 hour, after which time the blacklights were turned on to initiate H_2O_2 photolysis. Particle number size distributions were measured using a cylindrical differential mobility analyzer coupled to a condensation particle counter. More details are available in SI Materials and Methods.

SOA Modeling. The statistical oxidation model (SOM) (14) was used to analyze the experimental observations. The SOM simulates the multi-generational gas-phase oxidation of a precursor VOC that has N_C carbon atoms and N_O oxygen atoms as reactions cause the precursor and product species to functionalize, increasing N_O, and/or fragment, decreasing N_C. Addition of oxygen atoms leads to a decrease in vapor pressure, which drives

condensation of the gas-phase species. Mass-transfer between the gas and particle phases is treated dynamically. The parameters that describe functionalization, fragmentation and the decrease in vapor pressure upon oxygen addition are adjusted by fitting to the experimental observations of time-dependent SOA formation. More details are provided in SI Materials and Methods.

Acknowledgements

We thank Alma Hodzic, Julia Lee-Taylor, Sasha Madronich (NCAR), Paul Ziemann (CU Boulder), Paul Wennberg (Caltech), Manabu Shiraiwa (MPIC) and Anthony Wexler (UC Davis) for useful discussions. This work was supported by the National Science Foundation grants ATM-1151062 and AGS-1057183, Department of Energy grant DE-SC 0006626, and the California Air Resources Board contract 12-312. Any opinions, findings, and conclusions or recommendations expressed in this material are those of the author(s) and do not necessarily reflect the views of the funding agencies.

References:

1. Odum JR, Jungkamp TPW, Griffin RJ, Flagan RC, & Seinfeld JH (1997) The atmospheric aerosol-forming potential of whole gasoline vapor. Science 276(5309):96-99.
2. Jimenez JL, et al. (2009) Evolution of organic aerosols in the atmosphere. Science 326(5959):1525-1529.
3. Odum JR, et al. (1996) Gas/particle partitioning and secondary organic aerosol yields. Environ. Sci. Technol. 30(8):2580-2585.
4. Carlton AG, et al. (2010) Model Representation of Secondary Organic Aerosol in CMAQv4.7. Environ. Sci. Technol. 44(22):8553-8560.
5. Heald CL, et al. (2005) A large organic aerosol source in the free troposphere missing from current models. Geophys. Res. Lett. 32:L18809.
6. Volkamer R, et al. (2006) Secondary organic aerosol formation from anthropogenic air pollution: Rapid and higher than expected. Geophys. Res. Lett. 33(doi:10.1029/2006GL026899):L17811.
7. Robinson AL, et al. (2007) Rethinking organic aerosols: Semivolatile emissions and photochemical aging. Science 315(5816):1259-1262.
8. Ervens B, Turpin BJ, & Weber RJ (2011) Secondary organic aerosol formation in cloud droplets and aqueous particles (aqSOA): a review of laboratory, field and model studies. Atmos. Chem. Phys. 11(21):11069-11102.

9. Ensberg JJ, et al. (2013) Emission factor ratios, SOA mass yields, and the impact of vehicular emissions on SOA formation. Atmos. Chem. Phys. Discuss. 13(10):27779-27810.

10. Dzepina K, et al. (2011) Modeling the Multiday Evolution and Aging of Secondary Organic Aerosol During MILAGRO 2006. Environ. Sci. Technol. 45(8):3496-3503.

11. Matsunaga A & Ziemann PJ (2010) Gas-Wall Partitioning of Organic Compounds in a Teflon Film Chamber and Potential Effects on Reaction Product and Aerosol Yield Measurements. Aerosol Sci. Technol. 44(10):881-892.

12. Kokkola H, et al. (2014) The role of low volatile organics on secondary organic aerosol formation. Atmos. Chem. Phys. 14(3):1689-1700.

13. Ehn M, et al. (2014) A large source of low-volatility secondary organic aerosol. Nature 506(7489):476-479.

14. Cappa CD & Wilson KR (2012) Multi-generation gas-phase oxidation, equilibrium partitioning, and the formation and evolution of secondary organic aerosol. Atmos. Chem. Phys. 12:9505-9528.

15. Cappa CD, et al. (2013) Application of the Statistical Oxidation Model (SOM) to secondary organic aerosol formation from photooxidation of C12 Alkanes. Atmos. Chem. Phys. 13:1591-1606.

16. McMurry PH & Grosjean D (1985) Gas and aerosol wall losses in Teflon film smog chambers. Environ. Sci. Technol. 19(12):1176-1182.

17. Loza CL, et al. (2013) Secondary organic aerosol yields of 12-carbon alkanes. Atmos. Chem. Phys. Discuss. 13(8):20677-20727.

18. Shiraiwa M, et al. (2013) Size distribution dynamics reveal particle-phase chemistry in organic aerosol formation. Proc. Nat. Acad. Sci.

19. Chhabra PS, et al. (2011) Elemental composition and oxidation of chamber organic aerosol. Atmos. Chem. Phys. 11(17):8827-8845.

20. Ng NL, et al. (2007) Secondary organic aerosol formation from m-xylene, toluene, and benzene. Atmos. Chem. Phys. 7(14):3909-3922.

21. Hildebrandt L, Donahue NM, & Pandis SN (2009) High formation of secondary organic aerosol from the photo-oxidation of toluene. Atmos. Chem. Phys. 9(9):2973-2986.

22. Loza CL, et al. (2012) Chemical aging of m-xylene secondary organic aerosol: laboratory chamber study. Atmos. Chem. Phys. 12(1):151-167.

23. Chan AWH, et al. (2009) Secondary organic aerosol formation from photooxidation of naphthalene and alkylnaphthalenes: implications for oxidation of intermediate volatility organic compounds (IVOCs). Atmos. Chem. Phys. 9(9):3049-3060.

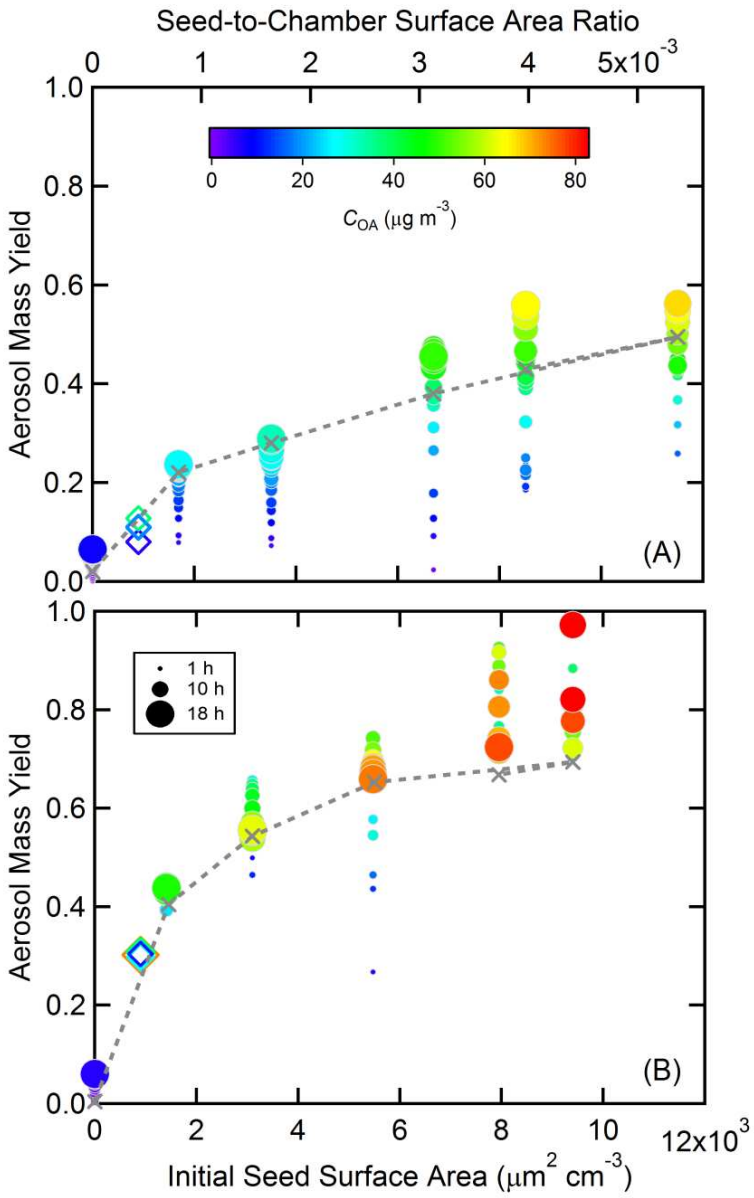

Figure 1. Hourly averaged lower bound SOA yields over the course of a toluene photooxidation experiment as a function of initial AS seed surface area for (**A**) high-NO_x and (**B**) low-NO_x conditions. Symbol color indicates the SOA mass concentration and symbol size the time after lights were turned on. The filled circles are from the current experiments and the open diamonds from (20). The dashed gray line and × are the end-of-experiment yields from the optimized best-fit SOM simulations.

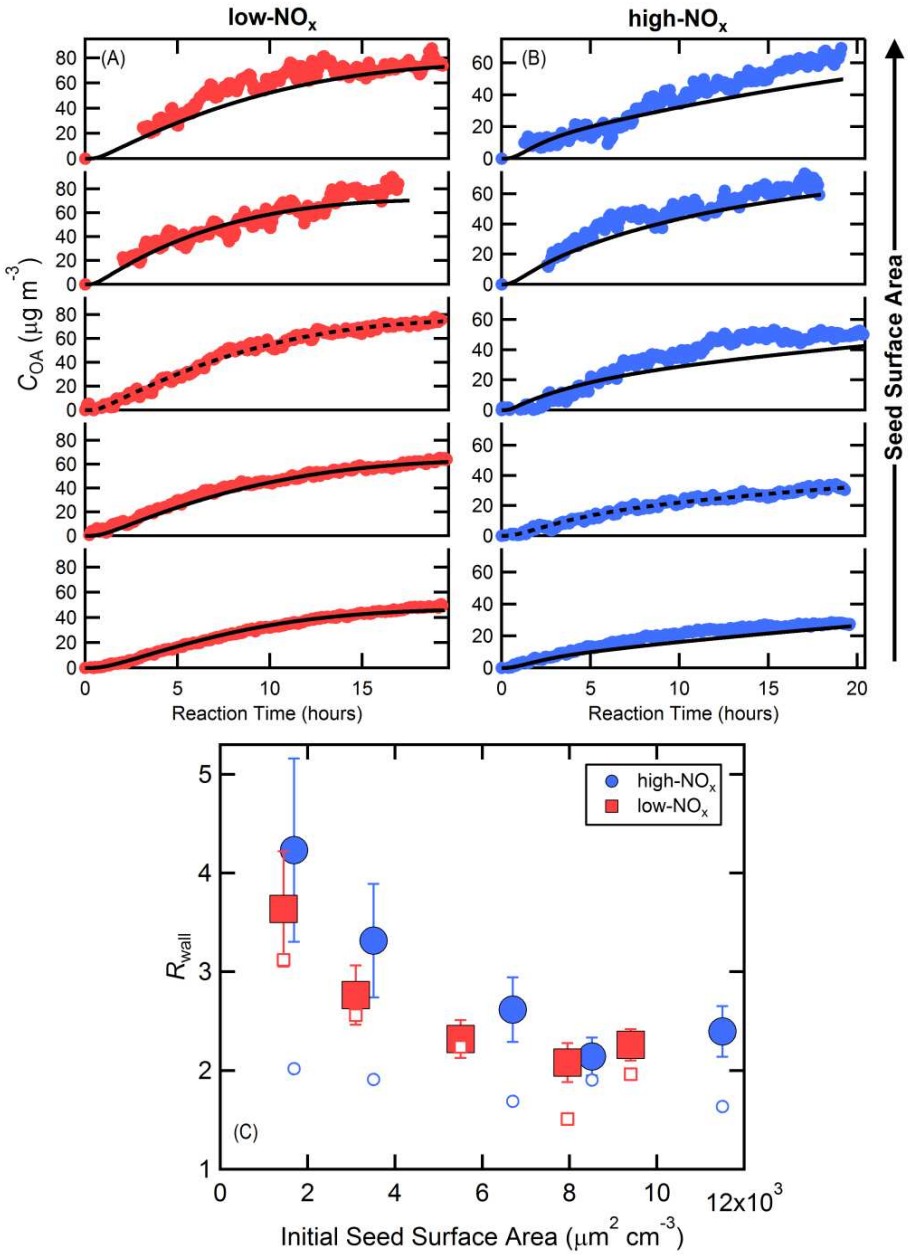

Figure 2. Observed (points) and simulated (lines) SOA concentrations for each photochemical oxidation experiment performed for different initial inorganic seed surface area for (**A**) low-NO_x and (**B**) high-NO_x conditions. The dashed lines indicate the experiment to which the SOM was explicitly fit, and the solid lines indicate simulation results based on those fits. (**C**) The wall-loss bias factor, R_{wall}, as a function of seed surface area. Filled symbols use the optimal k_w/α pair and the corresponding best-fit SOM parameters determined from (A) and (B). Open symbols assume $\alpha = 1$ and each experiment was individually fit using the optimal k_w. The error bars indicate the 1σ standard deviation in R_{wall} for each experiment over the period when $C_{OA} > 0.5$ μg m^{-3}.

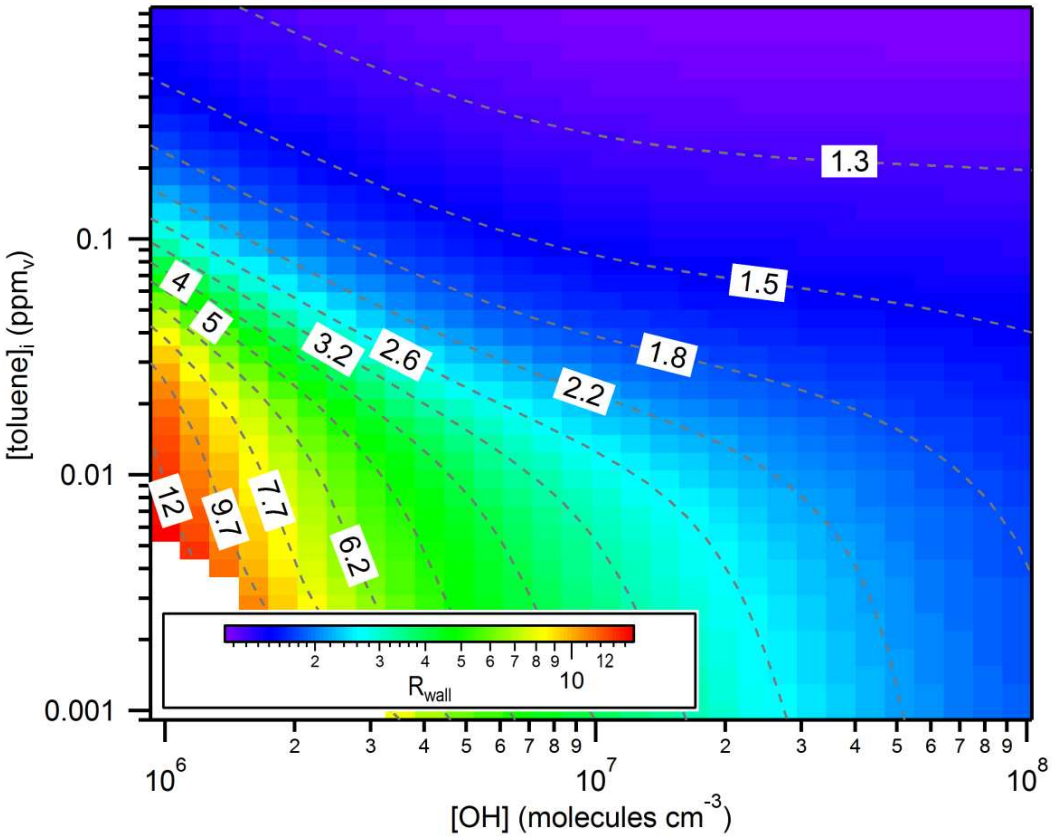

Figure 3. Calculated SOA yield bias as a function of initial toluene concentration and OH concentration when k_w = 2.5 x 10^{-4} s^{-1} and C_w = 10 mg m^{-3}. The R_{wall} values for a given [toluene] and [OH] are indicated by colors and contours and are averaged over the period when C_{SOA} > 0.5 μg m^{-3} to the end of an experiment at 18 h. Results are based on the optimal fit of the SOM to the low-NO_x experiments.

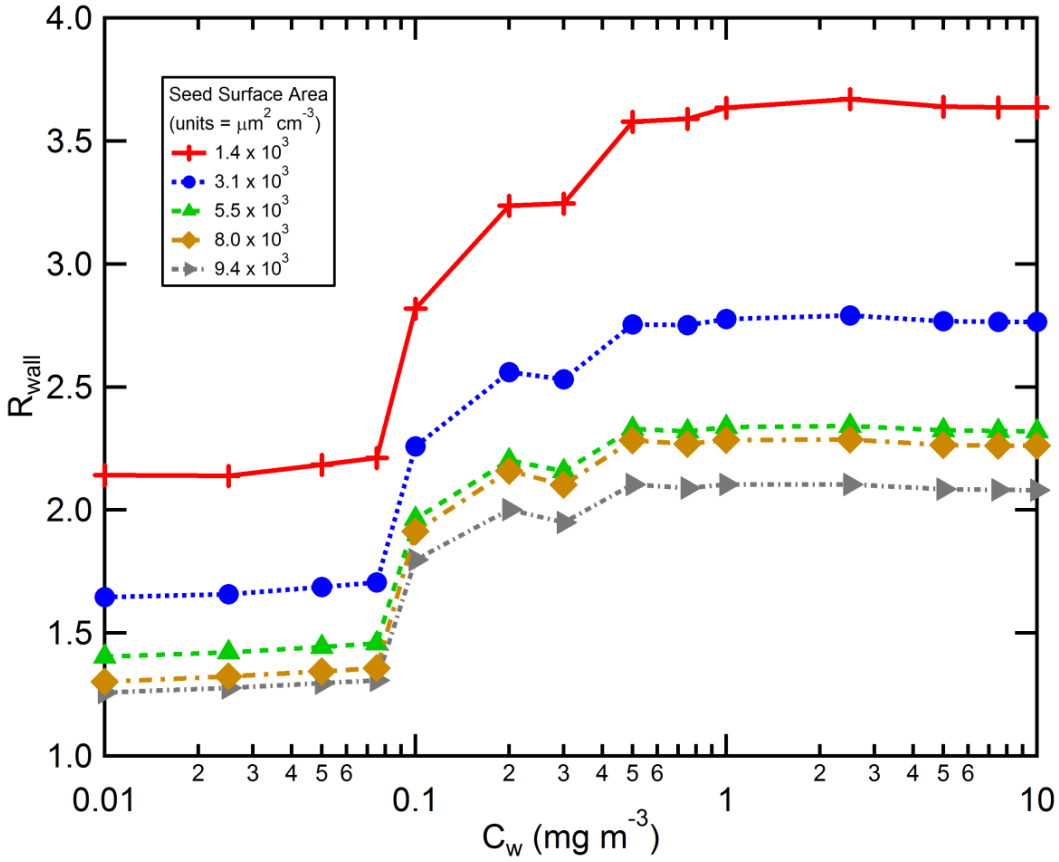

Figure 4. Calculated vapor wall-loss bias, R_{wall}, as a function of the effective wall mass concentration, C_w, for the low-NO_x toluene photooxidation experiments at varying initial seed surface area. For each C_w, the SOM was fit to the experiment with seed surface area = 5.5 x 10^3 μm^2 cm^{-3} using k_w = 2.5 x 10^{-4} s^{-1} and α = 2 x 10^{-3}. The determined best-fit SOM parameters were then used to simulate SOA formation for the experiments performed at other seed concentrations but assuming the same C_w.

Tables

Table 1. Average biases in SOA yields due to vapor wall-losses for various VOCs under low- and high-NO_x conditions.

VOC[a]	Low-NO_x R_{wall}[b]	High-NO_x R_{wall}[b]
toluene[c] (this study)	2.1 – 3.6	2.1 – 4.2
n-dodecane (15)	4.1 ± 0.8[d]	1.16 ± 0.08
2-methylundecane (15)	3.7 ± 0.5	1.4 ± 0.2
cyclododecane (15)	3.0 ± 0.3	1.10 ± 0.05
hexylcyclohexane (15)	2.4 ± 0.3	1.16 ± 0.07
toluene (20)	1.9 ± 0.4	1.13 ± 0.06
benzene (20)	1.8 ± 0.4	1.25 ± 0.1
m-xylene (20)	1.8 ± 0.4	1.2 ± 0.1
m-xylene (22)	1.6 ± 0.3	
naphthalene (23)	1.2 ± 0.1	1.2 ± 0.1
α-pinene + OH (19)	1.6 ± 0.3	1.3 ± 0.1
isoprene + OH	3.14	2.22

[a] For all VOC's except toluene (this study), $k_w = 1x10^{-4}$ s^{-1} and $\alpha = 1$. For toluene (this study), $k_w = 2.5x10^{-4}$ s^{-1} and $\alpha = 0.002$ (low-NO_x) or 0.001 (high-NO_x).
[b] Calculated for the period when $C_{SOA} > 0.5$ μg m^{-3} through the end of a given experiment.
[c] For toluene, the reported R_{wall} indicate the range of values determined at different initial seed SA.
[d] Uncertainties are 1σ over the averaging period.

Supporting Information for Influence of vapor wall-loss in laboratory chambers on yields of secondary organic aerosol

Xuan Zhang, Christopher D. Cappa, Shantanu Jathar, Renee C. McVay, Joseph J. Ensberg, Michael J. Kleeman, and John H. Seinfeld

correspondence to: cdcappa@ucdavis.edu or seinfeld@caltech.edu

This file includes:

Section 1. Materials and Methods 186

The Supplementary information contains an overview of the new and historical chamber experiments (S1.1), optimization of k_w and α (S1.2), the statistical oxidation model (S1.3), the treatment of vapor wall loss within the SOM and a discussion of vapor-particle equilibrium timescales (S1.4), and the fitting of historical chamber data (S1.5).

S1.1. Experiments

S1.1.1. Toluene Photooxidation Experiments

Toluene SOA formation experiments were conducted in the new Caltech dual 24-m^3 Environmental Chambers, in which the temperature (T) and relative humidity (RH) are automatically controlled. Prior to each experiment, the Teflon chambers were flushed with clean, dry air for 24 h until the particle number concentration < 10 cm^{-3} and volume concentration < 0.01 μm^3 cm^{-3}. Ammonium sulfate (AS) seed aerosol was injected into the chamber by atomizing 0.015 or 0.1 M aqueous $(NH_4)_2SO_4$ solution into the chamber for 30 to 120 min. The resulting total AS seed surface area ranged from ~ 1×10^3 μm^2 cm^{-3} up to ~ 1×10^4 μm^2 cm^{-3}, and the corresponding particle-to-wall surface area ratio ranged from ~ 1×10^{-3} to 7×10^{-3}. Hydrogen peroxide (H_2O_2) was used for the OH source by evaporating 120 μL of 50% wt aqueous solution into the chamber with 5 L min^{-1} of purified air for ~ 100 min, resulting in an approximate starting H_2O_2 concentration of 2.0 ppm. 3 μL toluene (Sigma-Aldrich, 99.8% purity) was injected into a glass bulb, which was connected into the Teflon chamber. 5 L min^{-1} of purified air flowed through the glass bulb into the chamber for ~ 15 min, introducing ~ 40 ppb toluene into the chamber. For experiments at elevated NO_x (i.e. high-NO_x conditions) NO and NO_2 were added to the chamber at the start of a given experiment until the concentrations were ~17 ppb and 30 ppb, respectively. The initial [VOC]/[NO_x] in the high-NO_x experiments ranged from 4.8-6.0 ppbC/ppb. After ~ 90 min mixing, photooxidation was initiated by irradiating the chamber with black lights with output wavelength ranging from 300 to 400 nm. The irradiation leads to photolysis of H_2O_2 to produce OH radicals with an approximately constant concentration throughout the entire experiment. Temperature and relative humidity of all experiments were ~298 K and ~3%,

respectively. The initial O_3 concentration was below detection limit in all experiments. H_2O_2 exerts an interference on the O_3 detection, increasing the O_3 monitor readout by ~ 2-3 ppb in the current study. NO was continuously injected into the chamber over the course of each experiment at 80 ppb h^{-1} for the first 2.5 h of reaction, then 50 ppb h^{-1} for the next 4.5 h of reaction, and then 30 ppb h^{-1} for the remainder of the reaction. Experimental conditions (e.g. [VOC], seed surface area, [NO_x]) for each experiment are reported in Table S1.

A suite of instruments was used to monitor toluene SOA formation and evolution. T, RH, NO, NO_x and O_3 were continuously monitored. Toluene concentration was monitored using a gas chromatograph with flame ionization detector (GC/FID, Agilent 6890N), equipped with a HP-5 column (15 m × 0.53 mm ID × 1.5 μm thickness, Hewlett-Packard). Particle size distribution and number concentration were measured by a cylindrical differential mobility analyzer (DMA; TSI Model 3081) coupled to a condensation particle counter (TSI Model 3010). The DMA was operated in a closed system with a recirculating sheath and excess flow of 2.67 L min^{-1} and a 5.4 : 1 ratio of sheath to aerosol flow rate. The column voltage was scanned from 15 to 9850 V over 45 s.

S1.1.2. Historical Experiments

All the other SOA formation experiments used in SOM optimal fitting were carried out in the Caltech dual 28-m^3 Environmental Chamber. Details of experimental protocols can be found in (1-6). Experimental conditions are reported in Tables S2 and S3 and differences in methodology from the above toluene photooxidation experiments are highlighted below. An identical suite of instrumentation was used as in the toluene photooxidation experiments. The historical experiments typically had seed SA around 1-2 x 10^3 cm^{-3}, corresponding to the lowest seeded experiments in the toluene photooxidation experiments. The majority of the historical low-NO_x experiments examined in this study used similar methods and conditions as the new toluene experiments, i.e. used H_2O_2 as the OH source. The experimental procedures associated with the high-NO_x experiments differed from the new toluene experiments. Specifically, for the historical high-NO_x experiments the primary OH source was HONO photolysis, as opposed to H_2O_2 photolysis. This has the practical implication of leading to reaction conditions where (i) the OH concentration is initially ~O(10^7 molecules cm^{-3}) and decays rapidly over a period of ~1-3 hours and (ii) the initial [VOC]/[NO_x] ratio tends to be much smaller compared to the current experiments. Thus, the timescales of SOA

formation during the historical high-NO_x experiments were, in general, very different than for the toluene photooxidation experiments: rapid formation over approximately 1-2 hours vs. continuous formation over 18 hours. For high-NO_x experiments, NO_x was added prior to the lights being turned on both from the HONO injection, which introduces some NO_2, and from addition of NO. Additional NO was produced upon photolysis of HONO. Typical initial NO_x concentrations were on the order of 500 ppb, corresponding to initial [VOC]/[NO_x] of ~0.5 ppbC/ppb (Table S3).

S1.1.3. Particle Wall-Loss Correction

Particle wall losses during an experiment must be accounted for. Two limiting assumptions have been made for the interactions between those particles that have deposited on the wall and suspended vapors in determining the corrected suspended SOA concentrations (5, 7, 8). In one case, particles deposited on the wall are assumed to cease interaction with the suspended vapors and no loss of vapors to the walls is accounted for. This case gives the lower bound of the total organic mass concentration, since particles remain the same size as at the moment they deposited on the wall for the remainder of the experiment. SOA concentrations determined from this case are used for the primary analysis in the manuscript, which is appropriate because vapor loss to the walls is treated separately. In the second limiting case, particles deposited on the wall are assumed to continue to interact with the suspended vapors as if they had remained suspended, with the wall-bound particles assumed to grow at the same rate as suspended particles in the chamber. The corrected SOA concentrations in this case are larger than in the first case because of the additional uptake of vapors to wall-bound particles. This case provides an upper-bound on the actual SOA formed under the assumption that the vapors interact with wall-bound particles, but not the Teflon walls (5, 7, 8). However, traditional application of this second case does not account for the substantially differing timescales of gas-particle vs. gas-wall transport, nor does it account for loss of vapors to the chamber walls and the substantially larger amount of effective absorbing mass of the walls (C_w) compared to the deposited particles. Compared with C_w (10 mg m^{-3}), which is assumed as a constant from the onset of the experiment, the total organic mass deposited on the chamber wall over the course of 18 h photooxidation is ~ 3 orders of magnitude lower. As such, this “upper bound” can underestimate the actual SOA formation,

as it accounts for only a subset of the overall vapor wall-loss correction. Nonetheless, the "upper bound" corrected results are provided for reference to previous experiments.

For either case, the Aerosol Parameter Estimation (APE) model (9), derived on the basis of the aerosol general dynamic equation (10), is employed to calculate these two limits. The suspended particle population evolves as a result of three processes: coagulation, condensation, and wall-loss. The change of suspended particle number-size distribution due to coagulation is well constrained. The size-dependent wall loss rate is determined by experimentally monitoring the decay of dry inert $(NH_4)_2SO_4$ particles assuming first-order kinetics. The condensation rate is the only free parameter in the model, which can be obtained by optimal fitting of the APE model predictions to the DMA measured particle size distribution at each time step. Once the condensation rate values are estimated, they can be applied to parameterize the growth of particles on the walls due to condensation of gaseous vapor and deposition of suspended particles. A factor that describes the extent of interactions between deposited particles and suspended vapors is applied when summing aerosol masses in the chamber core and on the walls. A value of 0 for this factor corresponds to no condensation to deposited particles. A value of 1 for this factor corresponds to the case where the condensation rate of gaseous vapors to deposited particles is the same as those suspended. The primary analysis in this work utilizes the corrected particle mass under the assumption of no condensation to deposited particles because vapor wall loss is treated separately. The evolution of the wall-loss corrected particle size distributions is shown for each experiment in Fig. S1 for the lower limit case. The time-dependent aerosol growth, from which the aerosol yield can be calculated, is shown for each experiment in Fig. S2 for both limiting cases.

S1.2. Optimizing k_w and α

The optimal values of k_w and α were determined using the general procedure as outlined below. There were a total of 6 experiments conducted for each NO_x condition, 5 with seed aerosol and 1 without. Only the seeded experiments are considered in the optimization method because of difficulties associated with specification of nucleation. The SOM was fit to one of these 5 seeded experiments for a variety of k_w and α values. For each k_w/α pair a set of best-fit SOM parameters (i.e. ΔLVP, m_{frag} and the P_{func} array) were determined. Specifically,

the experiments with seed SA = 5.5 x 10^3 μm^2 cm^{-3} (low-NO_x) and SA = 3.5 x 10^3 μm^2 cm^{-3} (high-NO_x) were used for fitting. These best-fit SOM parameters and the associated k_w/α pair were then used to simulate SOA formation for the other 4 seeded experiments. Reduced goodness of fit metric (χ^2_{red}) values were calculated for each experiment as:

$$\chi^2_{red} = \frac{1}{n-6-1}\sum\left(\frac{C_{OA,obs}(t)-C_{OA,model}(t)}{\sigma_{OA,obs}(t)}\right)^2 \quad \text{(S1)}$$

where n is the number of data points per experiment, 6 is the number of model degrees of freedom and $\sigma_{OA,obs}$ is the uncertainty in the observations. For each experiment, the minimum χ^2_{red} across all k_w/α pairs was determined, and the set of χ^2_{red} values for each experiment was normalized by the minimum in that set. Normalization ensures that the different experiments carry equal weight in the next step. The composite χ^2_{red} across all seeded experiments was then determined as:

$$\chi^2_{red,composite}(k_w,\alpha) = \sum_{i=1}^{5}\chi^2_{red,norm,i}(k_w,\alpha) \quad \text{(S2)}$$

where the sum is over the normalized χ^2_{red} for all seeded experiments. Smaller values of the composite χ^2_{red} indicate overall better agreement across all of the seeded experiments for a given set of best-fit SOM parameters, k_w and α. A contour diagram of the calculated composite χ^2_{red} as a function of k_w and α (Fig. S3) illustrates that only certain combinations of k_w and α provide for good agreement across all experiments. There is almost no seed effect when $\alpha > 0.1$, and therefore the overall agreement is poor no matter what k_w is used. As α is lowered, a seed effect becomes evident. However, only when α is O(10^{-3}) and k_w is O(10^{-4}) can overall good agreement with all experiments be obtained. Since the k_w and α values were not determined from a specific fitting algorithm, we refer to the values that provide for best agreement as the "optimal" values rather than "best fit" values. These are: k_w = 2.5 x 10^{-4} s^{-1} and α = 2 x 10^{-3} for low-NO_x experiments and k_w = 2.5 x 10^{-4} s^{-1} and α = 1 x 10^{-3} for high-NO_x experiments.

S1.3. The Statistical Oxidation Model

The SOM simulates the oxidation of a given hydrocarbon as a trajectory through a 2-D grid of carbon and oxygen atoms in which "species" are considered particular carbon/oxygen combinations (e.g. $C_{12}O_4$). Specific rules define the movement through this space, describing the probability that a reaction leads to functionalization or fragmentation, how many oxygen atoms are added per reaction, and the decrease in vapor pressure that occurs upon addition of a single oxygen atom. SOM effectively simulates the multi-generational chemistry that characterizes photooxidation experiments. Full details are provided in (6, 11). The fragmentation probability (P_{frag}) depends on the oxygen content of the reacting species and is parameterized as:

$$P_{frag} = \left(\frac{N_O}{N_C}\right)^{m_{frag}} \quad \text{(S3)}$$

where m_{frag} is an adjustable parameter, and N_O and N_C are the number of oxygen and carbon atoms comprising an SOM species, respectively. The P_{frag} is always constrained to be ≤ 1. (Recently, a "bug" in the SOM code was found related to how the fragmentation was being treated. Rather than the probability of fragmentation depending on the oxygen content of the reacting species, it was being determined based on the oxygen content of the product species. This has now been fixed. The SOM was originally written in the IGOR programming language. The SOM has now been independently implemented in Fortan using the framework outlined in (11) and the IGOR and Fortan versions produce equivalent results, suggesting that no further "bugs" of this sort exist. The best-fit SOM parameters for the alkanes differ from those reported in (6) as a result of this update and because vapor wall-loss has been included.)

The functionalization probability (P_{func}) describes the likelihood of adding 1, 2, 3 or 4 oxygen atoms per reaction, and each can be adjusted independently, subject to the constraint that they are positive and must sum to 1. The decrease in vapor pressure (or more specifically, in the log of the saturation concentration, C^*, in $\mu g\ m^{-3}$) per oxygen added is referred to as ΔLVP, and ranges from ~0.7 to 2.5, depending on the type of functional group added. Thus, there are

6 total adjustable (tunable) parameters in the base model: (i) fragmentation, (ii) volatility decrease per oxygen added and (iii-vi) oxygen addition probability. For this study, heterogeneous OH reactions are not simulated.

The reaction rate coefficient matrix associated with reactions of product species with OH radicals has been updated from the original SOM on the basis of comparison with output from the GECKO-A model for simulations of the outflow from Mexico City (12). The reaction rate coefficient of the parent hydrocarbon with OH, k_{OH} (cm^3 $molecules^{-1}$ s^{-1}), is specified to be consistent with literature results, e.g. for toluene k_{OH} = 5.2 x 10^{-12} cm^3 $molecules^{-1}$ s^{-1}. For all other species within the SOM grid, the k_{OH} are determined referenced to the reaction rate coefficient for species with the same number of carbon atoms but zero oxygen atoms as:

$$\log\left(k_{OH,base}\right) = A_1 + A_2 \times N_C^{A_3} \quad \text{(S4)}$$

and where A_1 = -15.103, A_2 =-3.9481, and A_3 = -0.79796. For a given N_C, the k_{OH} is temperature dependent and varies with N_O as

$$k_{OH}(T) = k_{OH,base} \times T^2 \times exp\left(-1 \times \frac{E_a}{8.314 \times T}\right) \times \left[1 + \frac{b_1}{\sigma\sqrt{2\pi}} \exp\left(-\frac{1(ln(N_O+0.01)-ln(b_2))^2}{2\sigma^2}\right)\right] \quad \text{(S5)}$$

and where the variables b_1, b_2, and σ are functions of N_C, with

$$\sigma(N_C \leq 15) = 0.0214 \times N_C + 0.5238; \;\; \sigma(N_C > 15) = -0.115 \times N_C + 2.695 \,, \quad \text{(S6)}$$

$$b_1 = -0.2583 \times N_C + 5.8944 \,, \quad \text{(S7)}$$

And

$$b_2(N_C \leq 15) = 0.0314 \times N_C + 0.9871 \; ; b_2(N_C > 15) = 0.25 \times N_C - 2.183 \; . \quad \text{(S8)}$$

Within the SOM gas-particle partitioning is treated through the framework of absorptive partitioning theory (13), in which compounds partition between the gas and particle phases according to their Raoult's Law adjusted vapour pressures. Unlike in previous usages of the SOM, which assumed instantaneous gas-particle equilibrium, the SOM here treats gas-particle mass transfer dynamically. The net flux of molecules to/from the particle is calculated at each timestep as:

$$\frac{\partial C_{OA,i}}{dt} = 4\pi D_{gas,i} R_p N_p F_{FS} \left(C^{\infty}_{gas,i} - \chi_i C^*_i \right) \quad \text{(S9)}$$

where $D_{gas,i}$ is the gas-phase diffusivity, R_p is particle radius, N_p is particle number concentration, F_{FS} is the Fuchs-Sutugin correction for noncontinuum mass transfer, $C^{\infty}_{gas,i}$ is the gas-phase concentration, χ_i is the mass fraction and C^*_i is the saturation concentration of species i. The entire SOA mass is considered absorbing in the calculation of χ_i. It is assumed that $D_{gas,i}$ varies with molecular weight (MW) and is equal to $D_{CO2}(MW_{CO2}/MW_i)$, with $D_{CO2} = 1.38 \times 10^{-5}$ m^2 s^{-1}. The Fuchs-Sutugin correction is equal to:

$$F_{FS} = \frac{0.75\alpha(1+Kn)}{Kn^2+Kn+0.283 \cdot Kn \cdot \alpha+0.75\alpha} \quad \text{(S10)}$$

where α is the mass accommodation coefficient onto particles and Kn is the Knudsen number, defined as:

$$Kn = \lambda / R_p \quad \text{(S11)}$$

and λ is the gas mean free path, which is equal to:

$$\lambda_i = 3 \cdot \frac{D_{gas,i}}{\bar{c}_i} \quad \text{(S12)}$$

with $\bar{c}_i$ equal to the root mean square speed of the gas, which is equal to:

$$\bar{c}_i = \left(\frac{8N_A kT}{\pi MW_i}\right)^{\frac{1}{2}} \quad \text{(S13)}$$

with N_A = Avagadro's number, k = the Boltzmann constant and T = temperature. The results obtained with the dynamic partitioning SOM are equivalent to those obtained using the instantaneous equilibrium assumption when $\alpha > 0.1$ and with seed aerosols present. It should be noted that α as used in Eqn. S8 represents the net mass transfer and can include resistances both in the gas-phase and at the particles surface. Full accommodation of vapors into the bulk particle can be limited by diffusion within the particles when particles are highly viscous (14). The dynamic SOM utilized here uses monodisperse particles with a size equal to the number mean diameter and the number concentration adjusted to give the desired initial seed surface area (SA). Although the ideal model would use the actual seed size distribution as input, we have established that for particle diameters larger than ~ 50 nm the model results are sufficiently insensitive to the selected particle diameter for a fixed seed SA. As such, the results here are not limited by the simplification of using monodisperse particles. Nucleation is not explicitly simulated by the SOM. Therefore, dynamic SOM calculations for the nucleation experiments have been carried out assuming an initial seed size of 5 nm and a seed concentration equal to that observed at the end of the experiment. Given that there is substantial uncertainty associated with this assumption the nucleation experiments have not been quantitatively assessed.

S1.4. Vapor Wall-Loss

Loss of vapors to the chamber walls is simulated as a first-order process, characterized by the first-order wall-loss coefficient k_w (s^{-1}). Vapor wall-losses are assumed to be reversible, characterized by the gas-wall partitioning coefficient, K_w, which is dependent upon compound vapor pressure,

$$K_w = \frac{RT}{M_w \gamma_w P_{sat}} \quad \text{(S14)}$$

where R is the ideal gas constant, T is temperature (assumed 298 K), M_w is the effective molecular weight of the wall material, γ_w is the activity coefficient, and P_{sat} is the saturation concentration of the species of interest. It is convenient to use the saturation concentration, C^* ($\mu g\ m^{-3}$), instead of the saturation vapor pressure, where

$$C^* = \frac{1}{K_p} = \frac{M_p \gamma_p P_{sat}}{RT} \quad \text{(S15)}$$

with K_p the gas-particle partitioning coefficient, M_p the average molecular weight of the organic species comprising the particles and γ_p is the activity coefficient. The rate coefficient for transfer of gas-phase species onto the walls is given as $k_{w,on}$ while that for evaporation from the walls is given as $k_{w,off}$. The $k_{w,on}$ is specified as a model input parameter (and is equivalent to the k_w in the main text). The $k_{w,off}$ is obtained from detailed balance as:

$$k_{w,off} = \frac{k_{w,on}}{K_w C_w} = k_{w,on}\left(\frac{C^* M_w \gamma_w}{C_w M_p \gamma_p}\right) \quad \text{(S16)}$$

and where C_w is the equivalent wall OA concentration ($\mu g\ m^{-3}$). If one makes the simple assumption that $M_w = M_p$ and $\gamma_w = \gamma_p$, then C_w can be viewed as an effective concentration that accounts for differences in molecular weight and activity between the particles and walls.

The C_w must therefore be estimated from experiments. Matsunaga and Ziemann (15) report a range of C_w values that are constant within a given class of molecules (e.g. ketones vs. alkanes), with C_w = 2, 4, 10 and 24 mg m^{-3} for alkanes, alkenes, alcohols and ketones. For all reported simulations here it has been assumed that C_w = 10 mg m^{-3}. Results are reasonably insensitive to the choice of C_w over the previously determined range because $C_w >> C_{OA}$. The sensitivity of our results to the assumed C_w is discussed further below in Section S1.4.3.

It is assumed that $k_{w,on}$ is not dependent on compound identity. Consequently, the $k_{w,off}$ terms vary with compound identity, specifically with C^*.

The value of $k_{w,on}$ can be estimated from consideration of just the gas-phase transport terms within a chamber. McMurry and Grosjean (16) report an expression for $k_{w,on}$,

$$k_{w,on} = \left(\frac{A}{V}\right) \frac{\left(\frac{\alpha_w \bar{c}}{4}\right)}{1.0 + \left(\frac{\pi}{2}\right)\left[\frac{\alpha_w \bar{c}}{4\left(k_e D_{gas}\right)^{0.5}}\right]} \quad \text{(S17)}$$

where A/V is the surface to volume ratio of the chamber (equal to 6/L for a square chamber, and where L is the length of one side), α_w is the mass accommodation coefficient of vapors onto the chamber walls, $\bar{c}$ is the mean thermal speed of the molecules, k_e is the coefficient of eddy diffusion, and D_{gas} is the molecular diffusivity. It should be noted that α_w is not necessarily equal to α for uptake onto particles. For the type of molecules here, D_{gas} is ~3 x 10^{-6} m^2 s^{-1} and $\bar{c}$ ~ 200 m s^{-1}. This leaves k_e and α_w as the two key unknowns. Values of $k_{w,on}$ have been calculated as a function of k_e for α_w ranging from 10^{-7} to 1, where 1 is perfect accommodation. k_e values from 10^{-3} s^{-1} to 1 s^{-1} have been used, which corresponds to mixing timescales of 17 min to 1 s (Fig. S4). McMurry and Grosjean (16) reported values for their actively mixed chambers of 0.02 s^{-1} (60 m^3 chamber) and 0.12 s^{-1} (4 m^{-3} chamber). Since the Caltech chamber is not actively mixed it is expected that the characteristic k_e value is considerably smaller.

The value of k_e for the Caltech chamber is estimated based on observed size-dependent deposition rates of particles in the chamber. The minimum in the k_w for particles as a function of size is dependent upon k_e. This minimum occurs at a diameter of ~350 nm for the 24 m^{-3}

Caltech chamber and at ~250 nm for the 28 m^{-3} chamber (5). For particles in a cubic chamber the k_w is related to the eddy diffusion coefficient through the equation (17):

$$k_w = \frac{1}{L}\left[\frac{8\sqrt{k_e D}}{\pi} + v \cdot \coth\left(\frac{x}{2}\right)\right] \quad \text{(S18)}$$

where v is the particle terminal settling velocity (m s^{-1}) and x is defined as:

$$x = \frac{\pi v}{2\sqrt{k_e D}} \quad \text{(S19)}$$

From Eqn. S5, k_w has been calculated as a function of particle diameter and the k_e value adjusted until the minimum occurs at 250 nm or 350 nm. The required k_e in the 24 m^3 chamber is 0.075 s^{-1} and in the 28 m^3 chamber is 0.015 s^{-1}, similar to the values reported by McMurry and Grosjean for 60 m^3 (k_e = 0.12 s^{-1}) and 4 m^3 (k_e = 0.02 s^{-1}) chambers (16). Therefore, it is expected that the maximum k_w ~ 6.0 x 10^{-4} s^{-1} for the 24 m^3 chamber and ~ 3 x 10^{-4} for the 28 m^3 chamber from consideration of Fig. S4. Since the accommodation coefficient for the condensing species on the Teflon chamber walls is not known, it is not possible to definitively put a lower bound on the k_w. However, the experimental results of Matsunaga and Ziemann (15) clearly demonstrate that vapors are taken up to their chamber walls quite rapidly, and they estimate that α_w ~ 10^{-5}, which suggests that k_w ~ 3 x 10^{-4} s^{-1} (24 m^3) or ~ 2 x 10^{-4} s^{-1} (28 m^3). This theoretical estimate is in very good agreement with the optimal k_w (= 2 x 10^{-4} s^{-1}) for the 24 m^3 chamber.

Loza et al. (18) report observations of vapor wall-loss rates for two compounds: 2,3-epoxy-1,4-butanediol (BEPOX) and glyoxal. BEPOX is the butadiene derivative of an epoxydiol of isoprene. The uptake of both compounds to the chamber walls was observed to depend strongly on RH and whether a "new" or "old" chamber was used, with the measured values ranging from ~2-7 x 10^{-5} s^{-1} (18). Such new vs. old dependence was not observed by Matsunaga and Ziemann (15), who investigated wall-losses of alkanes, alkenes, 2-ketones and 2-alcohols. This suggests that the mechanism involved in the uptake of BEPOX and glyoxal

was somewhat different than that for the hydrocarbons considered by Matsunaga and Ziemann (15), or may alternatively indicate complications associated with capturing fast initial decay during the fill period in the much larger Caltech chamber. Such fill and mixing complications likely also explain the strong differences between the wall-loss rate coefficients for 2-dodecanol determined by Loza et al. (19) and Matsunaga and Ziemann (15). Since the vapor uptake to the Teflon chamber walls is reversible, care must be taken in the interpretation of observed wall-loss rates. Only measurements made in the very early stages of uptake will correspond directly to the first-order wall-loss rate coefficient, since as the system approaches equilibrium net vapor uptake will slow. As such, we suggest that the estimates of k_w using the α from Matsunaga and Ziemann (15) may be more relevant to the current study given the nature of the compounds involved.

S1.4.1. Gas-Particle Partitioning Timescales

The timescale associated with reaching gas-particle equilibrium varies with seed SA, and for a distribution is approximately:

$$\tau_{g-p} \sim \left(2\pi N_p \overline{D_p} D_{gas} \bar{F}_{FS}\right)^{-1} \quad \text{(S20)}$$

where N_p is the particle number concentration, $\overline{D_p}$ is the number mean diameter, D_{gas} is the gas-phase diffusivity and $\bar{F}_{FS}$ is the correction to the mass transfer flux due to noncontinuum effects and imperfect accommodation given in Eqn. S8. Values for τ_{g-p} have been calculated for the low-NO_x experiments based on the initial seed number concentration and mean diameter as a function of α (Fig. S5), using D_{gas} = 1 x 10^{-5} m^2 s^{-1} and λ = 150 nm. The τ_{g-p} vary approximately inversely with α. The optimal α was determined to be α ~ 0.002, corresponding to an optimal k_w = 2 x 10^{-4} s^{-1}, or a lifetime with respect to wall loss of τ_w = $1/k_w$ = 83 min. The τ_{g-p} for the experiment with the smallest seed concentration (1.4 x 10^3 μm^2 cm^{-3}) when α = 0.001 is 230 min, very similar to τ_w. As seed SA increases, the τ_{g-p} decrease to ~30 min for the highest seed SA. This difference in the relative values of τ_{g-p} vs. τ_w explains why the seed effect is seen most strongly when seed SA is less than ~ 3 x 10^3 μm^2 cm^{-3}, because this is the point at which the two timescales become highly competitive. Similarly, it

helps to explain why larger values of α do not lead to a noticeable seed SA dependence; when $\alpha > 0.1$ the $\tau_{g\text{-}p} = 2$ min for the experiment with the smallest seed SA.

S1.4.2. Dependence on VOC and OH concentrations

Calculations were performed to determine the magnitude of the wall-loss bias (R_{wall}) as a function of the initial [toluene] and [OH] based on the best-fit of the SOM to the low-NO_x set of experiments. Fig. S6 shows the variation in the end of experiment SOA concentration as a function of initial toluene and OH, and corresponds to the results shown in Fig. 3 in the main text.

S1.4.3. Sensitivity to C_w

As discussed in the main text, the sensitivity of our results to the assumed C_w is has been established by performing fits to the observations for varying values of C_w, from 0.01 to 10 mg m^{-3} for the suite of low-NO_x toluene photooxidation experiments (c.f. Fig. 4). Here, it was assumed that $k_w = 2 \times 10^{-4}$ s^{-1} and $\alpha = 2 \times 10^{-3}$, consistent with the optimized values determined in the main text. Good fits are obtained over the entire range of C_w. Above C_w = 0.2 mg m^{-3} (= 200 μg m^{-3}) the calculated wall-loss bias, R_{wall}, is constant. Below 0.2 mg m^{-3} the calculated R_{wall} falls off, reaching a second plateau at small C_w that is still above unity. The best-fit SOM parameters vary systematically with C_w (Fig. S7), apparently compensating for the varying levels of vapor wall-loss.

S1.5. Fitting of Historical Chamber Data

Beyond the toluene experiments, which are the focus of the manuscript, best-fit SOM parameters have been determined for a suite of historical photooxidation experiments conducted using a variety of other precursor compounds, both under low- and high-NO_x conditions. The historical experiments were all carried out in the prior 28 m^3 Caltech chamber. Experimental conditions are given in Tables S2 and S3. Fitting of the SOM to the observations is performed for these experiments assuming that $k_w = 1 \times 10^{-4}$ s^{-1}, $\alpha = 2 \times 10^{-3}$ and $C_w = 10$ mg m^{-3}. The results are relatively insensitive to C_w when varied over the range 2-24 mg m^{-3}, as discussed above. The value of k_w for the historical chamber is estimated to be slightly smaller than the optimal value determined for the new 24 m^3 chamber based on

consideration of the size-dependent particle wall-loss rates, as discussed in Section S1.4. Best fit SOM parameters for low-NO_x and high-NO_x conditions are given in Table S4. Wall-loss bias values were calculated in the same manner as for the toluene experiments. Experimental data and simulation results are shown in Fig. S8-9.

S1.6. References

1. A. W. H. Chan, K. E. Kautzman, P. S. Chhabra, J. D. Surratt, M. N. Chan, J. D. Crounse, A. Kurten, P. O. Wennberg, R. C. Flagan, J. H. Seinfeld, Secondary organic aerosol formation from photooxidation of naphthalene and alkylnaphthalenes: implications for oxidation of intermediate volatility organic compounds (IVOCs). Atmos. Chem. Phys. **9**, 3049-3060 (2009); doi: 10.5194/acp-9-3049-2009.
2. P. S. Chhabra, R. C. Flagan, J. H. Seinfeld, Elemental analysis of chamber organic aerosol using an aerodyne high-resolution aerosol mass spectrometer. Atmos. Chem. Phys. **10**, 4111-4131 (2010); doi: 10.5194/acp-10-4111-2010.
3. N. L. Ng, J. H. Kroll, A. W. H. Chan, P. S. Chhabra, R. C. Flagan, J. H. Seinfeld, Secondary organic aerosol formation from m-xylene, toluene, and benzene. Atmos. Chem. Phys. **7**, 3909-3922 (2007); doi: 10.5194/acp-7-3909-2007.
4. P. S. Chhabra, N. L. Ng, M. R. Canagaratna, A. L. Corrigan, L. M. Russell, D. R. Worsnop, R. C. Flagan, J. H. Seinfeld, Elemental composition and oxidation of chamber organic aerosol. Atmos. Chem. Phys. **11**, 8827-8845 (2011); doi: 10.5194/acp-11-8827-2011.
5. C. L. Loza, P. S. Chhabra, L. D. Yee, J. S. Craven, R. C. Flagan, J. H. Seinfeld, Chemical aging of m-xylene secondary organic aerosol: laboratory chamber study. Atmos. Chem. Phys. **12**, 151-167 (2012); doi: 10.5194/acp-12-151-2012.
6. C. D. Cappa, X. Zhang, C. L. Loza, J. S. Craven, L. D. Yee, J. H. Seinfeld, Application of the Statistical Oxidation Model (SOM) to secondary organic aerosol formation from photooxidation of C12 Alkanes. Atmos. Chem. Phys. **13**, 1591-1606 (2013); doi: 10.5194/acp-13-1591-2013.
7. L. Hildebrandt, N. M. Donahue, S. N. Pandis, High formation of secondary organic aerosol from the photo-oxidation of toluene. Atmos. Chem. Phys. **9**, 2973-2986 (2009); doi: 10.5194/acp-9-2973-2009.
8. E. A. Weitkamp, A. M. Sage, J. R. Pierce, N. M. Donahue, A. L. Robinson, Organic aerosol formation from photochemical oxidation of diesel exhaust in a smog chamber. Environmental Science & Technology **41**, 6969-6975 (2007); doi: 10.1021/es070193r.
9. J. R. Pierce, G. J. Engelhart, L. Hildebrandt, E. A. Weitkamp, R. K. Pathak, N. M. Donahue, A. L. Robinson, P. J. Adams, S. N. Pandis, Constraining Particle Evolution from Wall Losses, Coagulation, and Condensation-Evaporation in Smog-Chamber Experiments: Optimal Estimation Based on Size Distribution Measurements. Aerosol Science and Technology **42**, 1001-1015 (2008); doi: 10.1080/02786820802389251.

10. Seinfeld, J. H. and Pandis, S. N.: Atmospheric chemistry and physics: From air pollution to climate change, Wiley, New Jersey, 612pp., 2006

11. C. D. Cappa, K. R. Wilson, Multi-generation gas-phase oxidation, equilibrium partitioning, and the formation and evolution of secondary organic aerosol. Atmos. Chem. Phys. **12**, 9505-9528 (2012); doi: 10.5194/acp-12-9505-2012.

12. J. Lee-Taylor, S. Madronich, B. Aumont, A. Baker, M. Camredon, A. Hodzic, G. S. Tyndall, E. Apel, R. A. Zaveri, Explicit modeling of organic chemistry and secondary organic aerosol partitioning for Mexico City and its outflow plume. Atmospheric Chemistry and Physics **11**, 13219-13241 (2011); doi: 10.5194/acp-11-13219-2011.

13. J. F. Pankow, An absorption-model of the gas aerosol partitioning involved in the formation of secondary organic aerosol. Atmos. Environ. **28**, 189-193 (1994); doi: 10.1016/1352-2310(94)90094-9.

14. M. Shiraiwa, L. D. Yee, K. A. Schilling, C. L. Loza, J. S. Craven, A. Zuend, P. J. Ziemann, J. H. Seinfeld, Size distribution dynamics reveal particle-phase chemistry in organic aerosol formation. Proc. Nat. Acad. Sci., (2013); doi: 10.1073/pnas.1307501110.

15. A. Matsunaga, P. J. Ziemann, Gas-Wall Partitioning of Organic Compounds in a Teflon Film Chamber and Potential Effects on Reaction Product and Aerosol Yield Measurements. Aerosol Sci. Technol. **44**, 881-892 (2010); doi: 10.1080/02786826.2010.501044.

16. P. H. McMurry, D. Grosjean, Gas and aerosol wall losses in Teflon film smog chambers. Environ. Sci. Technol. **19**, 1176-1182 (1985); doi: 10.1021/es00142a006.

17. J. G. Crump, J. H. Seinfeld, Turbulent deposition and gravitational sedimentation of an aerosol in a vessel of arbitrary shape. J Aerosol Sci **12**, 405-415 (1981); doi: 10.1016/0021-8502(81)90036-7.

18. C. L. Loza, A. W. H. Chan, M. M. Galloway, F. N. Keutsch, R. C. Flagan, J. H. Seinfeld, Characterization of Vapor Wall Loss in Laboratory Chambers. Environ. Sci. Technol. **44**, 5074-5078 (2010); doi: 10.1021/es100727v.

19. C. L. Loza, J. S. Craven, L. D. Yee, M. M. Coggon, R. H. Schwantes, M. Shiraiwa, X. Zhang, K. A. Schilling, N. L. Ng, M. R. Canagaratna, P. J. Ziemann, R. C. Flagan, J. H. Seinfeld, Secondary organic aerosol yields of 12-carbon alkanes. Atmos. Chem. Phys. Discuss. **13**, 20677-20727 (2013); doi: 10.5194/acpd-13-20677-2013.

20. A. W. H. Chan, M. N. Chan, J. D. Surratt, P. S. Chhabra, C. L. Loza, J. D. Crounse, L. D. Yee, R. C. Flagan, P. O. Wennberg, J. H. Seinfeld, Role of aldehyde chemistry and NOx concentrations in secondary organic aerosol formation. Atmospheric Chemistry and Physics **10**, 7169-7188 (2010); doi: 10.5194/acp-10-7169-2010.

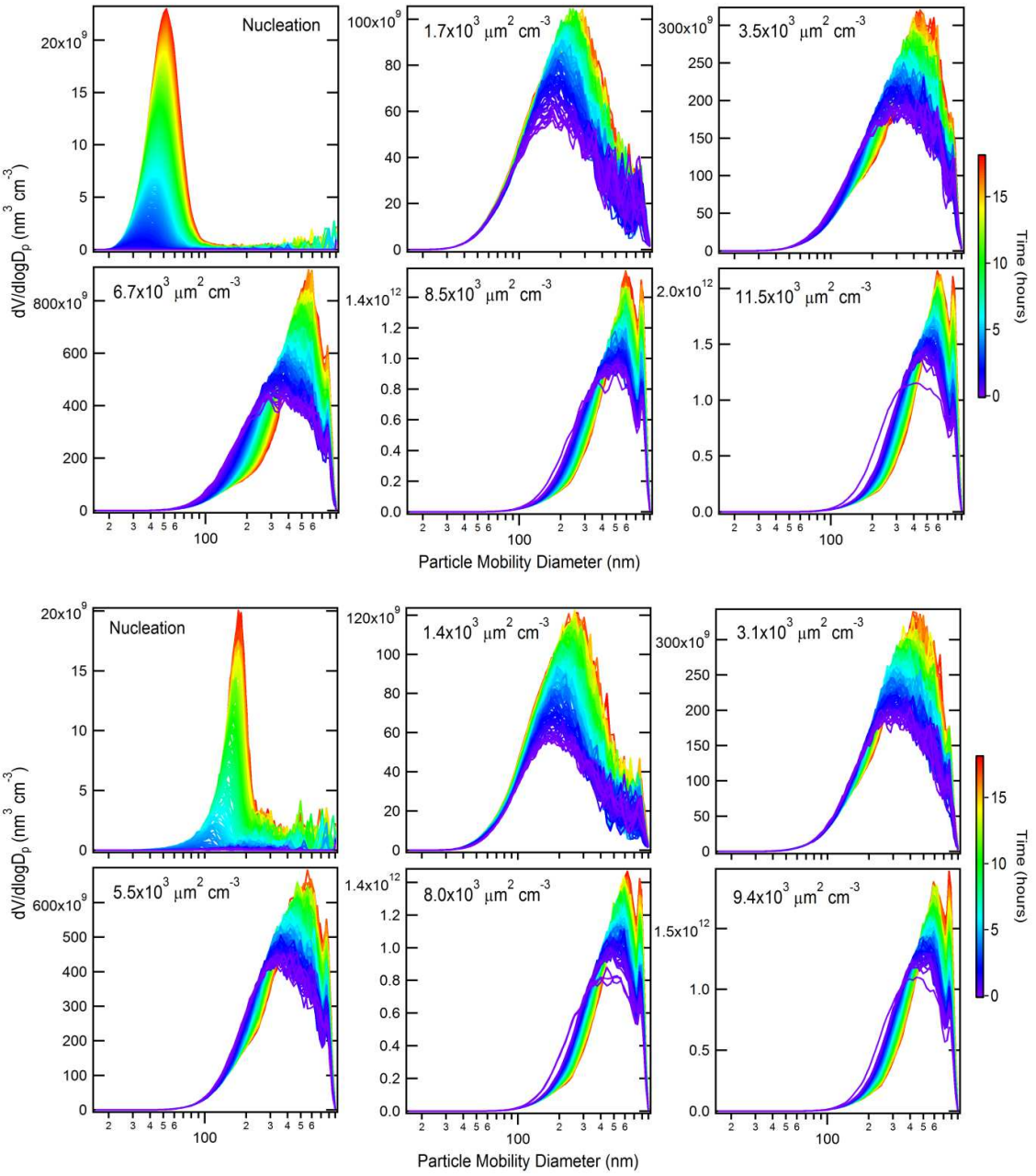

Fig. S1: Time-dependent volume distributions ($dV/dlogD_p$) of AS seed and organic aerosols after 0 - 18 h of photoxidation of toluene under (top panels) high-NO_x and (bottom panels) low-NO_x conditions. Distributions are colored according to the time after lights were turned on. The lower bound wall-loss correction is used here. For the experiments at higher seed SA, the influence of coagulation on the particle evolution is evident.

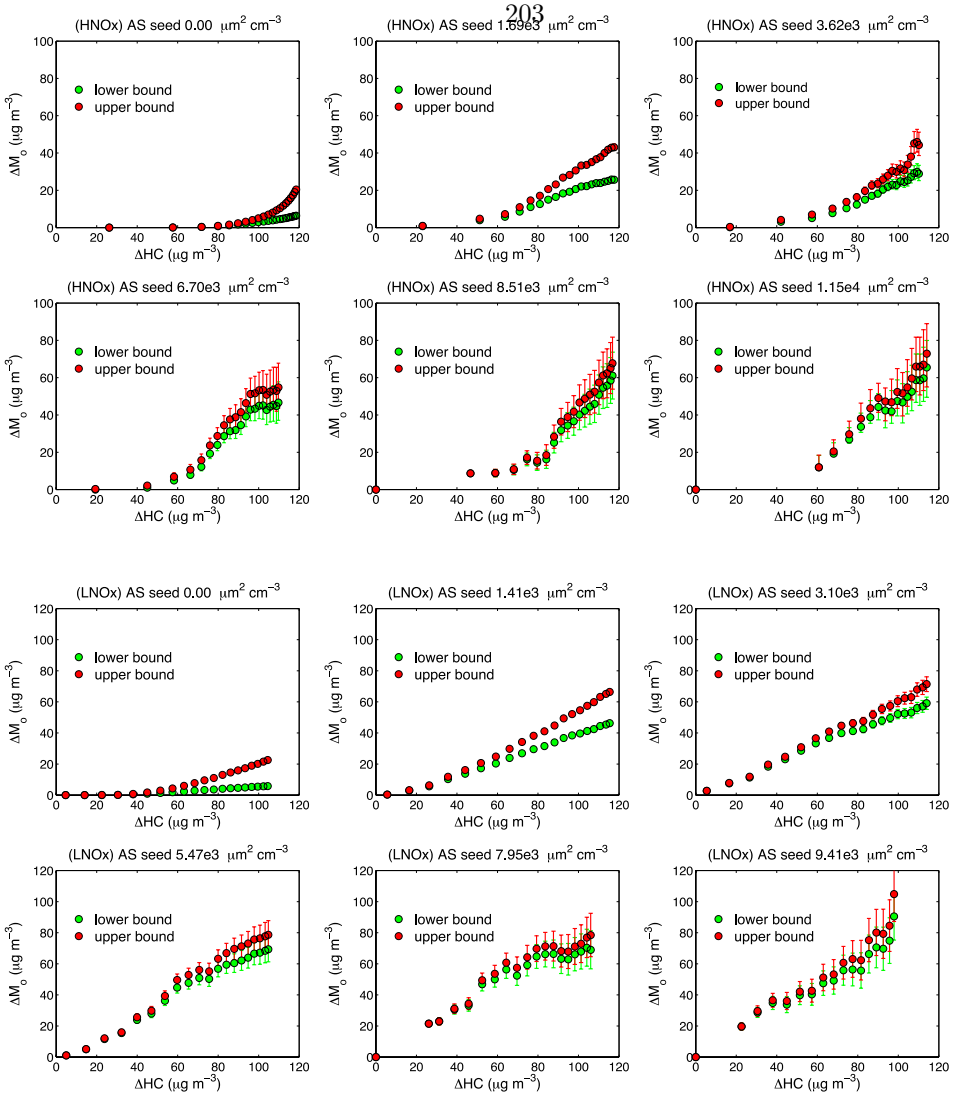

Fig. S2: Time-dependent SOA growth curves for toluene photooxidation under high-NO_x (HNO_x) and low-NO_x (LNO_x) conditions. Error bars come from the 95% confidence interval associated with determining the size-dependent first-order wall-loss rate for dry inert ammonium sulfate ($(NH_4)_2SO_4$) particles.

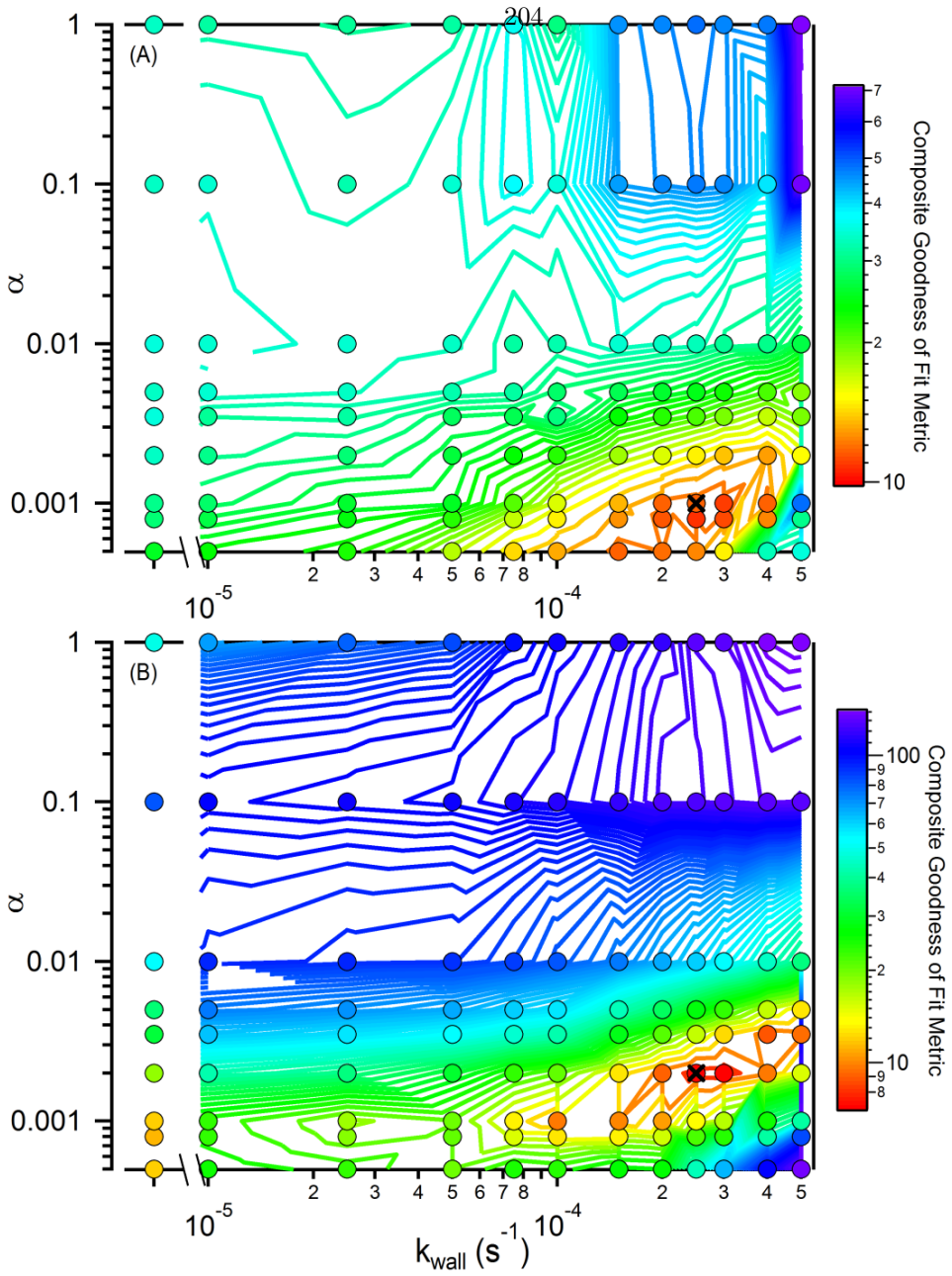

Fig. S3: Calculated composite reduced chi-square values for (A) high-NO_x and (B) low-NO_x toluene experiments as a function of the mass accommodation coefficient, α, and the first order wall-loss rate coefficient, k_w. The colors indicate the magnitude of the calculated composite reduced goodness of fit metric, with the contours based on the circles. The black x indicates the optimal value: $k_w = 2.5 \times 10^{-4}$ s^{-1} and $\alpha = 1 \times 10^{-3}$ (high-NO_x) and $k_w = 2.5 \times 10^{-4}$ s^{-1} and $\alpha = 2 \times 10^{-3}$ (low-NO_x).

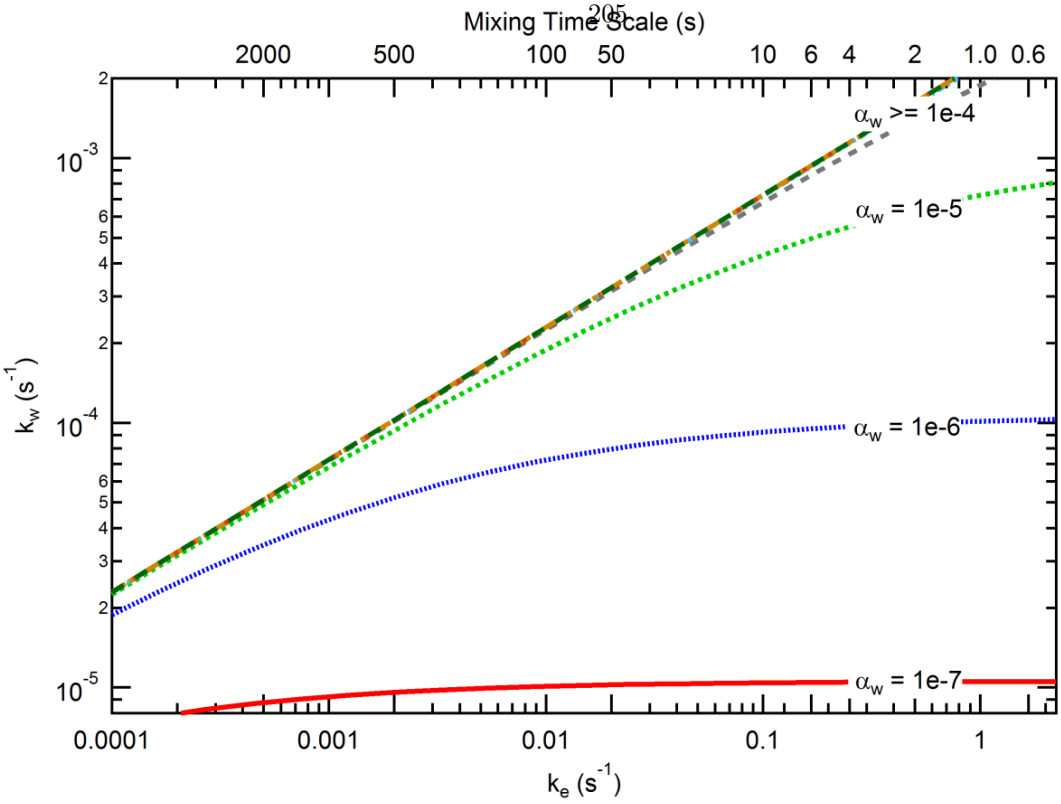

Fig. S4: Calculated wall-loss coefficients k_w as a function of the coefficient of eddy diffusion, k_e, which characterizes the state of turbulent diffusion in the chamber, for different values of the mass accommodation coefficient onto the walls, α_w. The top axis shows the time-scales corresponding to the eddy diffusion coefficients.

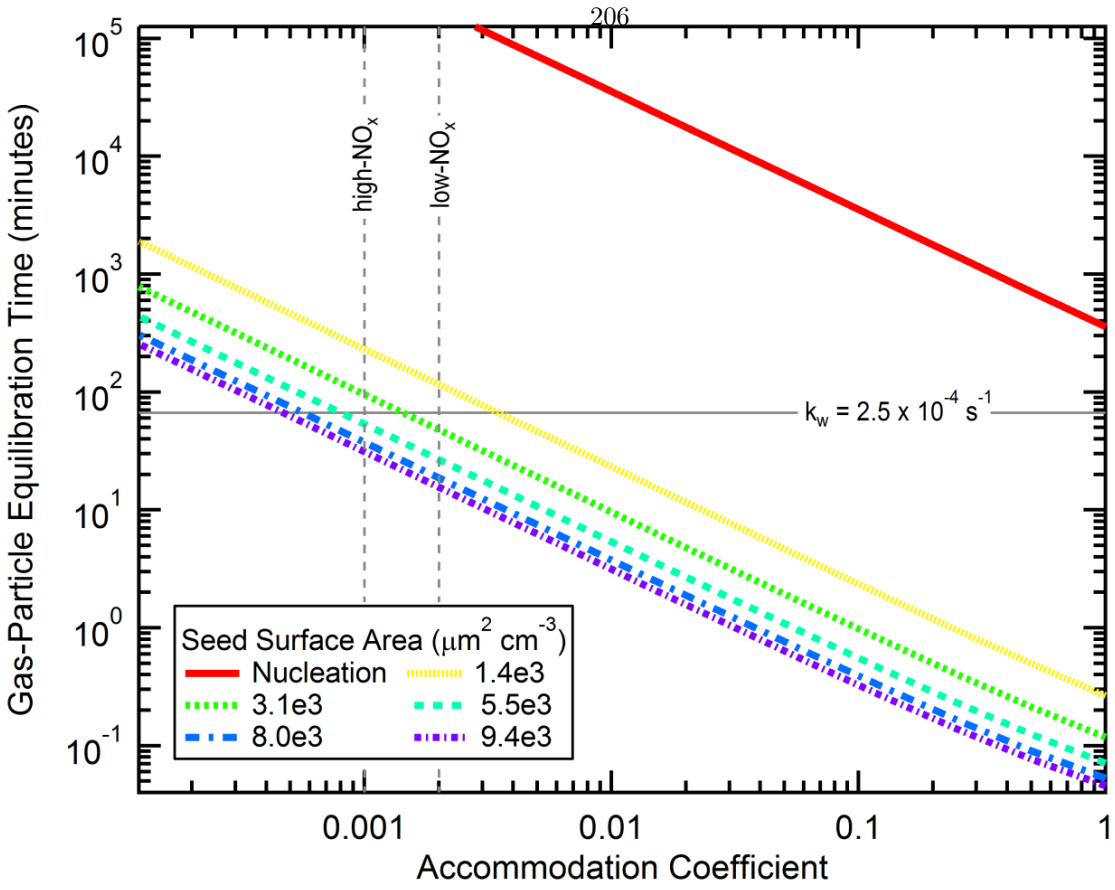

Fig. S5: Calculated gas-particle equilibration time as a function of the gas-particle mass accommodation coefficient, α, for different seed surface areas corresponding to the low-NO_x experiments. The horizontal gray line indicates the timescale associated with vapour wall-loss for $k_w = 2.5 \times 10^{-4}$ s^{-1}. The vertical dashed gray lines indicate the optimal values of α determined here for the high- and low-NO_x toluene systems. For the nucleation experiments, it is assumed that the particles are 10 nm diameter.

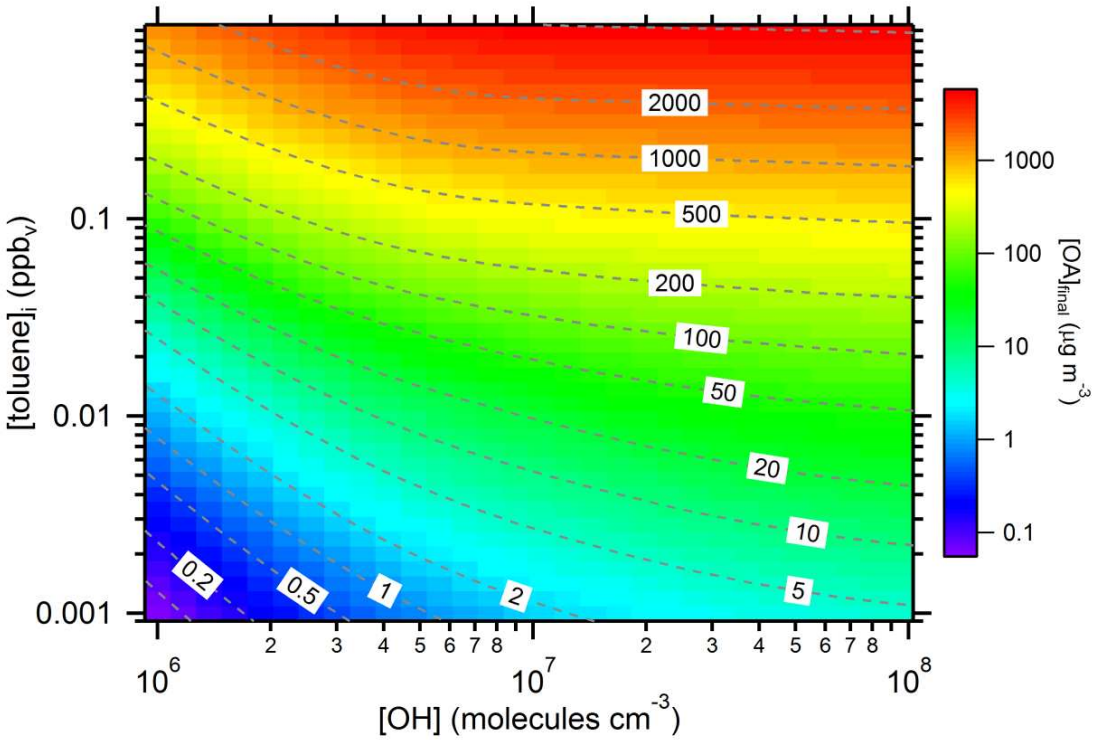

Fig. S6: Calculated end-of-experiment SOA mass concentrations corresponding to the results shown in Figure 3. The SOA concentration is shown as a function of initial toluene concentration and OH concentration when k_w = 2.5 x 10^{-4} s^{-1} and C_w = 10 mg m^{-3}. The SOA concentrations for a given [toluene] and [OH] are indicated by colors and contours. Results are based on the optimal fit of the SOM to the low-NO_x experiments.

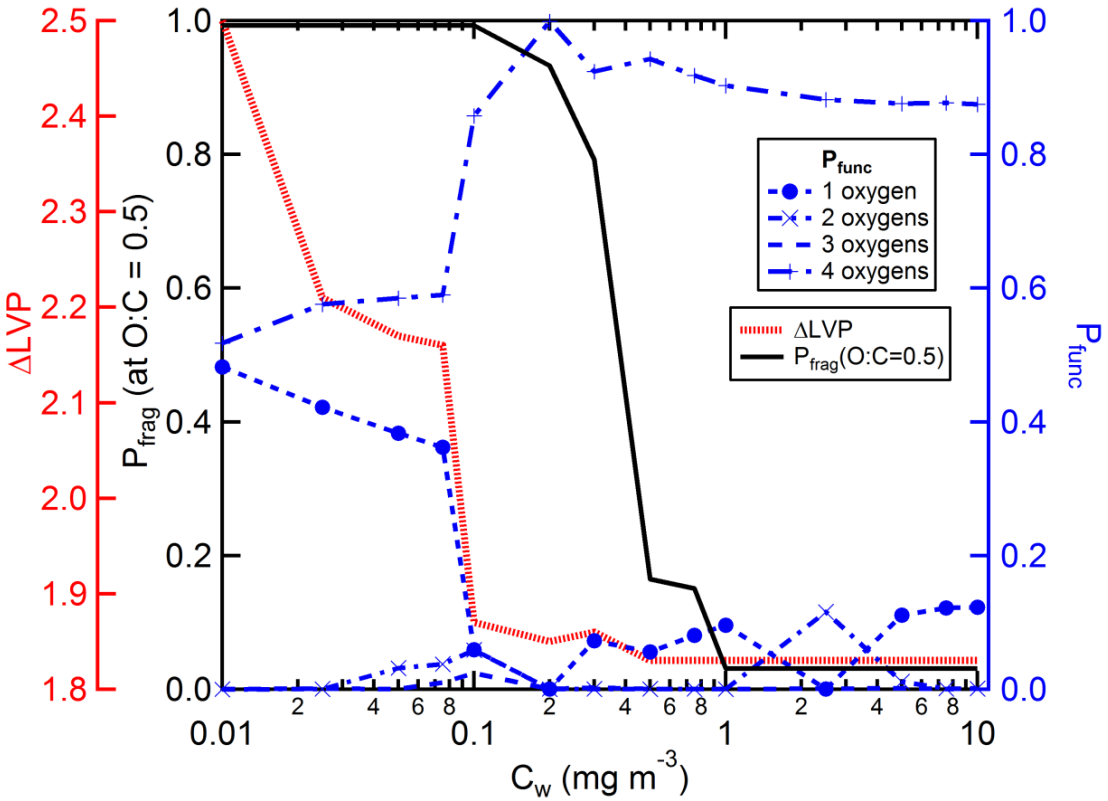

Fig. S7: The best-fit SOM parameters determined at each C_w corresponding to the results shown in Fig. 4 in the main text. The fragmentation probabilities, P_{frag}, were calculated from the best-fit m_{frag} values and Eqn. S3 using O:C = 0.5. ΔLVP corresponds to the decrease in vapor saturation concentration per oxygen added and P_{func} corresponds to the probability of adding 1, 2, 3 or 4 oxygen atoms per reaction.

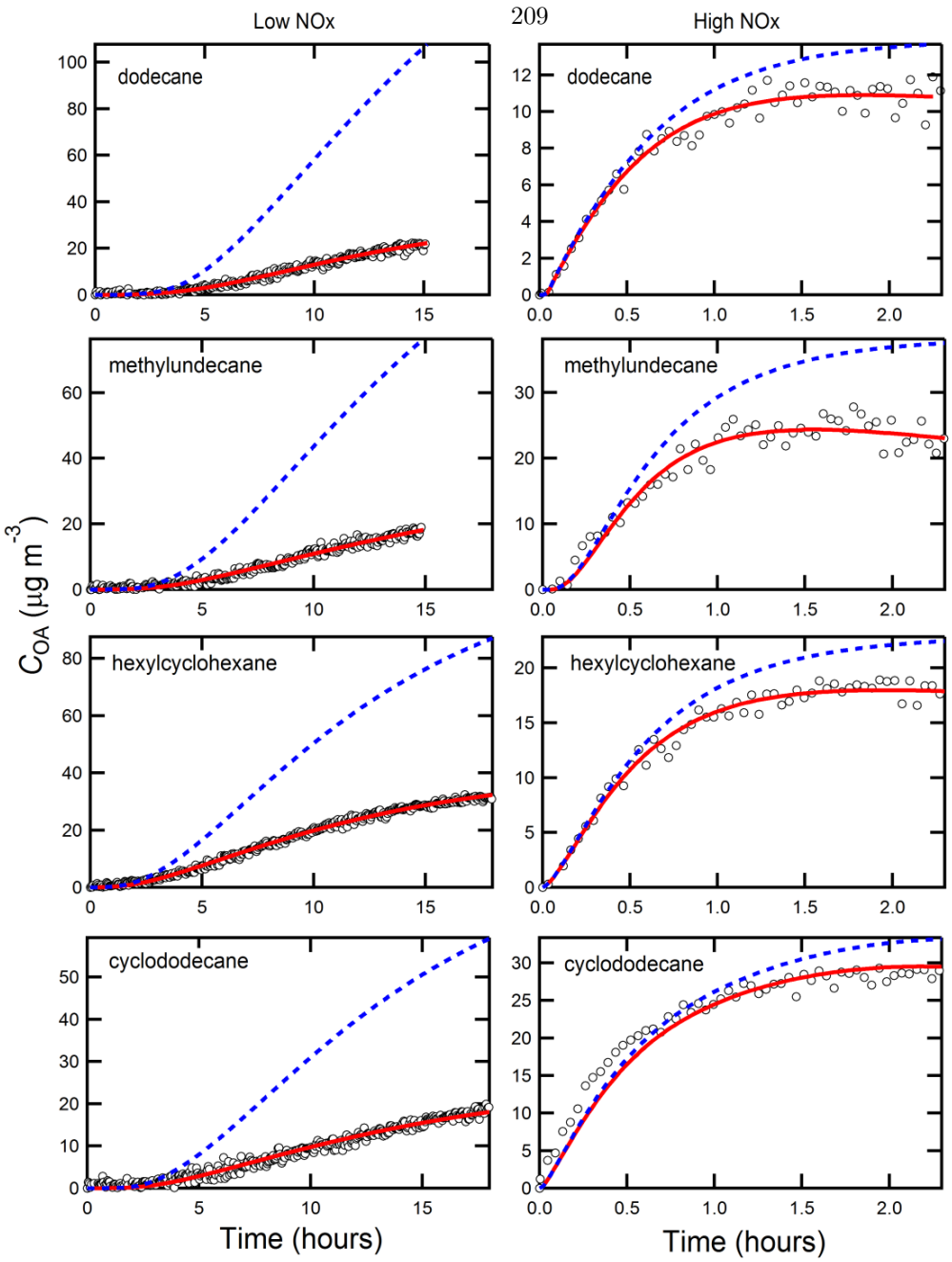

Fig. S8: Results from historical low (left panels) and high (right panels) NO_x SOA formation experiments for alkane photooxidation (open circles). The solid red lines are best-fit SOM results when wall losses are accounted for assuming that k_w = 1 x 10^{-4}, α = 1 and C_w = 10 μg m^{-3}. The blue dashed lines are the simulated SOA concentrations when wall-loss is turned off, but the SOM parameters determined from the best-fit with wall-loss on are retained.

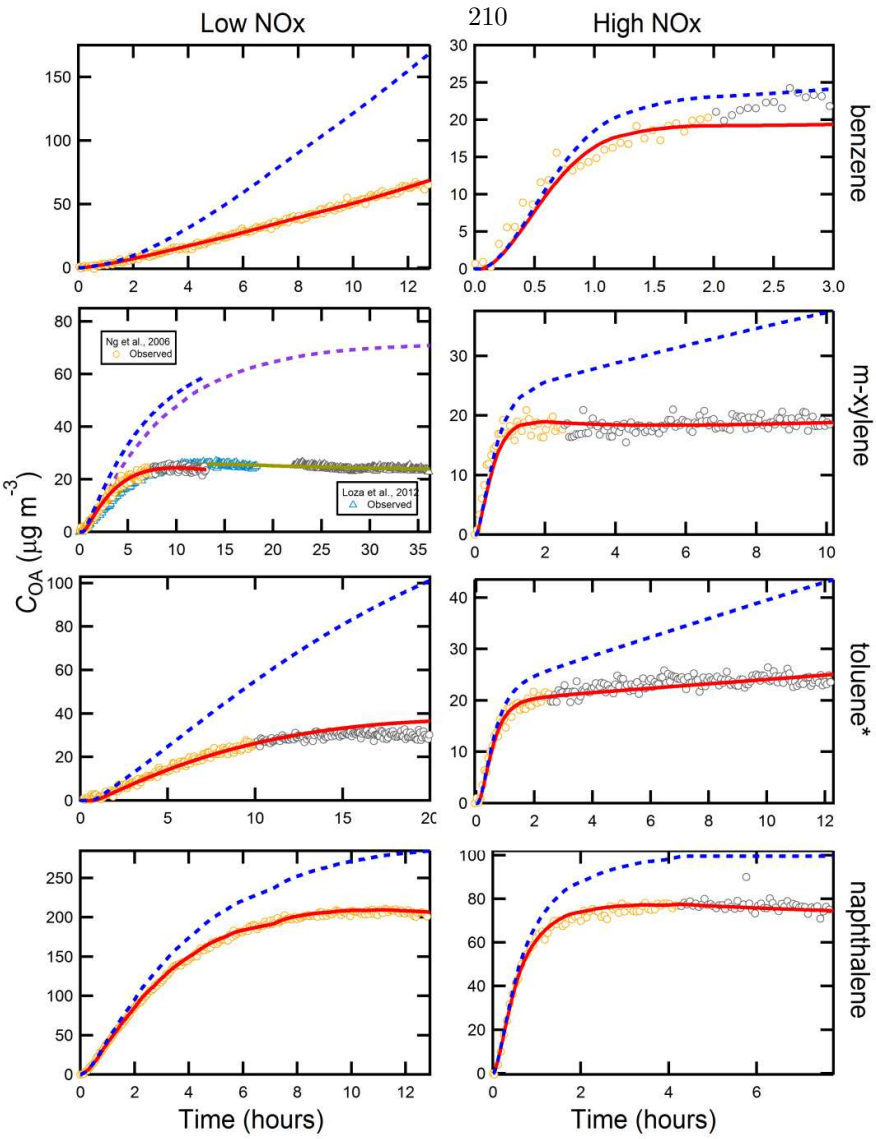

Fig. S9: Same as Fig. S3, but for aromatics. Importantly, the toluene experimental results are from Ng et al. (3), not from the current set of experiments. For each experiment, data collected over the full experiment time is shown. However, the SOM fitting has been restricted to the periods shown as colors other than gray (orange or blue). The gray points are data that were collected, but not used in fitting. These data have been excluded to be consistent with the range of data considered in Ng et al. (3) and Chan et al. (1), where 2-product fits have been performed. For m-xylene, low-NO_x, fits to data from Ng et al. (3) and Loza et al. (5) are shown separately.

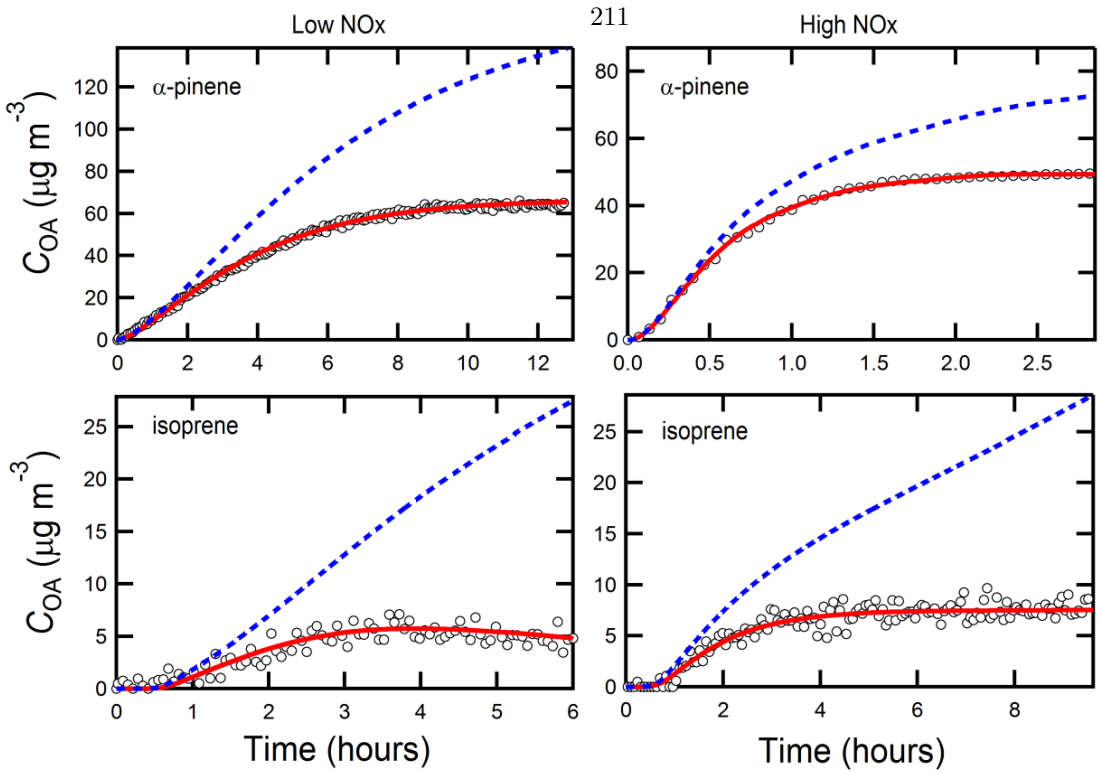

Fig. S10: Same as Fig. S8, but for α-pinene (4) and isoprene (20) photooxidation.

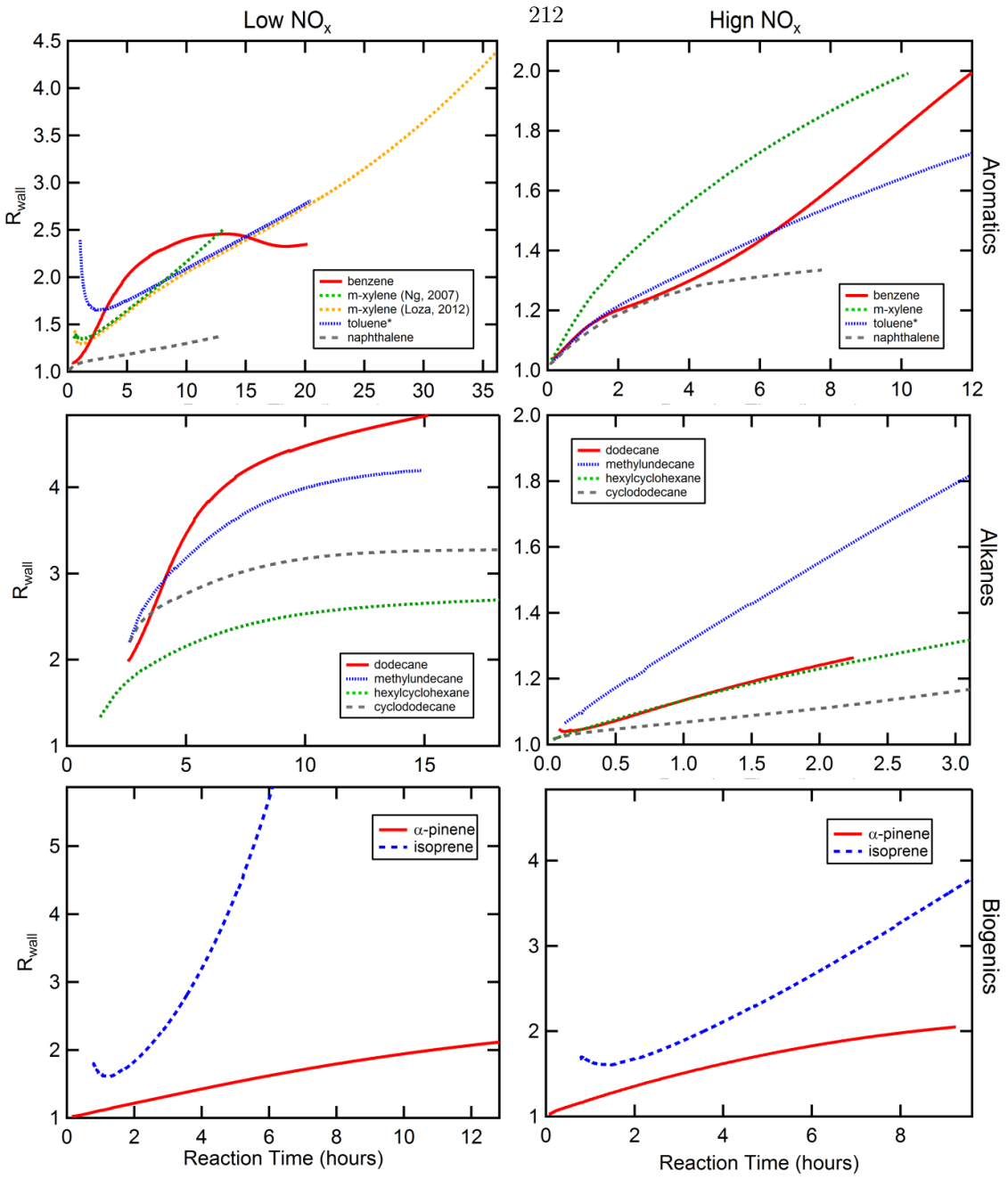

Fig. S11: Calculated time-dependent R_{wall} values for historical experiments based on the results shown in Fig. S8 - Fig. S10. Results are grouped according to species type and NO_x level. Left panels are low-NO_x and right panels high-NO_x results. Note that the toluene results in the top panels are based on data presented in Ng et al. (3), not from the current set of experiments. Results are shown for m-xylene, low-NO_x for two separate experimental data sets: Ng et al. (3) and Loza et al. (5). The presented results are limited to the period where $C_{OA} > 0.5$ μg m^{-3}.

Table S1. Experimental conditions for toluene SOA photooxidation experiments in the 24 m^3 Caltech chamber.

	Exp. (#)	$[HC]_0$ (ppb)	$[NO]_0$ (ppb)	$[NO_2]_0$ (ppb)	Initial [VOC]/[NO_x] (ppbC/ppb)	Additional NO injection	Initial seed surface area (μm^2 cm^{-3})	Initial surface area ratio (Aerosol/Wall)
High NO_x	1	~36.8	~ 19.0	~ 34.4	4.8	yes	~ 0	~ 0
	2	~38.7	~ 19.6	~ 32.2	5.2	yes	1.69×10^3	8.57×10^{-4}
	3	~37.9	~ 15.5	~ 34.9	5.3	yes	3.51×10^3	1.88×10^{-3}
	4	~37.9	~ 17.5	~ 31.7	5.4	yes	6.70×10^3	3.32×10^{-3}
	5	~38.2	~ 13.1	~ 31.5	6.0	yes	8.51×10^3	4.83×10^{-3}
	6	~38.7	~ 16.8	~ 35.3	5.2	yes	1.15×10^4	5.72×10^{-3}
Low NO_x	1	~33.9	< DL[c]	< DL	--	--	~ 0	~ 0
	2	~37.6	< DL	< DL	--	--	1.41×10^3	1.03×10^{-3}
	3	~37.3	< DL	< DL	--	--	3.10×10^3	2.13×10^{-3}
	4	~36.8	< DL	< DL	--	--	5.47×10^3	4.07×10^{-3}
	5	~38.7	< DL	< DL	--	--	7.95×10^3	5.17×10^{-3}
	6	~37.9	< DL	< DL	--	--	9.41×10^3	6.70×10^{-3}

[a] Detection limits (DL) for O_3, NO, and NO_2 are 0.5 ppb, 0.4 ppb, and 0.4 ppb, respectively.

Table S2. Conditions for low-NO_x experiments in the 28 m^3 Caltech chamber.

VOC	Ref	Date [mm/dd/yy]	$[VOC]_0$ (ppb)	$[NO_x]_0$ (ppb)	Initial [VOC]/[NO_x] (ppbC/ppb)	[OH][a] (molecules/cm^3)	% Yield at C_{OA} = 10 μg m^{-3}	k_{OH} (cm^3 molecules^{-1} s^{-1})
n-dodecane	(6)	03/16/11	34.0	<2	--	$2.5x10^6$	6.1	$1.34x10^{-11}$
methylundecane	(6)	02/25/11	28.1	<2	--	$2.4x10^6$	7.2	$1.34x10^{-11}$
cyclododecane	(6)	02/23/11	9.8	<2	--	$2.7x10^6$	17.2	$1.34x10^{-11}$
hexylcyclohexane	(6)	03/21/11	15.6	<2	--	$3.0x10^6$	15.4	$1.34x10^{-11}$
benzene	(3)	11/04/06	414	<2	--	$3x10^6$	23.8	$1.22x10^{-12}$
toluene[c]	(3)	10/24/06	52.7	<2	--	$3.3x10^6$	26.7	$5.63x10^{-12}$
m-xylene[d]	(3)	10/27/06	19.3	<2	--	$3x10^6$	28.2	$2.31x10^{-11}$
m-xylene[d]	(5)	10/11/10	29.2	<2	--	$2.5x10^6$	21.4	$2.31x10^{-11}$
naphthalene	(1, 2)	08/13/08	31.5	2	--	$2x10^6$	19.0	$2.44x10^{-11}$
α-pinene	(4)	06/02/10	66.2	<2	--	$3x10^6$	36.8	$5.3x10^{-10}$
isoprene	(20)	02/25/09	49	<2	--	$2x10^6$	4.3[b]	$1x10^{-10}$

[a] Average over the experiment
[b] Maximum yield, since maximum C_{OA} < 10 μg m^{-3}.
[c] From historical experiments by Ng et al. (2007), not the current set of experiments.
[d] m-xylene data are available from two independent sets of experiments.

Table S3. Conditions for high-NO_x experiments in the 28 m^3 Caltech chamber.

VOC	Ref.	Date [mm/dd/yy]	$[VOC]_0$ (ppb)	$[NO]_0$ & $[NO_2]_0$ (ppb)	Initial $[VOC]/[NO_x]$ (ppbC/ppb)	$[OH]^a$ (molecules/cm^3)	% Yield at C_{OA} = 10 μg m^{-3}	k_{OH} (cm^3 $molecules^{-1}$ s^{-1})
n-dodecane	(6)	05/12/11	32.2	343/--	1.13	$4.5x10^7$	6.2	$1.34x10^{-11}$
methylundecane	(6)	03/01/11	72.4	366/--	2.37	$3.3x10^7$	5.1	$1.34x10^{-11}$
cyclododecane	(6)	05/23/11	13.8	362/--	0.46	$2.7x10^7$	38.3	$1.34x10^{-11}$
hexylcyclohexane	(6)	03/22/11	22.1	320/--	0.83	$4.1x10^7$	12.3	$1.34x10^{-11}$
benzene	(3)	01/15/07	336	83/86	11.9	$3.2x10^7$	15.6	$1.22x10^{-12}$
toluene[c]	(3)	10/14/06	138	373/568	1.03	$3.6x10^7$	8.3	$5.63x10^{-12}$
m-xylene	(3)	10/05/06	89.8	469/474	0.76	$4.2x10^7$	3.9	$2.31x10^{-11}$
naphthalene	(1, 2)	08/14/08	48.6	404/171	0.85	$2.5x10^7$	11.2	$2.44x10^{-11}$
α-pinene	(4)	06/03/10	44.9	446/398	0.53	$1.4x10^7$	9.5	$5.3x10^{-11}$
isoprene	(20)	04/04/09	268	535/402	1.43	$6.6x10^6$	1.0[b]	$1x10^{-11}$

[a] For all high-NOx experiments HONO was used as the OH source. The [OH] was not constant in time, but decreased rapidly from the start of the experiment by at least an order of magnitude. The [OH] derived from the first [VOC] measurement after the lights were turned on is given here.
[b] Maximum yield, since maximum C_{OA} < 10 μg m^{-3}.
[c] From historical experiments by Ng et al. (2007), not the current set of experiments.

Table S4. Derived SOM parameters for the experiments when vapor wall-loss is accounted for (assuming C_w = 10 µg m^{-3}).

VOC[a]	Fragmentation	ΔLVP	P1	P2	P3	P4	χ^2_{red}[b]
		Low NO_x					
toluene (this study)	5	1.83	0.123	0.001	0.002	0.875	1.74
n-dodecane (6)	0.671	1.58	0.977	0.016	0.003	0.004	1.47
methylundecane (6)	0.433	1.92	0.997	0.000	0.001	0.002	1.33
cyclododecane (6)	1.56	1.90	0.994	0.000	0.001	0.005	1.73
hexylcyclohexane (6)	0.78	1.84	0.885	0.106	0.001	0.008	0.56
benzene[c] (3)	0.01	2.29	0.284	0.000	0.644	0.072	0.42
toluene[c] (3)	0.01	1.88	0.001	0.001	0.727	0.271	1.36
m-xylene[c] (3)	0.245	1.96	0.000	0.085	0.836	0.079	0.57
m-xylene[c] (5)	0.069	1.88	0.285	0.000	0.613	0.101	0.20
naphthalene (1, 2)	0.072	1.76	0.382	0.027	0.431	0.161	0.04
α-pinene (4)	0.151	1.91	0.262	0.619	0.075	0.044	0.19
isoprene (20)	0.01	2.23	0.000	0.146	0.826	0.028	1.61
		High NO_x					
toluene (this study)	1.02	1.42	0.000	0.000	1.000	0.000	1.10
n-dodecane (6)	0.188	1.45	0.963	0.000	0.001	0.036	0.07
methylundecane (6)	0.188	1.12	0.263	0.277	0.455	0.005	0.61
cyclododecane (6)	0.01	1.69	0.664	0.002	0.004	0.33	0.64
hexylcyclohexane (6)	0.153	1.75	0.832	0.086	0.055	0.028	0.14
benzene[c] (3)	0.912	1.47	0.105	0.001	0.893	0.001	1.15
m-xylene[c] (3)	0.18	1.54	0.000	0.000	1.000	0.000	0.64
toluene[c] (3)	0.039	1.46	0.001	0.001	0.906	0.094	1.13
naphthalene[c] (1, 2)	0.64	1.41	0.835	0.001	0.002	0.162	0.17
α-pinene (4)	0.080	1.81	0.193	0.694	0.101	0.012	0.04
isoprene (20)	0.322	2.23	0.679	0.321	0.000	0.000	0.79

[a] The toluene experiments from this study were conducted in the 24 m^3 Caltech chamber (i.e. "new" experiments) and simulated using k_w = 2.5 x 10^{-4} s^{-1} and the experimentally-determined optimal α (~2 x 10^{-3}). All other experiments, including the toluene experiments from (3) were conducted in the 28 m^3 Caltech chamber (i.e. "historical" experiments") and simulated using k_w = 1 x 10^{-4} s^{-1} and α = 1.

[b] The reduced χ^2 associated with the best fit.

[c] Fits were performed over the ranges shown in Fig. S8.

Appendix B

Supplemental Material Chapter 2

In this section we show that the SVOOA/ΔCO enhancement ratios measured at the Pasadena ground site cannot be explained even if 100% of the NMOG is assumed to have reacted after 0.45 days of photochemical aging, and even if the highest SOA yields reported by *Gordon et al.* (2013) are used. To do so, we have conducted additional analyses assuming $Y_{gas} = 16\%$ and $Y_{gas} = 25\%$, which are the upper limits of the LEV1 and LEV2 vehicle classes, respectively, reported by *Gordon et al.* (2013). As shown in Figures 2.5B-C, although increasing Y_{gas} to its upper limit does improve agreement to some extent, the predicted and required yields still differ by more than a factor of 3 even when using the highest yields reported by *Gordon et al.* (2013). To account for the uncertainty associated with calculating the fraction of emitted SOA precursors that have undergone chemical reaction after 0.45 days of photochemical aging, an additional sensitivity analysis was conducted in which 100% of the emitted NMOG is assumed to have reacted (see Figure B.2). As shown in Figure B.2, assuming 100% conversion of NMOG effectively reduces the required SOA mass yields by a factor of 2. The predicted yields shown in Figure B.2C are still lower than the required yields by a factor of $\sim$1.7. We emphasize that there is a significant lack of closure between expected and observed organic aerosol concentrations attributable to fossil-fuel emissions even when assuming 100% NMOG conversion and an LDGV fleet-averaged SOA mass yield of 25%. Both assumptions are expected to be very unrepresentative of ambient conditions in California.

Bibliography

Gordon, T. D., Presto, A. A., May, A. A., Nguyen, N. T., Lipsky, E. M., Donahue, N. M., Gutierrez, A., Zhang, M., Maddox, C., Rieger, P., Chattopadhyay, S., Maldonado, H., Maricq, M. M., and Robinson, A. L.: Secondary organic aerosol formation exceeds primary particulate matter emissions for light-duty gasoline vehicles, *Atmos. Chem. Phys.*, *13*, 23173-23216, doi:10.5194/acpd-13-23173-2013, 2013.

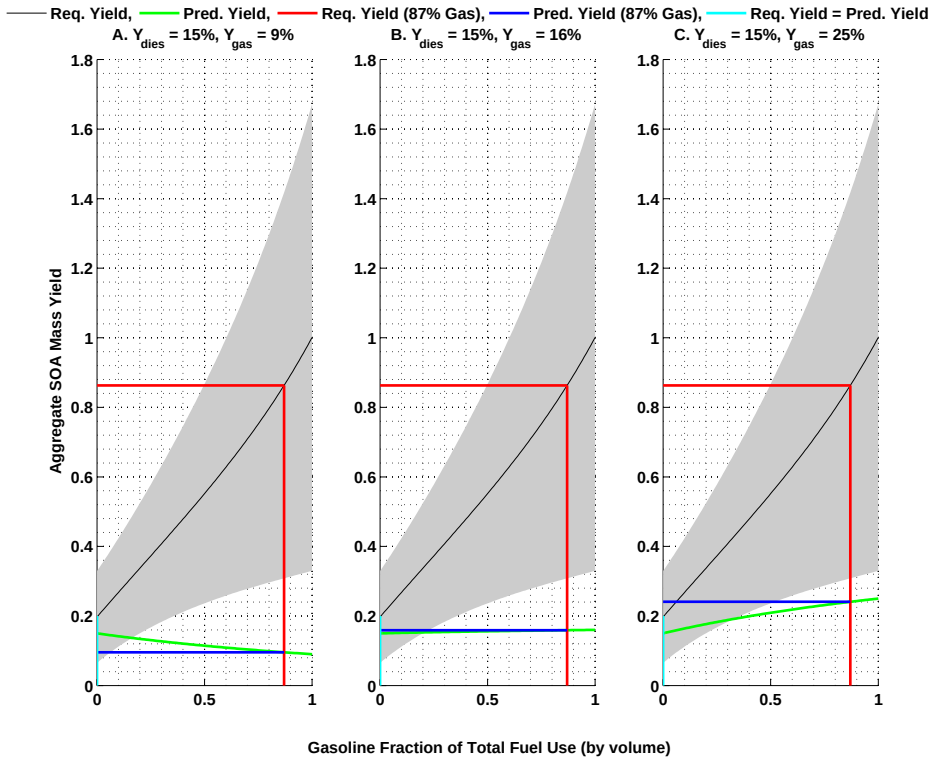

Figure B.1: Same as Figure 3, except emission factors for gasoline-fueled vehicles and aggregate SOA mass yields are based on the experimentally derived values reported in *Gordon et al.* (2013). (A) Aggregate SOA mass yield for gasoline exhaust is 9%, which is considered representative of the California LDGV fleet. (B) Aggregate SOA mass yield for gasoline exhaust is 16%, which is the upper limit for LEV1 vehicles (*Gordon et al.*, 2013). (C) Aggregate SOA mass yield for gasoline exhaust is 25%, which is the upper limit for LEV2 vehicles (*Gordon et al.*, 2013). Predicted yield error bars are not included because the predicted yields in (C) are a conservative upper limit.

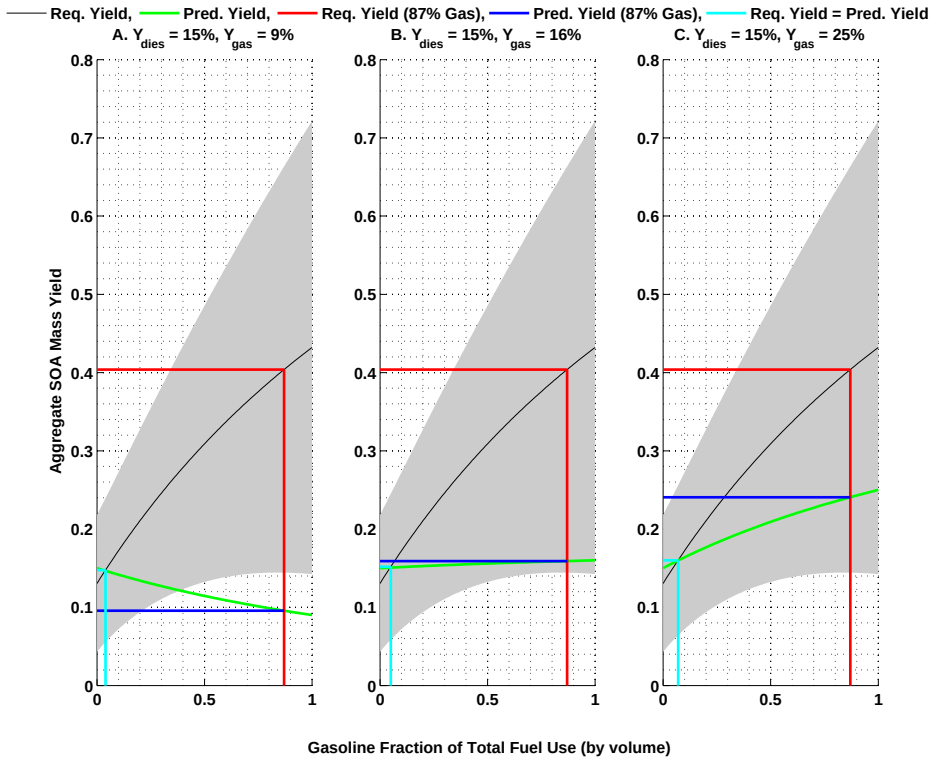

Figure B.2: Same as Figure 2.5, except 100% of the gas-phase emissions are assumed to have reacted after 0.45 days of photochemical aging.

Appendix C

Supplemental Material for Chapter 4

C.1 FLEXPART

The FLEXPART model used in this study has been modified to use time-averaged winds from the Weather Research and Forecasting (WRF version 3.3) meteorology model instead of instantaneous winds to reduce uncertainties within the FLEXPART model (*Nehrkorn et al.*, 2010). The WRF output has a horizontal grid of 4 km x 4 km, with a temporal resolution of 30 min and 60 vertical levels. In reverse mode, FLEXPART releases virtual tracer particles at receptors (in this study, a receptor is the instantaneous spatial and temporal location of the Pasadena ground site, the Twin Otter aircraft, or the P3 aircraft) and integrates their trajectories backward in time using predicted wind fields combined with random turbulent motion. The turbulent transport is parametrized in FLEXPART. Based on a parametrization from *Hanna* (1982), FLEXPART uses the boundary layer height, Monin-Obukhov length and friction velocity to calculate a turbulent vertical velocity and its standard deviation at a given trajectory position. Based on those two terms, a random distribution of turbulent velocity is calculated and then used in the calculation of the vertical transport of the trajectories in the boundary layer. FLEXPART then maps the individual particles to a grid (8 km x 8 km horizontal resolution) every 2 h over a 24-h period and calculates the average particle residence times in each grid box. Surface-level contributions to air masses are determined by averaging the residence times of particles between the surface and 200 m altitude. The species contributions from air masses aloft may be estimated based on mean column residence times, but are not included in this study because surface emissions are expected to influence measurements most strongly at low altitudes ($\sim$300 m above ground). WRF meteorological fields were generated by NOAA for use in FLEXPART, and were not used to drive CMAQ because the WRF map projection is not the same as the map projection on which the ARCTAS-CARB emission inventory is based. However, the agreement between the WRF meteorological fields and observations is well documented in *Angevine et al.* (2012).

C.2 Derivation of equations used to adjust predicted mass concentrations to match the AMS transmission efficiencies

The following piece-wise defined function is used to approximate the transmission curves of the AMSs used in this study:

$$\begin{aligned} &\mathrm{f}(40\text{ nm} < \mathrm{D_{va}} < 100\text{ nm}) &&= \frac{\ln(\mathrm{D_{va}}/40\text{ nm})}{\ln(100\text{ nm}/40\text{ nm})} \\ &\mathrm{f}(100\text{ nm} < \mathrm{D_{va}} < 550\text{ nm}) &&= 1 \\ &\mathrm{f}(550\text{ nm} < \mathrm{D_{va}} < 2000\text{ nm}) &&= \frac{\ln(\mathrm{D_{va}}/2000\text{ nm})}{\ln(550\text{ nm}/2000\text{ nm})} \end{aligned}$$

A log-normal mass distribution is defined as follows:

$$\mathrm{m(D_p)} = \frac{\mathrm{M_{tot}}}{\sqrt{2\pi}\ \mathrm{D_p}\ \ln(\sigma_{\mathrm{dry}})} \exp\left[\frac{-(\ln(\mathrm{D_p}) - \ln(\overline{\mathrm{D}}^{\mathrm{dry}}_{\mathrm{pgV}}))^2}{2\ln^2(\sigma_{\mathrm{dry}})}\right]$$

For the diameter range with 100% transmission, the cumulative mass-distribution function for a log-normal mass distribution is:

$$\begin{aligned} &\mathrm{M} \quad (100\text{ nm} < \mathrm{D_{va}} < 550\text{ nm}) \\ &= \mathrm{M}(100\text{ nm}/\rho_{\mathrm{dry}} < \mathrm{D_p} < 550\text{ nm}/\rho_{\mathrm{dry}}) \\ &= \int_0^{550\text{ nm}/\rho_{\mathrm{dry}}} \mathrm{m(D_p)dD_p} - \int_0^{100\text{ nm}/\rho_{\mathrm{dry}}} \mathrm{m(D_p)dD_p} \\ &= \frac{\mathrm{M_{tot}}}{2}\mathrm{erf}\left[\frac{\ln((550\text{ nm}/\rho_{\mathrm{dry}})/\overline{\mathrm{D}}^{\mathrm{dry}}_{\mathrm{pgV}})}{\sqrt{2}\ln\sigma_{\mathrm{dry}}}\right] - \frac{\mathrm{M_{tot}}}{2}\mathrm{erf}\left[\frac{\ln((100\text{ nm}/\rho_{\mathrm{dry}})/\overline{\mathrm{D}}^{\mathrm{dry}}_{\mathrm{pgV}})}{\sqrt{2}\ln\sigma_{\mathrm{dry}}}\right] \end{aligned}$$

Therefore,

$$\mathrm{M}(100\ \mathrm{nm} < \mathrm{D_{va}} < 550\ \mathrm{nm}) = \frac{\mathrm{M_{tot}}}{2}\left(\mathrm{erf}\left[\frac{\ln((550\ \mathrm{nm}/\rho_{\mathrm{dry}})/\overline{\mathrm{D}}^{\mathrm{dry}}_{\mathrm{pgV}})}{\sqrt{2}\ln\sigma_{\mathrm{dry}}}\right] - \mathrm{erf}\left[\frac{\ln((100\ \mathrm{nm}/\rho_{\mathrm{dry}})/\overline{\mathrm{D}}^{\mathrm{dry}}_{\mathrm{pgV}})}{\sqrt{2}\ln\sigma_{\mathrm{dry}}}\right]\right)$$

For 40 nm <$\mathrm{D_{va}}$ <100 nm, we apply the transmission function to the log-normal mass distribution as follows:

$$\begin{aligned}
\mathrm{f} \quad & (40\ \mathrm{nm} < \mathrm{D_{va}} < 100\ \mathrm{nm}) = \frac{\ln(\mathrm{D_{va}}/40\ \mathrm{nm})}{\ln(100\ \mathrm{nm}/40\ \mathrm{nm})} = \frac{\ln(\mathrm{D_p}/(40\ \mathrm{nm}/\rho_{\mathrm{dry}}))}{\ln(100\ \mathrm{nm}/40\ \mathrm{nm})} \\
\mathrm{M} \quad & (40\ \mathrm{nm} < \mathrm{D_{va}} < 100\ \mathrm{nm}) = \int_{40\ \mathrm{nm}/\rho_{\mathrm{dry}}}^{100\ \mathrm{nm}/\rho_{\mathrm{dry}}} \mathrm{f(D_p)m(D_p)dD_p} \\
= \quad & \int_{40\ \mathrm{nm}/\rho_{\mathrm{dry}}}^{100\ \mathrm{nm}/\rho_{\mathrm{dry}}} \frac{\ln(\mathrm{D_p}/(40\ \mathrm{nm}/\rho_{\mathrm{dry}}))}{\ln(100\ \mathrm{nm}/40\ \mathrm{nm})} \frac{\mathrm{M_{tot}}}{\sqrt{2\pi}\ \mathrm{D_p}\ \ln\sigma_{\mathrm{dry}}} \exp\left[\frac{-(\ln(\mathrm{D_p}) - \ln(\overline{\mathrm{D}}^{\mathrm{dry}}_{\mathrm{pgV}}))^2}{2\ln^2\sigma_{\mathrm{dry}}}\right] \mathrm{dD_p} \\
= \quad & \frac{\mathrm{M_{tot}}}{\sqrt{2\pi}\ln(\sigma_{\mathrm{dry}})\ln(100\ \mathrm{nm}/40\ \mathrm{nm})} \int_{40\ \mathrm{nm}/\rho_{\mathrm{dry}}}^{100\ \mathrm{nm}/\rho_{\mathrm{dry}}} \frac{\ln(\mathrm{D_p})}{\mathrm{D_p}} \exp\left[\frac{-(\ln(\mathrm{D_p}) - \ln(\overline{\mathrm{D}}^{\mathrm{dry}}_{\mathrm{pgV}}))^2}{2\ln^2\sigma_{\mathrm{dry}}}\right] \mathrm{dD_p} \\
- \quad & \frac{\mathrm{M_{tot}}}{\sqrt{2\pi}\ln(\sigma_{\mathrm{dry}})\ln(100\ \mathrm{nm}/40\ \mathrm{nm})} \int_{40\ \mathrm{nm}/\rho_{\mathrm{dry}}}^{100\ \mathrm{nm}/\rho_{\mathrm{dry}}} \frac{\ln((40\ \mathrm{nm}/\rho_{\mathrm{dry}}))}{\mathrm{D_p}} \exp\left[\frac{-(\ln(\mathrm{D_p}) - \ln(\overline{\mathrm{D}}^{\mathrm{dry}}_{\mathrm{pgV}}))^2}{2\ln^2\sigma_{\mathrm{dry}}}\right] \mathrm{dD_p}
\end{aligned}$$

Now we perform a change of variable:

$$\begin{aligned}
\ln(\mathrm{D_p}) &= \sqrt{2}\ln(\sigma_{\mathrm{dry}})\eta + \ln(\overline{\mathrm{D}}^{\mathrm{dry}}_{\mathrm{pgV}}) \\
\eta &= \frac{\ln(\mathrm{D_p}) - \ln(\overline{\mathrm{D}}^{\mathrm{dry}}_{\mathrm{pgV}})}{\sqrt{2}\ln(\sigma_{\mathrm{dry}})} \\
\mathrm{d}\eta &= \frac{1}{\mathrm{D_p}\sqrt{2}\ln(\sigma_{\mathrm{dry}})}\mathrm{dD_p}
\end{aligned}$$

Now substitute η into equation for M(40 nm < $\mathrm{D_{va}}$ < 100 nm) and simplify:

$$
\begin{aligned}
&\mathrm{M}(40\ \mathrm{nm} < \mathrm{D_{va}} < 100\ \mathrm{nm}) \\
&= \frac{\mathrm{M_{tot}}}{\sqrt{2\pi}\ln(\sigma_{\mathrm{dry}})\ln(100\ \mathrm{nm}/40\ \mathrm{nm})} \int_{\eta(40\ \mathrm{nm}/\rho_{\mathrm{dry}})}^{\eta(100\ \mathrm{nm}/\rho_{\mathrm{dry}})} \frac{\sqrt{2}\ln(\sigma_{\mathrm{dry}})\eta + \ln(\overline{\mathrm{D}}_{\mathrm{pgV}}^{\mathrm{dry}})}{\mathrm{D_p}} \exp\left[-(\eta)^2\right] \mathrm{D_p}\sqrt{2}\ln(\sigma_{\mathrm{dry}})\mathrm{d}\eta \\
&- \frac{\mathrm{M_{tot}}}{\sqrt{2\pi}\ln(\sigma_{\mathrm{dry}})\ln(100\ \mathrm{nm}/40\ \mathrm{nm})} \int_{\eta(40\ \mathrm{nm}/\rho_{\mathrm{dry}})}^{\eta(100\ \mathrm{nm}/\rho_{\mathrm{dry}})} \frac{\ln((40\ \mathrm{nm}/\rho_{\mathrm{dry}}))}{\mathrm{D_p}} \exp\left[-(\eta)^2\right] \mathrm{D_p}\sqrt{2}\ln(\sigma_{\mathrm{dry}})\mathrm{d}\eta \\
&= \frac{\mathrm{M_{tot}}}{\sqrt{\pi}\ln(100\ \mathrm{nm}/40\ \mathrm{nm})} \int_{\eta(40\ \mathrm{nm}/\rho_{\mathrm{dry}})}^{\eta(100\ \mathrm{nm}/\rho_{\mathrm{dry}})} (\sqrt{2}\ln(\sigma_{\mathrm{dry}})\eta + \ln(\overline{\mathrm{D}}_{\mathrm{pgV}}^{\mathrm{dry}})) \exp\left[-(\eta)^2\right] \mathrm{d}\eta \\
&- \frac{\mathrm{M_{tot}}}{\sqrt{\pi}\ln(100\ \mathrm{nm}/40\ \mathrm{nm})} \int_{\eta(40\ \mathrm{nm}/\rho_{\mathrm{dry}})}^{\eta(100\ \mathrm{nm}/\rho_{\mathrm{dry}})} \ln((40\ \mathrm{nm}/\rho_{\mathrm{dry}})) \exp\left[-(\eta)^2\right] \mathrm{d}\eta \\
&= \frac{\mathrm{M_{tot}}\ln(\sigma_{\mathrm{dry}})}{\sqrt{\frac{\pi}{2}}\ln(100\ \mathrm{nm}/40\ \mathrm{nm})} \int_{\eta(40\ \mathrm{nm}/\rho_{\mathrm{dry}})}^{\eta(100\ \mathrm{nm}/\rho_{\mathrm{dry}})} (\eta)\exp(-(\eta)^2)\mathrm{d}\eta \\
&+ \frac{\mathrm{M_{tot}}\ln(\overline{\mathrm{D}}_{\mathrm{pgV}}^{\mathrm{dry}}/(40\ \mathrm{nm}/\rho_{\mathrm{dry}}))}{\sqrt{\pi}\ln(100\ \mathrm{nm}/40\ \mathrm{nm})} \int_{\eta(40\ \mathrm{nm}/\rho_{\mathrm{dry}})}^{\eta(100\ \mathrm{nm}/\rho_{\mathrm{dry}})} \exp\left[-(\eta)^2\right] \mathrm{d}\eta
\end{aligned}
$$

Therefore,

$$
\begin{aligned}
&\mathrm{M}(40\ \mathrm{nm} < \mathrm{D_{va}} < 100\ \mathrm{nm}) \\
&= \left[\frac{\mathrm{M_{tot}}}{2}\right] \left[\frac{\ln(\sigma_{\mathrm{dry}})}{\ln(100\ \mathrm{nm}/40\ \mathrm{nm})\sqrt{\frac{\pi}{2}}}\right] \left[\exp(-(\eta(40\ \mathrm{nm}/\rho_{\mathrm{dry}}))^2) - \exp(-(\eta(100\ \mathrm{nm}/\rho_{\mathrm{dry}}))^2\right] \\
&+ \left[\frac{\mathrm{M_{tot}}}{2}\right] \left[\frac{\ln(\overline{\mathrm{D}}_{\mathrm{pgV}}^{\mathrm{dry}}/(40\ \mathrm{nm}/\rho_{\mathrm{dry}}))}{\ln(100\ \mathrm{nm}/40\ \mathrm{nm})}\right] \left[\mathrm{erf}(\eta(100\ \mathrm{nm}/\rho_{\mathrm{dry}})) - \mathrm{erf}(\eta(40\ \mathrm{nm}/\rho_{\mathrm{dry}})\right]
\end{aligned}
$$

A similar derivation can be done for $\mathrm{M}(550\ \mathrm{nm} < \mathrm{D_{va}} < 2000\ \mathrm{nm})$, which yields:

Table C.1: Sulfate sources in the Aitken, accumulation, and coarse aerosol modes in CMAQ.

Aitken mode	Accumulation mode	Coarse mode
Aqueous-phase Oxidation		
	H_2O_2 + S(IV) → S(VI) + H_2O	
	O_3 + S(IV) → S(VI) + O_2	
	O_2 + S(IV) → S(VI)	
	MHP[a] + S(IV) → S(VI)	
	PAA[b] + S(IV) → S(VI)	
Gas-phase Oxidation		
$SO_2 + OH \xrightarrow{O_2,H_2O} H_2SO_4 + HO_2$	$SO_2 + OH \xrightarrow{O_2,H_2O} H_2SO_4 + HO_2$	$SO_2 + OH \xrightarrow{O_2,H_2O} H_2SO_4 + HO_2$
Primary Emissions		
0.1% Primary Anthropogenic Sulfate	99.9% Primary Anthropogenic Sulfate	
	Sulfate Sea-spray	Sulfate Sea-spray
Initial conditions (IC) and boundary conditions (BC)		
Sulfate from ICBC	Sulfate from ICBC	Sulfate from ICBC

[a] MHP stands for methylhydrogenperoxide. [b] PAA stands for peroxyacetic acid.

$$
\begin{aligned}
&\mathrm{M}(550\ \mathrm{nm} < \mathrm{D_{va}} < 2000\ \mathrm{nm}) \\
&= \left[\frac{\mathrm{M_{tot}}}{2}\right]\left[\frac{\ln(\sigma_{\mathrm{dry}})}{\ln(550\ \mathrm{nm}/2000\ \mathrm{nm})\sqrt{\frac{\pi}{2}}}\right]\left[\exp(-(\eta(550\ \mathrm{nm}/\rho_{\mathrm{dry}}))^2) - \exp(-(\eta(2000\ \mathrm{nm}/\rho_{\mathrm{dry}}))^2\right] \\
&+ \left[\frac{\mathrm{M_{tot}}}{2}\right]\left[\frac{\ln(\overline{\mathrm{D}}^{\mathrm{dry}}_{\mathrm{pgV}}/2000\ \mathrm{nm}/\rho_{\mathrm{dry}})}{\ln(550\ \mathrm{nm}/2000\ \mathrm{nm}}\right]\left[\mathrm{erf}(\eta(2000\ \mathrm{nm}/\rho_{\mathrm{dry}})) - \mathrm{erf}(\eta(550\ \mathrm{nm}/\rho_{\mathrm{dry}})\right]
\end{aligned}
$$

The total mass in each mode that should be compared to the AMS measurements is then:

$$\mathrm{M^{AMS}_{mode}} = \mathrm{M}(40\ \mathrm{nm} < \mathrm{D_{va}} < 100\ \mathrm{nm}) + \mathrm{M}(100\ \mathrm{nm} < \mathrm{D_{va}} < 550\ \mathrm{nm}) + \mathrm{M}(550\ \mathrm{nm} < \mathrm{D_{va}} < 2000\ \mathrm{nm})$$

$$\mathrm{M^{AMS}_{tot}} = \mathrm{M^{AMS}_{I}} + \mathrm{M^{AMS}_{J}} + \mathrm{M^{AMS}_{K}}$$

Table C.2: Statistical metrics based on measured and predicted total nitrate (NO_3^- + HNO_3) mixing ratios for P3 flights during May 2010.

P3, AMS Transmission					
Flight Date	N	ME [ppbv]	MB [ppbv]	NME	NMB
Total Nitrate (HNO_3 + NO_3^-)					
4	17219	0.99	-0.69	0.45	-0.31
8	25439	0.90	-0.01	0.49	0.00
14	22258	1.93	1.61	1.07	0.89
16	27899	0.87	-0.29	0.38	-0.13
19	24239	1.59	-1.39	0.48	-0.42
P3, Full Transmission					
Flight Date	N	ME [ppbv]	MB [ppbv]	NME	NMB
Total Nitrate (HNO_3 + NO_3^-)					
4	17219	0.99	-0.60	0.44	-0.27
8	25439	1.05	0.25	0.58	0.14
14	22258	2.14	1.87	1.19	1.04
16	27899	0.90	-0.07	0.39	-0.03
19	24239	1.31	-1.08	0.40	-0.33

Table C.3: Statistical metrics based on measured and predicted temperature, RH, wind speed, and wind direction at six surface sites in the Los Angeles Basin.

Temperature				
Site	ME [K]	MB [K]		
Los Angeles-International Airport	2.39	1.54		
Long Beach Airport	2.54	1.47		
Riverside-March Air Force Base	2.78	1.35		
Chino Airport	2.27	1.61		
Fullerton Municipal Airport	2.43	1.85		
Los Alamitos Army Airfield	1.94	1.02		
Relative Humidity				
Site	ME [%]	MB [%]		
Los Angeles-International Airport	11.8	-3.71		
Long Beach Airport	14.3	-9.42		
Riverside-March Air Force Base	15.9	-11.2		
Chino Airport	11.5	-6.19		
Fullerton Municipal Airport	14.4	-5.87		
Los Alamitos Army Airfield	12.3	-5.64		
Wind Speed				
Site	ME [m/s]	MB [m/s]	NME	NMB
Los Angeles-International Airport	1.24	0.837	0.700	0.470
Long Beach Airport	1.51	0.884	0.527	0.308
Riverside-March Air Force Base	1.77	1.29	0.672	0.489
Chino Airport	0.974	0.0795	0.448	0.0366
Fullerton Municipal Airport	1.66	0.215	0.448	0.0580
Los Alamitos Army Airfield	1.31	0.796	0.494	0.301
Wind Direction				
Site	ME [°]			
Los Angeles-International Airport	53.1			
Long Beach Airport	45.0			
Riverside-March Air Force Base	55.8			
Chino Airport	45.8			
Fullerton Municipal Airport	43.1			
Los Alamitos Army Airfield	49.5			

Table C.4: ARCTAS-CARB domain-wide daily gaseous emission rates.

Species	Weekday Emission Rate (kmol/day)	Weekend Emission Rate (kmol/day)
NO	1.19e+05	9.33e+04
NO2	1.35e+04	1.06e+04
HONO	2.69e+03	2.11e+03
SO2	1.01e+04	1.01e+04
SULF	3.18e+02	3.16e+02
CO	7.72e+05	8.27e+05
HCHO	3.68e+03	3.43e+03
CCHO	2.27e+03	2.56e+03
RCHO	8.29e+02	7.61e+02
ACET	6.54e+03	7.69e+03
MEK	4.66e+02	3.51e+02
PROD	1.39e+02	8.89e+01
BALD	1.38e+02	1.78e+02
PHEN	1.11e+01	9.38e+00
GLY	3.34e+01	3.34e+01
MGLY	2.17e+01	2.17e+01
HCOOH	3.88e-01	3.08e-01
NROG	1.32e+04	1.28e+04
MEOH	1.08e+04	1.41e+04
CH4	2.06e+05	1.84e+05
ETHENE	8.31e+03	8.94e+03
ISOPRENE	5.02e+03	9.71e+03
ALK1	1.50e+04	1.47e+04

Continued on Next Page...

Table C.4 – Continued

Species	Weekday Emission Rate (kmol/day)	Weekend Emission Rate (kmol/day)
ALK2	6.82e+03	6.82e+03
ALK3	1.28e+04	1.25e+04
ALK4	1.50e+04	1.52e+04
ALK5	8.09e+03	7.47e+03
ARO1NBZ	4.08e+03	4.14e+03
ARO2	2.80e+03	2.95e+03
OLE1	5.27e+03	7.44e+03
OLE2	1.88e+03	2.12e+03
TRP1	3.65e+03	4.76e+03
CRES	1.19e+00	1.15e+00
NH3	5.35e+04	5.34e+04
BENZENE	9.19e+01	9.32e+01
SESQ	1.51e+02	2.10e+02

Table C.5: ARCTAS-CARB domain-wide daily particulate emission rates.

Species	Weekday Emission Rate (kg/day)	Weekend Emission Rate (kg/day)
POA	1.25e+05	9.83e+04
PEC	5.50e+04	5.52e+04
PSO4	5.77e+04	6.46e+04
PMFINE	6.40e+05	5.72e+05
PMC	3.30e+06	2.77e+06

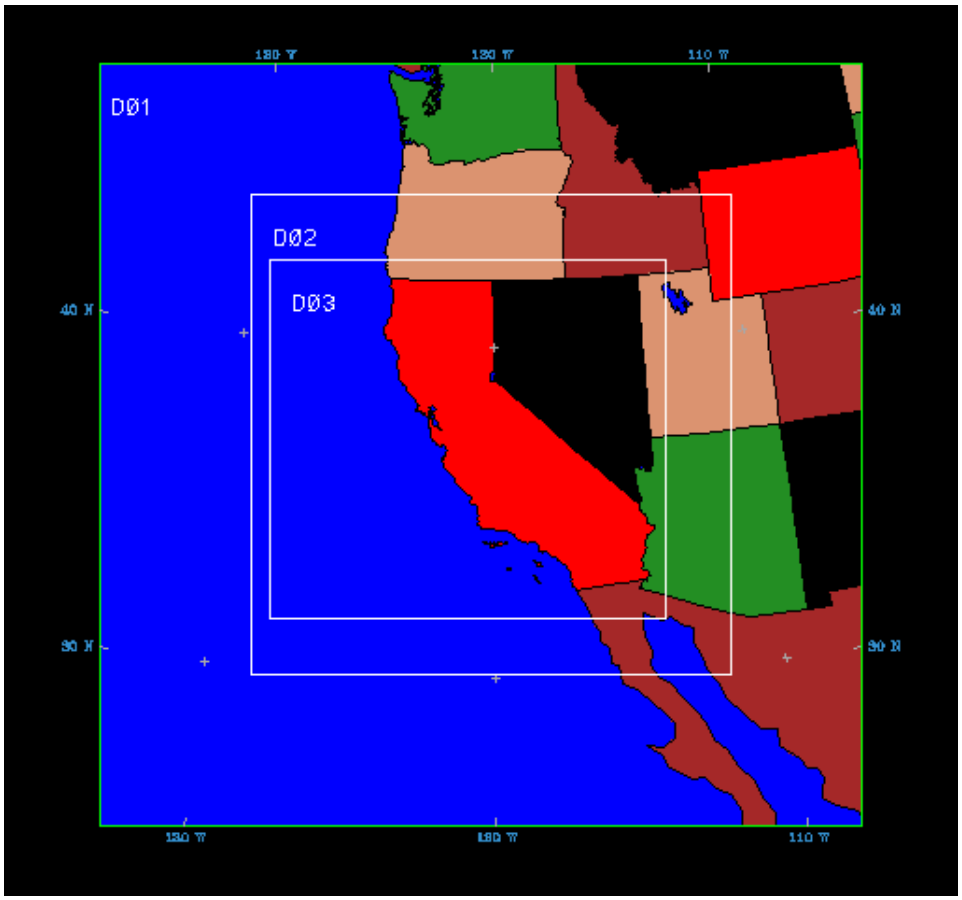

Figure C.1: Map of nested MM5 domains. The three grids have horizontal resolutions of 36, 12, and 4 km, and have (71 x 71), (133 x 133), (298 x 328) grid points, respectively, in (west-east) and (south-north) directions. Meteorological fields were extracted from the inner-most domain for the CTM domain shown in Figure 4.1.

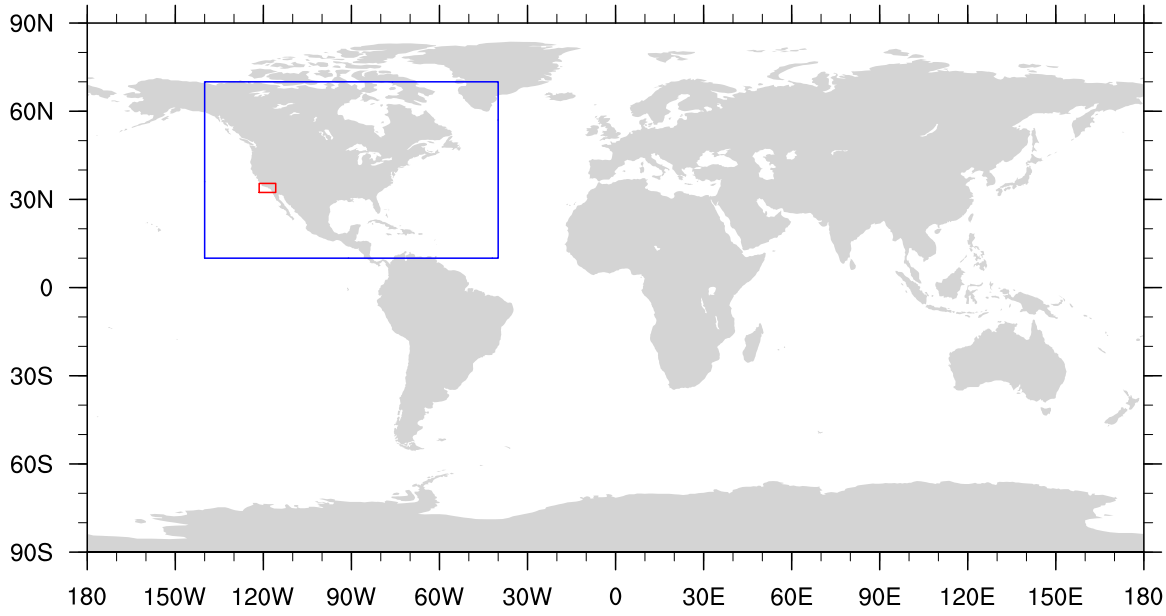

Figure C.2: Map of nested CTM domains. The global map represents the global GEOS-Chem domain (2°Lat by 2.5°Lon horizontal grid resolution). The blue line represents the nested GEOS-Chem North America domain (0.5°Lat by 0.667°Lon horizontal grid resolution), from which dynamic CMAQ boundary conditions are derived. The red line represents the nested CMAQ Southern California domain (4 km by 4 km horizontal grid resolution).

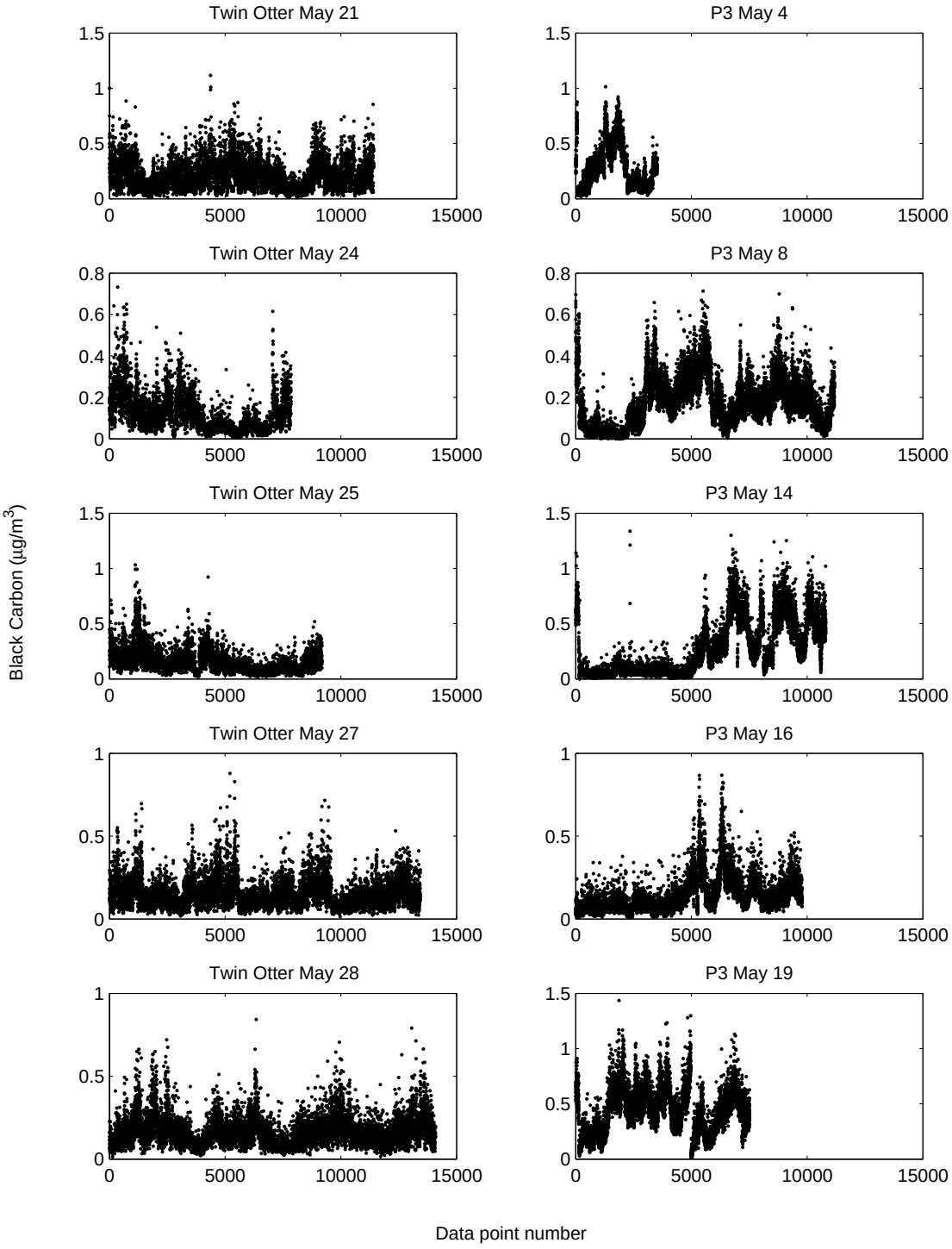

Figure C.3: Observed (black) black carbon concentrations along P3 and Twin Otter flight paths. Data points above 1000 m a.s.l. have been removed in order to accurately show that the noise levels in both SP2s are comparable during most flights. The data series are plotted as functions of data-point number so that the plots appear continuous, and all x-axes have been set to [0 15000].

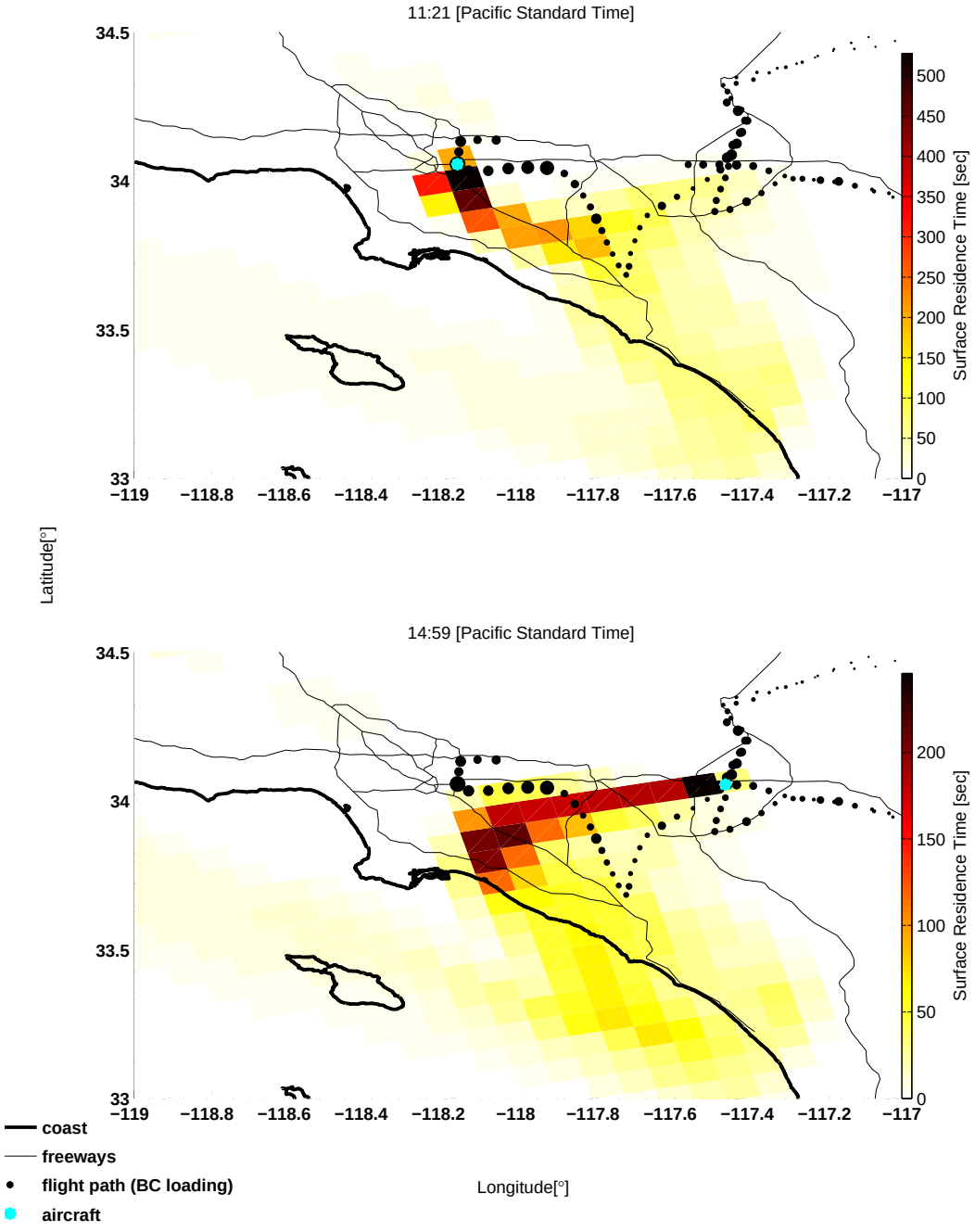

Figure C.4: Map of mean residence times based on integrated 24-h back trajectories for the surface level particles (particles at < 200 m altitude) arriving in the vicinity of the Twin Otter for flights on May 24. Flight path marker (black dots) sizes are proportional to 1-min average measured BC concentrations (maximum concentration is 0.29 μg m^{-3}).

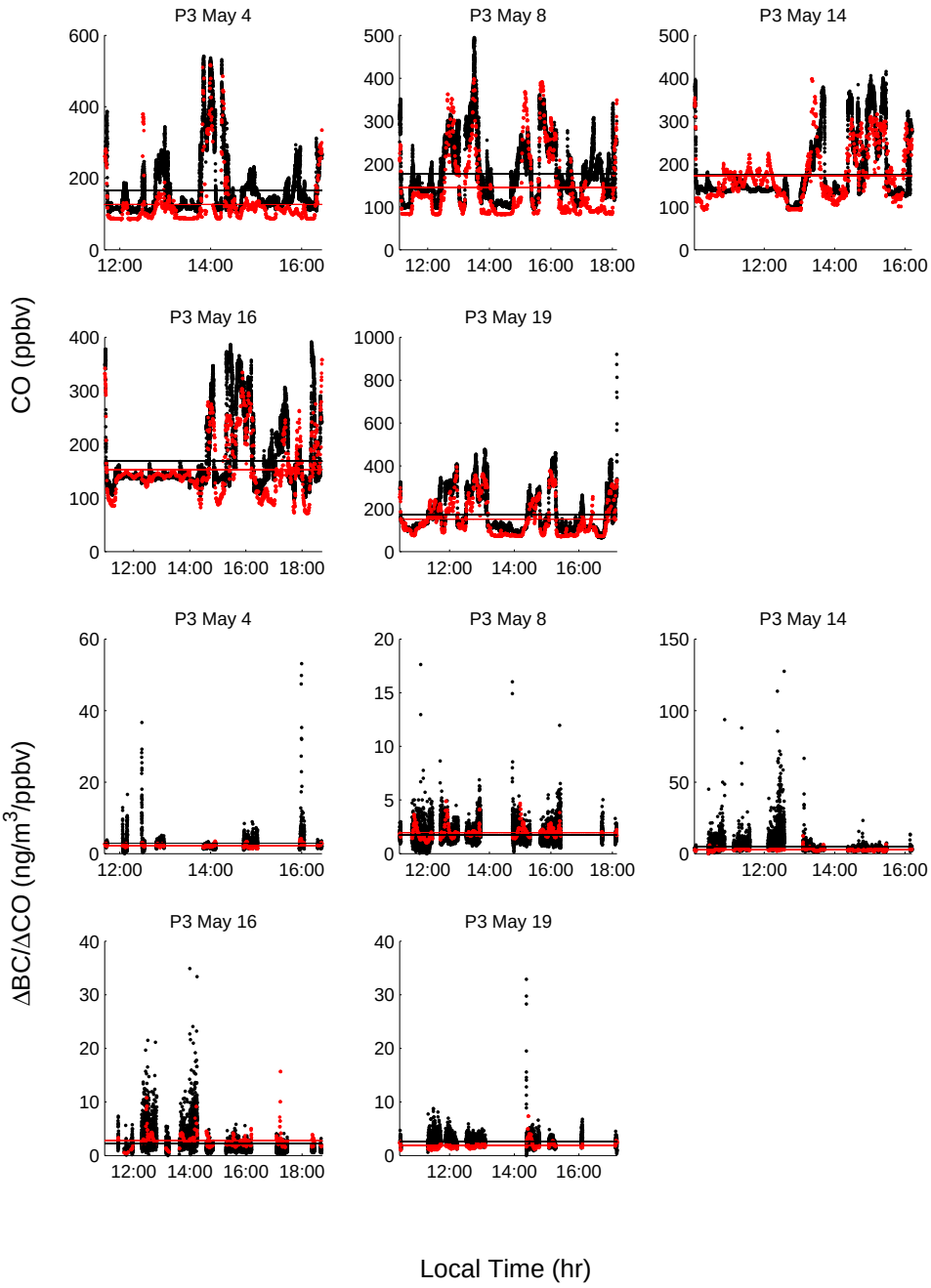

Figure C.5: Top five panels show measured (black) and predicted (red) CO mixing ratios. Bottom five panels show measured and predicted ratios of black carbon (ΔBC) mass concentrations and ΔCO mixing ratios. ΔBC/ΔCO are calculated by subtracting the minimum BC and CO measurements (background values) below 1000 m a.s.l. from all BC and CO measurements, respectively, below 1000 m a.s.l. Data points for which ΔCO < 1 ppbv are also removed. Note that, owing to data points lying on top of each other in Figure S4, the average ΔBC/ΔCO ratios (horizontal lines) can appear lower than the spread of individual data points may suggest. Horizontal lines represent flight averages.

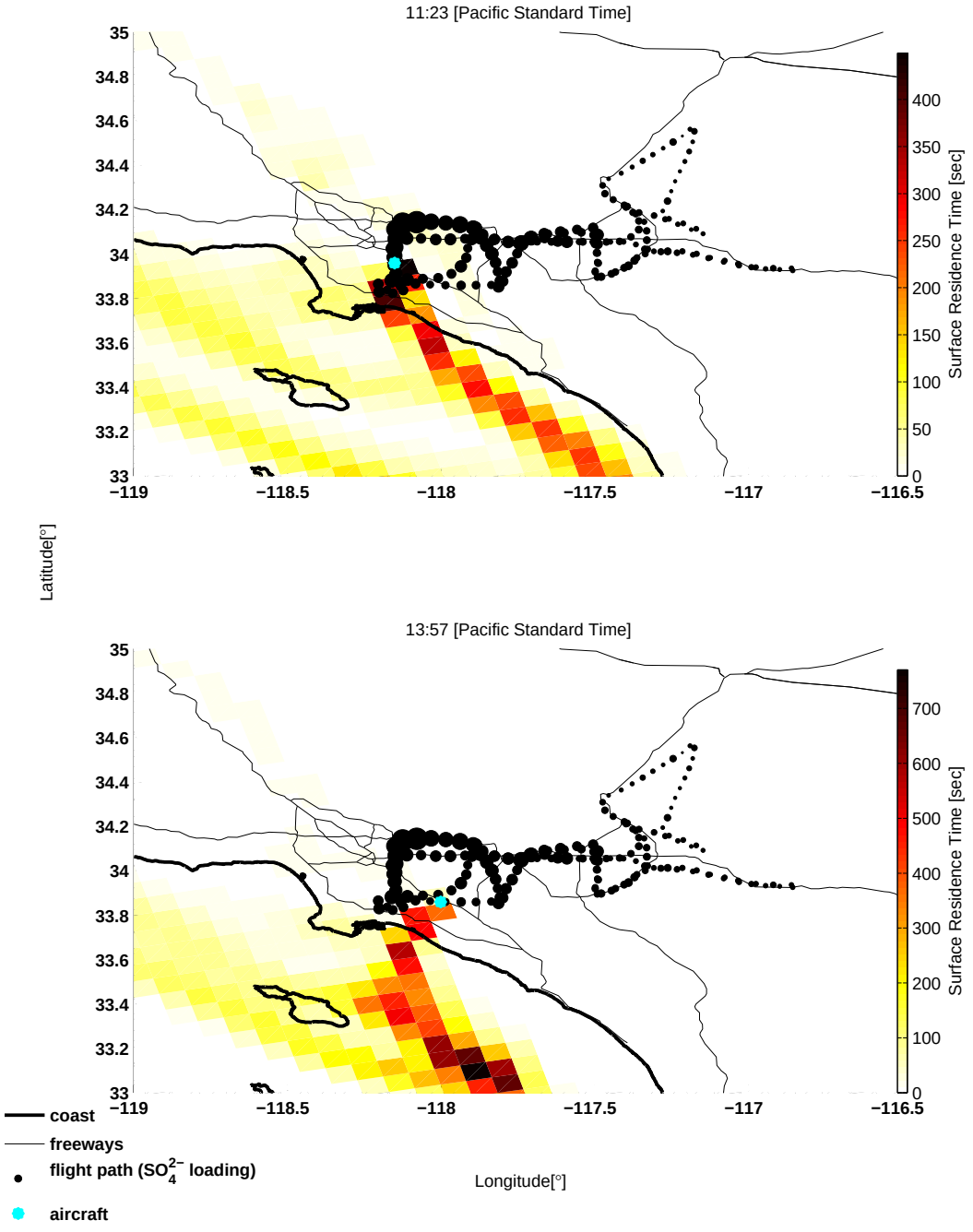

Figure C.6: Map of mean residence times based on integrated 24-h back trajectories for the surface level particles (particles at < 200 m altitude) arriving in the vicinity of the Twin Otter for flights on May 21. Flight path marker (black dots) sizes are proportional to 10-sec average measured sulfate concentrations (maximum concentration is 1.26 μg m^{-3})

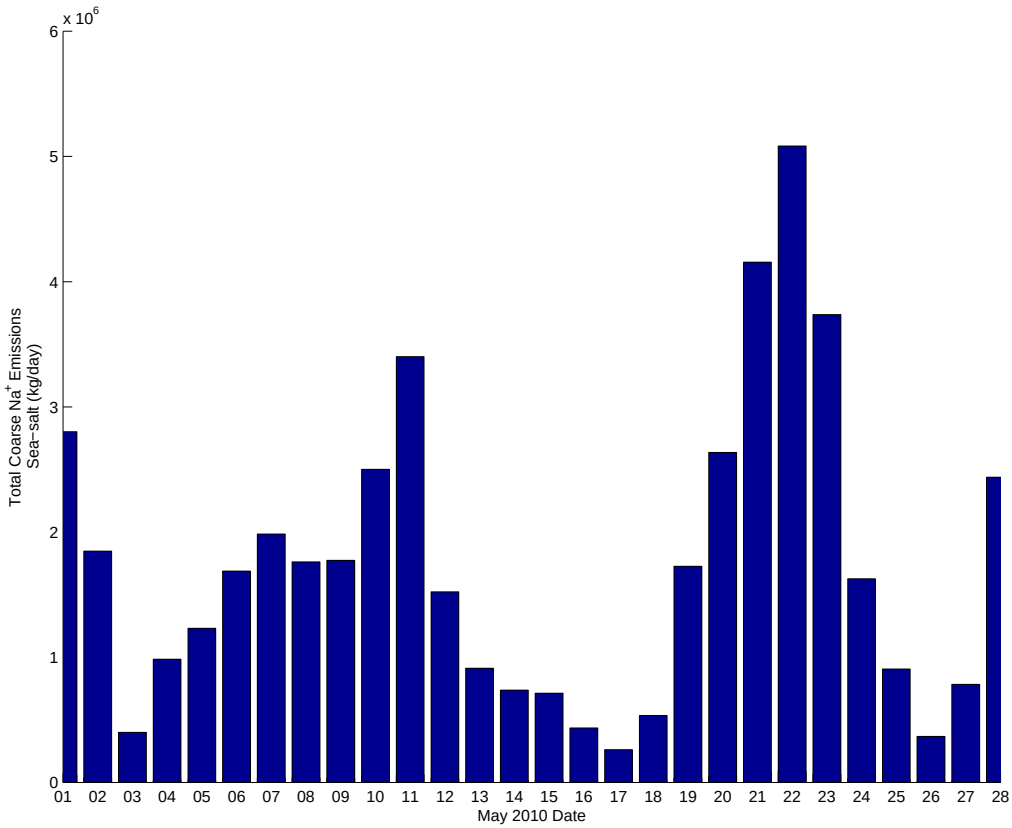

Figure C.7: Daily domain total Na^+ emissions from sea-spray. Emission rates are calculated using the sea-salt diagnostic file generated by CMAQ.

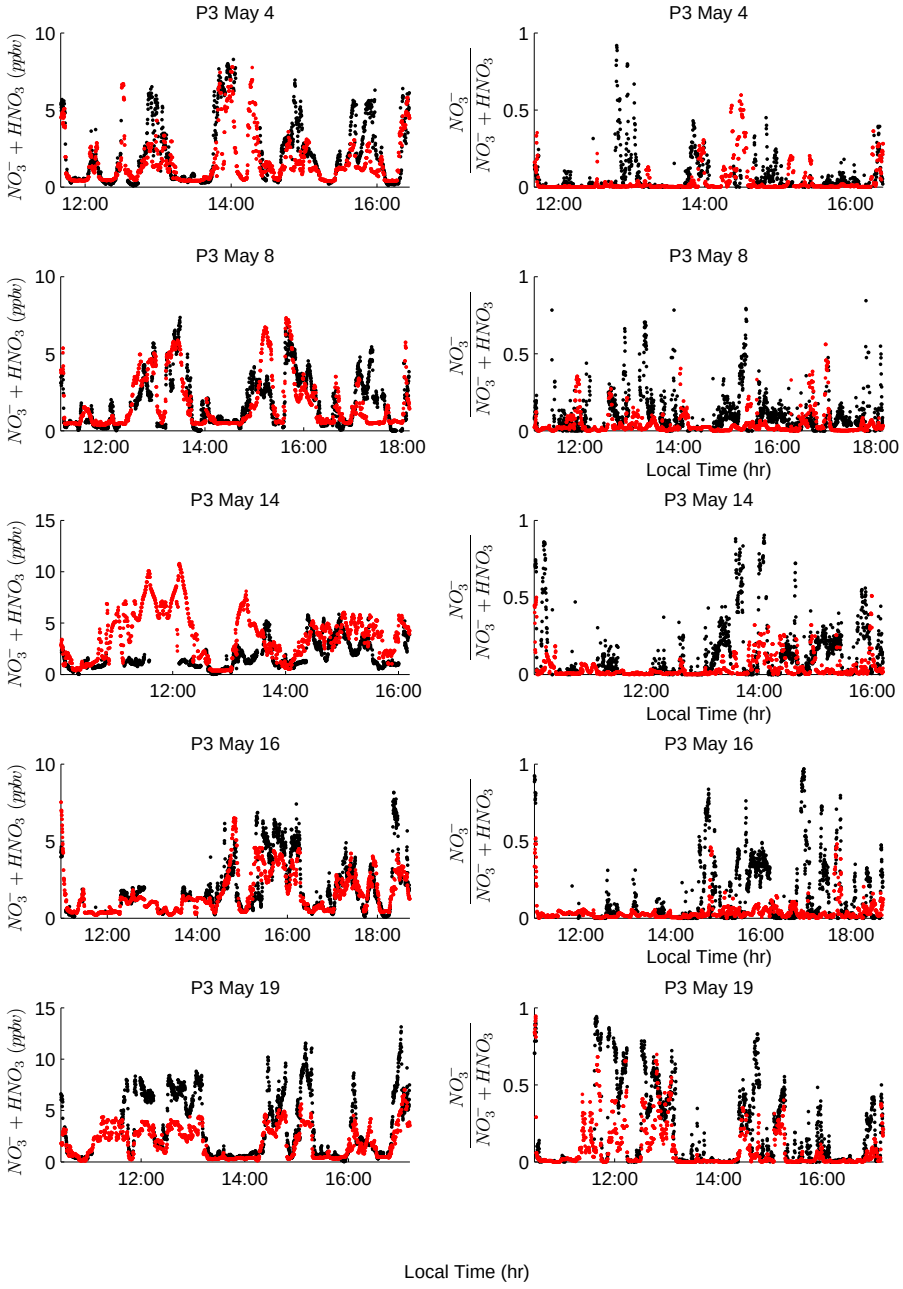

Figure C.8: Predicted (red) and observed (black) total nitrate (NO_3^- + HNO_3) mixing ratios (left column) and predicted and observed fraction of total nitrate in the particle-phase (right column) for P3 flights. Predicted nitrate concentrations are adjusted to match the transmission efficiency of the AMS based as described in the text.

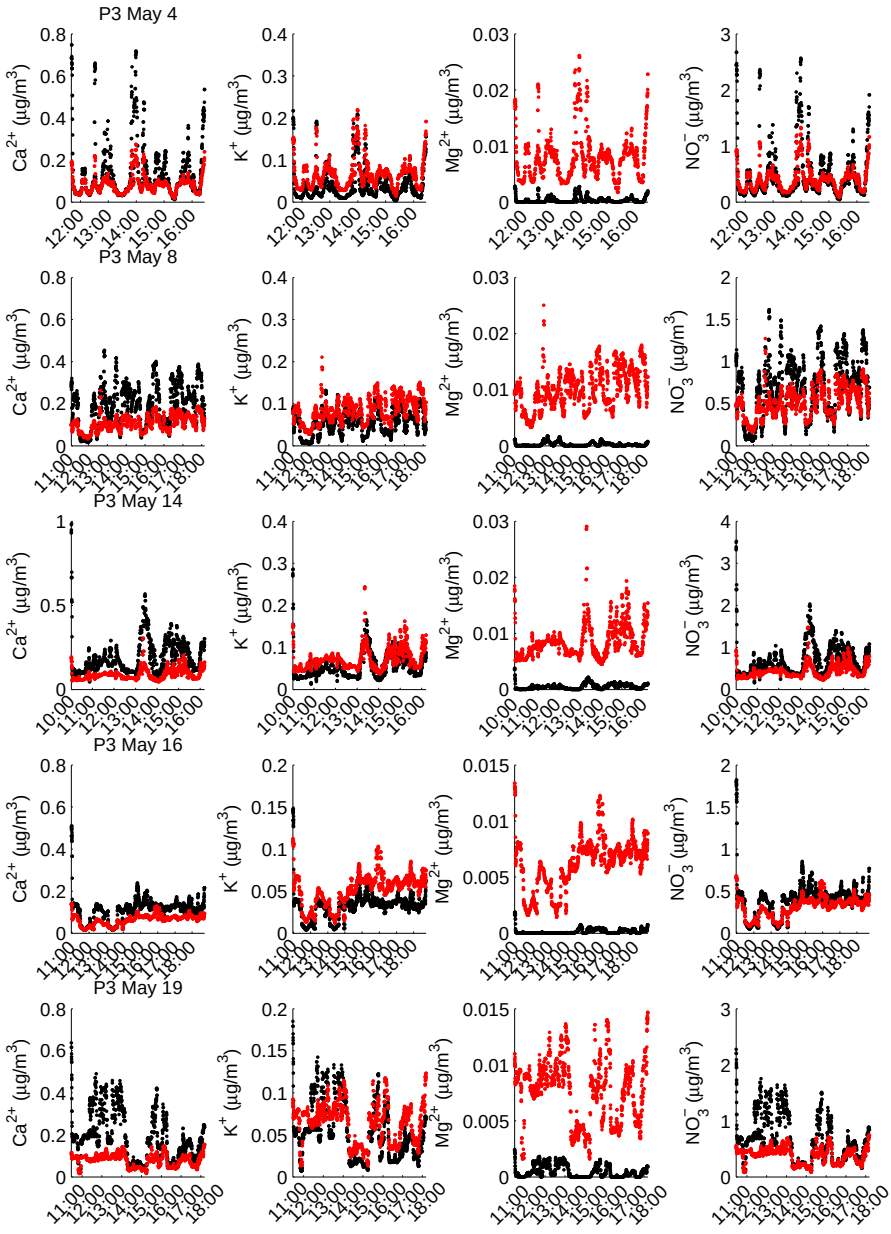

Figure C.9: Predicted crustal species (Ca^{2+}, K^{+}, and Mg^{2+}) concentrations along P3 flight paths. Predictions are based on speciation factors given in Table 4.8 of the manuscript. Nitrate concentrations that could potentially be neutralized by crustal species are shown in the right-most column. Coarse particles are in black and fine particles are in red.

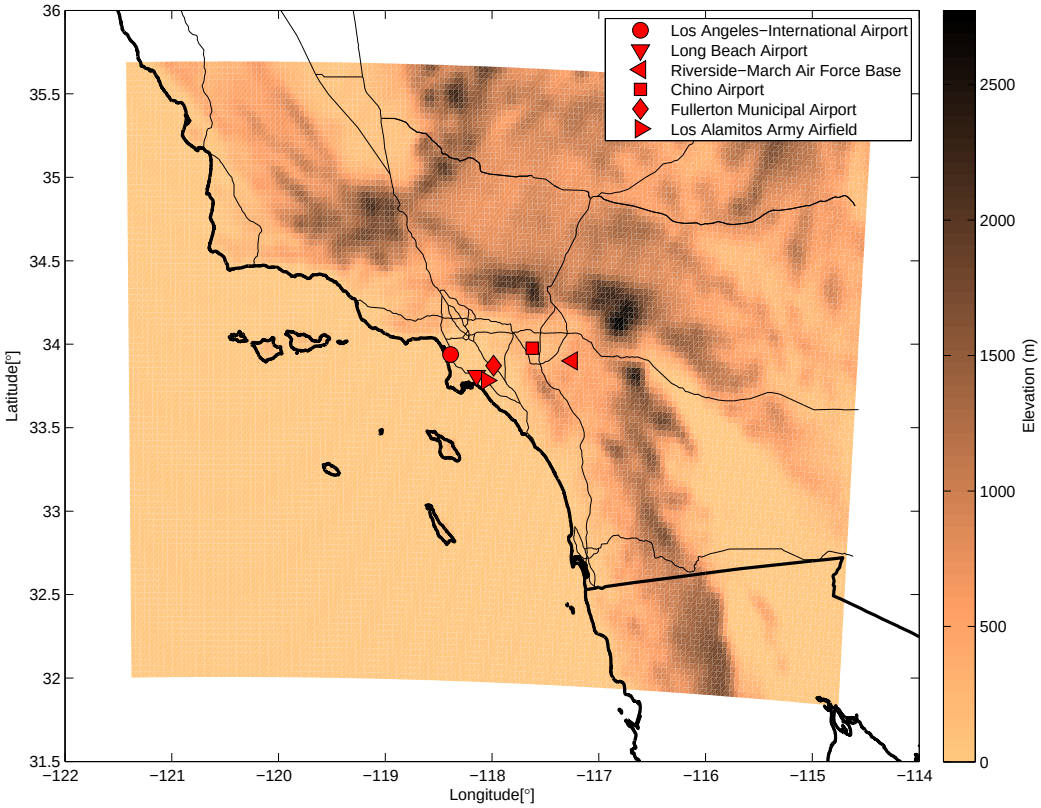

Figure C.10: Ground-site locations used for comparison of predicted (MM5) and observed meteorology for May 2010.

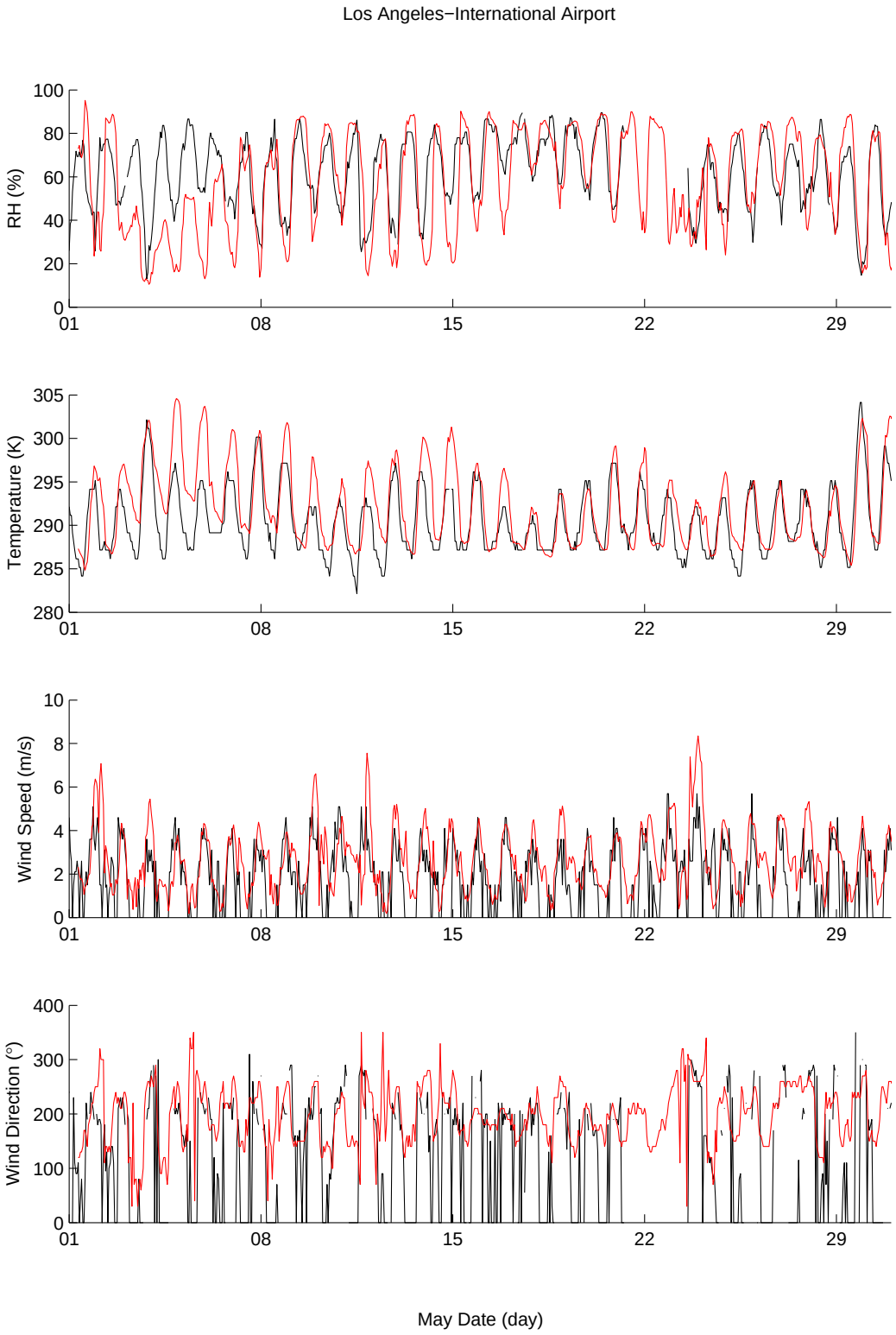

Figure C.11: Predicted (red) and observed (black) temperature, RH, wind speed, and wind direction.

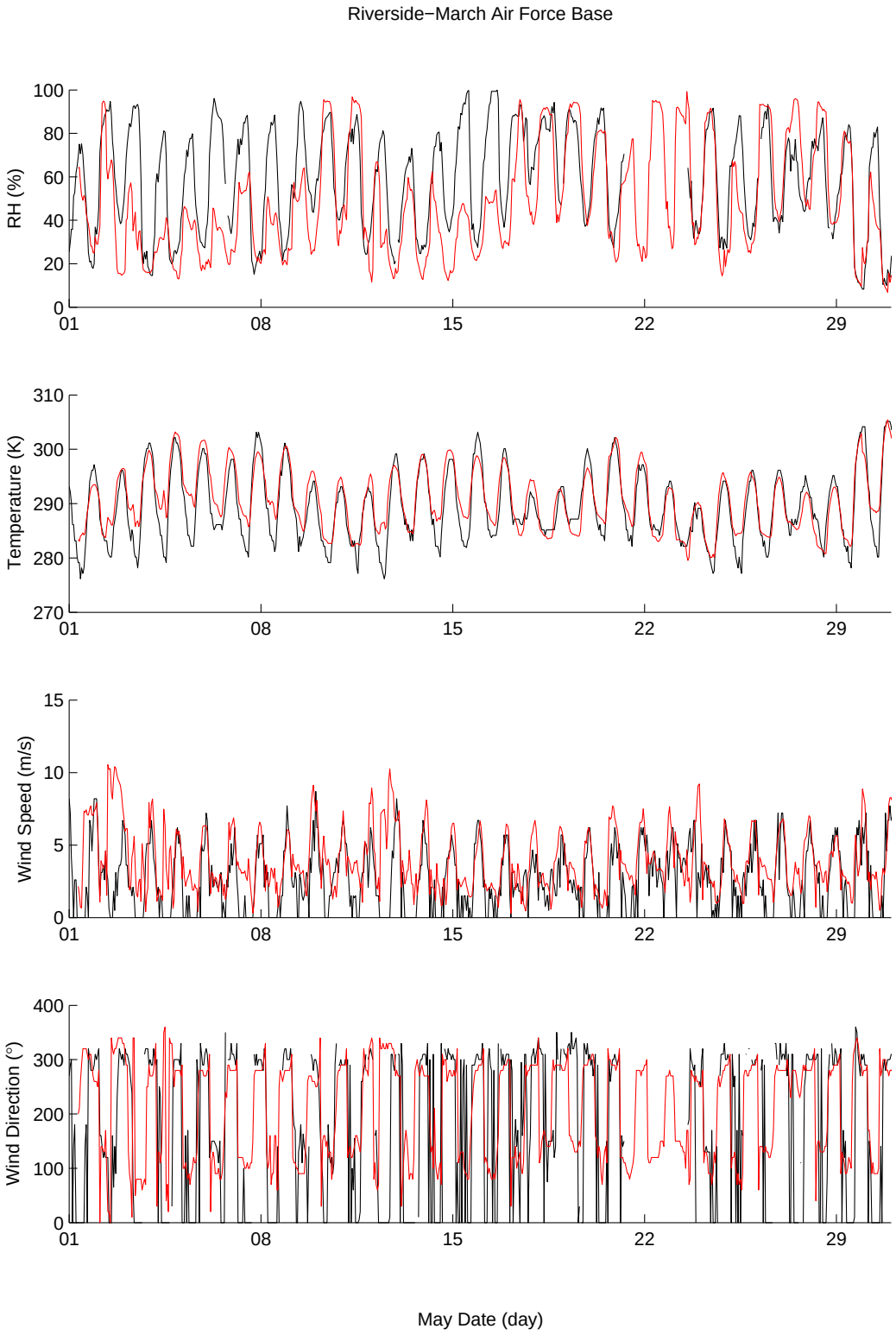

Figure C.12: Predicted (red) and observed (black) temperature, RH, wind speed, and wind direction.

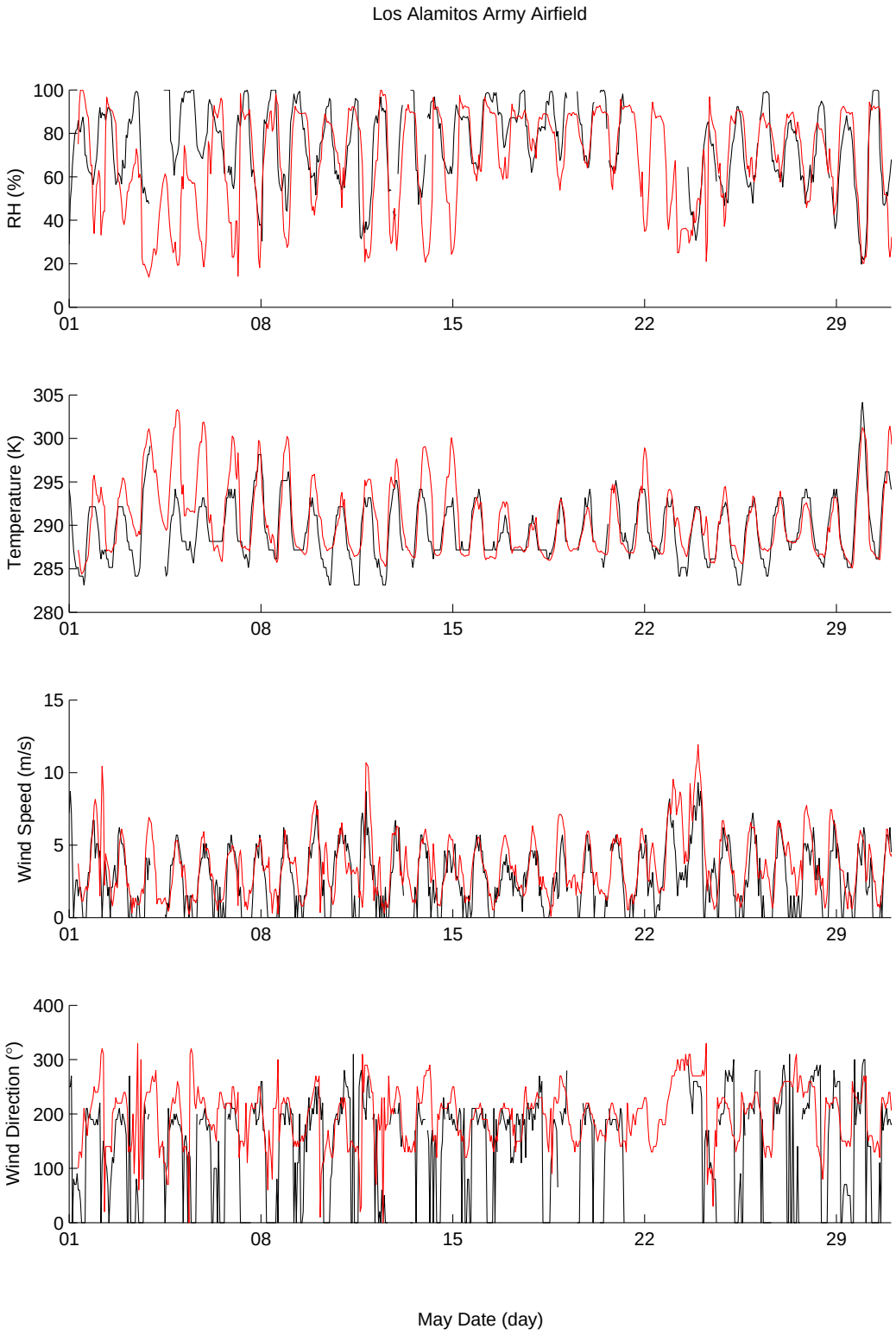

Figure C.13: Predicted (red) and observed (black) temperature, RH, wind speed, and wind direction.

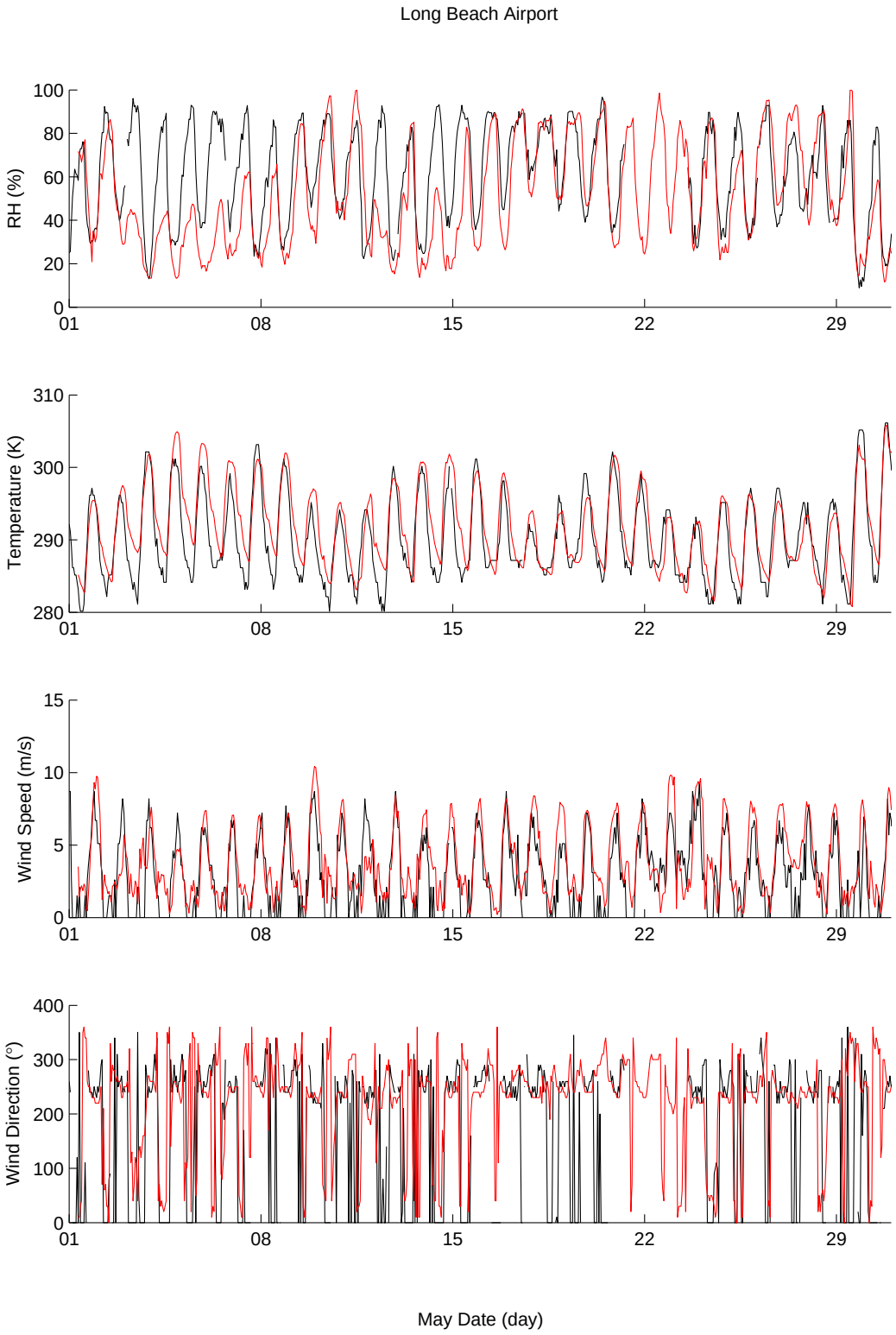

Figure C.14: Predicted (red) and observed (black) temperature, RH, wind speed, and wind direction.

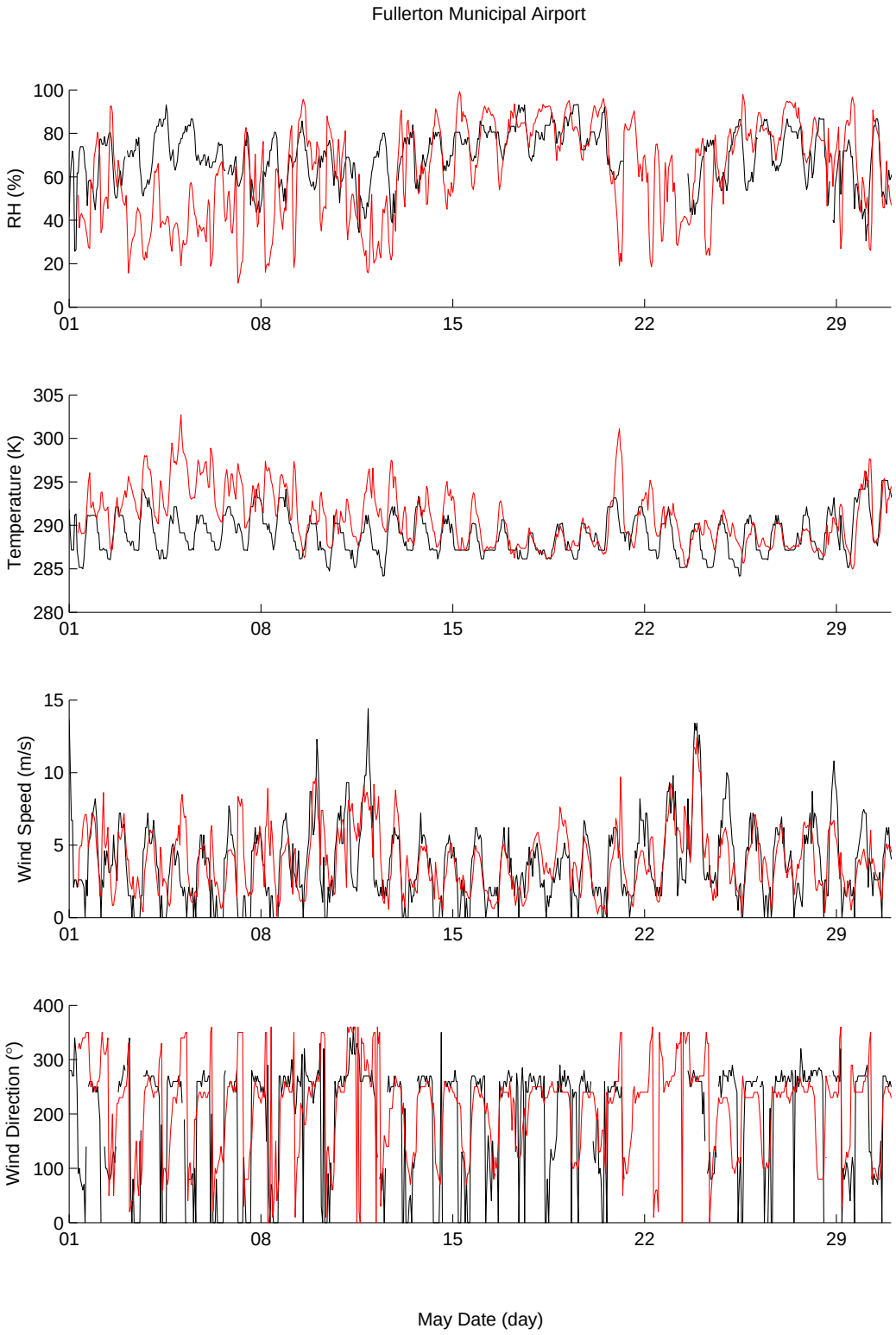

Figure C.15: Predicted (red) and observed (black) temperature, RH, wind speed, and wind direction.

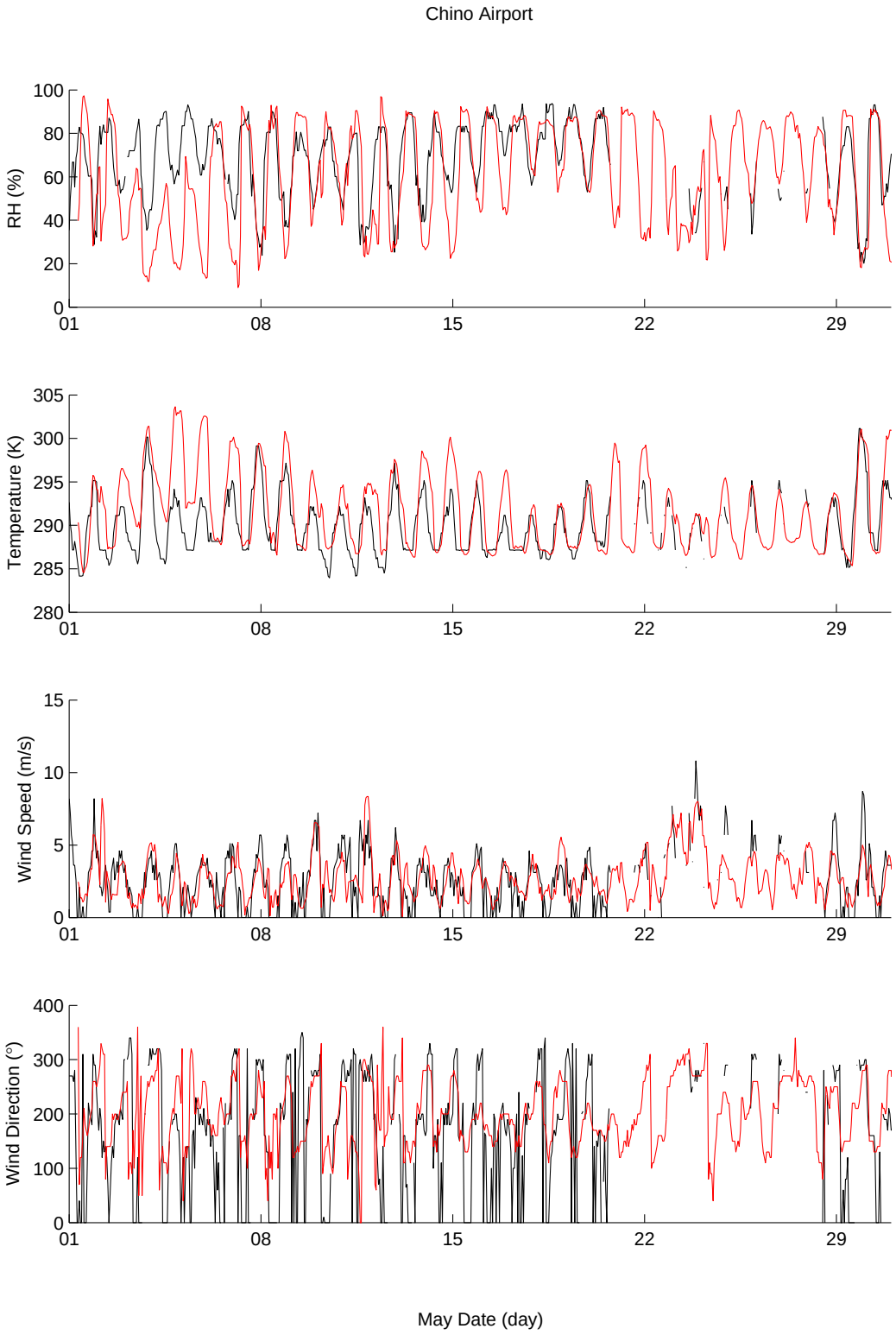

Figure C.16: Predicted (red) and observed (black) temperature, RH, wind speed, and wind direction.

Bibliography

Angevine, W. M., Eddington, L., Durkee, K., Fairall, C., Bianco, L., Brioude, J. (2012), Meteorological model evaluation for CalNex 2010 *Mon. Wea. Rev.*, *140*, 3885–3906. doi:http://dx.doi.org/10.1175/MWR-D-12-00042.1.

Hanna, S. R. (1982), Applications in air pollution modeling, in: Atmospheric Turbulence and Air Pollution Modelling, edited by: Nieuwstadt, F. T. M. and van Dop, H., D. Reidel Publishing Company, Dordrecht, Holland, 1982.

Nehrkorn, T., Eluszkiewicz, J., Wofsy, S. C., Lin, J. C., Gerbig, C., Longo, M., and Freitas, S. (2010): Coupled weather research and forecasting-stochastic time-inverted lagrangian transport (WRF-STILT) model, *Met. Atmos. Phys*, *107*, 51–64,doi:{10.1007/s00703-010-0068-x}.